FLIGHT SIMULATION OF THE MODEL 347 ADVANCED TANDEM-ROTOR HELICOPTER

Don F. Kesler, et al

Northrop Corporation

Prepared for:

Army Air Mobility Research and Development Laboratory

November 1974

EUSTIS DIRECTORATE POSITION STATEMENT

This report has been reviewed by the Eustis Directorate, U. S. Army Air Mobility Research and Development Laboratory and is considered to be technically sound.

In essence, the simulation developed is a full-maneuvering, large-perturbation model capable of a mission envelope from precision hover to forward flight and is capable of being used for (a) flight control system design and verification, (b) pilot evaluation and training, (c) subsystem evaluation, (d) flight test planning, and (e) a research device for handling and flying qualities criteria.

The technical monitor for the contract was Mr. Robert P. Smith, Technology Applications Division.

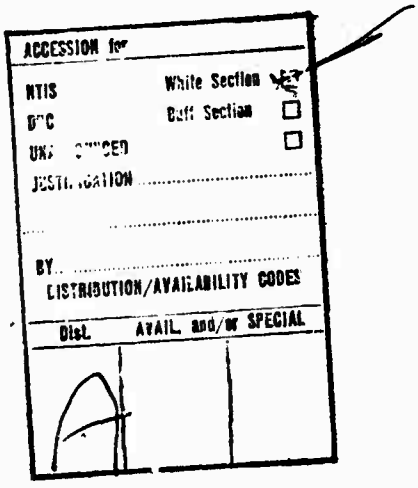

ii

UNCLASSIFIED

SECURITY CLASSIFICATION OF THIS PAGE (When Data Entered)

REPORT DOCUMENTATION PAGE		READ INSTRUCTIONS BEFORE COMPLETING FORM
1. REPORT NUMBER USAAMRDL-TR-74-21	2. GOVT ACCESSION NO.	3. RECIPIENT'S CATALOG NUMBER AD/A-005050
4. TITLE (and Subtitle) FLIGHT SIMULATION OF THE MODEL 347 ADVANCED TANDEM-ROTOR HELICOPTER		5. TYPE OF REPORT & PERIOD COVERED Final Report July 1972 - October 1974
		6. PERFORMING ORG. REPORT NUMBER NOR 73-190
7. AUTHOR(s) Don F. Kesler Allen Y. Murakoshi John B. Sinacori		8. CONTRACT OR GRANT NUMBER(s) DAAJ02-72-C-0112
9. PERFORMING ORGANIZATION NAME AND ADDRESS Northrop Corporation, Aircraft Division 3901 West Broadway Hawthorne, Calif. 90250		10. PROGRAM ELEMENT, PROJECT, TASK AREA & WORK UNIT NUMBERS Task 1F163204D15714
11. CONTROLLING OFFICE NAME AND ADDRESS Eustis Directorate, U. S. Army Air Mobility Research and Development Laboratory Fort Eustis, Va. 23604		12. REPORT DATE November 1974 13. NUMBER OF PAGES 162
14. MONITORING AGENCY NAME & ADDRESS(if different from Controlling Office)		15. SECURITY CLASS. (of this report) Unclassified 15a. DECLASSIFICATION/DOWNGRADING SCHEDULE

16. DISTRIBUTION STATEMENT (of this Report)

Approved for public release; distribution unlimited.

17. DISTRIBUTION STATEMENT (of the abstract entered in Block 20, if different from Report)

18. SUPPLEMENTARY NOTES

PRICES SUBJECT TO CHANGE

19. KEY WORDS (Continue on reverse side if necessary and identify by block number)

Flight simulation	Handling qualities criteria	Sling load
Helicopters	Heavy lift helicopters	Aerodynamics
Tandem rotor helicopters	Load carrying	
Flight control system design	Moving base simulator	

20. ABSTRACT (Continue on reverse side if necessary and identify by block number)

The basic purpose of the study was to define important flight control system design and handling qualities criteria for moving loads slung beneath tandem-rotor heavy lift helicopters. The principal study effort involved flight simulation of the Model 347 advanced tandem-rotor helicopter. Methodologies used in developing data included theoretical analyses, acquisition and evaluation of wind tunnel and flight test data, derivation of motion equations, analysis of sling load carrying problems, development of the dynamics of a container slung

DD FORM 1 JAN 73 1473

Unclassified

SECURITY CLASSIFICATION OF THIS PAGE (When Data Entered)

20. continued

beneath a tandem-rotor helicopter, and the actual flight simulation of a Model 347 helicopter with external loads using Northrop's advanced large-amplitude moving-base simulator and its associated hybrid computers.

The results of this and several other helicopter simulation studies conducted concurrently generated a considerable body of data which should prove to be useful in heavy lift helicopter flight control system design as well as in determining the dynamic characteristics of moving sling loads under varying flight conditions.

The conclusions reached were that the flight simulation provided an effective representation of a large tandem-rotor helicopter, that unsteady aerodynamic effects are a predominant factor in sling load dynamics, and that the use of a nominal 10-degree load angle of attack in pitch and yaw and the use of wide cable separation and short cable lengths will minimize sling load dynamics.

PREFACE

This final technical report covers a study program conducted to define important flight control system design and handling quality criteria for moving loads slung beneath tandem-rotor heavy lift helicopters. The study was conducted by members of the Flight Simulation Test Group, with Mr. J.B. Sinacori serving as Principal Investigator. Principal contributors to the simulation portion of the study were Messrs. A.Y. Murakoshi, R. Silvestri, W.G. Spring, and W.L. Ross. The non-linear sling loads analysis was performed by G.L. Danek.

The basic study involved flight simulation of the Model 347 advanced tandem-rotor helicopter and was sponsored by the U.S. Army Air Mobility Research and Development Laboratories (USAAMRDL), under Contract DAAJ02-72-C-0112. Mr. Robert P. Smith served as USAAMRDL monitor. Work was started in July 1972 and the study was completed in October 1973. During that 15-month period, a detailed mechanization of a tandem-rotor heavy lift helicopter was developed for use with Northrop's large-amplitude moving-base simulator and its integrated computer facilities. These simulation facilities and the detailed helicopter mechanization were used during the 15-month contract period on a directly related USAAMRDL study (Contract DAAJ02-72-C-0047) involving the stabilization of externally slung helicopter loads and for related HLH control system studies conducted by Boeing-Vertol and a closely related study conducted by Northrop under direct contract with Boeing.

As work on these closely related study projects progressed, the commonality of many study objectives became apparent. The impact of this commonality resulted in modification of certain aspects of the Contract DAAJ02-72-C-0112 study to avoid duplication of effort and to take advantage of the detailed simulator mechanization set up for the other directly related control system simulation studies. Thus, a substantial body of data developed during the conduct of the Contract DAAJ02-72-C-0047 study and certain data developed during the Boeing-Vertol simulator studies have been integrated with Contract DAAJ02-72-C-0112 data and are contained in this report.

The major subsections that comprise the body of this report discuss derivation of the equations of motion, analysis of sling load carrying problems, the dynamics of an 8-by-8-by-20-foot container slung beneath a tandem-rotor helicopter, and a Model 347 helicopter flight simulation with external loads. Methodologies used in developing this data include theoretical analyses, acquisition and evaluation of static and dynamic wind tunnel and flight test data, and piloted ground-based simulation. The discussion is followed by a brief statement of conclusions reached, and the report concludes with an appendix containing functional block diagrams and other data relative to the computerized flight simulation of the Model 347 helicopter.

TABLE OF CONTENTS

LIST OF ILLUSTRATIONS

LIST OF TABLES

AIRFRAME DYNAMIC MODEL AND EQUATIONS OF MOTION

The mathematical model used for simulation of the full flight envelope of the Model 347 tandem-rotor heavy lift helicopter is described in detail in Reference 1 and is summarized in this section. Brief descriptions of each major calculation are presented in the general order of their performance, starting with equations of motion and concluding with the forces and moments that drive the motion equations.

The helicopter is modeled as a rigid body, with symmetry assumed about the X-Z plane so that I_{xy} and I_{yz} are zero. Linear and angular accelerations of the airframe are expressed in the helicopter body axis system. The forces X, Y, and Z and moments L, M, and N contain only aerodynamic terms. Euler angle rotations are performed to orient the airframe in inertial space. The basic equations of motion providing linear and angular accelerations about the X, Y, and Z axes are:

Linear Acceleration

$$\dot{u} = \frac{X}{m} - g \sin\theta + Rv - Qw$$

$$\dot{v} = \frac{Y}{m} + g \sin\phi \cos\theta + Pw - Ru$$

$$\dot{w} = \frac{Z}{m} + g \cos\phi \cos\theta + Qu - Pv$$

Angular Acceleration

$$\dot{P} = \frac{L}{I_{xx}} + \left(\frac{I_{xz}}{I_{xx}}\right)\dot{R} + \left[\frac{(I_{yy} - I_{zz})}{I_{xx}}\right] QR + \left(\frac{I_{xz}}{I_{xx}}\right) PQ$$

$$\dot{Q} = \frac{M}{I_{yy}} + \left(\frac{I_{xz}}{I_{yy}}\right)(R^2 - P^2) + \left[\frac{(I_{zz} - I_{xx})}{I_{yy}}\right] RP$$

$$\dot{R} = \frac{N}{I_{zz}} + \left(\frac{I_{xz}}{I_{zz}}\right)\dot{P} + \left[\frac{(I_{xx} - I_{yy})}{I_{zz}}\right] PQ - \left(\frac{I_{xz}}{I_{zz}}\right) QR$$

---

1. Cogan, C., Gajkowski, B.J., and Gurnett, T.S., Jr., FULL FLIGHT ENVELOPE MATHEMATICAL MODEL FOR 347/HLH CONTROL SYSTEM ANALYSIS, The Boeing Company Report No. D301-10148-1, December 1972.

The linear and angular accelerations of the helicopter were mechanized for the hybrid simulation on an analog computer. By integrating these accelerations with time, linear and angular velocities in the body axis are produced. Fuselage angle of attack and sideslip information are derived from body axis linear velocity resolutions, corrected for the influence of rotor downwash on the fuselage and for steady wind or gust velocity.

The total linear aerodynamic velocities associated with fuselage α_{FUS} and β consist of body axis ground speed, steady wind velocity resolved into the aircraft body axis, and gust velocity resolved into the aircraft body axis. Steady wind velocities introduced into the linear velocity equations are based on a steady wind (V_W) blowing from a fixed azimuth (Ψ_W) in the inertial X-Y plane on to the helicopter. This wind from the fixed inertial axis is resolved into the body axis and rotor axes of the helicopter.

Before the fuselage angle of attack can be defined, using aerodynamic velocities, the effect of rotor downwash on the fuselage must also be considered. The forward and aft rotors both produce a downwash component on the fuselage that is assumed to be equal to an "average" induced velocity of the rotor system. Fuselage sideslip angles do not require correction for rotor downwash interference and may therefore be defined as functions of total longitudinal and lateral aerodynamic velocity.

Rotor forces and moments can be calculated as soon as the rotor control inputs, angle of attack and sideslip values, and both inflow and advance ratios are known. Rotor angle of attack and sideslip are computed from linear velocity components in the same way as described for the fuselage.

The first step in computing rotor sideslip or angle of attack is to sum the total velocity components with the velocity of each rotor relative to the aircraft center of gravity created by the aircraft's angular pitching motion (tangential velocity component resulting from airframe angular velocities).

Next, the linear velocities at each rotor hub are resolved through the shaft incidence angle into the shaft normal plane (SNP). According to classical rotor theory, all rotor force, moment, and flapping calculations are based on the assumption that the rotor faces directly into the wind, with no sideward velocity component existing. To meet this requirement for zero sideward velocity, the longitudinal and lateral velocity components at the rotor hubs are resolved through the rotor sideslip angle (β') into the SNP wind axis. A single velocity vector in the rotor SNP is formed and is defined as being parallel to the local wind direction in the rotor.

Rotor advance and inflow ratios (μ and λ) are defined as the ratio of the rotor SNP wind axis longitudinal and vertical velocity components, respectively, to the rotor tip speed. These values of advance ratio are used for all rotor calculations carried out with the classical equation approach. Rotor maps, on the other hand, require the use of a modified advance ratio because the tabular map data is nondimensional.

Inflow ratio is comprised of terms resulting from free-stream velocity (normal to the rotor) and induced velocity. Two terms are added to the free-stream velocity component of the inflow ratio. One accounts for the uniform induced velocity of the rotor under consideration, and the second reflects the interference downwash of the other rotor imposed on the rotor under consideration.

Each rotor of a tandem-rotor helicopter receives only three types of input under pilot control:

- Collective Pitch θ_o, produced by longitudinal and collective stick or Stability Augmentation System (SAS)/Automatic Flight Control System (AFCS) inputs.
- Longitudinal Cyclic (B_{IC}), normally comprised of "q" sensed cyclic trim and/or AFCS cyclic "on the stick" inputs.
- Lateral Cyclic (A_{IC}), comprising a combination of lateral stick and pedal or AFCS/SAS inputs.

Rotor input collective and cyclic controls (θ_o, B_{IC}, A_{IC}) are compiled and both longitudinal and lateral cyclics are resolved through the rotor sideslip angle to align controls orthogonally to the local wind. Forward rotor cyclic inputs are corrected for delta three (δ_3) hinging effects. These corrections account for the phasing of the control system to produce orthogonal flap response and for the change in blade pitch occurring because of the δ_3 pitch-flap coupling effects.

Coning (a_0), longitudinal (a_I), and lateral (b_I) first harmonic flapping coefficients are computed and first-order dynamic lags are applied to account for rotor system flapping response. Representation of rotor flapping in the dynamic model is accomplished by using quasi steady-state classical calculations based on the following assumptions:

- First harmonic theory
- Uniform inflow
- No reverse-flow effects

- Identical forms for front and rear equations
- Uniformly twisted untapered blades
- No δ_2 effects (accounted for by correcting input controls, as discussed earlier)
- Zero tip-loss factor
- Negligible hinge offset
- Rigid blades
- No stall and compressibility effects
- Constant lift-slope and drag coefficients varying only with C_L.

Rotor forces and moments are computed, using either the classical equation method or the rotor map approach. In the former case, forces are resolved perpendicular and parallel to the SNP and aligned with the SNP wind axis. In the latter case, rotor thrust, power, and propulsive forces are derived from isolated tabular rotor or wind tunnel data and expressed in the rotor wind axis.

Fuselage aerodynamic forces and moments are calculated from tabular data derived from wind tunnel tests. Rotor aerodynamic forces and moments are resolved through rotor sideslip and shaft incidence angles back into the aircraft body axis. These resolved forces and moments are summed with body axis (fuselage) forces and added to each moment imposed on the aircraft by individual rotor T, H, and Y forces. These force and moment sums are inserted in the equations of motion to compute the airframe acceleration set.

Engine governor response to aerodynamic rotor power requirements is computed along with individual rotor speed degrees of freedom. Rotor shaft windup spring rates are accounted for in the governor model.

The external sling load is coupled with the rigid-body helicopter equations of motion described on page 6. The aerodynamic force and moment data used with the sling load equations is given in Table 1.

TABLE 1. EXTERNAL SLING LOAD AERODYNAMIC FORCE AND MOMENT DATA

(Sharp-Edged Box - Body Axis)

α_L / β_L	DRAG, D_{LT}			YAWING MOMENT, N_{LT}			SIDE FORCE, Y_{LT}		
	0	-10	-20	0	-10	-20	0	-10	-20
0	54.94	62.99	67.72	9.2	-4.8	-11.5	-2.3	-1.9	-4.0
2	57.27	63.69	68.70	42.7	-12.6	-39.6	-9.8	-12.4	-19.8
4	58.76	64.39	69.68	64.8	-19.0	-65.5	-14.8	-20.9	-35.5
6	60.73	66.62	70.47	88.3	-27.0	-89.4	-21.6	-30.9	-49.9
8	62.17	67.94	71.17	93.6	-26.8	-87.9	-27.4	-38.2	-61.5
10	63.31	68.56	70.39	84.9	-31.9	-87.7	-32.4	-44.3	-68.4
12	65.19	68.80	69.80	59.4	-51.9	-94.7	-38.5	-52.2	-75.8
14	67.50	68.86	71.26	33.9	-72.1	-117.4	-44.6	-59.4	-85.9
16	68.22	69.96	71.04	4.3	-75.3	-122.6	-50.8	-67.0	-93.4
20	70.47	72.63	71.37	-62.8	-59.6	-130.4	-65.7	-82.1	-103.5
25	69.5	70.38	71.01	-121.3	-87.5	-146.4	-86.0	-99.0	-113.0
30	68.6	68.12	70.65	-179.8	-115.3	-164.4	-107.5	-115.6	-122.6
40	58.28	58.86	61.75	-232.9	-175.9	-200.2	-144.6	-144.1	-155.3
50	45.42	48.33	46.21	-259.2	-227.3	-223.6	-175.0	-180.9	-184.8
90	.30	-1.32	-4.54	-3.1	-8.0	-1.6	-225.8	-225.7	-225.7

NOTE: Units for the aerodynamic forces and moments above are:
$D_{LT}(FT^2) = D/q$, $N_{LT}(FT^3) = N/q$, and $Y_{LT}(FT^2) = Y/q$.

The method of integrating the sling load equations with those of the helicopter is described in following paragraphs.

The rigid-body equations for two vehicles (helicopter and load) were linked by additional equations describing cable tension forces. These forces and their corresponding moments were added to the forces and moments due to gravitational and aerodynamic effects. The key is to describe the movements of the lower attach point relative to the upper one for each cable, and compute the tension force as a function of the cable elongation beyond the zero tension value. The cable forces are written in terms of the stretched length and length rate and are used together with matrix representations for the displacements of the lower attach points (load) relative to helicopter-fixed axes. The coupled equations describing the movements of two vehicles in twelve degrees of freedom when there is a single cable attached to both vehicles follow:

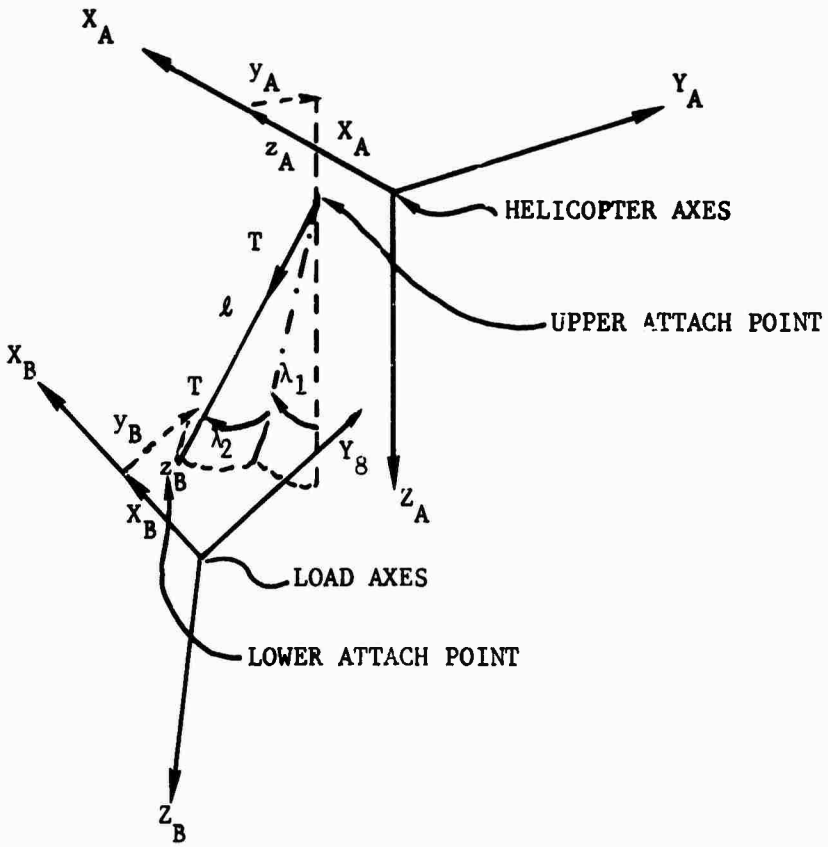

The nomenclature describing the axes systems used and attach points for one cable is shown above. In this diagram, ℓ is the straight line distance between the attach points. When this distance ℓ is greater than ℓ_o, the zero tension cable length, a tension T exists which will produce forces and moments on helicopter and load, thereby coupling them together dynamically. It now remains to compute the angles λ_1 and λ_2 and postulate the cable tension T as a function of ℓ and its derivatives. The format for these computations shown for n^{th} number of cable systems is given on the following pages.

1) Difference between lower attach point velocity and upper attach point velocity, relative to helicopter axes for the n^{th} cable.

$$\begin{bmatrix} u_{BA_n} \\ v_{BA_n} \\ w_{BA_n} \end{bmatrix} = [A][B]^T \begin{bmatrix} u_B + q_B z_{B_n} - r_B y_{B_n} \\ v_B + r_B x_{B_n} - p_B z_{B_n} \\ w_B + p_B y_{B_n} - q_B x_{B_n} \end{bmatrix} - \begin{bmatrix} u_A + q_A z_{A_n} - r_A y_{A_n} \\ v_A + r_A x_{A_n} - p_A z_{A_n} \\ w_A + p_A y_{A_n} - q_A x_{A_n} \end{bmatrix}$$

2) Difference between attach points, computation of ℓ_n, λ_{1n}, λ_{2n} and their rates.

$$X_{BA_n} = \int_0^t u_{BA_n} dt \quad , \quad Y_{BA_n} = \int_0^t v_{BA_n} dt \quad , \quad Z_{BA_n} = \int_0^t w_{BA_n} dt$$

$$\lambda_{1n} = \tan^{-1}\left(\frac{X_{BA_n}}{Z_{BA_n}}\right), \quad \lambda_{2n} = \sin^{-1}\left(\frac{-Y_{BA_n}}{\ell_n}\right)$$

$$\ell_n = (X_{BA_n}^2 + Y_{BA_n}^2 + Z_{BA_n}^2)^{\frac{1}{2}}$$

$$\dot{\lambda}_{1n} = \frac{\dot{X}_{BA_n}}{Z_{BA_n}} + \left(\frac{-\dot{\ell}_n}{\ell_n} + \dot{\lambda}_{2n}\right) \tan \lambda_{1n} \tan \lambda_{2n}$$

$$\dot{\lambda}_{2n} = \frac{-\dot{Y}_{BA_n}}{\ell_n \cos\lambda_{2n}} - \frac{\dot{\ell}_n}{\ell_n} \tan \lambda_{2n}$$

$$\dot{\ell}_n = \dot{X}_{BA_n} \sin\lambda_{1n} \cos\lambda_{2n} - \dot{Y}_{BA_n} \sin\lambda_{2n} + \dot{Z}_{BA_n} \cos\lambda_{1n} \cos\lambda_{2n}$$

3) Resolution of the nth cable tension T_n into forces and moments in helicopter and load axes.

$$\begin{bmatrix} X_{BT_n} \\ Y_{BT_n} \\ Z_{BT_n} \end{bmatrix} = [B][A]^T [\lambda_n]^T \begin{bmatrix} 0 \\ 0 \\ -T_n \end{bmatrix}, \quad \begin{bmatrix} L_{BT_n} \\ M_{BT_n} \\ N_{BT_n} \end{bmatrix} = \begin{bmatrix} x_{B_n} \\ y_{B_n} \\ z_{B_n} \end{bmatrix} X \begin{bmatrix} X_{BT_n} \\ Y_{BT_n} \\ Z_{BT_n} \end{bmatrix}$$

$$\begin{bmatrix} X_{AT_n} \\ Y_{AT_n} \\ Z_{AT_n} \end{bmatrix} = [\lambda_n]^T \begin{bmatrix} 0 \\ 0 \\ T_n \end{bmatrix}, \quad \begin{bmatrix} L_{AT_n} \\ M_{AT_n} \\ N_{AT_n} \end{bmatrix} = \begin{bmatrix} x_{A_n} \\ y_{A_n} \\ Z_{A_n} \end{bmatrix} X \begin{bmatrix} X_{AT_n} \\ Y_{AT_n} \\ Z_{AT_n} \end{bmatrix}$$

In the above expressions, the matrices $[A]$ and $[B]$ represent the commonly used orientation matrices of direction cosines for the helicopter ($[A]$) and the load ($[B]$) respectively. The matrix $[\lambda n]^T$ represents the transpose of the orthogonal matrix of direction cosines of the taut cable after being rotated through the angles λ_{1n} and λ_{2n}.

$$[\lambda_n]^T = \begin{bmatrix} \cos\lambda_{1n} & \sin\lambda_{1n}\sin\lambda_{2n} & \sin\lambda_{1n}\cos\lambda_{2n} \\ 0 & \cos\lambda_{2n} & -\sin\lambda_{2n} \\ -\sin\lambda_{1n} & \cos\lambda_{1n}\sin\lambda_{2n} & \cos\lambda_{1n}\cos\lambda_{2n} \end{bmatrix}$$

4) Finally, the cable tension equations must be written. In the case chosen, the cable is assumed to tense when its length is greater than its zero-tension value. The tension functions are assumed to be linear; i.e., the force is proportional to the cable stretch and stretch rate.

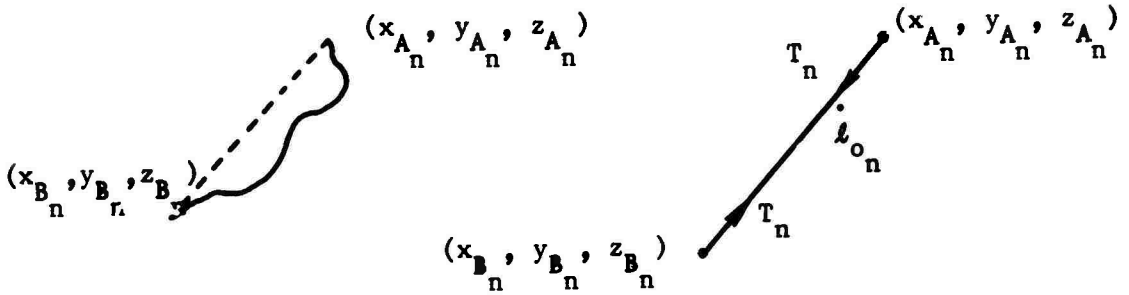

$\ell_n < \ell_{o_n}$ $\qquad$ $\ell_n \geq \ell_{o_n}$

$T_n = 0$ $\qquad$ $T_n = K_{\ell_n}(\ell_n - \ell_{o_n}) + K_{\dot{\ell}_n}\dot{\ell}_n$

(CABLE SLACK) $\qquad$ (CABLE TAUT)

Other tension functions may be used to represent sling material such as nylon, which is known to have nonlinear tensile properties.

ANALYSIS OF SLING LOAD CARRYING PROBLEMS

The validity of the linear analysis of sling loads was tested by comparing its results with flight data. A number of candidate sling-load flight tests were examined, and two well-documented cases were selected for comparison. The first case involved a test of an empty MILVAN container on a two-cable suspension by a CH-47C helicopter as described in Reference 2. The container was carried small-end-into-the-wind, using a spreader beam weighing 3505 pounds. Reports of the pilot and observer about container motions, and the pilot's judgments about maximum allowable carrying speed, were studied. The results are summarized in Table 2.

The second case involved a lift made in Colorado by a CH-54 Tarhe. The load was a 13,500-pound mobile home slung on a single cable with cross-slings and spreader bars. Observer reports from a chase helicopter and film records were examined in detail. The findings are summarized in Table 3.

In general, the comparisons are very poor, particularly when the container is carried small-end-forward on a two-point suspension. The linearized analysis predicted no instabilities, with an increasing yaw frequency as airspeed increases, while the observations showed sustained yaw oscillations t about the zero airspeed (bifilar) frequency. In the broadside case, .o pilot reports of oscillatory frequency were available. Indeed, the analysis predicted a damped oscillatory motion which was not apparent in the film records. The comparison, therefore, is quantitatively inconclusive but qualitatively interesting because the load did stabilize to a broadside position and the airspeeds flown were less than the predicted maximum stable airspeed.

This generally poor correlation coupled with the lack of good data for dynamic comparison prompted the setup of an analog computer to conduct a nonlinear analysis. A parallel theoretical effort was also initiated. The simple linearized equations of motion previously described were programmed, the yaw axis was made to allow continuous rotation, and yawing

---

2. Watkins, T.C., Sinacori, J.B., and Kesler, D.F., STABILIZATION OF EXTERNALLY SLUNG HELICOPTER LOADS, Northrop Corporation Aircraft Division; USAAMRDL Technical Report 73-42, Eustis Directorate, U. S. Army Air Mobility Research and Development Laboratory, Fort Eustis, Va., August 1974.

TABLE 2. FLIGHT DATA ANALYSIS COMPARISON
(8-By-8-By-20-Foot Empty Container, Two-Point Suspension)

FLIGHT DATA

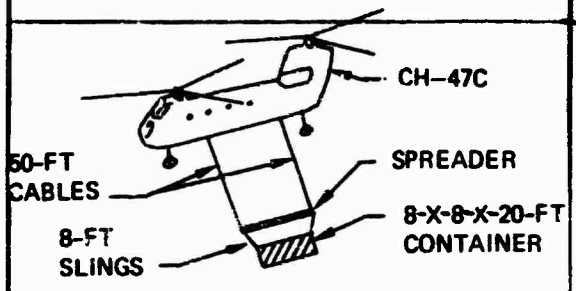

Load Weight
- Container.....5200 lb
- Spreader Beam.....3505 lb

Cable Length..... 50 ft
Sling Length..... 8 ft
Cable Separation..... 24 ft
Rigged Pitch Angle..... 0°

OBSERVATIONS

The level container with 50-ft cables exhibited a yaw oscillation of 0.25 Hz (1.57 rad/sec) with an amplitude of ±35° at an airspeed of 90 kn. This load oscillation coupled with a lateral swinging induced an aircraft roll oscillation of ±5°. The load motion fed forces into the aircraft which were heavy and uncomfortable. The maximum recommended airspeed for operational conditions was considered to be 70 kn.

ANALYSIS

Load Weight.....8705 lb
Estimated Yaw Inertia .9011 slug-ft^2

ℓ.....62 ft
ℓ_B^p.....50 ft
X_C.....12 ft
Angle of Attack..... 0°

C_{n_β} = + 1.74/rad $(-10° < \beta < 10°)$

C_{Y_β} = -2.06/rad $(-10° < \beta < 10°)$

C_{n_r} = -1.625 $(-10° < \beta < 10°)$

ROOT PLOT

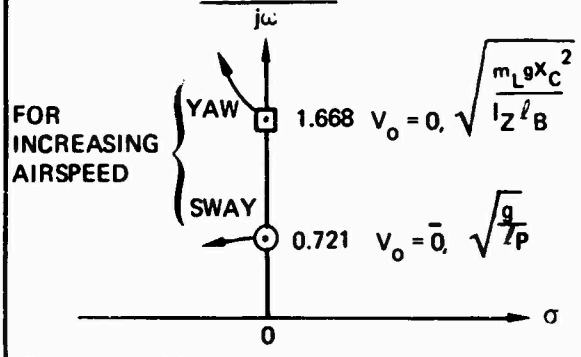

No instability occurs up to airspeeds of 100 kn.

*Estimated from the assumption of a longitudinally uniform container

$$I_Z = \frac{m_L X_{B_L}^2}{3}, \quad X_{B_L} = 10 \text{ ft}$$

SYNOPSIS

Results of the analysis show no instability with damped yaw oscillation of frequency that increases with airspeed. Sway damping increases, but frequency is nearly constant. Flight observation shows a sustained yaw oscillation at the zero airspeed frequency of the analysis. The yaw amplitude is obviously exceeding the sideslip constraint for the aerodynamic data of the analysis. Generally, there is very poor correlation between analytical results and flight observations.

TABLE 3. FLIGHT DATA ANALYSIS COMPARISON
(Mobile Home, Single-Point Suspension)

FLIGHT DATA

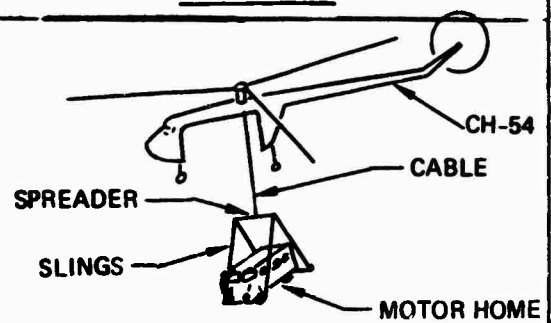

Load Weight.....13,500 lb

Load Dimensions

Length.....	23 ft
Width.....	7 ft
Height.....	8 ft

Cable Length
Hook to load ctr of mass...40 ft

Rigged Pitch Angle..... -5°

ANALYSIS

Load Weight.....13,500 lb
Estimated Yaw Inertia 18,482 slug-ft^2

ℓ_p.....	40 ft
X_c.....	0
Angle of Attack.....	-5°

C_{n_β} = 0.87/rad ($\pm 80° < \beta_L < \pm 100°$)

C_{Y_β} = -0.07/rad ($\pm 80° < \beta_L < \pm 100°$)

C_{n_r} = -1.625 ($\pm 80° < \beta_L < \pm 100°$)

$$*I_Z = \frac{m_L X_{B_L}^2}{3}, \quad X_{B_L} = 11.5 \text{ ft}$$

OBSERVATIONS

The load tended to rotate in yaw, but stabilized in the broadside position. Maximum airspeed reached was about 60 kn. No instability was encountered, even in turbulence.

ROOT PLOT

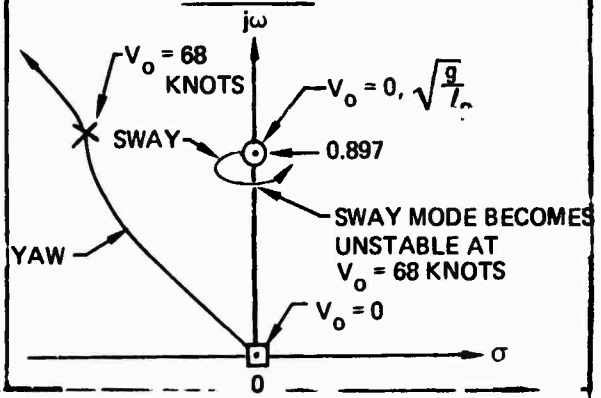

SYNOPSIS

The significance of this comparison is that the load stabilized in the broadside position, which is verified by the analysis in which two broadside yawing moment nulls are predicted, with dynamic stability about those points below an airspeed of 68 knots. A specific yaw frequency check is not possible because it was not observed in flight. This case indicates positively that the static aerodynamics used with a simple analysis may in fact be predicting reality correctly.

moment data for any value of yaw and sideslip angle was incorporated. This extension of the analysis did not provide results that compared favorably with flight data. No sustained oscillation could be produced, although many of the properties of the broadside case could be reproduced. Therefore, a redirection of effort became necessary and is described in the following section.

DYNAMIC WIND TUNNEL TESTS

TEST PROCEDURE

Previous attempts to predict the action of sling loads by using a linearized dynamic model based on static wind tunnel data resulted in a poor prediction for the small-end-forward case and a somewhat better prediction for the broadside case. Since the broadside case is not likely to be the candidate position for high-speed operations (due to drag), a better analytical method is needed before an understanding of sling load behavior can be achieved. Certainly, what has been learned to date is not sufficient to justify a formal study of all the variables and all the possible stabilization schemes.

With this in mind, our effort was redirected so that a dynamic wind tunnel test could be performed. The belief at this point was that unsteady aerodynamic effects were present which dominated the dynamics, particularly for the more important small-end-forward ca e.

The 0.1-scale model of the 8-by-8-by-20-foot container used for the static tests was available and was modified slightly so that it could be hung in the tunnel test section. The suspension system consisted of two cables with end fittings that allowed the creation of a number of single- and two-point suspension systems. Attach points were available at 1, 3, 5, 7, and 9 inches on either side of center.

Tufts were taped to the model for airflow identification, and the floor of the tunnel was striped for a camera reference. All the pertinent variables were measured, including yawing moment of inertia, weight and center-of-gravity location, cable length, and cable separation. The primary instrumentation consisted of a 16mm camera located above the tunnel as depicted in Figure 1. An airspeed cone was hung in the tunnel for a visual indication of airspeed.

A rigorous analysis of the model was made before the tests began, using the linearized equations of motion and the static wind tunnel test results. To measure the yaw damping function C_{N_r}, a variety of cases sensitive to this parameter were isolated and incorporated in the test plan.

The basic test procedure was to restrain the model by a hand-held fork, bring the tunnel up to speed, start the camera, and then release the model. The initial sway angle was set to either zero, six, or twelve degrees. Zero was generally used for the more active conditions, and six degrees was generally used for the milder ones.

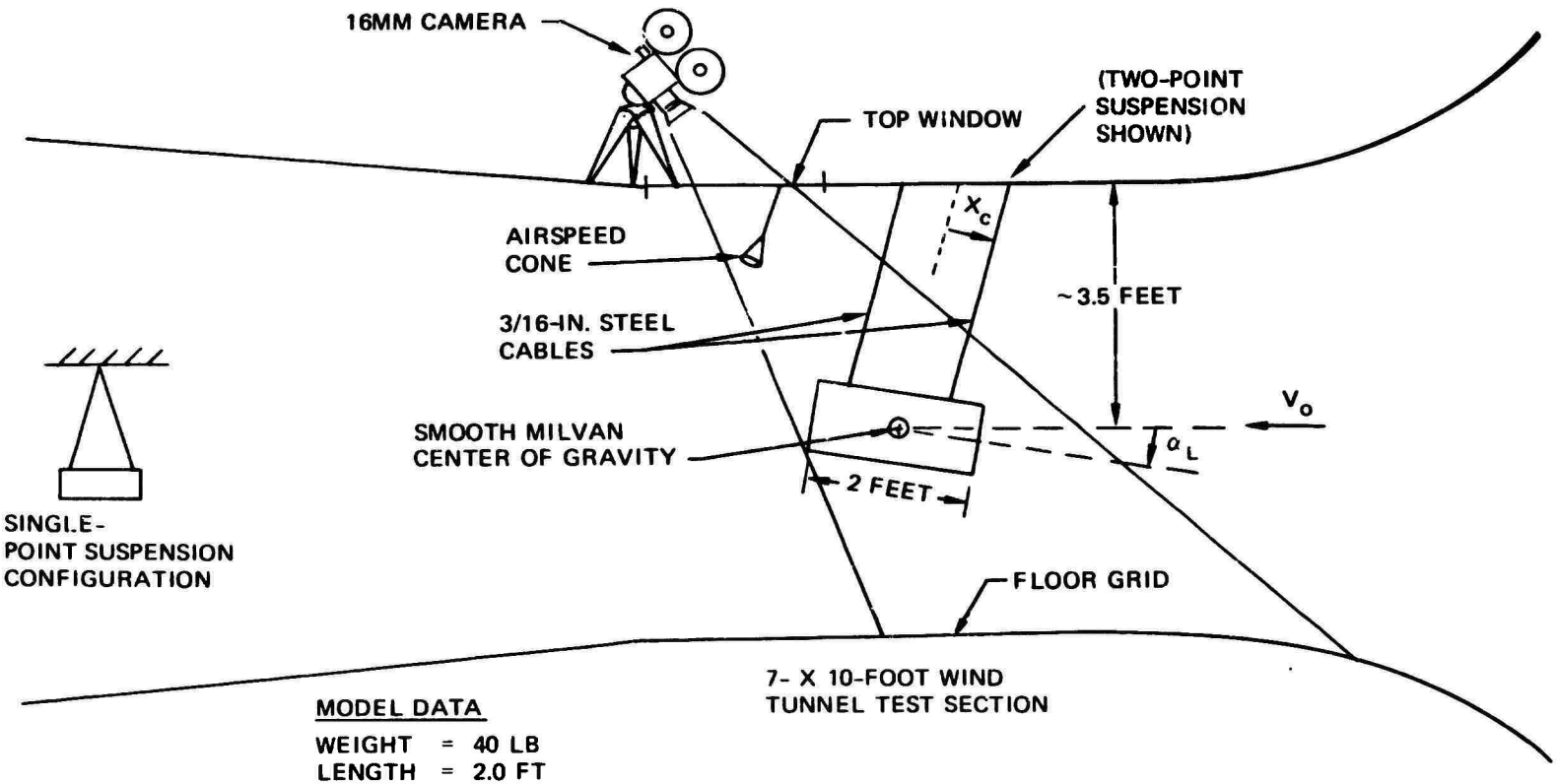

FIGURE 1. 0.1-SCALE MILVAN DYNAMIC WIND TUNNEL TEST SETUP.

Documented runs totalled 47, including 3 calibration runs, 17 basic container runs, 22 with fixed fins added, 3 with drogue chutes, and 2 for smoke flow visualization tests. Included in the basic and finned tests were level and drooped runs (to vary angle of attack), narrow cable runs, unequally spaced cable runs, and single cable runs.

TEST RESULTS

1. The first free model run at 20 knots tunnel speed for the level box showed a surprising disparity from the analog computer runs using the static aerodynamic data. It was clear that an energy-producing device was causing a large yaw limit cycle of approximately ±20 degrees amplitude at the bifilar frequency. As the tunnel speed was increased to 40 knots, the amplitude increased and the fixed point of rotation moved forward to the front of the model. All stable limit cycle motions occurred at the bifilar frequency.

When hung from a single cable, the model turned broadside and developed a lateral swaying motion. With closely spaced cables, the center of rotation moved toward the rear of the model. For angles of attack of -10 and -14 degrees, the model was almost completely still.

2. Eight finned configurations were tested, three of which produced very little motion. The successful configurations incorporated a long fin projecting out of the center of the rear face (Runs 12-15) or two fins projecting back from the rear corners, simulating opening the rear doors of the MILVAN. The fin length was 20 percent of the length of the MILVAN. Fins of 10 percent MILVAN length were not effective. Tilting the finned MILVAN 10 degrees down was even better, as the tunnel speed could be taken to 67 knots. Initial sway angles of 12 degrees were successfully tested at this speed.

3. Drogue chutes had little effect on the stability of the MILVAN. One drogue chute was simulated by a paint filter cone and was attached to the center of the rear of the MILVAN. This configuration showed almost no reduction in yaw amplitude. When the chute was connected by two cables to the outer corners of the container, the yaw amplitude was reduced when no initial sway angle was introduced; however, it reached a stable limit cycle in yaw after a disturbance.

4. For smoke tests (Runs 34 and 35), a smoke generator was hand-held in the vicinity of the model and the path of the smoke was observed from above and at the sides of the test section. Smoke released near the center of the forward face would billow out around the sides, revealing a separation pattern. As the model oscillated, the pattern alternated asymmetrically. The face on the downstream side exhibited a large separation plume, while the plume on the upstream side appeared to subside.

Of more significance was the rapidity with which the plume changed. Smoke emitted just above the rear face, followed one of two curved paths, and appeared to snap from one to the other just after the sideslip angle passed through zero.

5. The behavior of tufts on the rear face was of considerable interest. They would snap back and forth just after the sideslip angle passed through zero. For example, as the rear face moved to the left from a maximum right position (nose left), the tufts would point left. As the rear face passed through the neutral position (about -3 degrees sideslip), the tufts reversed quickly and pointed right. This action then reversed itself.

NONLINEAR ANALYSIS OF THE 8-BY-8-BY-20-FOOT CONTAINER

The poor correlation between flight data and the results of the linearized analysis prompted the initiation of a nonlinear analysis. It was decided to use a small analog computer so that on-line comparisons with film records could be made in real time. Incorporation of the nonlinear aerodynamic yawing moment and the extension of the yaw degree of freedom to allow continuous rotation did not produce results that compared with flight data, particularly for the small-end-forward case.

INTERPRETATION OF DYNAMIC WIND TUNNEL TEST RESULTS

It was obvious from the beginning of these tests that a dynamic yawing moment existed that could not be attributed to damping moments due to yaw rate. The identification of this additional dynamic moment began with a detailed examination of the tuft behavior on the rear face. It is likely that the "switching" back and forth of the tufts was caused by a rapidly reversing flow pattern which, in turn, was caused by the transition of the flow back and forth from a partially separated state to a fully separated one. The resulting flow required time to establish itself and, in the process of doing so, generated unsteady flow effects. For example, when a two-dimensional airfoil is oscillated in a wind tunnel, a vortex is generated on the suction side while the angle of attack is increasing. This vortex precedes the separation and is accompanied by a low-pressure region which propagates downstream and creates a "pulse" of pitching moment.

It appears that this mechanism is responsible for creating the dynamic yawing moment. Specifically, as sideslip reaches about 3 degrees and is increasing, a vortex propagates downstream along the downstream side. When it reaches the rear face where the vortex can now "draw in" more flow, it does so, and a small sharp pulse of negative pressure appears on that side of the rear face. This causes the tufts to reverse and creates a small pulse of yawing moment that reinforces the oscillation. With this hypothesis in mind, Figure 2 depicts the dynamic yawing moment evolved from the analog matching study. Note that a moment hysteresis is present; i.e., a dynamic moment is present only when the product of sideslip and sideslip rate is positive and sideslip remains within certain limits.

ANALOG MATCHING STUDY

The motion of the tufts and the smoke pattern suggested that a vortex was being shed as the model rotated through nearly zero sideslip. The purpose of the analog matching study was to find a vortex model that could be added to the wind tunnel static aerodynamics and conventional rotary derivatives which would satisfactorily match the observed dynamic tunnel test results over a wide range of conditions. Ground rules were established for the vortex model as follows:

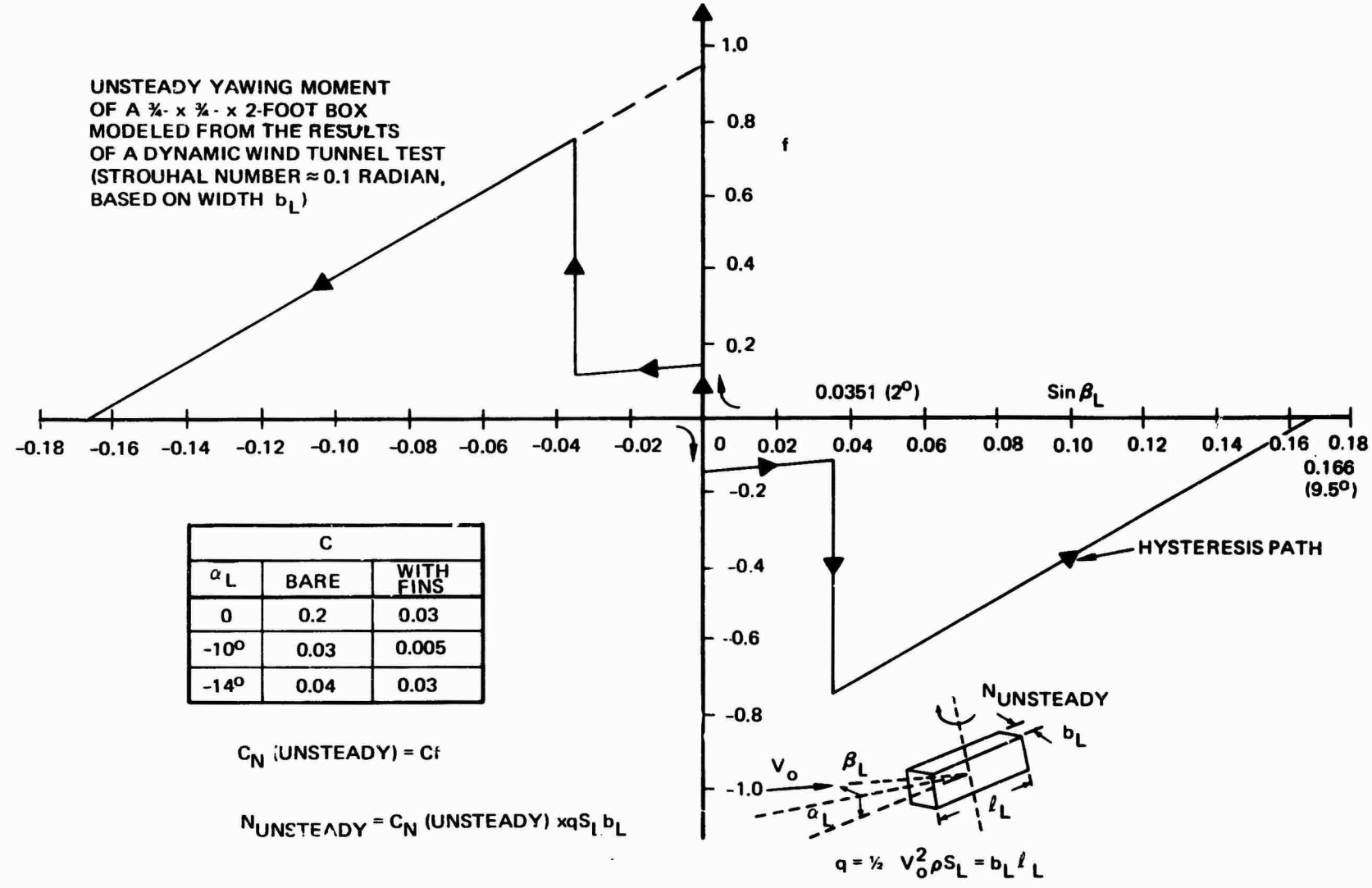

C		
α_L	BARE	WITH FINS
0	0.2	0.03
-10°	0.03	0.005
-14°	0.04	0.03

FIGURE 2. DYNAMIC (UNSTEADY) YAWING MOMENT FUNCTION.

1. The model should be compatible with established concepts of unsteady flow effects.

2. No changes to accommodate a match at different speeds should be necessary.

3. Changes could be made to accommodate different angles of attack and the addition of fins.

The matching conditions consisted of first generating an oscilloscope display representing the centerline of the MILVAN, scaled so that the sway and yaw modes appeared as if viewed from above. Next to the oscilloscope, the films of the tests were projected at approximately the same size. A computer, programmed with the appropriate initial conditions, was set to start computing when the projected film showed the model being released.

It was obvious at the start that an exact movement-for-movement match could not be made; therefore, an attempt was made to match the limit cycle frequency, growth and decay rates, and fixed point of rotation or phasing of the modes. Since C_{N_r} was an unknown parameter, initial attempts were made to match, using this parameter. It was found that a match could be made at various levels of C_{N_r}. Hence, it was set to a "reasonable" level and not changed. The larger the C_{N_r}, the larger the value of the unsteady moment that was required to match the wind tunnel data. This led to the energy balance concept presented in a following subsection. The shape and magnitude of the unsteady moment function had considerable influence on the growth and steady-state magnitude of the limit cycle. The shape could not be defined precisely because of the inaccuracy of the test data and the use of an eyeball match; however, as more test runs were matched, more confidence was gained in the model.

Some of the conditions that have a substantial impact on the shape of the unsteady function (Figure 2) are illustrated by the following examples. Three runs at a 14-degree angle of attack displayed an extreme speed sensitivity and a dual mode stability. These cases and others tended to have a small-amplitude stable limit cycle with no initial disturbance and, when disturbed, a large-amplitude limit cycle. An increase in speed in one run at -14 degrees of attack angle caused a change in limit cycle. There were no cases of limit cycle amplitudes between approximately ± 2 and ± 10 degrees. These conditions were met by reducing the magnitude of the unsteady function at sideslip angles near zero and forcing it to zero beyond ± 9.5 degrees sideslip. After this form of unsteady moment function was used, only changes in magnitude were required to match the

various configurations. The fact that the unsteady function was zero beyond ±10 degrees sideslip and the fact that the container had its best stability at angles of attack of ±10 degrees are probably related.

Because of the phasing of the sway and yaw motions, one point on the container appeared to be fixed relative to the tunnel. This is referred to as the "fixed point of rotation." It is interesting to note that this fixed point of rotation was near the front and moved forward with increased speed when X_c = 9 inches. However, with reduced cable separation (X_c = 2 inches), the fixed point was near the rear of the container.

In all cases with the wide cable separation, the sway mode quickly dissipated and the sway motion was forced by the yaw mode. With the cable separation such that the yaw frequency and sway frequency are nearly the same, the modes couple and instability of the classical nature results.

The single-cable cases matched to near perfection.

The analog model matched quite well with the wind tunnel results. The limit cycle frequency matched to approximately 1/4-cycle in 10 cycles, or 2.5 percent. Nothing was done to the model to change the frequency because it was primarily controlled by the cable separation. With small-amplitude limit cycles the static yawing moment had an effect; however, with large-amplitude limit cycles it averaged out to nearly zero. The growth rate of the limit cycle is probably accurate to between 10 and 20 percent. The amplitude of the limit cycle, while the most easily changed variable, is probably 15 to 20 percent in error, due primarily to the camera angle not being vertical.

The shape of the unsteady moment curve is undoubtedly in gross error because of the lack of precise data. The straight lines of the function do not reflect the lags associated with unsteady aerodynamics; however, the general characteristics of the unsteady moment which evolved must have some correlation with reality because the predicted MILVAN motions agreed well over a wide range of speeds and geometric conditions.

DYNAMIC MODEL AND PREDICTIONS

Figure 3 is a block diagram of the dynamic model. A logic representation of the unsteady yawing moment function is shown and the static yawing moment is also included. The model has a single degree of freedom describing the motions about the yaw axis only, which is usually a stable limit cycle. This model is valid as long as the yawing limit cycle frequency (bifilar frequency) is significantly greater than the sway pendulum frequency. If, for example, the bifilar frequency is lowered to about 1.5 times the sway pendulum frequency, the sway mode will be unduly perturbed by yaw and a classical instability usually begins to appear.

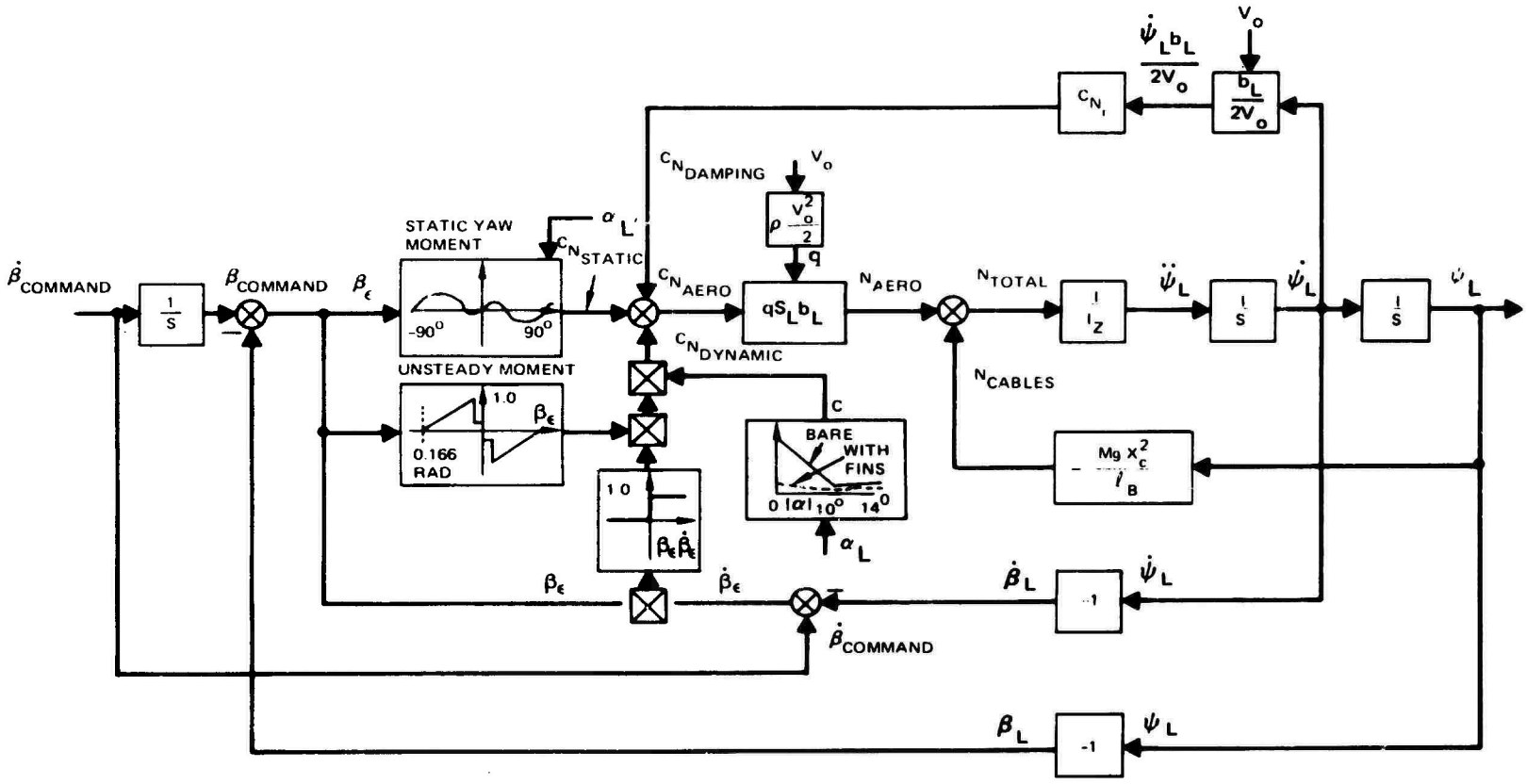

FIGURE 3. BLOCK DIAGRAM OF THE DYNAMIC MODEL OF THE 8-BY-8-BY-20-FOOT CONTAINER FOR THE LIMIT CYCLE CLASS OF MOTION.

ENERGY BALANCE

PREDICTION OF LIMIT CYCLE (DYNAMIC MODEL)

An attempt was made to estimate the amplitude of the yaw limit cycle based on the conservation of energy concept. Specifically, the yaw motion is assumed to be a stable limit cycle at the bifilar frequency, and the energy added to the system by the unsteady aerodynamics is exactly removed by the damping function C_{N_r} with the assumption of sinusoidal motion.

Integration of the unsteady moment function into energy is complex for amplitudes less than ±9.5 degrees; however, for larger amplitudes, a closed-form solution can be derived as given below.

$$\psi_{max} = \frac{-.1126C}{\pi C_{N_r}} \frac{2V_o}{b\omega_\psi} \quad (|\psi_{max}| \geq .166 \text{ rad})$$

In this expression, the negative sign reflects the damping offered by C_{N_r}, which is usually taken as minus; 0.1126 is the integral value of the unsteady moment function, and C is the normalized value of the unsteady function and is a function of fins and angle of attack. For a peak amplitude greater than 0.166 radian, C is only a function of angle of attack as given in Figure 4. A straight-line function was assumed between the measured points.

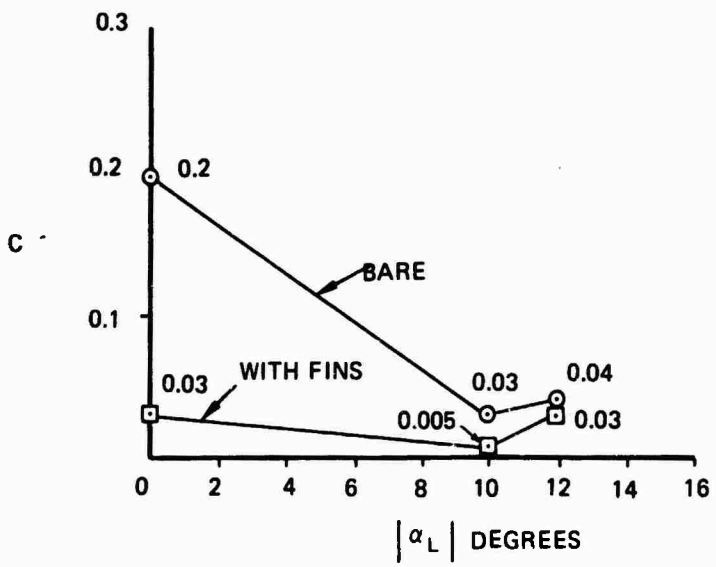

FIGURE 4. EFFECT OF ANGLE OF ATTACK AND FINS.

It is convenient to express the relation in terms of the Strouhal number ($S_T = \omega_\psi b/V_o$) thus:

$$\Psi_{max} = \sqrt{\frac{-2C \times .1226}{\pi C_{N_r}}} \sqrt{\frac{1}{S_T}}$$

where b is container width, ω_ψ is the bifilar frequency in rad/sec, and V_o is forward speed in ft/sec. The value of C_{N_r} derived from the analog matching study is -0.94. When this is substituted in the equation, a relatively simple expression results:

$$\Psi_{max} = \sqrt{\frac{2X.1126}{\pi X.94}} \; X \sqrt{\frac{C}{S_T}} = 0.276\sqrt{\frac{C}{S_T}}$$

Figure 5 shows the model data points, the full-scale points from Reference 2, computer predictions, and the energy balance estimate. The agreement between the computer results and the energy balance prediction is very good. The flight data from Reference 2 also shows good agreement with the model for short cables and low yaw amplitude (±15 degrees). The agreement between the energy balance prediction and flight data for large-amplitude (long cables) yawing is not as good. The reason for this is that the simple formula assumes the motion to be sinusoidal and the computer prediction shows it to be approaching a triangular form. This will certainly affect the calculation for the damping function C_{N_r}. The reasonably good match between the model prediction of flight results and the flight results themselves is remarkable considering the strong effect of angle of attack and the lack of documentation of angle of attack in the flight data.

STROUHAL NUMBER

This is a nondimensional frequency used in dynamic wind tunnel testing. It is a frequency in radians per second or cycles per second multiplied by length and divided by velocity. Holding this number constant from model to full scale gives the same result as for Froude's number; namely, full-scale speed is 3.16 times model speed. The Strouhal number is useful in describing vortex shedding and other properties of a turbulent wake. It is reasonable to hold it constant for dynamic wind tunnel testing of this kind because in doing so the relation between wake motions (vorticity, etc.) and model motions is maintained, thus increasing the probability of correctly representing the unsteady aerodynamic effects.

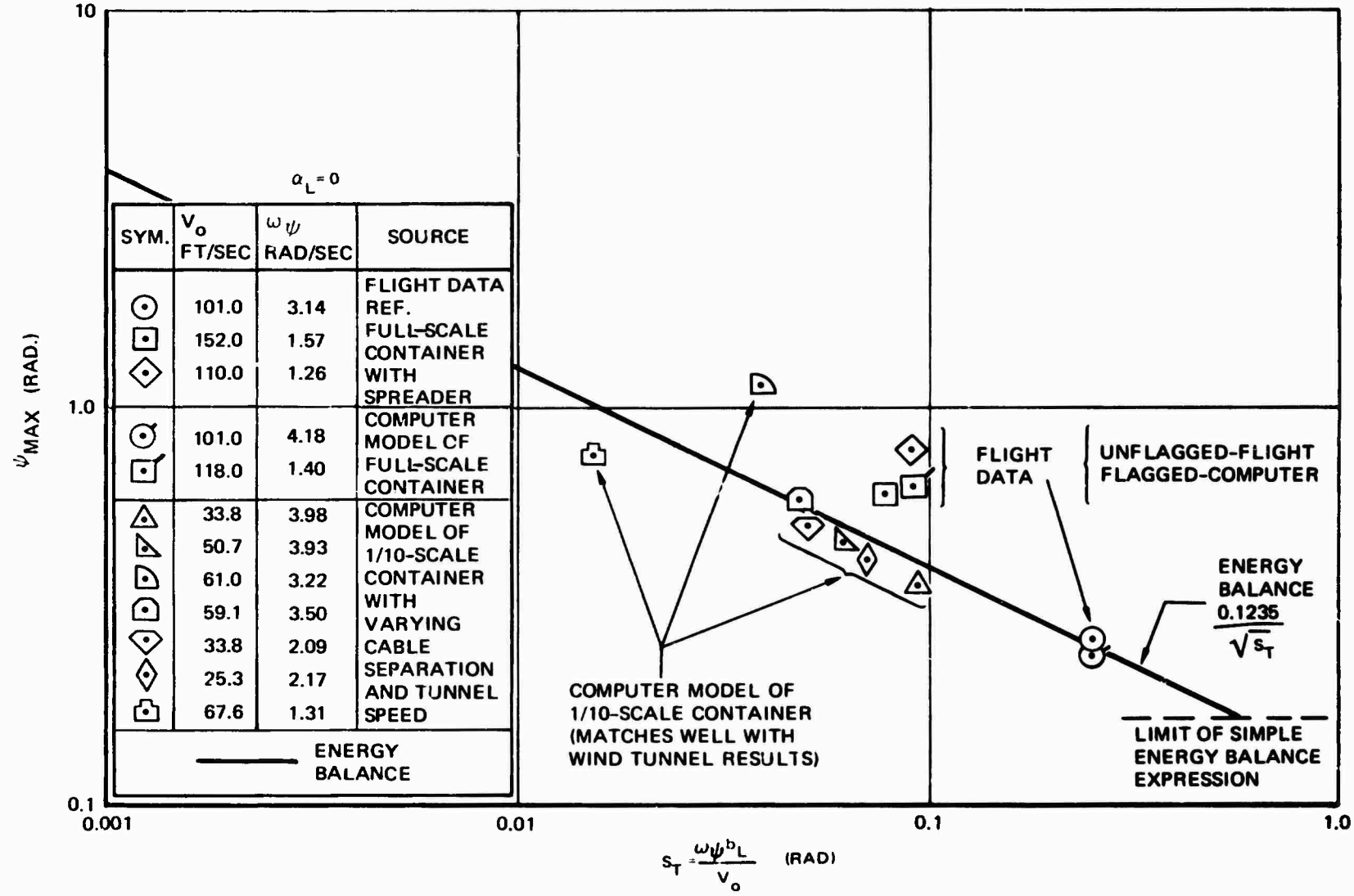

FIGURE 5. COMPARISON OF COMPUTER MODEL DATA WITH FLIGHT RESULTS (α = 0)

MODEL 347 HELICOPTER SIMULATION

SIMULATION FACILITY

The Northrop simulation facility used for the Model 347 helicopter simulation comprises a large-amplitude beam-type motion subsystem that carries a cockpit, projectors for sky/earth/horizon/target imaging, and a spherical display screen for the visual display, all on the end of a 30-foot beam as shown in Figure 6. This motion system provides vertical and lateral beam translation and cockpit pitch, roll, and yaw rotation as shown in Table 4.

TABLE 4. SIMULATOR PERFORMANCE

COCKPIT MOTION AMPLITUDES	DISPLACEMENT (USABLE TRAVEL)	PEAK NO-LOAD VELOCITY	PEAK ACCELERATION
Vertical Translation (Beam)	± 10.4 Ft*	13.2 Ft/Sec	2.5 G
Lateral Translation (Beam)	± 10.1 Ft*	9.0 Ft/Sec	1.6 G
Pitch Rotation (Cockpit)	± 25 Deg	1.0 Rad/Sec	16.0 Rad/Sec^2
Roll Rotation (Cockpit)	± 20 Deg	1.1 Rad/Sec	4.6 Rad/Sec^2
Yaw Rotation (Cockpit)	± 20 Deg	1.3 Rad/Sec	8.6 Rad/Sec^2

*Measured at the pilot's eye level

In operation, the motion subsystem produces movements in precise phase and amplitude, with electrical signals supplied by an integrated hybrid computer complex to provide the pilot with realistic perceptual cues related to actual motions of the simulated aircraft. The large vertical and lateral translations of the 30-foot gimbaled beam are controlled by two electrohydraulic servo systems. The cockpit is also gimbaled on the beam to provide pitch, roll, and yaw rotations, all controlled by electrohydraulic servos. Figure 7 shows the gimbaled structure supporting the cockpit. The dynamic performance of the large-amplitude simulator is shown graphically in Figure 8.

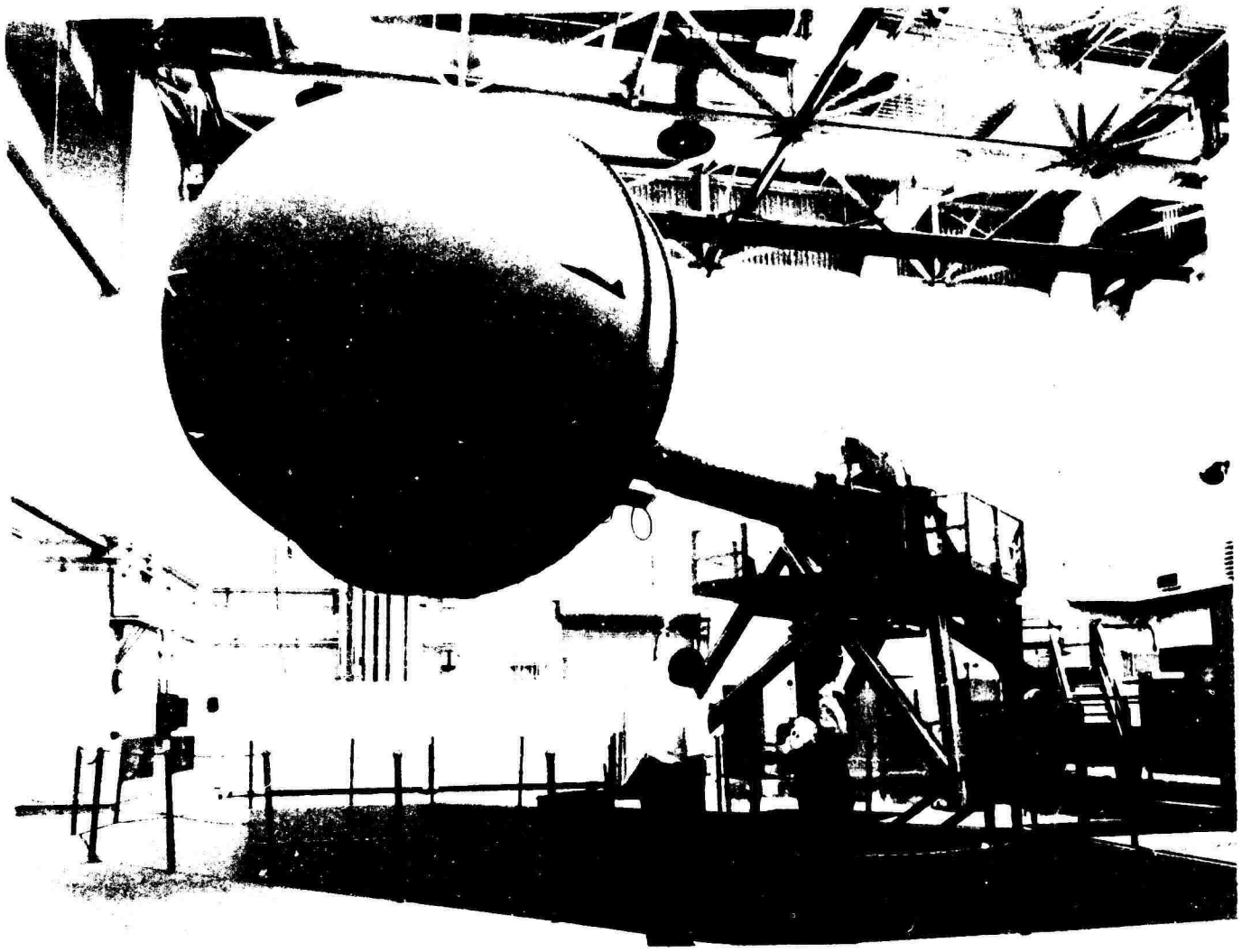

FIGURE 6. LAS - GENERAL ARRANGEMENT.

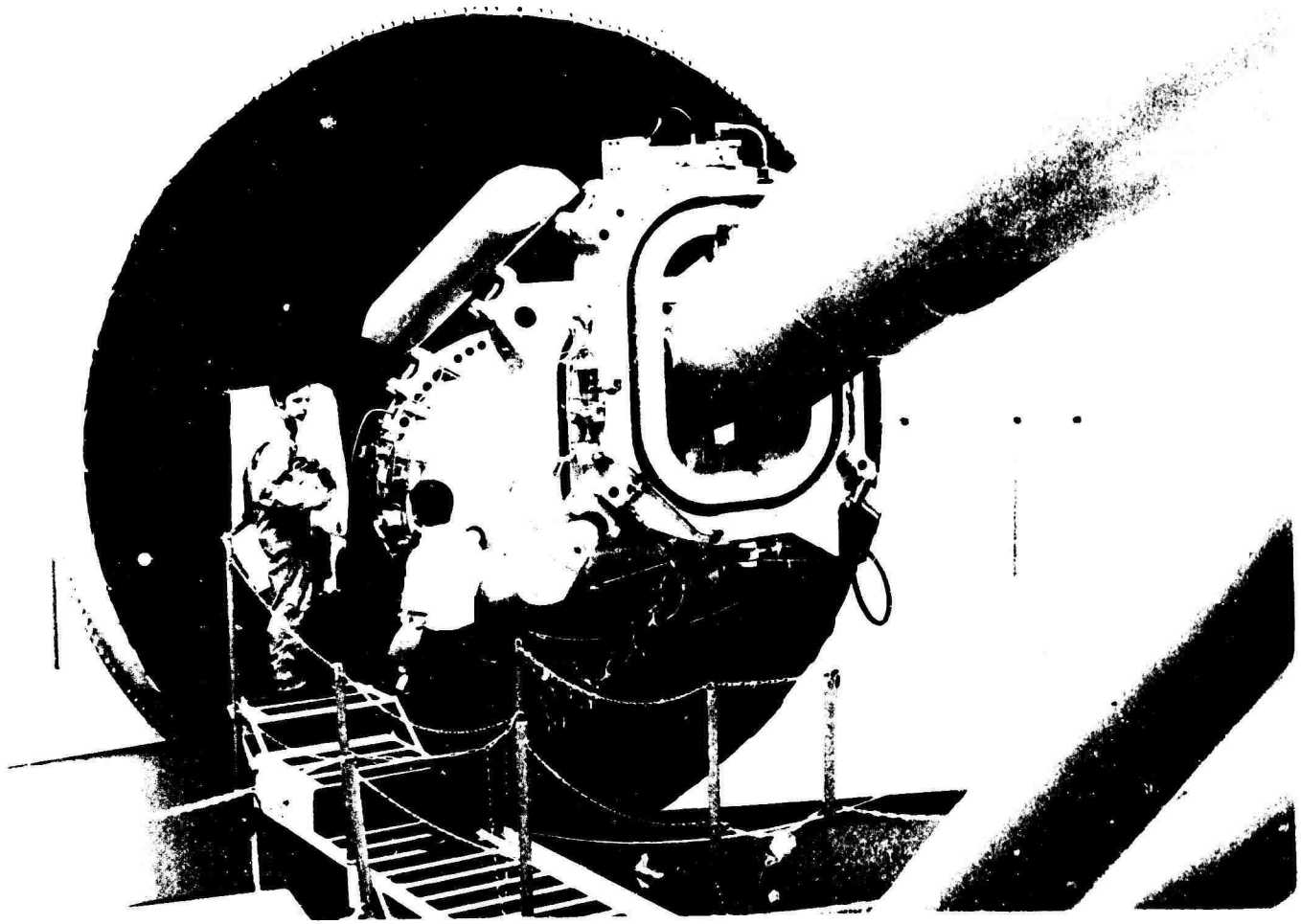

FIGURE 7. LAS - COCKPIT AND BEAM END CONFIGURATION.

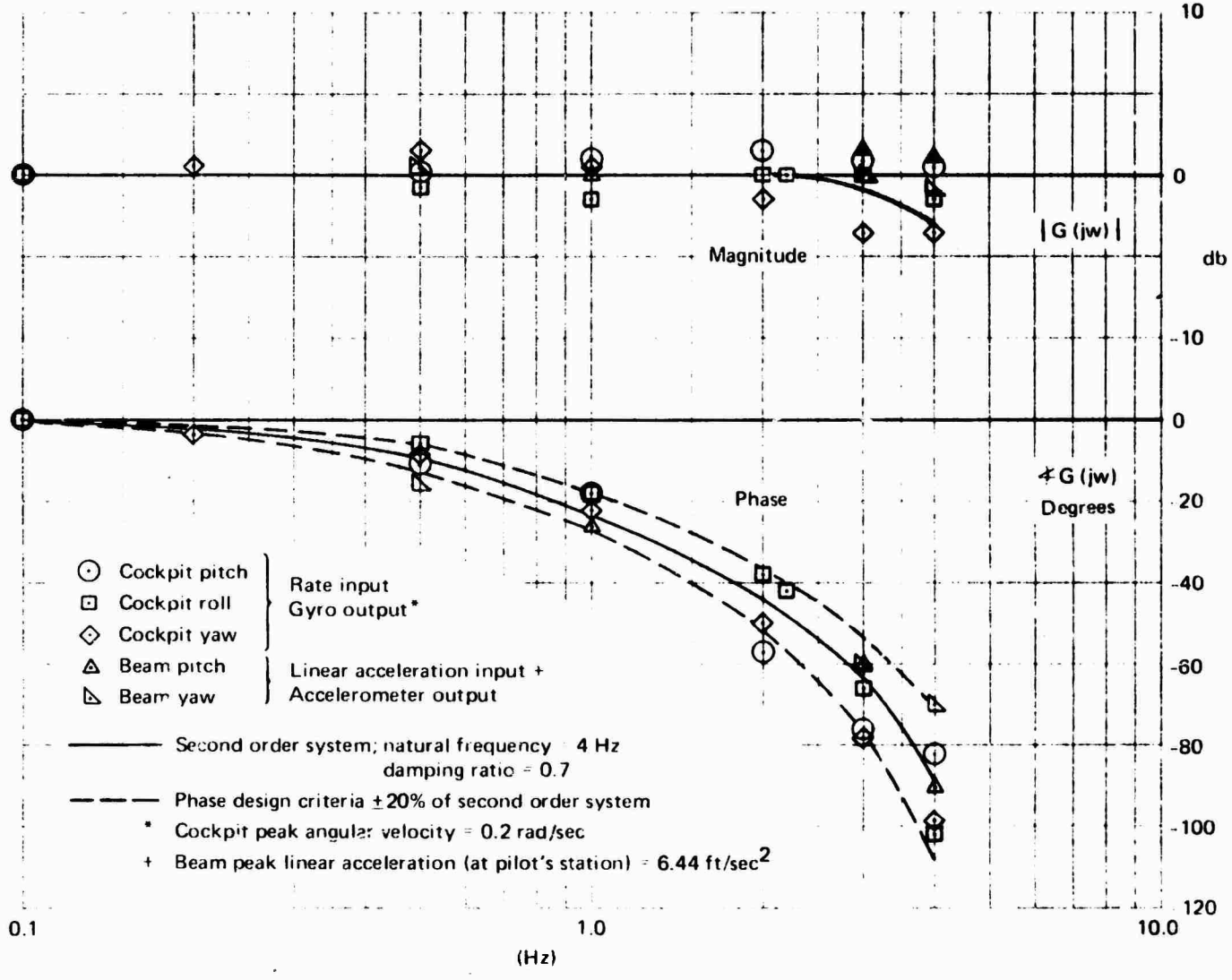

FIGURE 8. LARGE-AMPLITUDE SIMULATOR - DYNAMIC PERFORMANCE.

The visual display subsystem consists of two different projectors mounted above the cockpit inside the spherical housing. A sky-earth projector provides the pilot with a horizon reference that continually gives visual indication of the simulated aircraft attitude. A target projector is used primarily for air-to-air simulation but can also be used for air-to-ground work. This target information is projected into the screen from a cathode-ray tube located above and behind the pilot's head.

The force feel for primary controls is provided by a three-axis electro-hydraulic servo system. This system consists of a conventional two-axis center stick and rudder pedals. Force is applied to the controls by rotary hydraulic actuators, and the force-feel characteristic is provided by the console servo electronics and/or the computer. A unique capability of this force servo system is that it is capable of stable operation with zero force applied to the controls, i.e., a true feel stick.

The monitor and control console is the central operating station for simulator control, monitoring, test, and maintenance. The console is shown in the lower part of Figure 9. It houses the electronic portions of the servo, cockpit, and television equipment and provides the signal interface between the simulator and the computer. An intercom system in the console provides communications between console operator, pilot, and the computer area.

Other support components of the simulator facility include an aircraft-engine sound generator, an anti-G suit pressurization system, a 3000-psi hydraulic power source, a hybrid computer complex, and software programs that drive the simulator.

MODEL 347 HELICOPTER SIMULATION SETUP

To understand the effects of various sling load stabilization concepts, a sophisticated simulation of the Model 347 helicopter was developed and mechanized on Northrop's advanced large-amplitude simulator. Linearized equations of motion for the sling load were used, and the dynamic model of the 8-by-8-by-20-foot cargo container (MILVAN) was incorporated in the simulation.

The existing simulator cockpit was modified to resemble the right-hand seat of the Model 347 helicopter. An instrument panel was fabricated to duplicate the configuration of the Model 347 helicopter; all primary instrumentation was actively driven by the computer. Instrumentation included attitude director indicator, horizontal situation indicator, airspeed, radar and barometric altimeters, rate of climb, engine rpm and rotor torque indicators. A Boeing-supplied collective control and Automatic Flight Control System (AFCS) control panel were also installed in the simulator cockpit and mechanized to operate similar to that in the helicopter. A computer mechanization of the control force-feel system

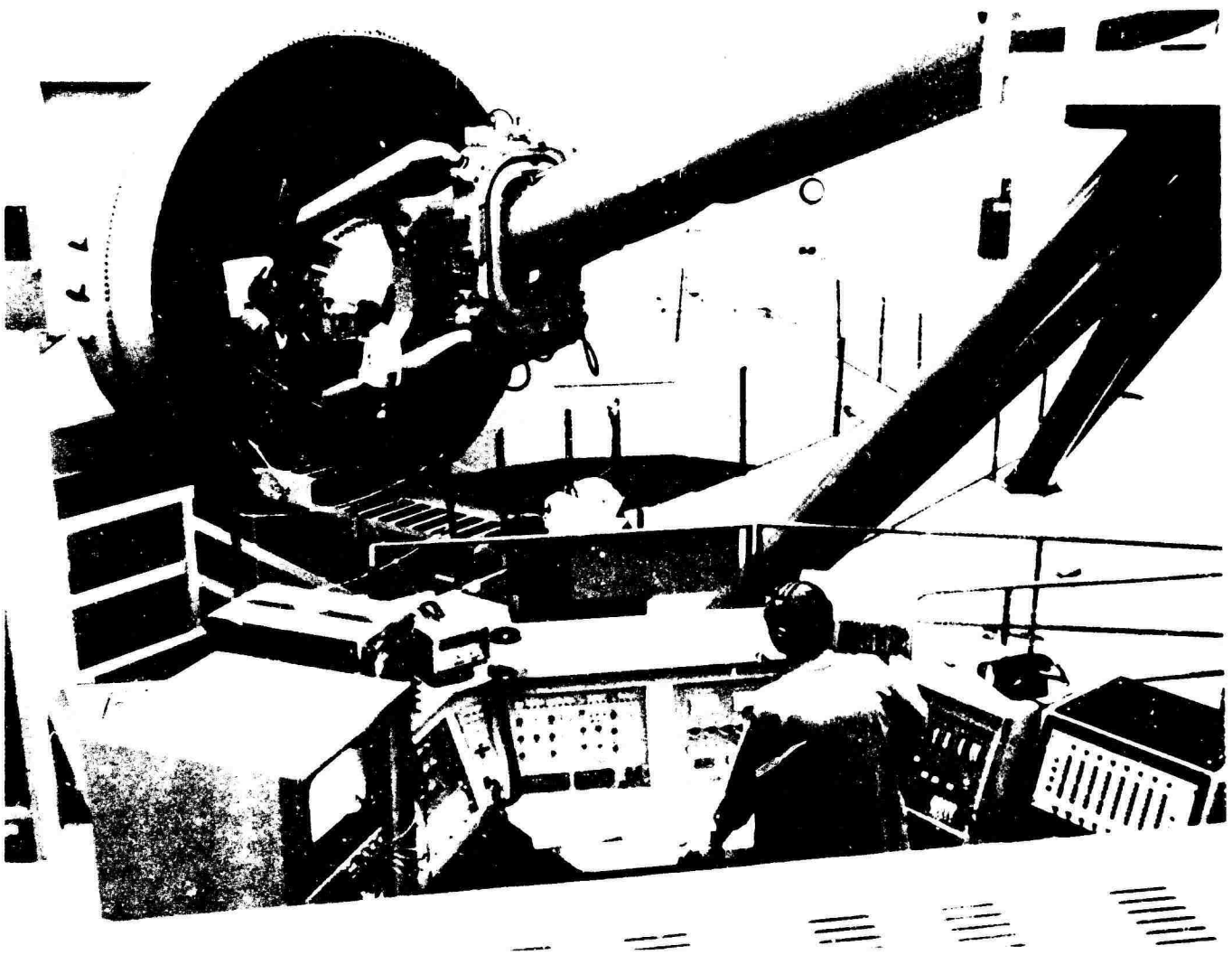

FIGURE 9. LAS - MONITOR/CONTROL CONSOLE

was developed to provide control forces as a function of airspeed, pitch rate, AFCS drive commands, and the magnetic brake function.

Additional instruments added to the cockpit for performance of the hover tasks were longitudinal and lateral airspeed indicators and a computer-generated CRT display. The CRT display could be presented in three modes:

1) Aircraft motion relative to a fixed point on the ground.
2) Motion of a fixed point on the ground relative to the aircraft.
3) Slung load motion relative to the aircraft.

The scale of the CRT display could be changed by the pilot to depict relative position (a coarse scale of 500 feet to a fine scale of 5 feet in position).

A validation effort to establish confidence in the simulation preceded the principal test phase. This validation consisted of setting in the coefficients which produced a simulation of a known flight condition and then having the pilot who flew the known flight condition fly the simulator.

VALIDATION

The mathematical model validation of the 347 Advanced Tandem-Rotor Helicopter was accomplished by comparison of steady-state trim and dynamic response data with theoretical predictions.

Level-flight data were obtained at airspeeds ranging from 40 knots rearward to 180 knots forward at a gross weight of 45,000 pounds and a center of gravity (c.g.) condition of 12 inches aft of the nominal c.g. location.

Trim validations were performed using two different approaches to generate rotor force and moment parameters: the "classical" equation approach and the "rotor map" approach. The classical approach utilized an equation format to generate rotor forces and moments, whereas the rotor mapping technique involved the use of precalculated values for thrust, propulsive force, and power. These precalculated values were then stored in the PDP9B digital computer which was used as a function generation device for the math model simulation.

The correlation between values predicted by Boeing Vertol (B-29) and Northrop hybrid results of steady-state trim data is shown on Figure 10. Data agreement as shown on these figures is generally good for all trim conditions. Improvements due to the "rotor map" approach to rotor forces and moments are noticeable for the higher airspeeds (140 to 180 knots).

Time history responses were obtained for both the augmented and unaugmented flight. The augmented flight consisted of longitudinal, lateral, and directional stability augmentation systems. Control inputs consisting of a series of steps and pulses were introduced into the longitudinal, lateral, and directional axes. The resulting dynamic characteristic comparisons with expected results were good.

The validation of the sling load model was accomplished with a 15,000-pound external load and a 30,000-pound helicopter at 12 inches aft c.g. at standard sea level conditions. Sling load pendulum (longitudinal and lateral) and bifilar (yaw) modes were excited by separately inputting 1-inch and ½-second pulses into the longitudinal, lateral, and directional axes of the 347 analog control system. Cable angle responses were measured and frequency and damping information recorded. The results obtained correlated well with the predictions.

The time history results of the aircraft and sling load models as well as the static trim data were compared with similar data acquired from the Boeing Vertol simulation of the 347 aircraft. The availability of data from the Boeing Vertol simulation enhanced the validation of the mathematical model at Northrop. Data correlations from the two math models were exact.

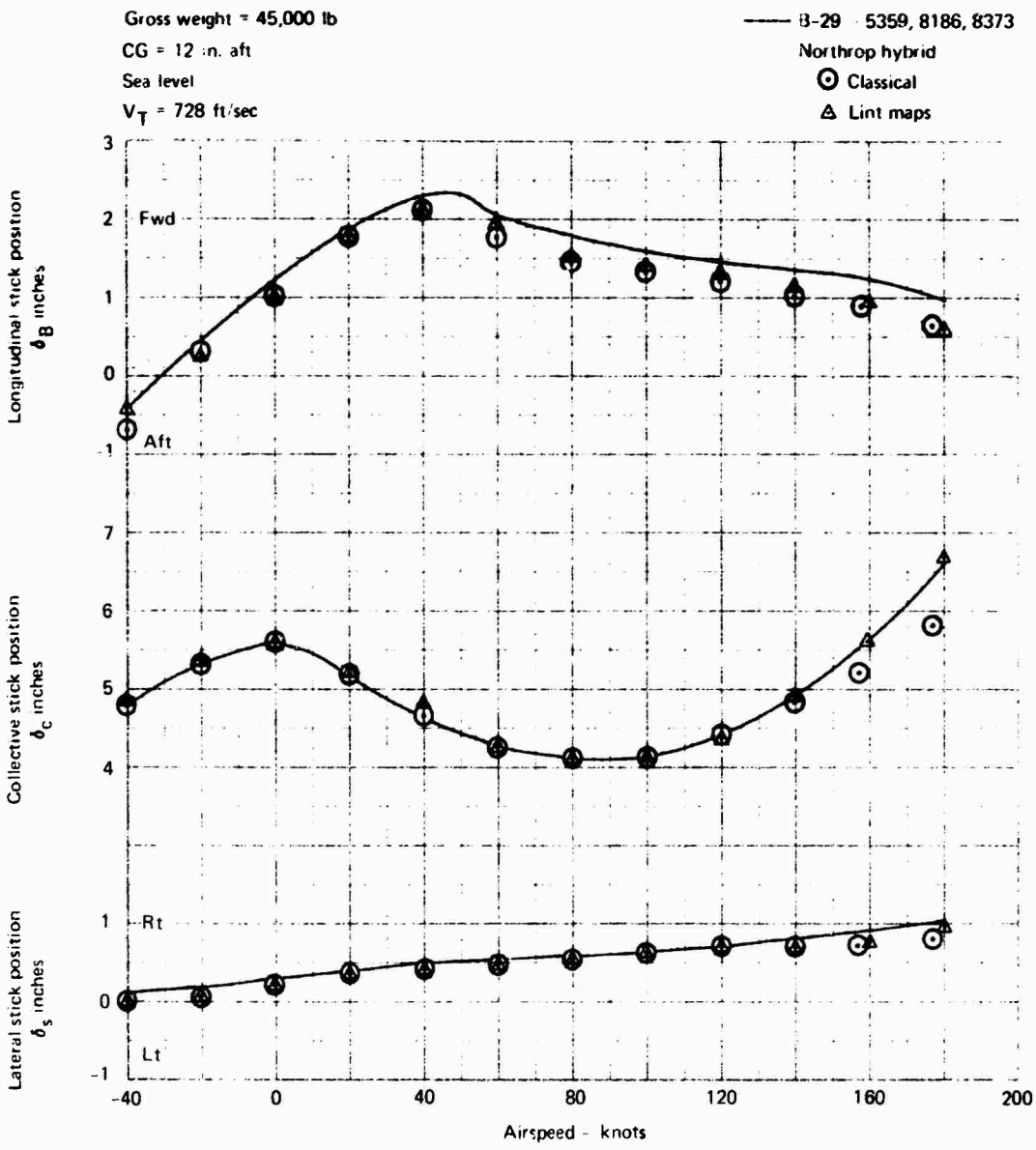

Figure 10. NORTHROP HYBRID VALIDATION OF THE MODEL 347 HELICOPTER (SHEET 1 OF 10).

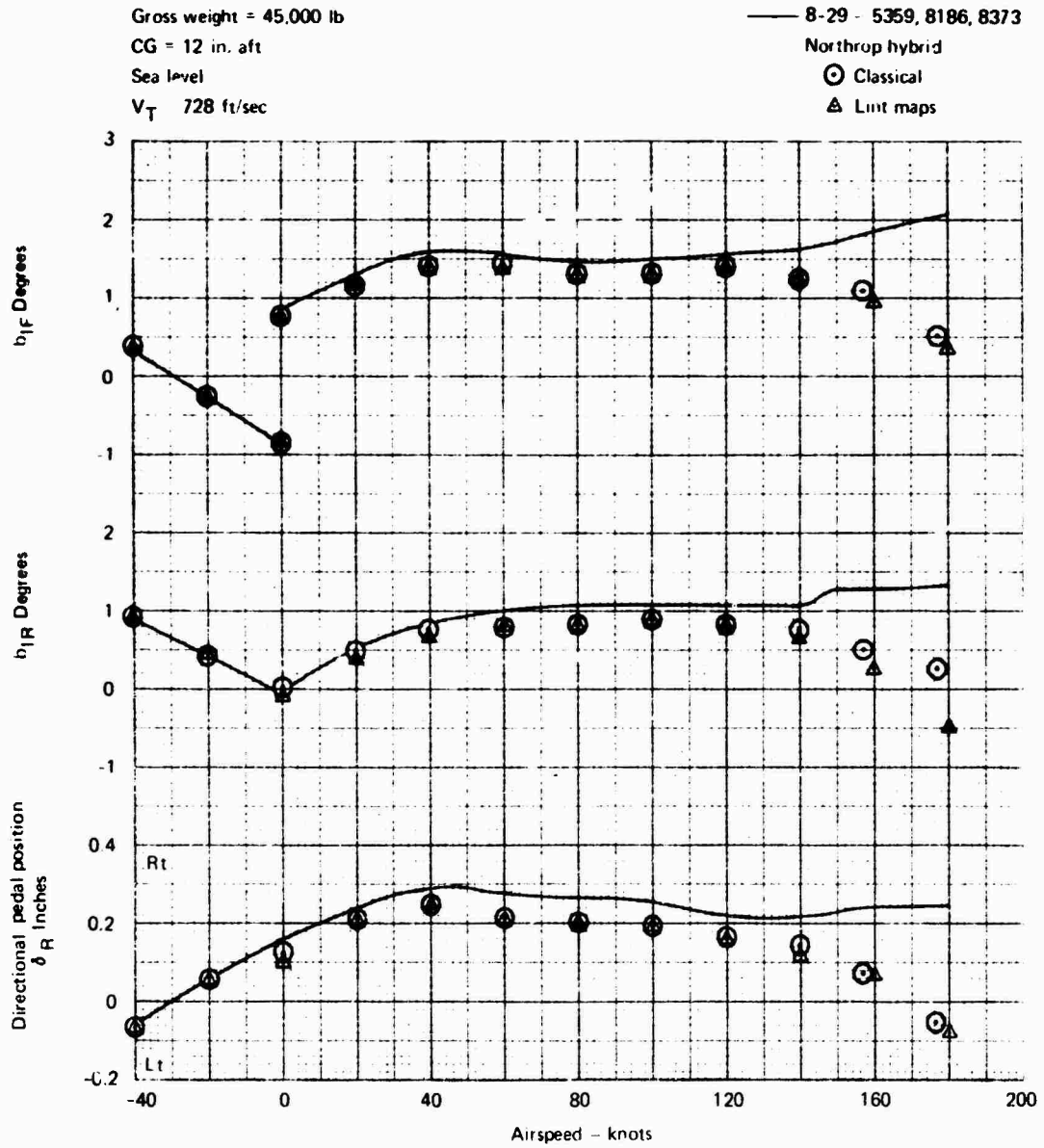

Figure 10. (Sheet 2 of 10).

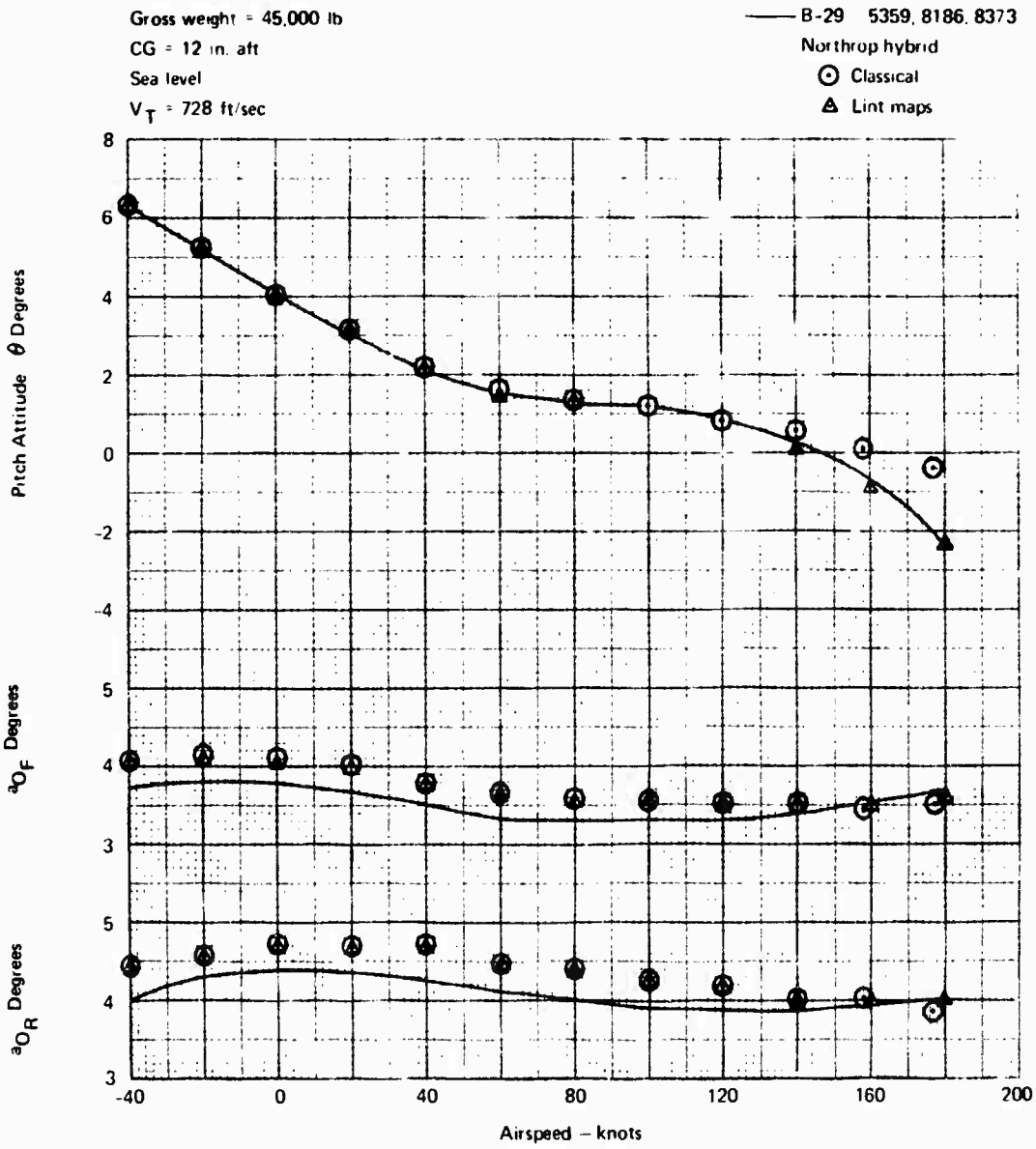

Figure 10. (Sheet 3 of 10).

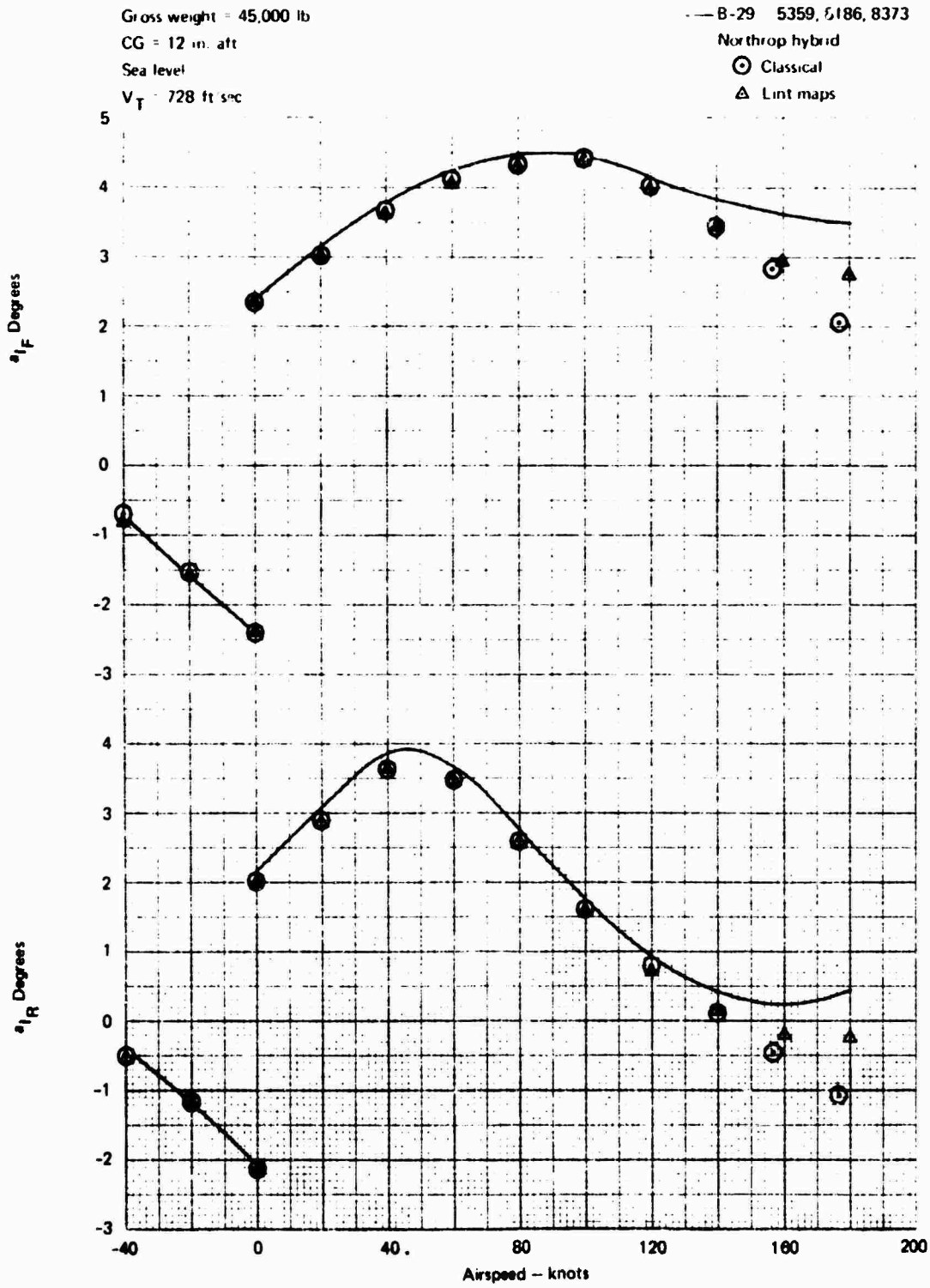

Figure 10. (Sheet 4 of 10).

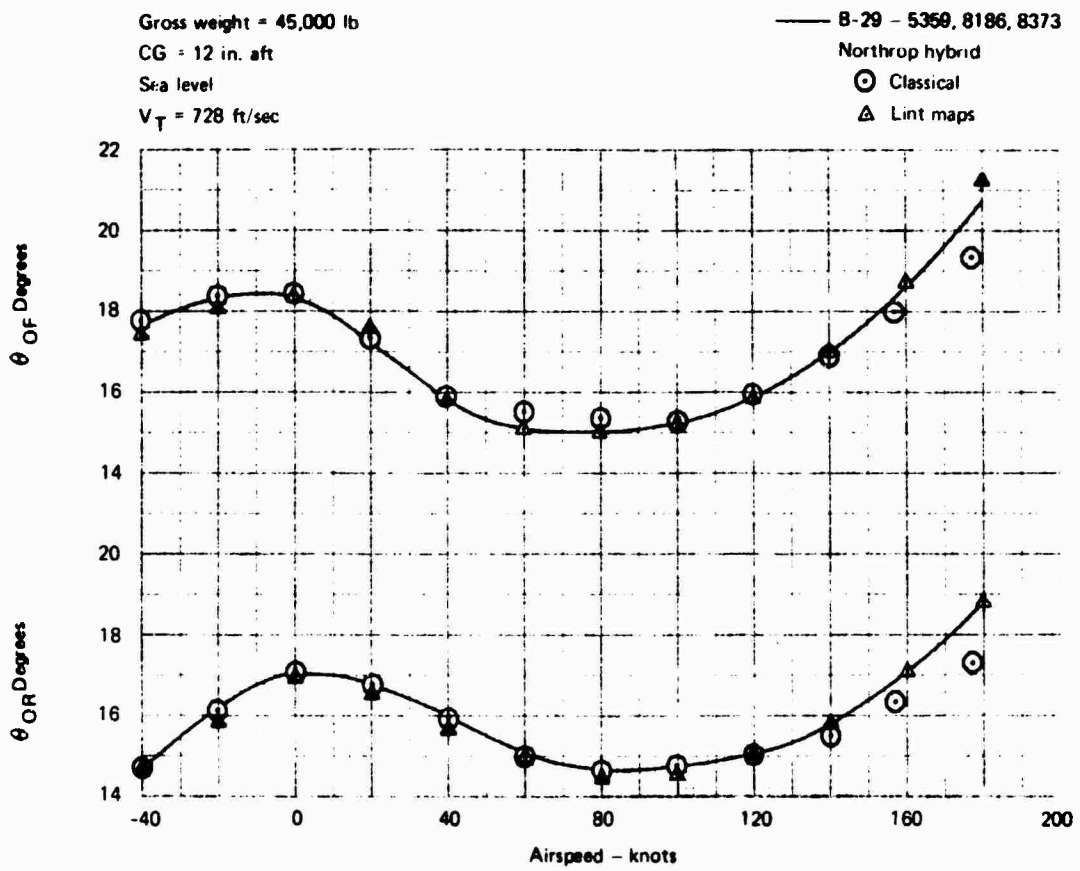

Figure 10. (Sheet 5 of 10).

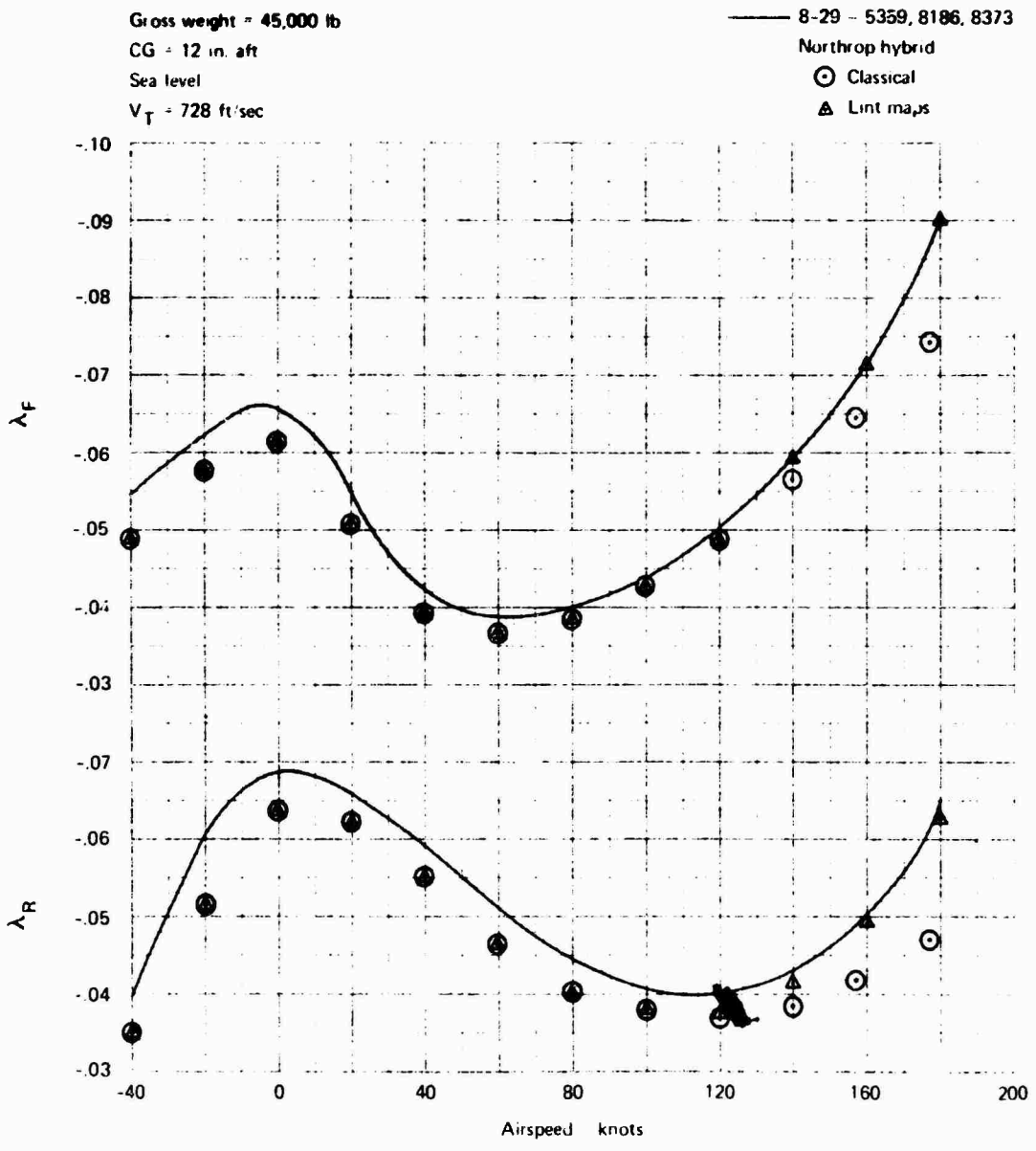

Figure 10. (Sheet 6 of 10).

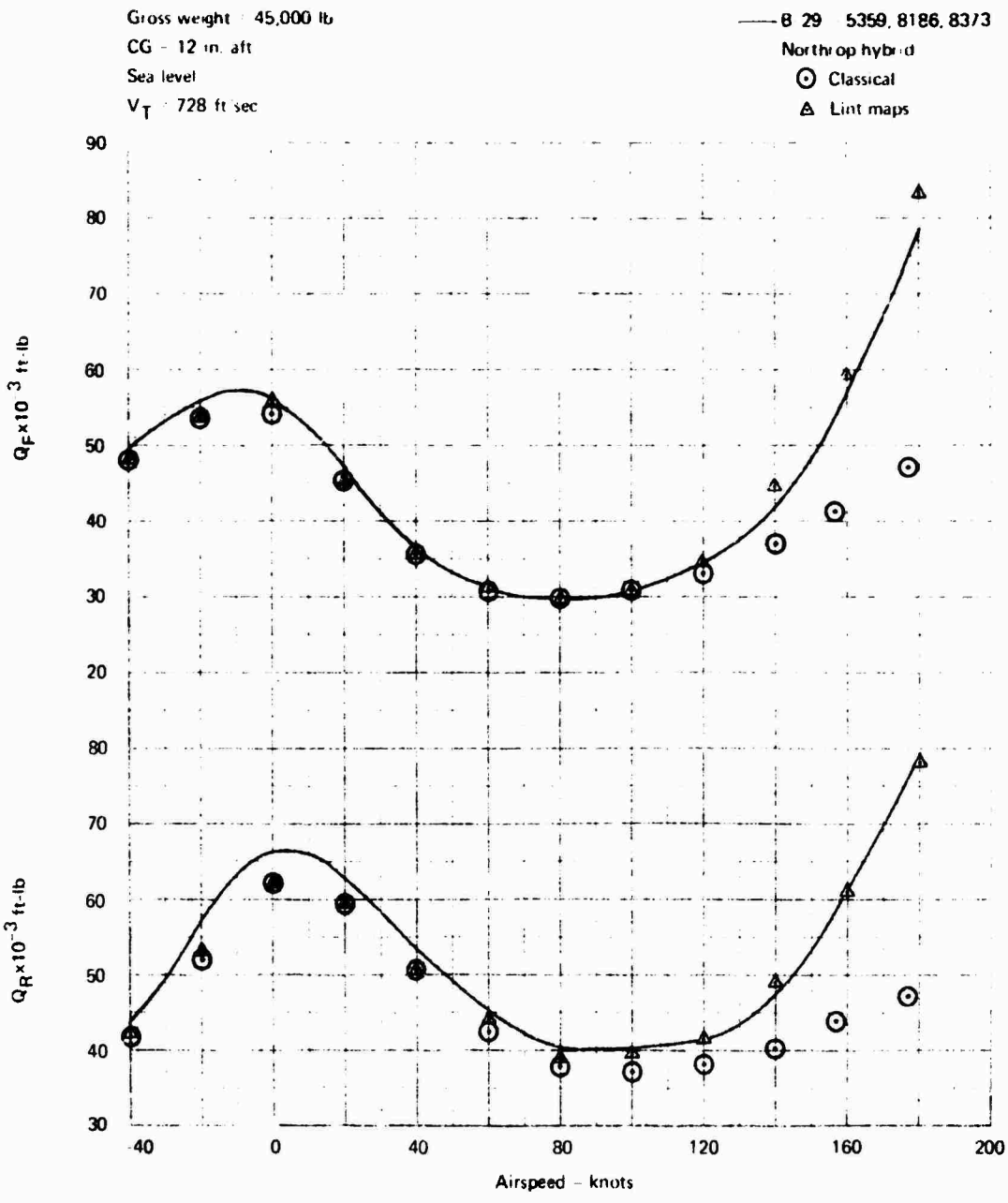

Figure 10. (Sheet 7 of 10).

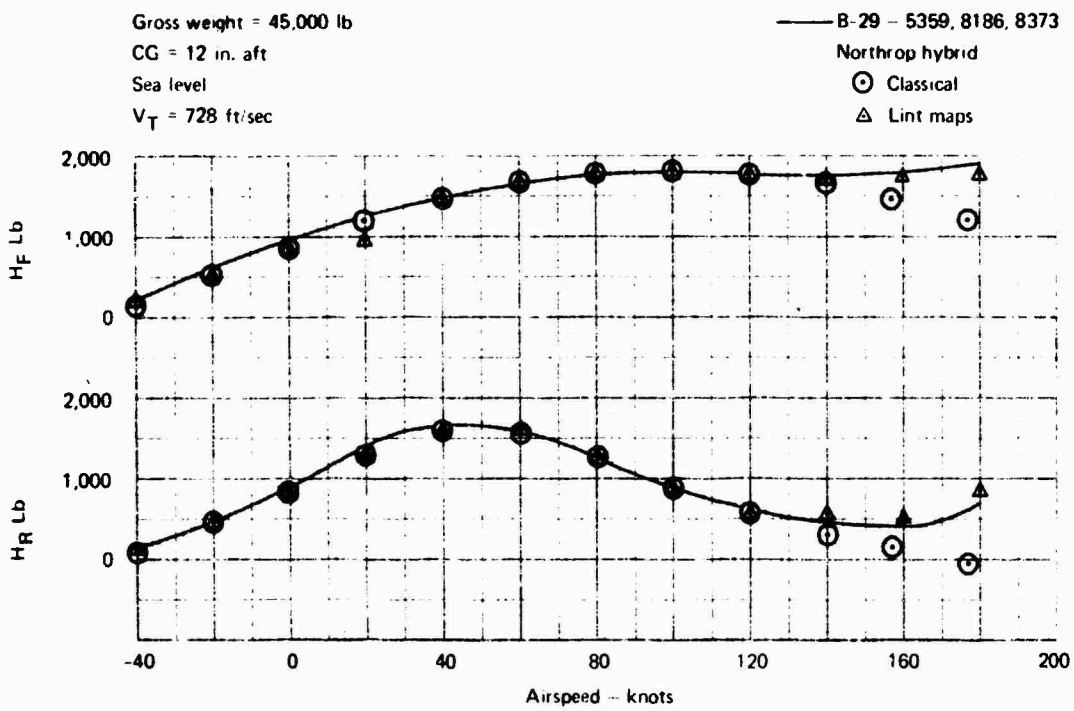

Figure 10. (Sheet 8 of 10).

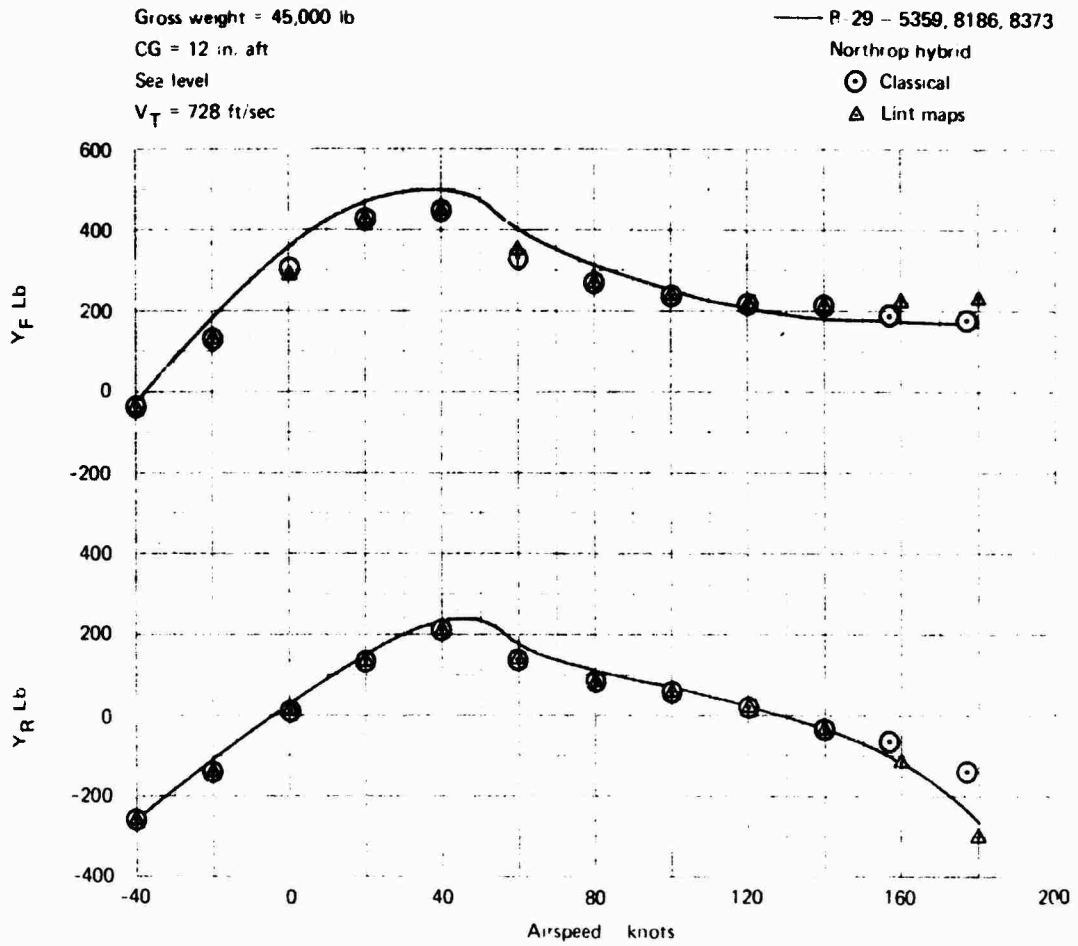

Figure 10. (Sheet 9 of 10).

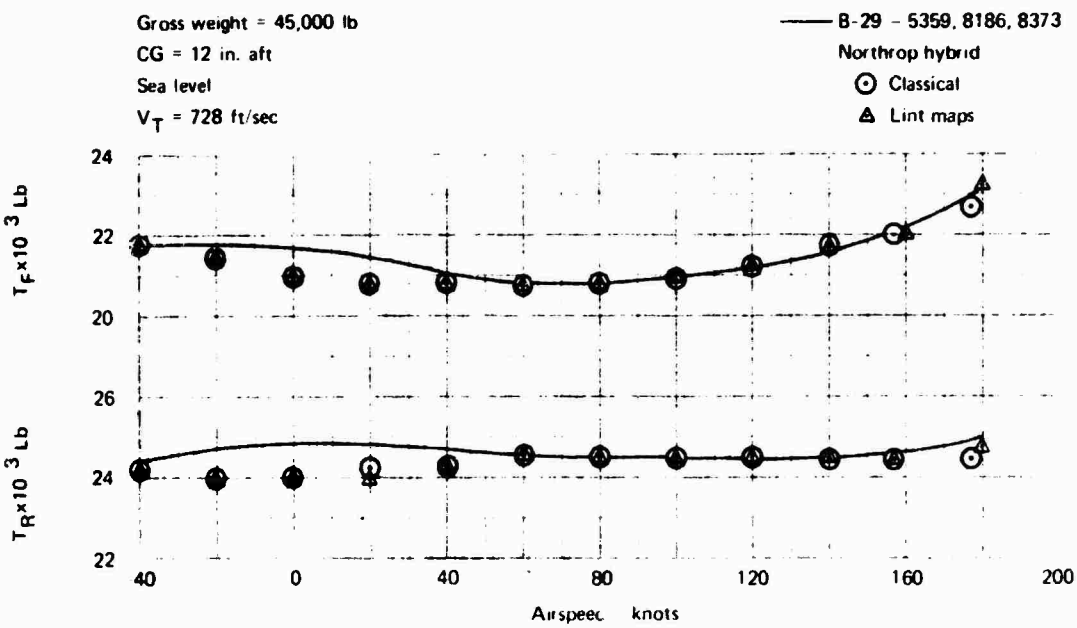

Figure 10. (Sheet 10 of 10).

The Boeing Vertol math model was validated by comparing theoretical results and model simulation results with actual flight test data. The comparison of the Vertol hybrid model with flight test data showed good correlation in the speed regimes modeled. The results of the Vertol simulation of the 347 aircraft were then used as the basis for comparison in the validation of the 347 aircraft math model here at Northrop.

Upon completion of the mathematical model validation the LAS/WAVS simulator validation was performed, utilizing a subjective approach in which pilot opinion was the sole indicator of fidelity. With a test pilot from the Boeing Vertol 347 Aircraft Flight Test Group flying the simulator, changes in the interface coefficients were made to "tune" the simulator such that the motion and visual stimuli presented to the pilot resembled those experienced on the actual 347 aircraft.

SIMULATION RESULTS

MASS RATIO EFFECTS

A two-degree-of-freedom nonlinear analysis, while rigorous, does not predict the limit cycle amplitude with precision when the load is attached to a helicopter of finite mass. For the empty MILVAN with spreader, the ratio of load mass to total mass is 8705 (37,000 + 8705) = 0.19. The ratio of load yawing inertia to helicopter inertia is even smaller, 9500/367,000 = 0.026. It would seem that the condition of infinite helicopter mass would be satisfied for the purpose of employing the two-degree-of-freedom analysis. However, when the dynamic model was incorporated into the simulation, the limit cycle amplitude matched the earlier model results precisely, but only if the helicopter was held fixed (by manipulating the computers.)

When the helicopter was released after trimming, the limit cycle amplitude was reduced to 0.75 of the helicopter fixed value. The difference amounted to about three degrees. The initial flight data for the validation flight condition was listed as having an amplitude of ±15 degrees, but the axes reference was not stated. In the simulation, the reference is body axes, since the helicopter yaws at the limit cycle frequency, the load yaws ±12 degrees relative to the helicopter, and the helicopter yaws ±3 degrees relative to the earth. If the phasing between them is 180 degrees, the load yaw angle relative to the helicopter is ±15 degrees. This, then, identifies a minor inconsistency in the comparison of the model results and flight simulation with flight data.

Figure 11 shows the results of an attempt to predict the carrying speed boundary for the empty container and spreader beam, using the model and the simulation-determined limit cycle restrictions. The yaw angle is referenced to helicopter body axes. The 0.75 factor was applied to the model prediction of yaw amplitude. The model prediction and the carrying speed amplitude restriction curves intersect at 60 knots. The flight report indicates that the pilots would not recommend carrying this load beyond 65 knots. This is a very good agreement, and it can be concluded that the dynamic model is a good representation of the real-world effects, particularly when integrated into a sophisticated simulation. However, use of the dynamic model alone to predict carrying speed boundaries is subject to the 0.75 uncertainty; i.e., the effect of load-to-helicopter mass ratio.

EMPIRICAL DATA FIT

When confidence in the simulation was established, a series of tests was conducted to determine the limit cycle amplitude that the pilots felt was the maximum allowable. To conduct this test series, the cable separation was varied so that the bifilar frequency could be controlled. Five data

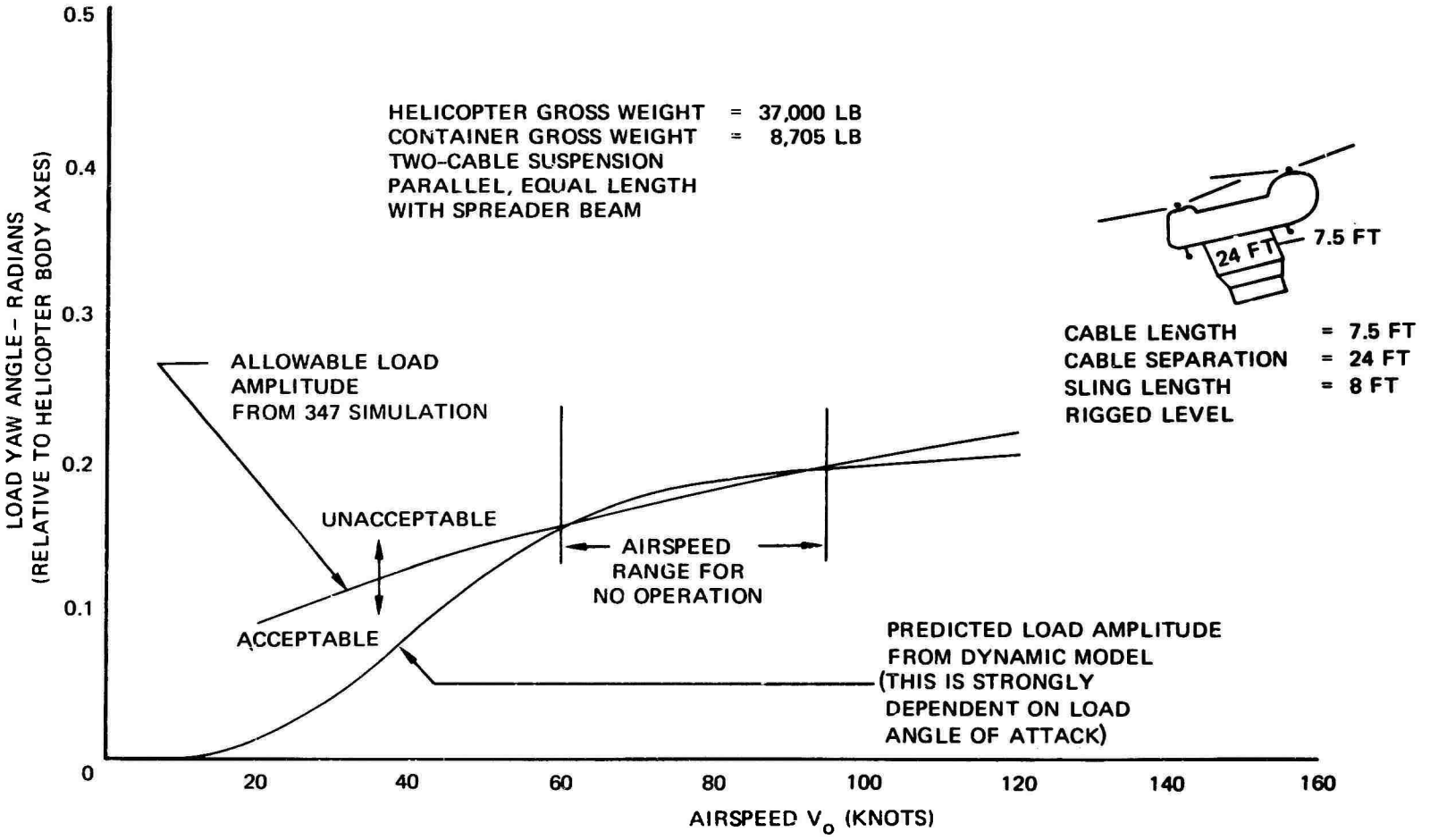

FIGURE 11. 8-BY-8-BY-20-FOOT CONTAINER CARRYING SPEED LIMITATION.

points were obtained for the range of bifilar frequency from 1.34 rad/sec to 5.22 rad/sec. For the spreader beam configuration with 7.5-foot cables, this corresponds to a cable separation range from 7.7 feet to 29 feet, respectively.

The five data points revealed that for a given airspeed the pilot will accept large-amplitude limit cycle load motions, provided these motions are slow; i.e., low bifilar frequency. Before he will carry the load any faster, the load motion amplitude must be made lower or its frequency reduced.

Curiously enough, these five data points can be fitted very well by the simple relation

$$\Psi_{max} = \frac{.091}{S_T}$$

This form resulted from an estimation of limit cycle amplitude, considering that the energy added to the system by the unsteady aerodynamics was equal to that removed by the damping function.

This relation is clarified by the plot of Figure 12, in which the maximum allowable amplitude is plotted versus airspeed and bifilar frequency. The five simulation data points are also shown.

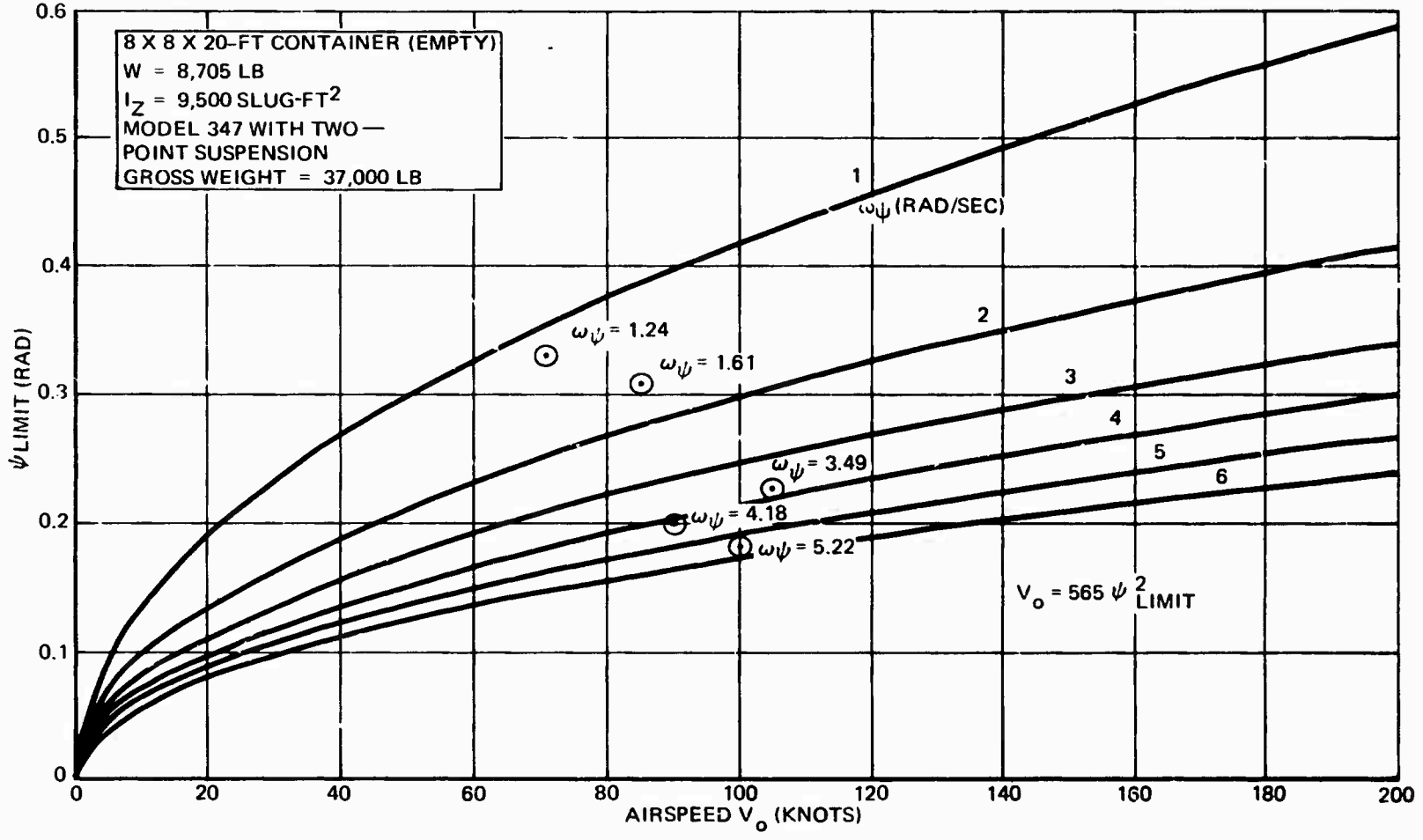

FIGURE 12. CARRYING SPEED VS ALLOWABLE LIMIT CYCLE AMPLITUDE AND FREQUENCY.

STABILIZATION CONCEPTS

It has been demonstrated that use of the dynamic model with simulation gives credible results. That is, an accurate assessment of carrying speed limitation can be determined for all combinations of cable geometry and load mass.

We have also seen how a carrying speed limitation based on pilot judgment was evolved. The limitation has some relation to a simple energy balance expression which describes the load limit cycle amplitude. The underlying laws governing the limitation criteria for the limit cycle are not well understood at this time. While it is important to acquire this understanding, it was more important for the purpose of this study to determine what factors affect the carrying speed limitation and how it can be extended within the current state of the art. To this end, the following stabilization concepts to extend carrying speed were examined:

1. Optimizing the suspension system.
2. Maneuvering the helicopter to take advantage of the inherently good aerodynamic properties of the bare container.
3. Modifying the container shape to improve its aerodynamic characteristics.
4. Using an active stability augmentation system that generates moments through the cables by moving cable guides in the helicopter.
5. Modifying the helicopter stability augmentation system to include load motion feedback.
6. Using an active stability augmentation system employing aerodynamic moments derived from an airfoil or similar device.

A summary of key properties of each concept is given in Figure 13.

1	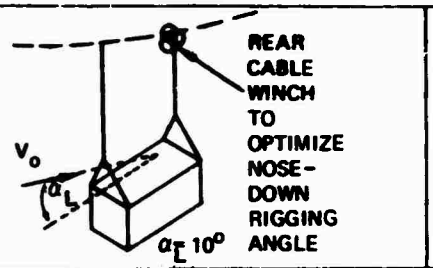	Optimized suspension: two-point, pendulum length less than 20 ft and 20-ft parallel cable separation. Aft winch to optimize angle of attack to -10 degrees. Sensitive to piloting technique.
2	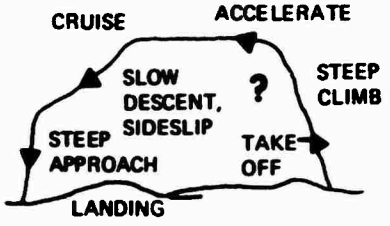	Optimum maneuvering; carrying maneuver is designed to maintain an angle of attack or sideslip of 10 degrees, while minimizing mission time. Contingency maneuvers in case of emergency (collision avoidance, etc) require additional pilot training.
3	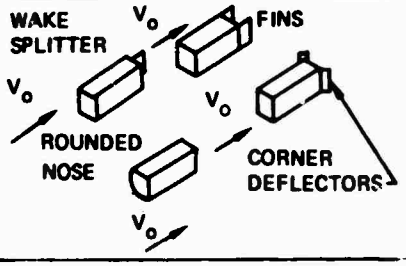	Modifying container shape; wake splitter plate, aft fins, corner deflector, round nose all tend to reduce unsteady aerodynamic yaw moments. Sensitive to normal operational abuse.
4	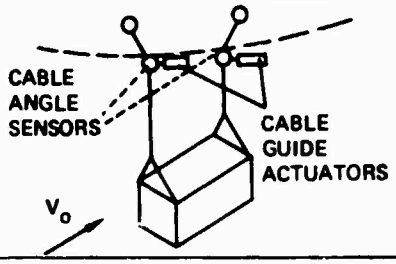	Cable guide actuators; two cable guide actuators deflect the cables laterally (collectively) in response to load sway rate, and laterally (diff.) in response to load yaw rate (relative to heli.). Desensitizes the problem, permits brisk maneuvering, but requires additional actuator and load-motion-sensor hardware.
5	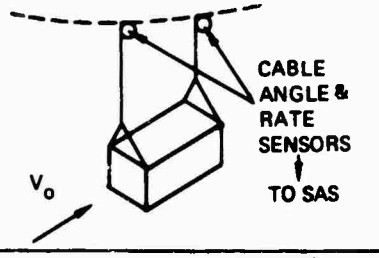	Helicopter SAS inputs from load motion sensors; lateral sway rate→lateral SAS; load yaw rate→yaw SAS. Improves carrying speed slightly, degrades helicopter ride qualities.
6	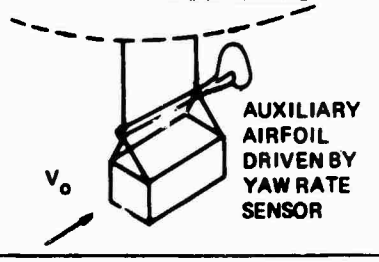	Auxiliary airfoil; driven by load yaw rate? May improve carrying speed if airfoil operates effectively in wake of container; airfoil may possibly be placed forward of load. Complex to handle, requires additional hardware.

FIGURE 13. KEY PROPERTIES OF STABILIZATION SYSTEMS STUDIED.

The effects of load mass have significant impact on sling load carrying speeds. One of the tests performed during the Model 347 helicopter simulation was an evaluation of a 15,000-pound container on a two-point suspension carried by a 30,000-pound 347 helicopter. The total mass was nearly the same as for tests with the empty container, but the carrying speed limitation was higher for this configuration. The load oscillated in yaw as before, but the maximum load yaw angles were much less, allowing the evaluation pilot to reach simulator speeds up to 150 knots.* The worst case occurs with the empty container.

SUSPENSION SYSTEM OPTIMIZATION

When single-point suspension is used, the effective pendulum length can rarely be made much shorter than the length of the container. Under these conditions, an acceptable speed of 40 knots is usually recommended. At this speed, the container trails in a small-end-forward position at a low angle of attack in level flight. To take advantage of the container's angle of attack, use of slings of different length would permit the load to be rigged in a nose-down attitude. An initial rigging angle of about five degrees may reduce the rapid nose departure from the small-end-forward position, thus allowing the pilots to increase their speed, perhaps to 50 knots. This configuration, however, will demonstrate high sensitivity to climbs and descents, since load angle of attack will vary widely during these maneuvers.

There is a greater possibility for improvement using suspension from two or more points. The bifilar and pendulum frequencies can be separated to eliminate classical sway mode instabilities. For the empty container, this requires a parallel cable separation of at least 12 feet, considering that in practical sling arrangements the bifilar length ℓ_B is generally less than the pendulum length ℓ_p. Increasing cable separation to the maximum practical extent is also advisable. Furthermore, the container may be rigged so that the load angle of attack is about -10 degrees under level cruise conditions. For the container and spreader beam carried by a 37,000-pound Model 347, a nose-down rigging angle of two degrees produces

*It is doubtful that the actual Model 347 helicopter could carry a 15,000-pound container faster than 120 knots. It could be reached in the simulator because the power plant limitations were artificially removed for these tests.

this condition at 180 knots. This angle will vary slightly with different helicopters. A further possibility is to winch the load up so that the cable length is zero. The theoretical bifilar frequency is infinite as the yaw stiffness is now provided by the triangular sling-box arrangement. The yaw stiffness will, in practice, be a large but finite value and this should allow higher speeds. There is a danger, however, that the increased bifilar frequency will now couple with the Von Kármán vortex shedding frequency. If this happens, the problem may return, but in a much higher frequency range, where vibration loads may be limiting. It is also not certain that the slings will always remain taut for this configuration.

MANEUVERING THE HELICOPTER

Maneuvering the helicopter to take advantage of the inherently good aerodynamic properties of the bare container is a good way to extend allowable carrying speeds. During the simulation of the empty container with spreader, a curious ambiguity appeared. When the container was rigged level, a speed limitation of 90 knots would be voiced by the evaluation pilot, but on subsequent runs he was able to reach a speed of 165 knots. Upon closer examination, it was found that on the higher speed run he had accelerated through the region of 90 knots. Obviously, the nosedown attitude during acceleration caused the load to assume an angle of attack which reduced the limit cycle amplitude. Figure 9 shows a region between 60 and 90 knots where no operation is expected. However, with an additional angle of attack, the two curves could not intersect until a much higher speed was reached. This point emphasizes the possibility of following a flight profile that minimizes the limit cycle amplitude. This could be achieved by climbing, descending, or introducing sideslip, recalling that a sideslip of 10 degrees or more suppresses the limit cycle. These properties make this case sensitive to pilot strategy, but of more importance is the possibility that a series of maneuvers could be followed that would allow the attainment of power-limited airspeeds for this container.

MODIFYING THE CONTAINER SHAPE

Modifying the container shape to improve its aerodynamic properties is a powerful but less practical way of extending carrying speed. Specifically, it was found that the addition of a wake splitter plate or rear fins suppressed the unsteady moments as much as the introduction of the optimum 10-degree angle of attack. The one configuration tested with fins could be carried to a speed of 120 knots, as opposed to 90 knots without them. Requirements for the fins and the wake splitter plate are modest. The fins could be the aft doors, and the splitter could be a plate about 10 feet in length mounted on the centerline of the aft face. These configurations are shown in Figure 14.

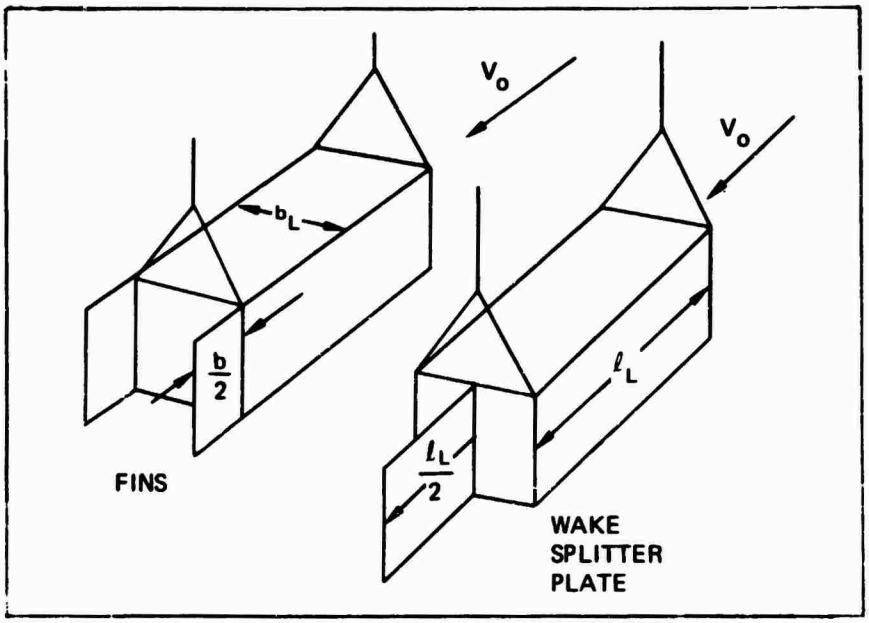

FIGURE 14. MODIFICATIONS TO CONTAINER CONFIGURATION.

An additional benefit of the fins is the added static directional stability, which should greatly aid the single-point suspension configuration. A test of this configuration during the dynamic wind tunnel tests showed that the container would remain in the small-end-forward position even when started at a 90-degree sideslip. The limits of stability for this configuration, however, were not explored in the tunnel. It is likely that the addition of fins to a single-point suspension will increase the limiting carrying speed to perhaps 60 knots.

ACTIVE STABILITY AUGMENTATION USING CABLE ACTUATORS

One form of an active stabilization device that was found to be highly effective is the concept of driving the cables in response to measured load motions. In its simplest form, a cable guide is moved in the horizontal plane by an actuator that is driven by load yaw rate with respect to the helicopter. This has the effect of damping the pendulum and bifilar modes. If gains are set to provide a damping ratio of 0.5 in hover, the configuration will be easily handled in forward flight to speeds approaching 200 knots. With a two-point suspension, such a device would incorporate two cable guides driving each cable laterally just below its attachment point to the helicopter. The guides would be driven laterally and collectively in response to lateral sway rate and differentially in response to load yaw rate (relative to helicopter body axes). If the gains are set to produce a damping ratio of 0.5, the limit cycle amplitude is suppressed to less than 1/10 of its unaugmented value, thus eliminating any load carrying speed limitations. This device was incorporated in the Model 347 simulation, and the evaluations revealed that speeds up to 180 knots could be reached. The maximum lateral cable guide displacements called for were slightly greater than ±2 feet for the transient, following turn-on with large load motions, and less than ± foot for normal maneuvering when the system was already turned on prior to acceleration to high speed.

The advantage of this system is its ability to suppress the limit cycle for all conditions of load angle of attack and sideslip, eliminating sensitivity to maneuvering. A disadvantage is, of course, the cost and complexity of the mechanisms required to sense the load motions and actuate the cable guides.

MODIFYING THE HELICOPTER STABILITY AUGMENTATION SYSTEM

Modifying the helicopter's stability augmentation system (SAS) is an attractive way of stabilizing external loads. The Model 347 helicopter system was modified to include lateral SAS inputs from lateral cable sway rate and directional SAS inputs from the load relative yaw rate. No shaping of these signals was incorporated, and the 347's normal low-authority SAS limits were retained. The gains were optimized, based on improving the load yaw and sway damping ratios. Improvements were possible up to a point, and then high-frequency instabilities associated with reaching SAS limits were observed. The gains were reduced until a nominal damping ratio of 0.3 - 0.4 was obtained. This configuration was then evaluated and found to offer only slight increases in allowable carrying speed.

A closer examination of the data and pilot comments revealed that the helicopter's ride qualities were being compromised by the load motion inputs into the SAS. Specifically, the load yaw rates were commanding the helicopter to "follow" the load in an attempt to reduce the differential yaw motion. Since the pilot's station is about 23 feet forward of the

helicopter center of gravity, this SAS activity showed up as a side force oscillation at the load yaw (bifilar) frequency. These side forces became uncomfortable with increasing speed and caused the pilot to downrate his judgment of allowable carrying speed. The lateral SAS input from load sway rate did not improve the situation. Other combinations of feedbacks incorporating combinations of load position and rate were attempted, without noticeable improvements.

In a sense, attempting to use the relatively low bandwidth helicopter to suppress the relatively high bandwidth load yaw limit cycle motions does not appear to offer significant improvements in allowable carrying speed. This can be related to the cable guide concept in which the inertial cable guide movements must be produced by moving the whole helicopter. These movements were found to be about ±1 foot, which translates to ±5 degrees of helicopter yaw angle for a cable separation of 24 feet.

ACTIVE STABILITY AUGMENTATION USING AUXILIARY AIRFOILS

The use of an active stability augmentation system employing aerodynamic surfaces driven by rate gyros is another interesting but less practical way of extending allowable carrying speed. This kind of device generally employs a servo-driven airfoil surface placed behind the load to introduce yawing moments proportional to yaw rate. Because the airfoil must operate in the wake of the load, predicting its moment characteristics will be difficult. If a pure damping moment could be produced, the device has the effect of augmenting C_{N_r}, which directly reduces the limit cycle amplitude. The amplitude is proportional to the reciprocal of the square root of C_{N_r}.

For the device to be effective, C_{N_r} must be at least doubled from its present value of -0.94. This is a decrement of about -1. A simple surface that is positioned a container-length aft of the center of mass may work; however, this is considered doubtful because of the highly separated and turbulent wake in which the surface must operate. This judgment is based on drag chute test results with the 0.1-scale container model in the wind tunnel. If a drag device could not stabilize the load, a lifting device such as an airfoil will not do much better.

SUMMARY

It is clear that optimizing the suspension system to increase the bifilar frequency, optimizing the angle of attack, and using maneuvering techniques can effectively extend carrying speeds. Similarly, it is clear that the addition of fins to suppress the unsteady aerodynamics and the use of more exotic devices such as active cable actuators will extend carrying speeds.

Direct feedback to the onboard SAS without an extensive optimization effort produced only minor improvements.

The allowable carrying speeds as determined from the Model 347 simulation of the empty 8-by-8-20-foot container on a two-point suspension are listed in Table 5. These data are the result of the evaluation of one highly skilled pilot experienced in sling load flight; a larger sample of pilot opinion would enhance the results.

TABLE 5. SIMULATOR RESULTS OF ALLOWABLE CARRYING SPEED FOR THE 8-BY-8-BY-20-FOOT CONTAINER

(Two-Point Suspension with Spreader, Carried by the Model 347 Helicopter; Total Weight 45,000 lb; 8-foot Slings, Container Rigged Level)

Cable and SAS Parameters / Configuration	Cable Separation (ft)	Cable Length (ft)	Speeds (Kn)			
			Bare Container*	With SAS Feedback	With Fins	With Cable Guide Stabilizer
Container Weight 8705 lb Helicopter Weight 36,000 lb	24	7.5	90	100	120	180
	30	7.5	100	100	NT	170
	20	7.5	105 150	NT	NT	165
	15	7.5	130	160	NT	160
	24	50	85	100	NT	150
	20	50	70	NT	NT	150
	15	50	100	90	NT	120
Container Weight 15,000 lb Helicopter Weight 30,000 lb	20	7.5	150	NT	NT	160

* - Steady State
\+ - By accelerating, peak load yaw amplitude occurred at 110 kn.
NT - Not Tested

CONCLUSIONS

Completion of the basic study involving flight simulation of the Model 347 tandem-rotor helicopter as well as the closely related simulation studies generated data which support the following conclusions:

1. The Model 347 flight simulation program produced an effective representation of a large tandem-rotor helicopter.
2. Unsteady aerodynamic effects are a predominant factor in helicopter sling load dynamics.
3. Use of a nominal 10-degree load angle of attack in pitch and yaw will minimize the unsteady effects of sling loads.
4. Sling load dynamics can also be minimized by using wide cable separation and short cable lengths.

APPENDIX

ADVANCED TANDEM-ROTOR HELICOPTER HYBRID COMPUTER MODEL

The schematic diagrams for the full flight envelope mathematical model of the basic 347 aircraft are presented in this appendix. Functional block diagrams included at the beginning of this section present a generalized picture of how the various portions of the mathematical model are related. The relationship of the various digital and analog computers and where the various mathematical computations were assigned are also shown. The longitudinal, lateral, and directional Stability Augmentation System, rotor speed governor, and engine dynamics and stick force models are also shown in functional block diagram format.

Detailed diagrams showing appropriate analog computer component patching follow. The equations which are being modelled have been annotated on the appropriate drawings.

A complete list of symbols for the report body and for the appendix is included following the diagrams.

347/HLH HELICOPTER MATHEMATICAL MODEL

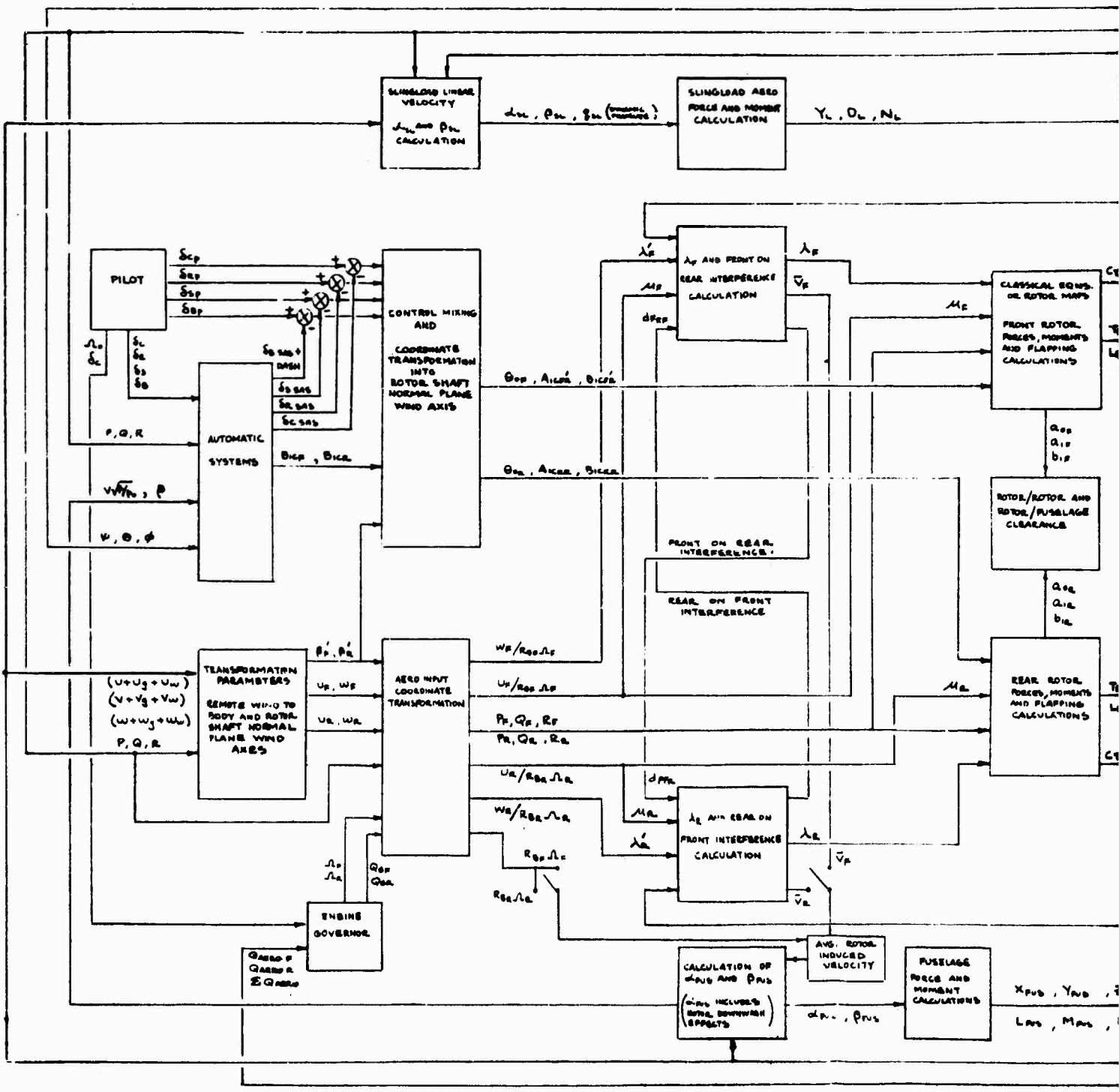

MATHEMATICAL MODEL

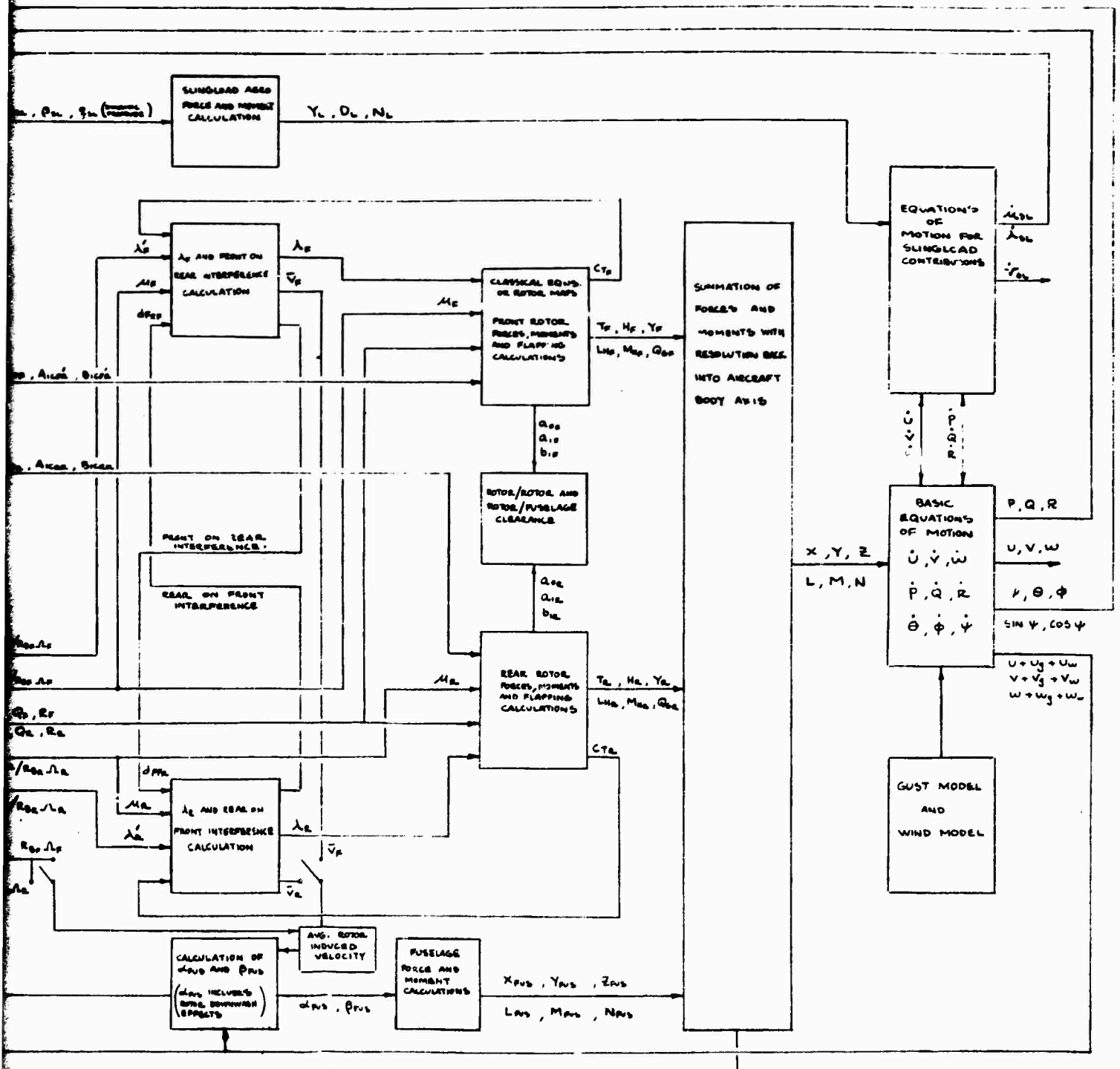

347/HLH FLIGHT SIMULATION COMPUTERS (NORT

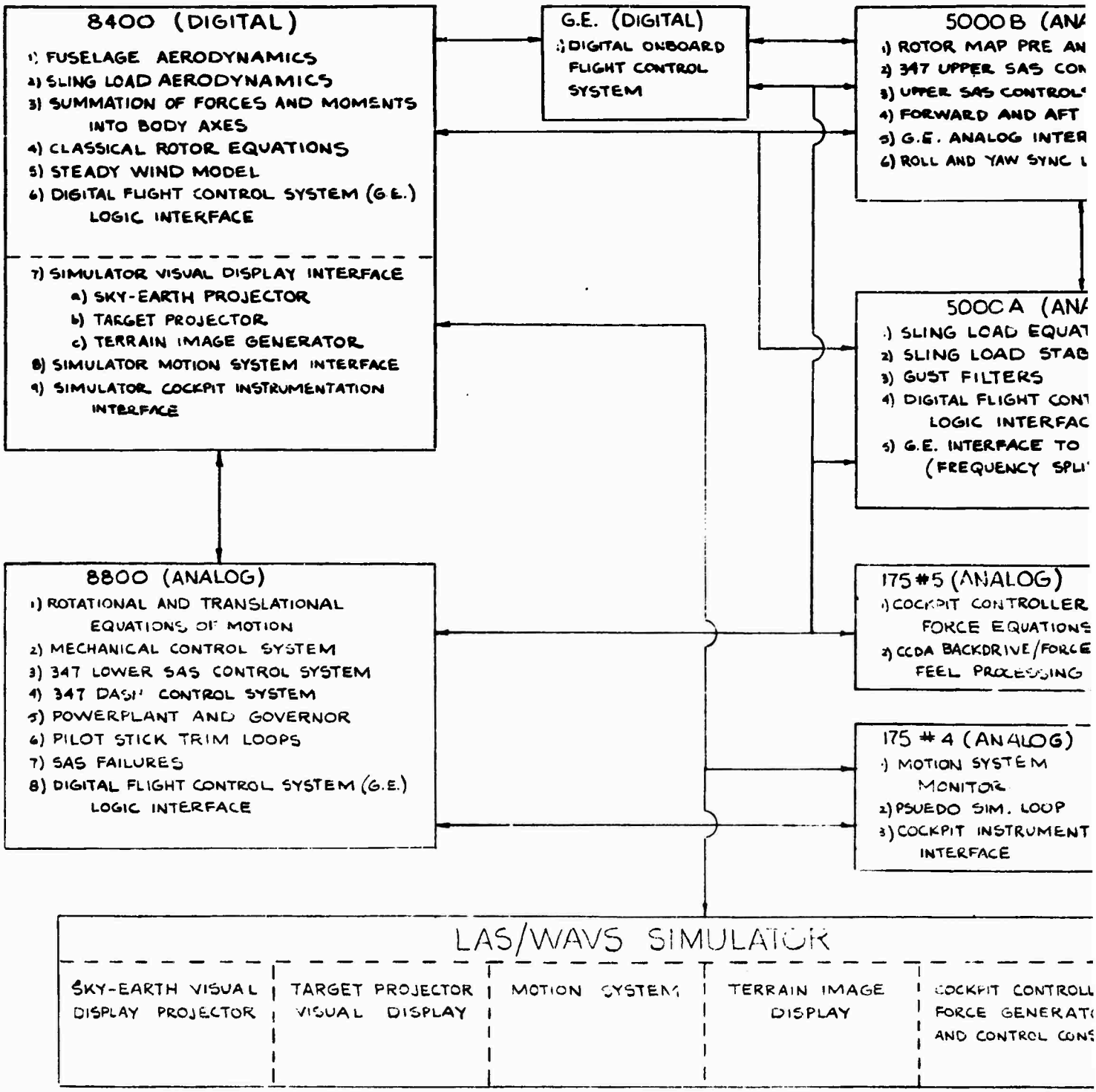

Preceding page blank

ON COMPUTERS (NORTHROP)

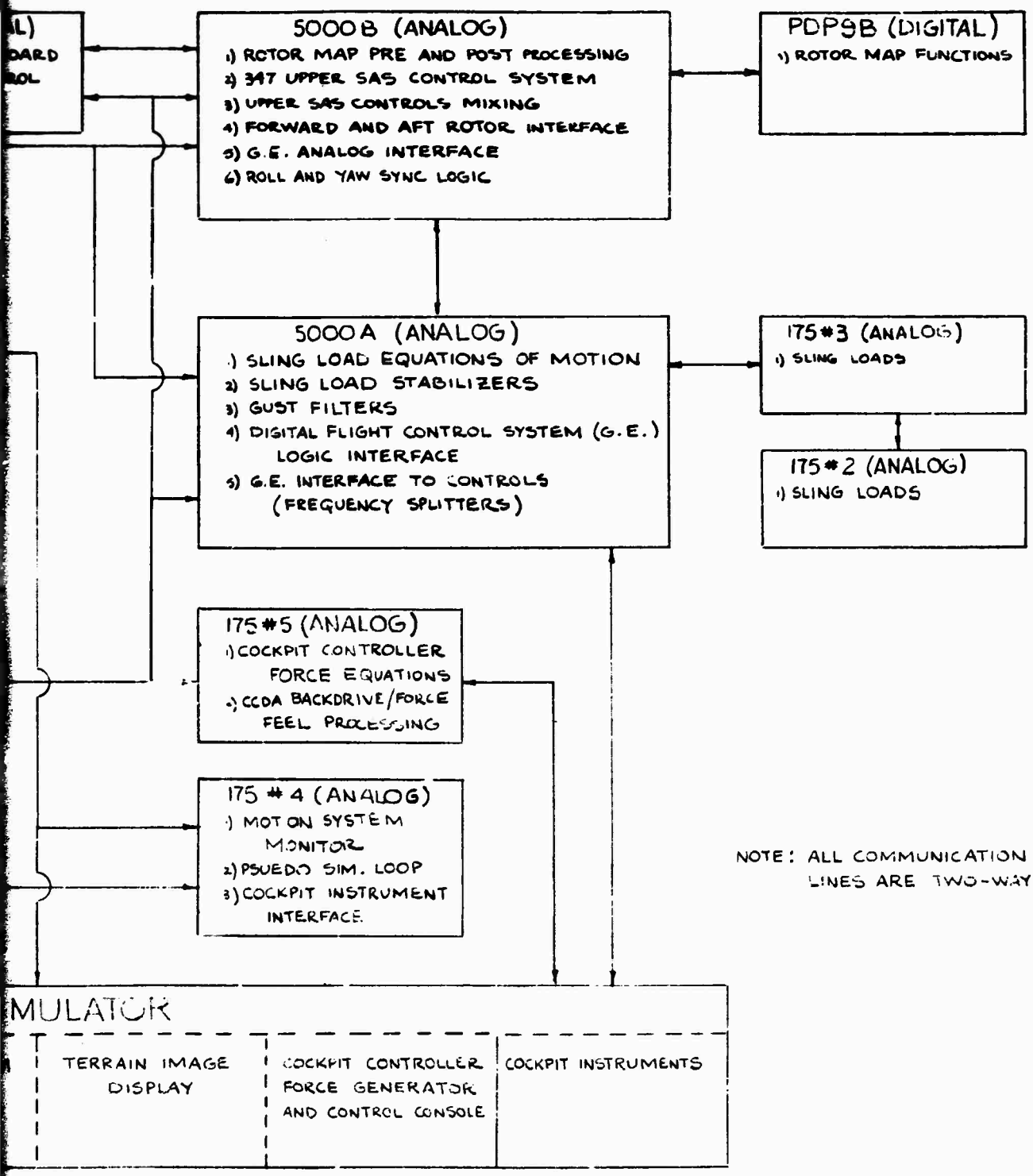

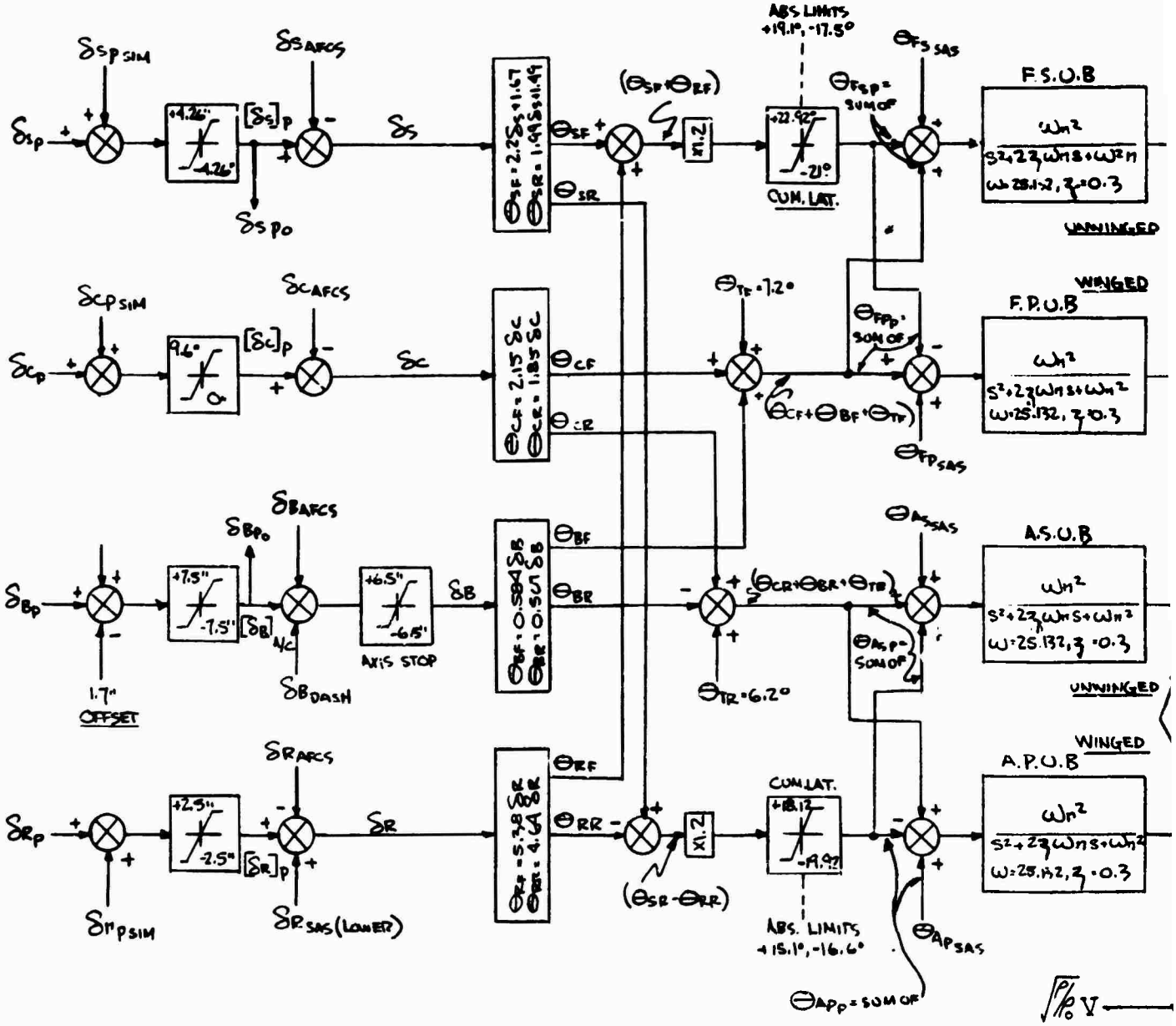

Preceding page blank

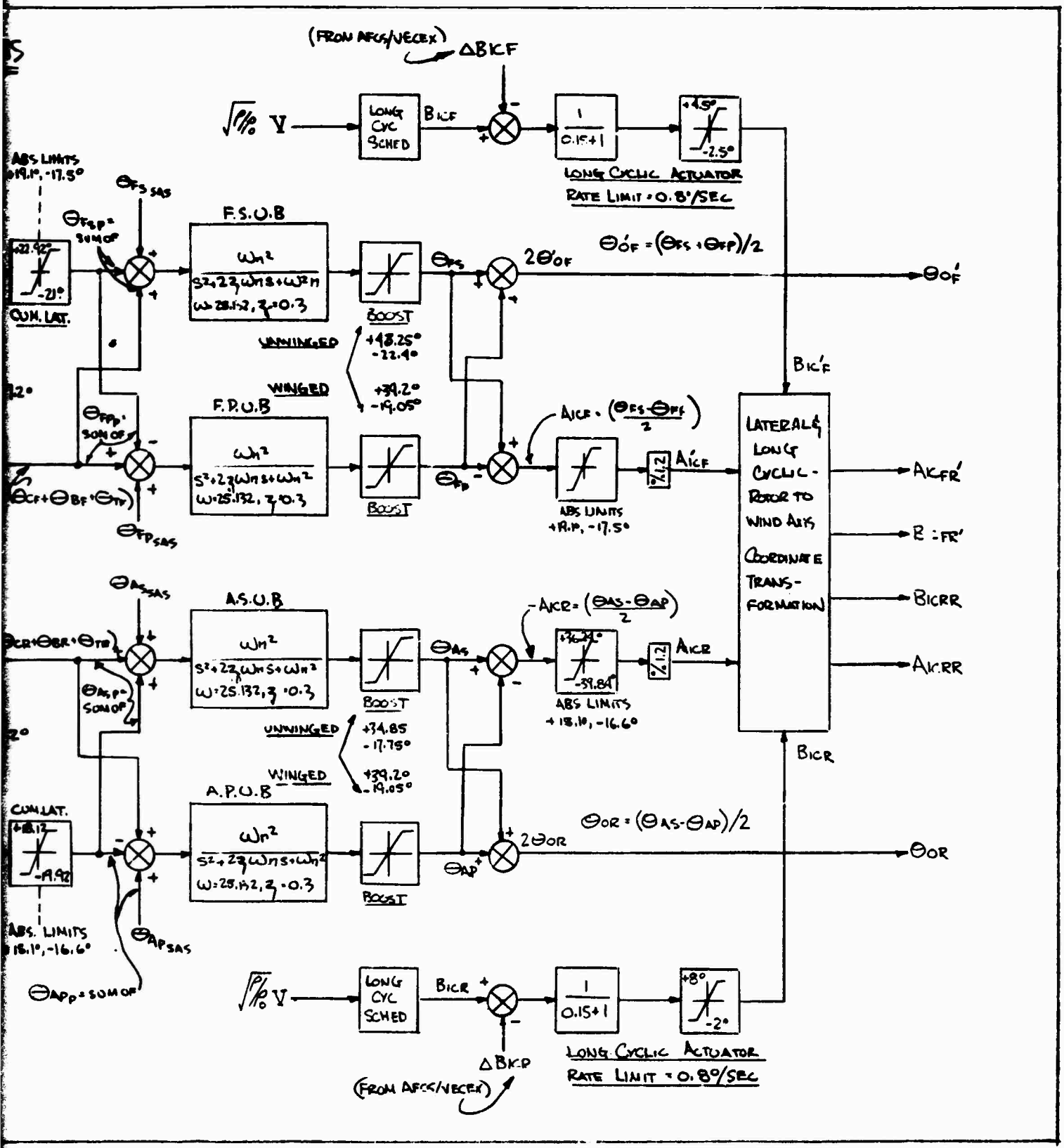
(FROM AFCS/VECEX)
ΔBICF
√P/P₀ V
LONG CYC SCHED
BICF
1/(0.15+1)
+4.5° / -2.5°
LONG CYCLIC ACTUATOR
RATE LIMIT = 0.8°/SEC
ABS LIMITS +19.1°, -17.5°
θFS SAS
θFSP = SUM OF
+22.92° / -21°
CUM. LAT.
F.S.U.B
ωn² / S²+2ζωnS+ωn² ω=25.132, ζ=0.3
BOOST
θFS
2θ'OF
θ'OF = (θFS + θFP)/2
θ'OF
UNWINGED
+18.25° -22.4°
WINGED
+39.2° -19.05°
BIC'F
F.P.U.B
θFPP = SUM OF
θFPSAS
AICF = (θFS - θFP)/2
θFP
ABS LIMITS +19.1°, -17.5°
×1/2
A'ICF
LATERAL & LONG CYCLIC - ROTOR TO WIND AXIS COORDINATE TRANSFORMATION
A'ICFR'
B'FR'
BICRR
AICRR
θAS SAS
A.S.U.B
ω=25.132, ζ=0.3
BOOST
θAS
-AICR = (θAS - θAP)/2
+36.24° / -39.84°
ABS LIMITS +18.1°, -16.6°
×1/2
AICR
θA,P = SUM OF
UNWINGED
+34.85 -17.75°
WINGED
+39.20 -19.05°
BICR
A.P.U.B
CUM LAT.
+18.12 / -19.92
ABS. LIMITS +18.1°, -16.6°
θAPSAS
θAPP = SUM OF
θOR = (θAS - θAP)/2
2θOR
θOR
θAP
√P/P₀ V
LONG CYC SCHED
BICR
1/(0.15+1)
+8° / -2°
LONG CYCLIC ACTUATOR
RATE LIMIT = 0.8°/SEC
ΔBICP
(FROM AFCS/VECEX)

347 / DASH - FUNCTIONAL BLOCK DIAGRAMS

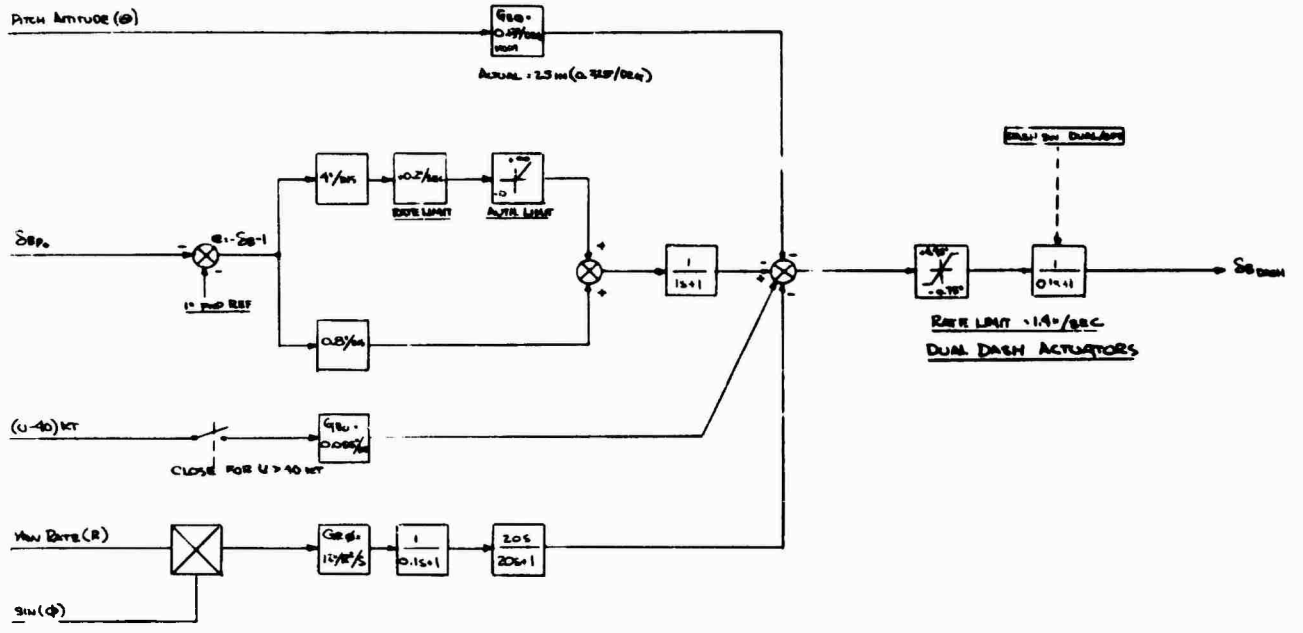

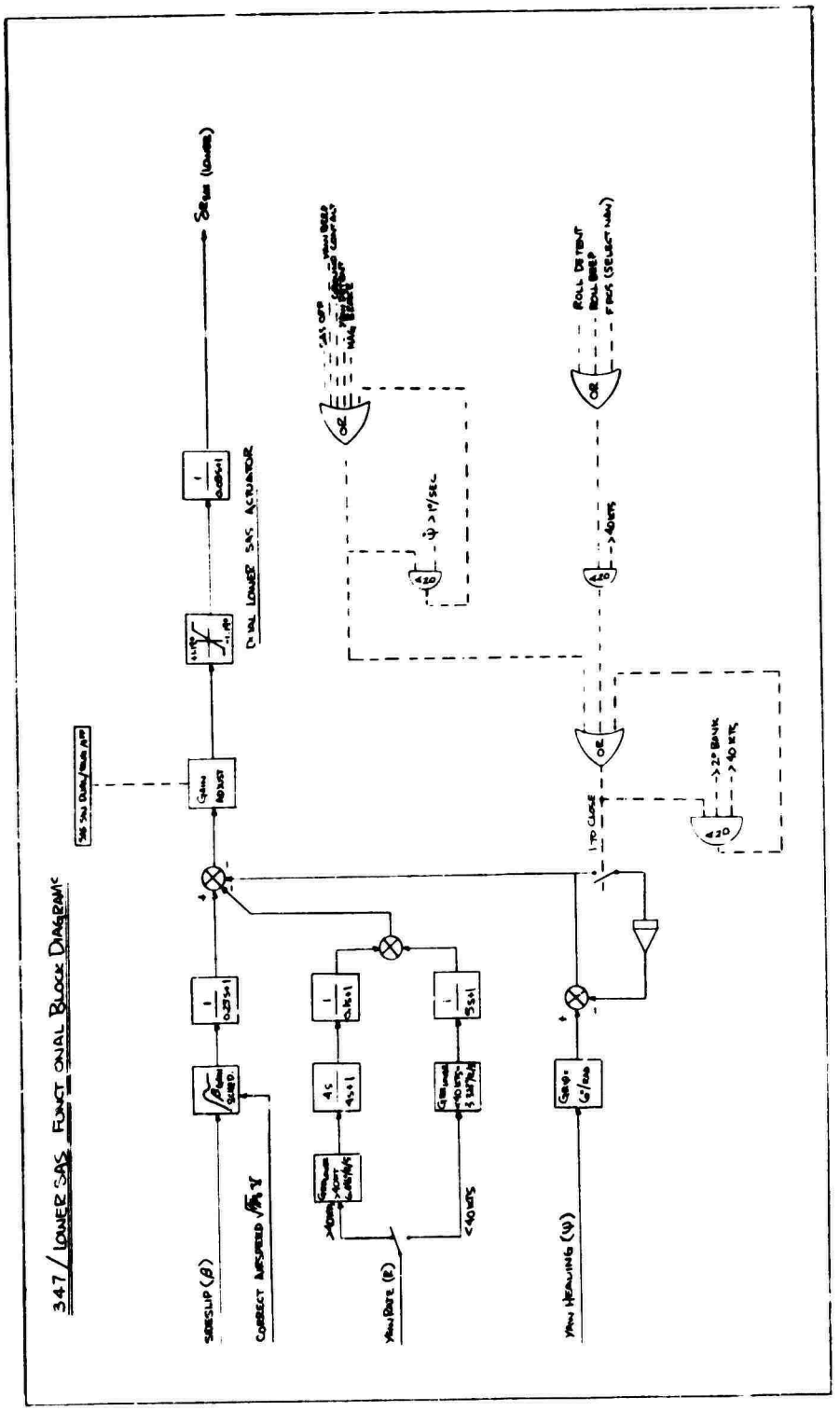
347/LOWER SAS FUNCTIONAL BLOCK DIAGRAM
SIDESLIP (β)
CORRECT AIRSPEED
YAW RATE (r)
YAW HEADING (ψ)
<40 KTS
LTD CLOSE
OR
OR
OR
ROLL DETENT
ROLL DISP
PEDS (SELECT YAW)
>40 KTS
>25° BANK
>40 KTS
ψ > 1°/SEC
DUAL LOWER SAS ACTUATOR

347/UPPER SAS - FUNCTIONAL BLOCK DIAGRAM

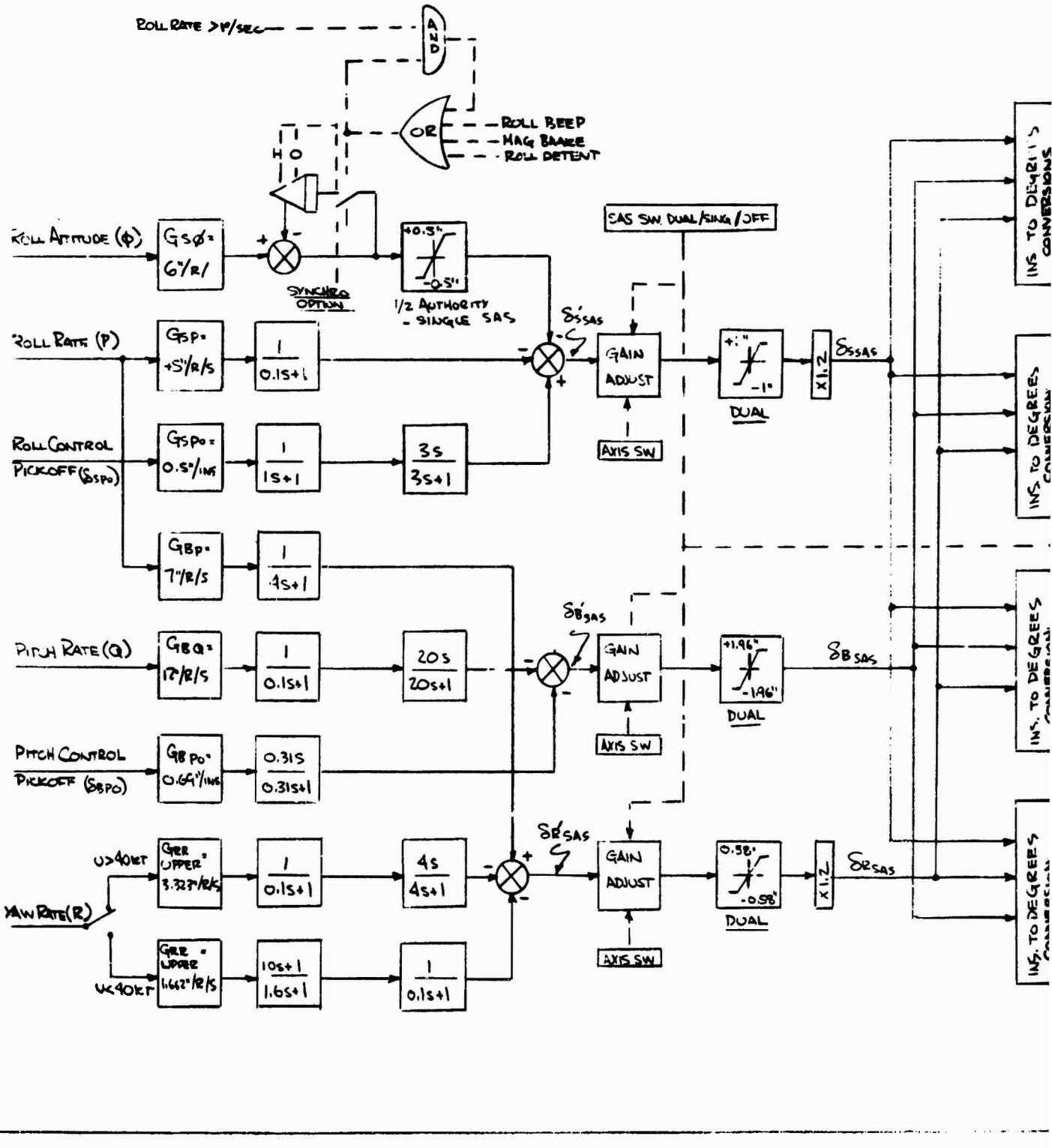

Preceding page blank

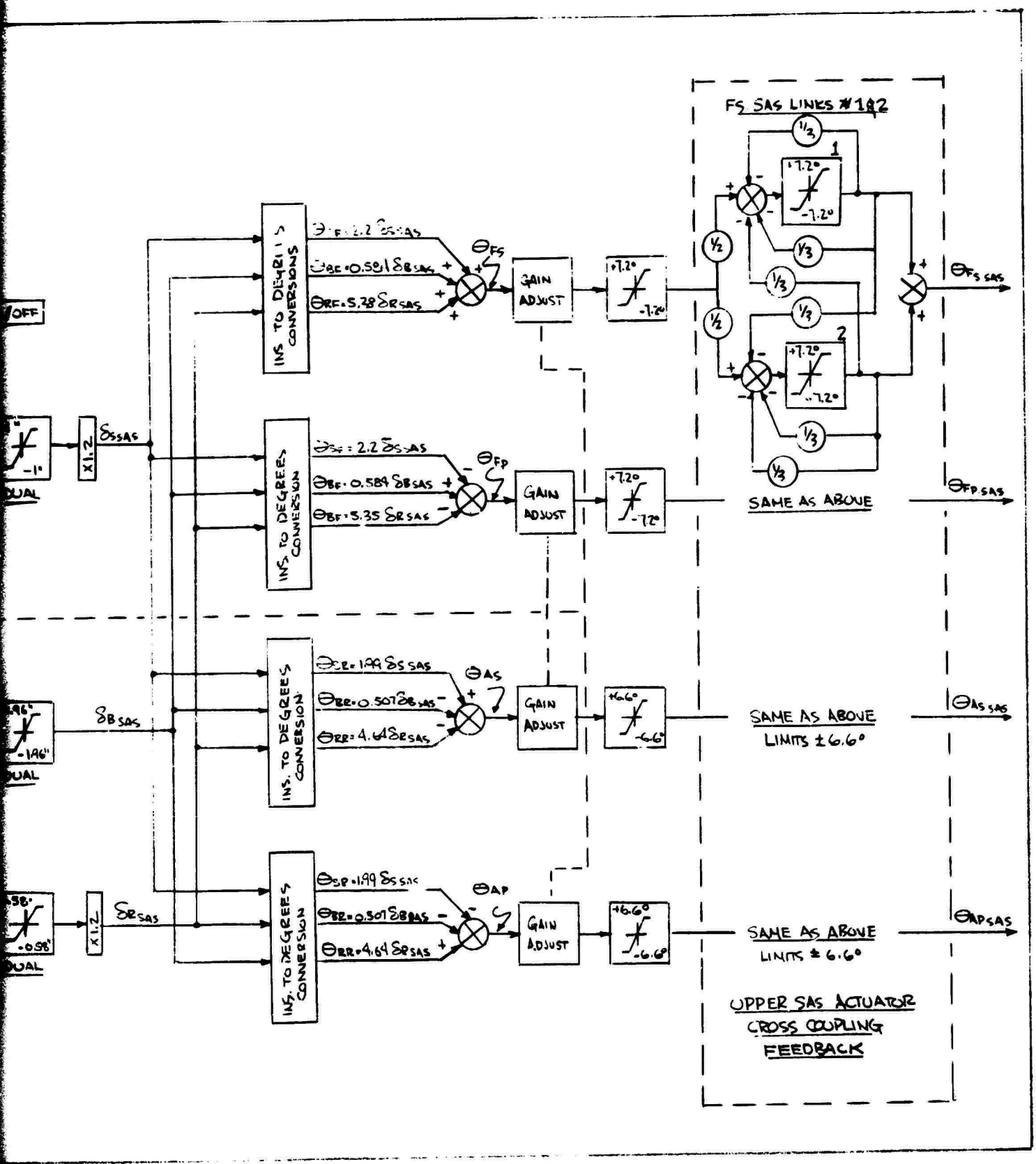
FS SAS LINES #1&2
INS TO DEGREES CONVERSIONS
INS TO DEGREES CONVERSION
INS. TO DEGREES CONVERSION
GAIN ADJUST
SAME AS ABOVE
SAME AS ABOVE
LIMITS ± 6.6°
SAME AS ABOVE
LIMITS ± 6.6°
UPPER SAS ACTUATOR
CROSS COUPLING
FEEDBACK
OFF
DUAL
DUAL
DUAL
X1.2
X1.2
+7.2°
-7.2°
+6.6°
-6.6°
1/3
1/2

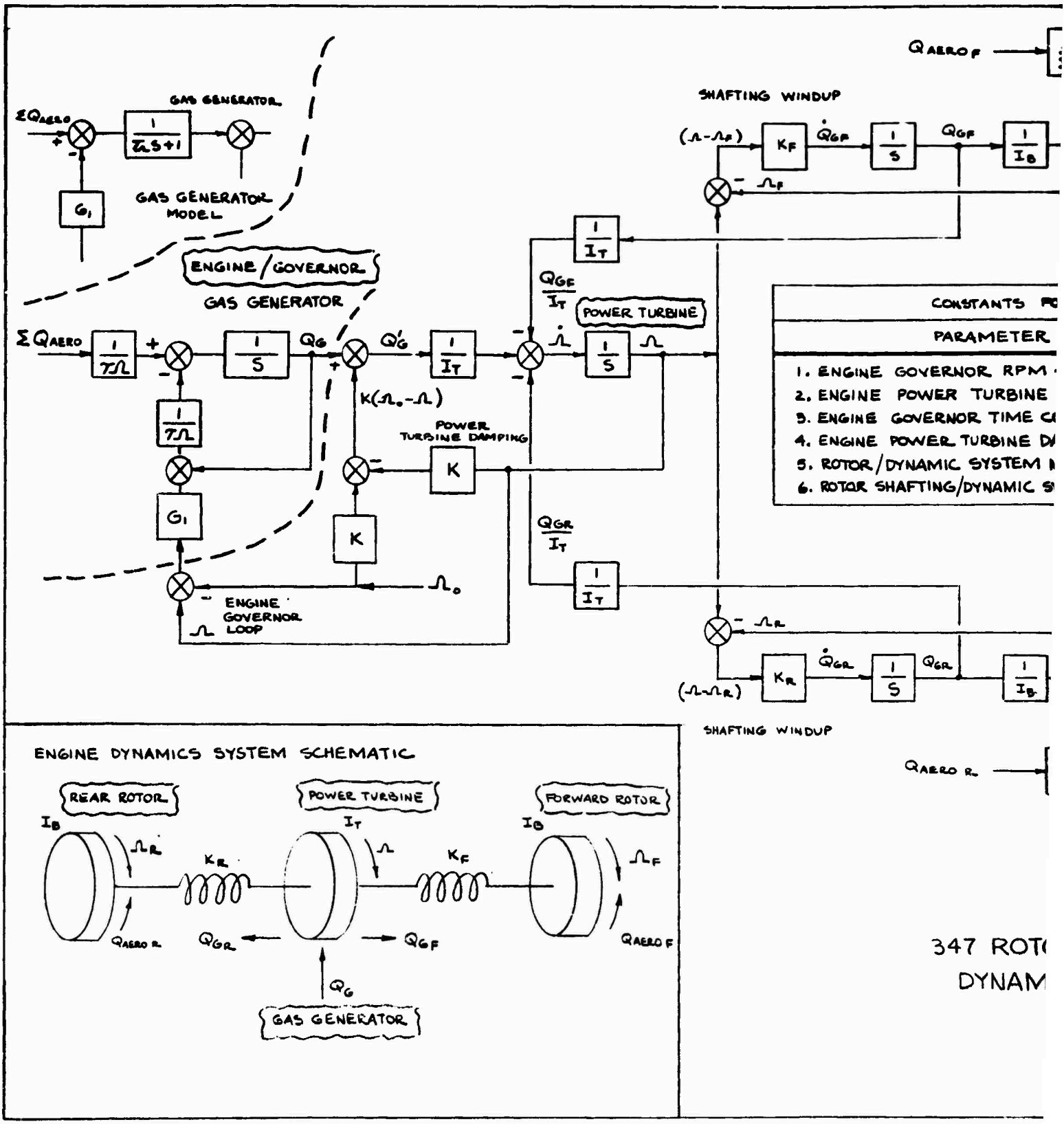

347 ROT
DYNAM

Preceding page blank

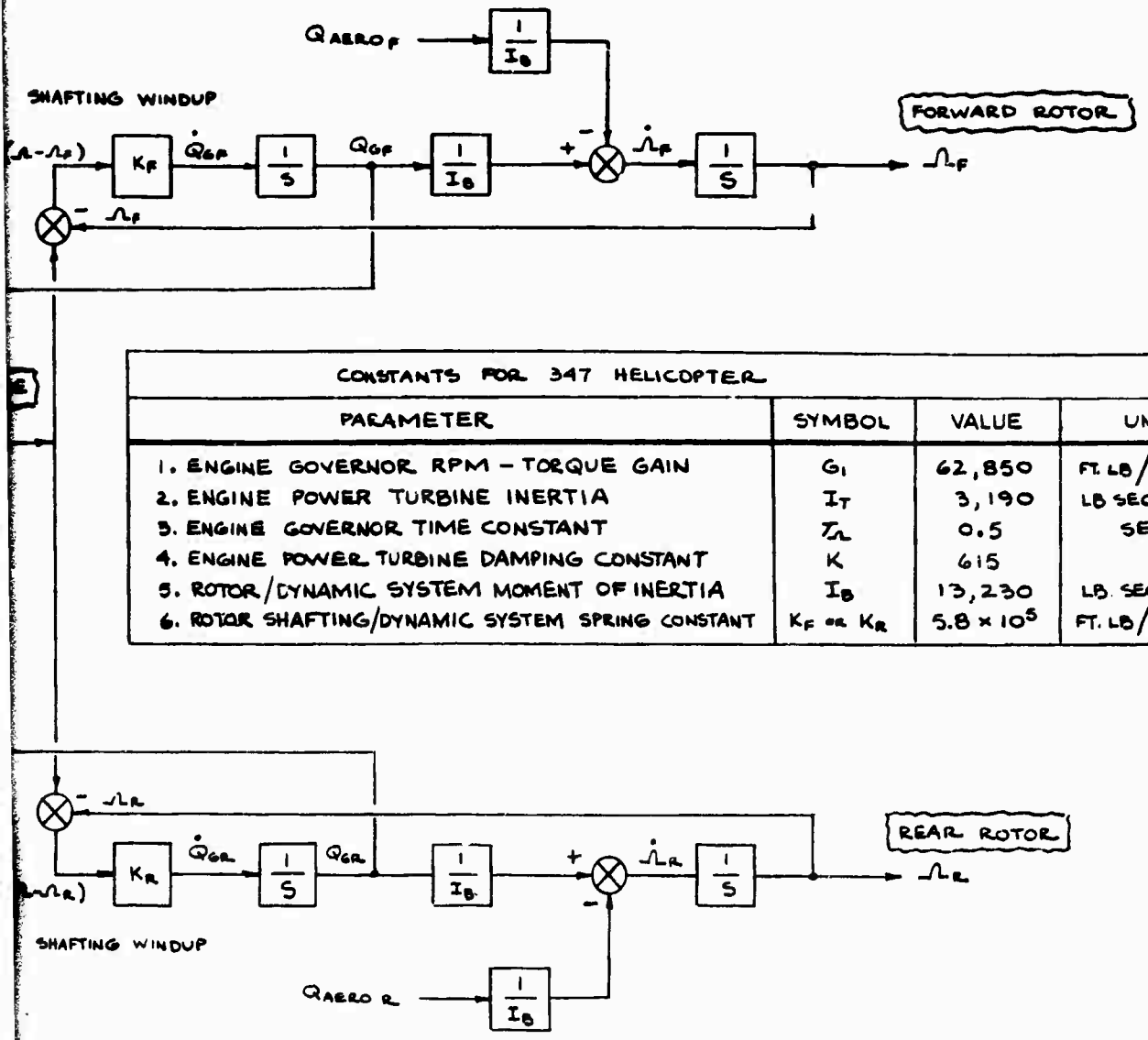

CONSTANTS FOR 347 HELICOPTER			
PARAMETER	SYMBOL	VALUE	UNITS
1. ENGINE GOVERNOR RPM – TORQUE GAIN	G_1	62,850	FT. LB / RAD/SEC.
2. ENGINE POWER TURBINE INERTIA	I_T	3,190	LB SEC^2 FT
3. ENGINE GOVERNOR TIME CONSTANT	τ_Ω	0.5	SEC
4. ENGINE POWER TURBINE DAMPING CONSTANT	K	615	
5. ROTOR/DYNAMIC SYSTEM MOMENT OF INERTIA	I_B	13,230	LB. SEC^2 FT
6. ROTOR SHAFTING/DYNAMIC SYSTEM SPRING CONSTANT	K_F or K_R	5.8×10^5	FT. LB / RAD/SEC.

347 ROTOR SPEED GOVERNOR AND ENGINE DYNAMICS FUNCTIONAL BLOCK DIAGRAM

347 HELICOPTER/FLIGHT SIMULATION STICK FORCE FUNCTIONAL BLOCK DIAGRAM

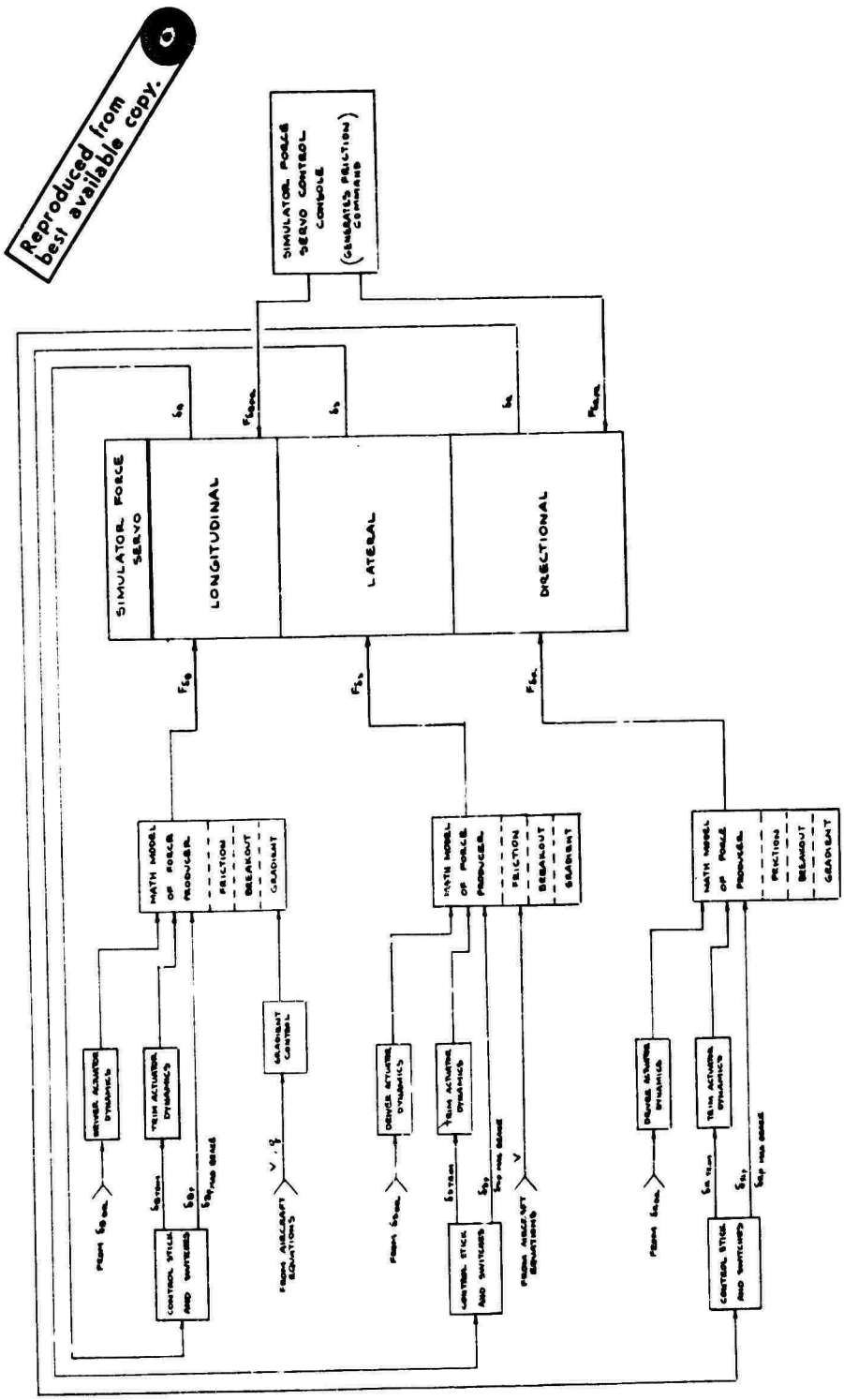

Preceding page blank

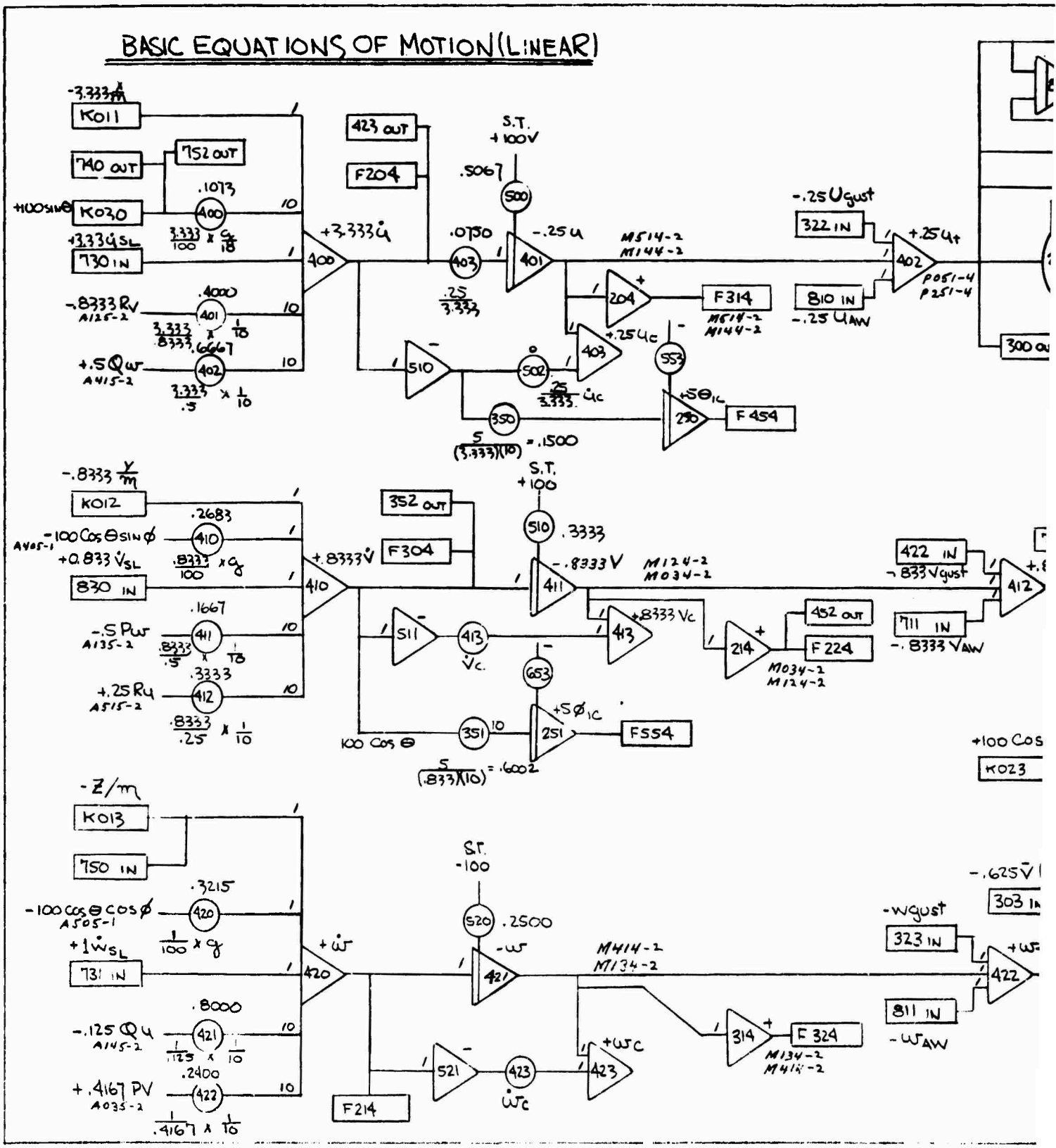

Preceding page blank

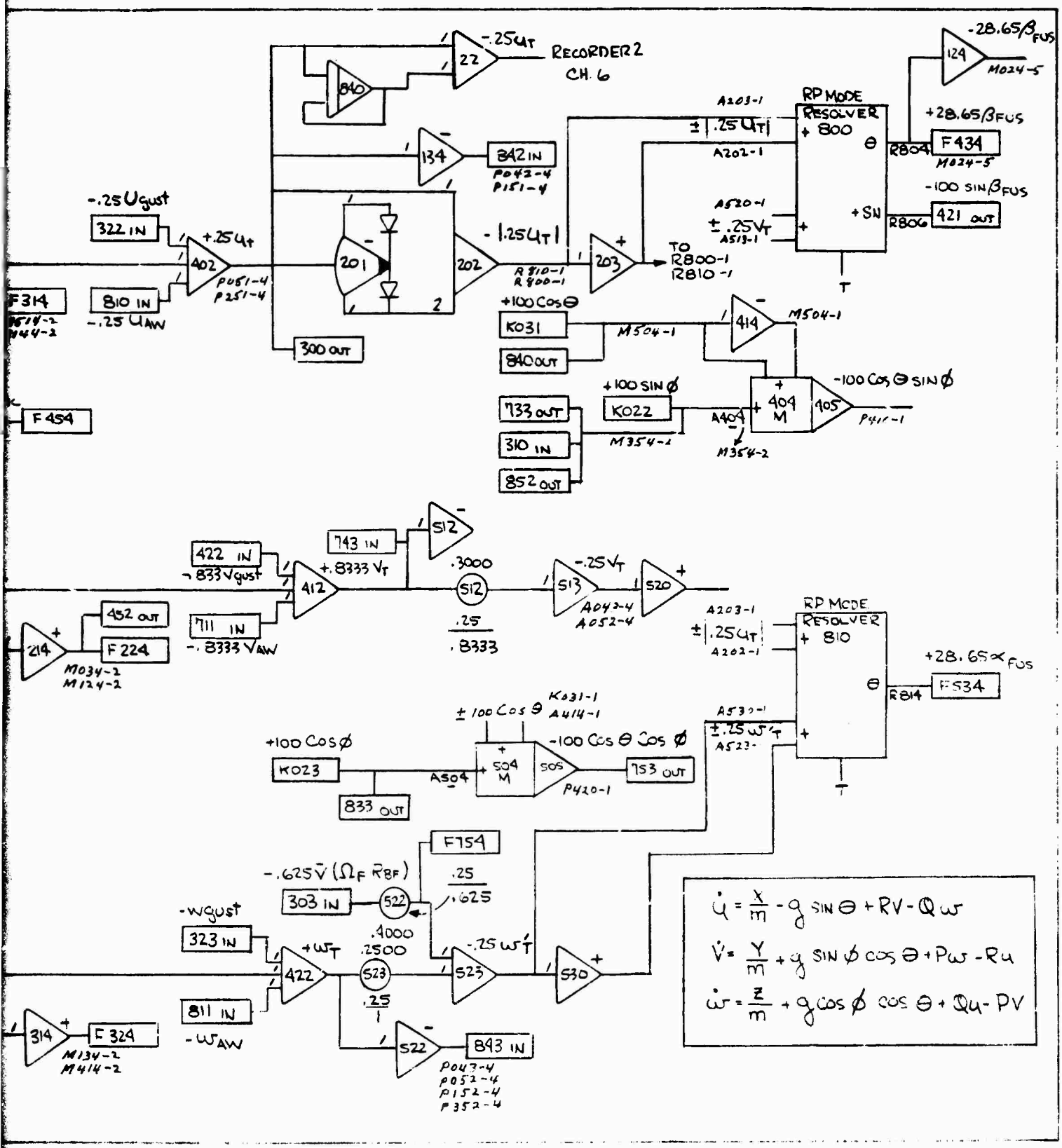

$$\dot{u} = \frac{X}{m} - g \sin\theta + RV - Qw$$

$$\dot{V} = \frac{Y}{m} + g \sin\phi \cos\theta + Pw - Ru$$

$$\dot{w} = \frac{Z}{m} + g \cos\phi \cos\theta + Qu - PV$$

BASIC EQUATIONS OF MOTION (ANGULAR)

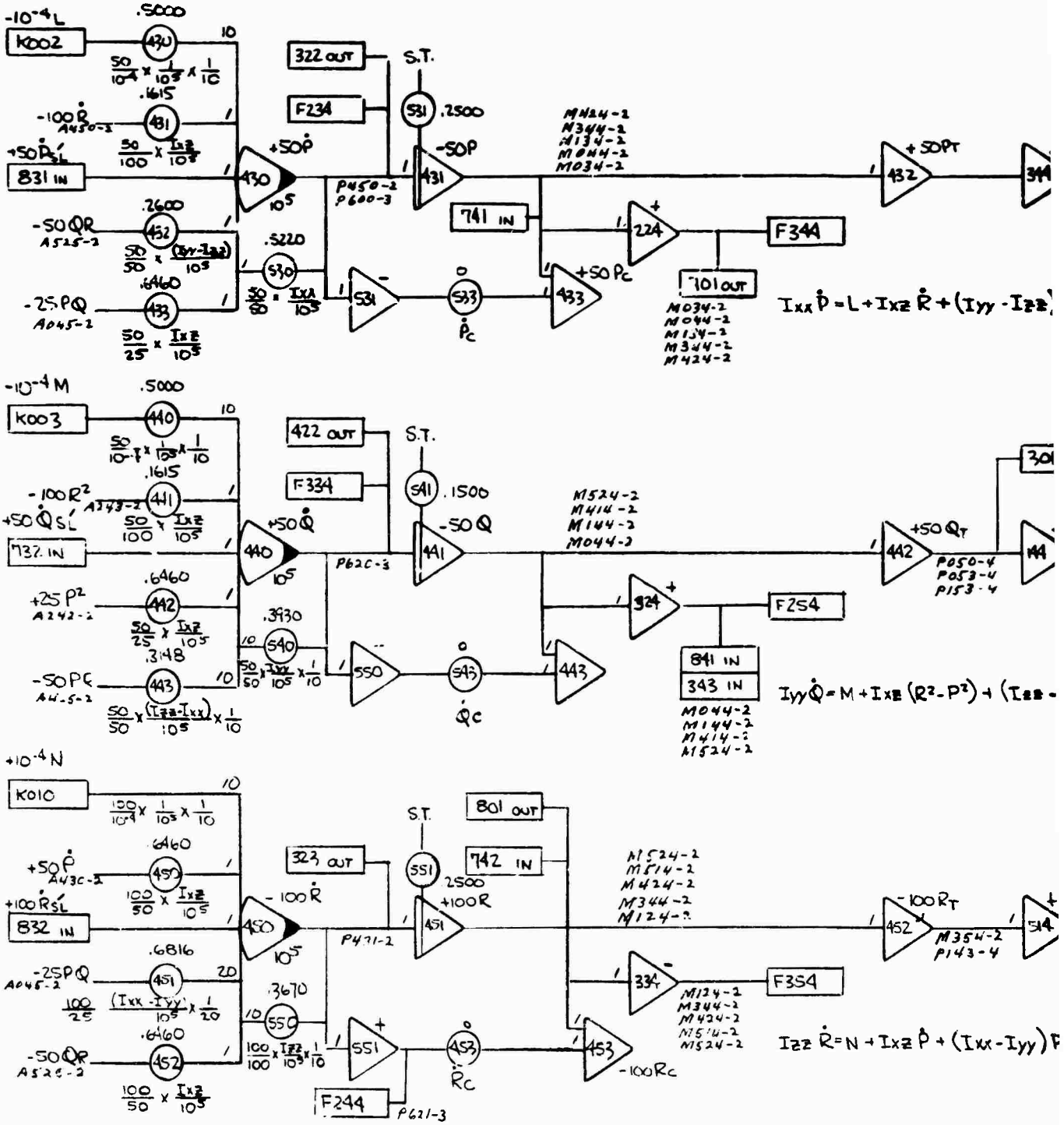

Preceding page blank

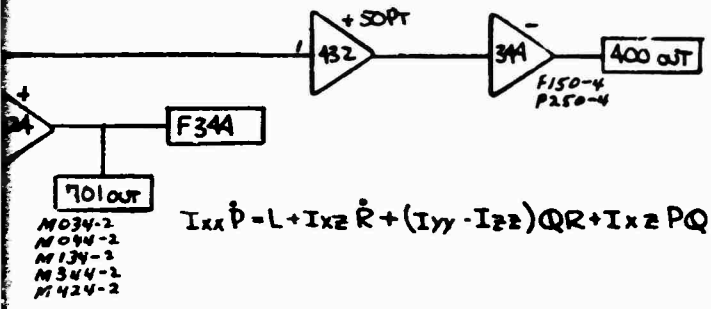

$$I_{xx}\dot{P} = L + I_{xz}\dot{R} + (I_{yy} - I_{zz})QR + I_{xz}PQ$$

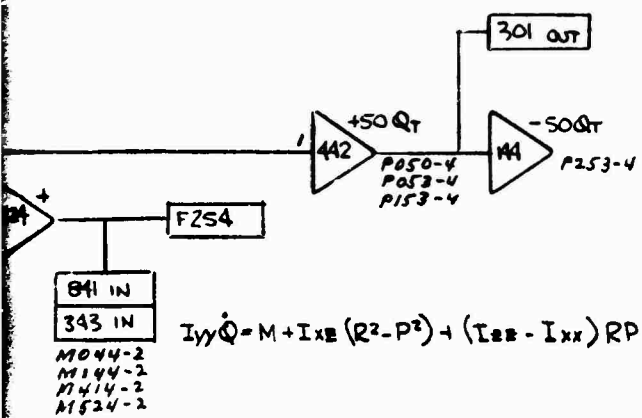

$$I_{yy}\dot{Q} = M + I_{xz}(R^2 - P^2) + (I_{zz} - I_{xx})RP$$

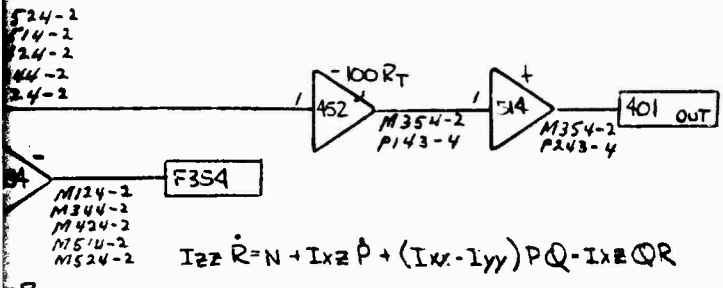

$$I_{zz}\dot{R} = N + I_{xz}\dot{P} + (I_{xx} - I_{yy})PQ - I_{xz}QR$$

oRc

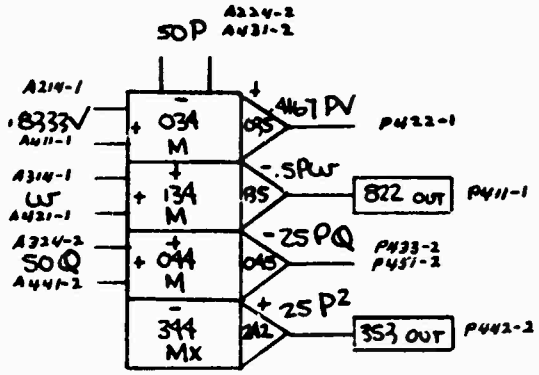

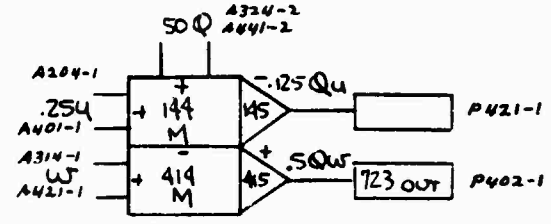

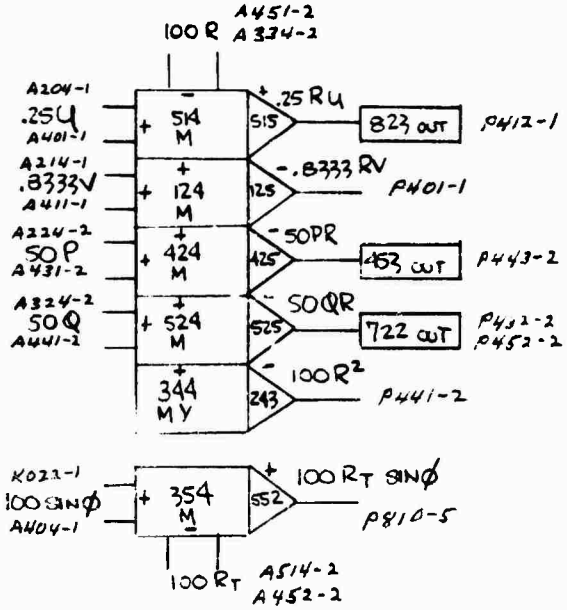

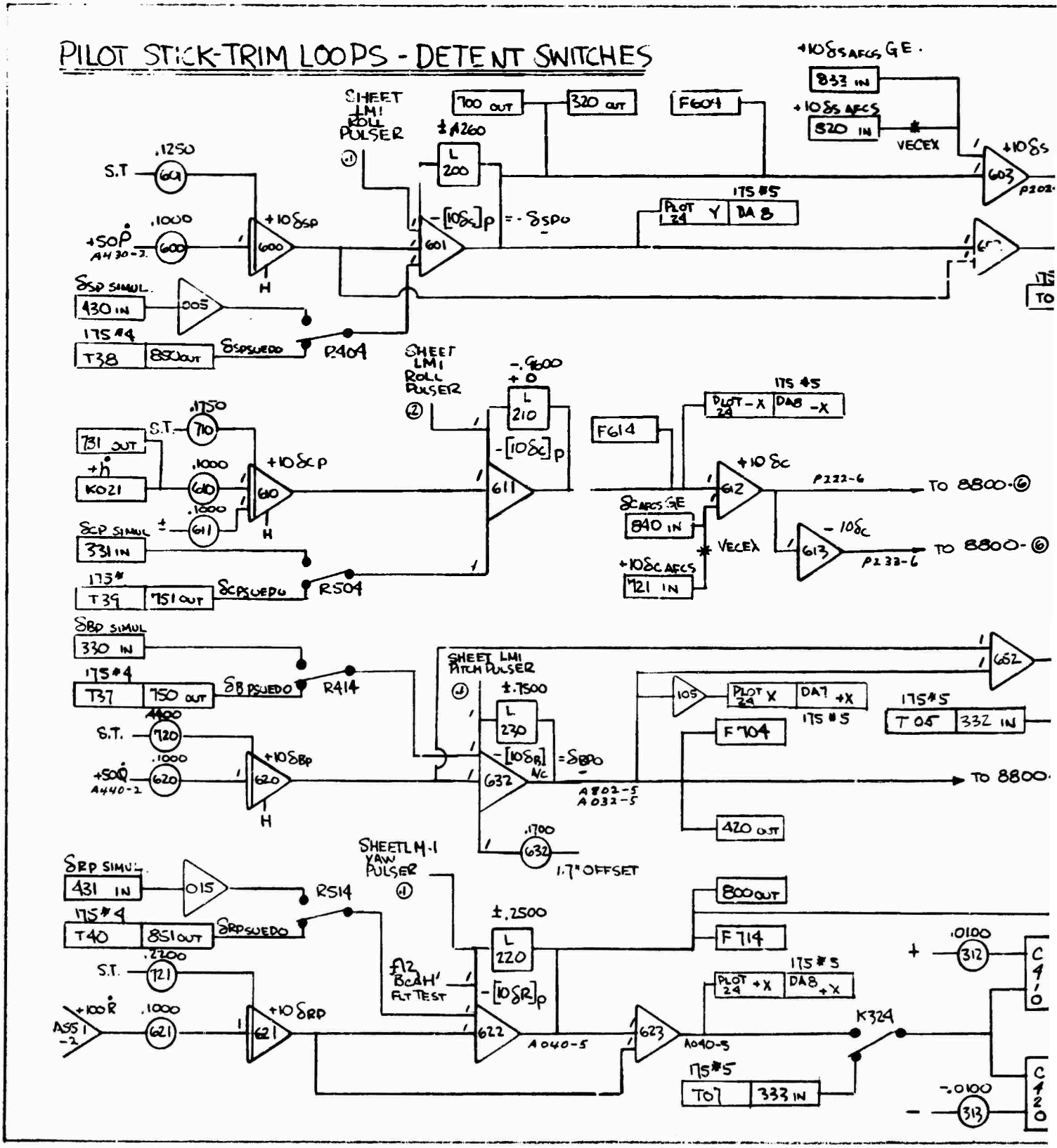

Preceding page blank

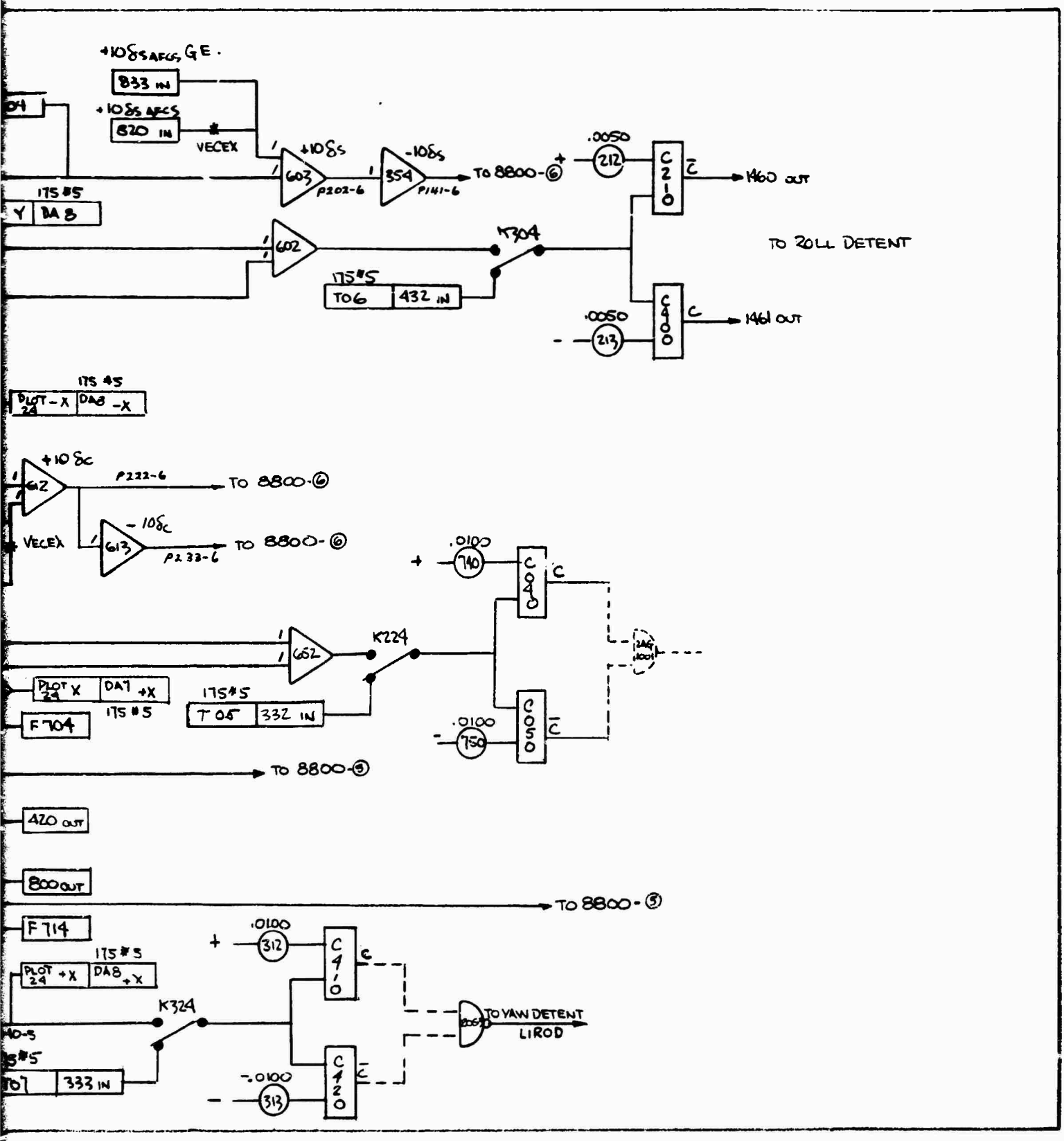
+10δs AFCS, GE.
833 IN
+10δs AFCS
820 IN
VECEX
+10δs
603
P202-6
-10δs
354
P141-6
TO 8800-⑥
.0050
212
C 2 1 0
1460 OUT
175 #5
Y DA 8
602
K304
TO ROLL DETENT
175#5
TO6
432 IN
.0050
213
C 4 0 0
1461 OUT
175 #5
PLOT -X 24
DAS -X
+10δc
612
P222-6
TO 8800-⑥
-10δc
613
P233-6
TO 8800-⑥
VECEX
.0100
740
C 4 4 0
C
K224
602
PLOT X 24
DAT +X
175 #5
F704
175#5
T05
332 IN
.0100
750
C 0 5 0
C
TO 8800-③
A20 OUT
800 OUT
TO 8800-③
F714
.0100
312
C 4 1 0
C
175 #5
PLOT +X 24
DAS +X
K324
TO YAW DETENT
LIROD
-.0100
313
C 4 2 0
C

MECH CONTROLS - LONGITUDINAL CYCLIC ACTUATORS

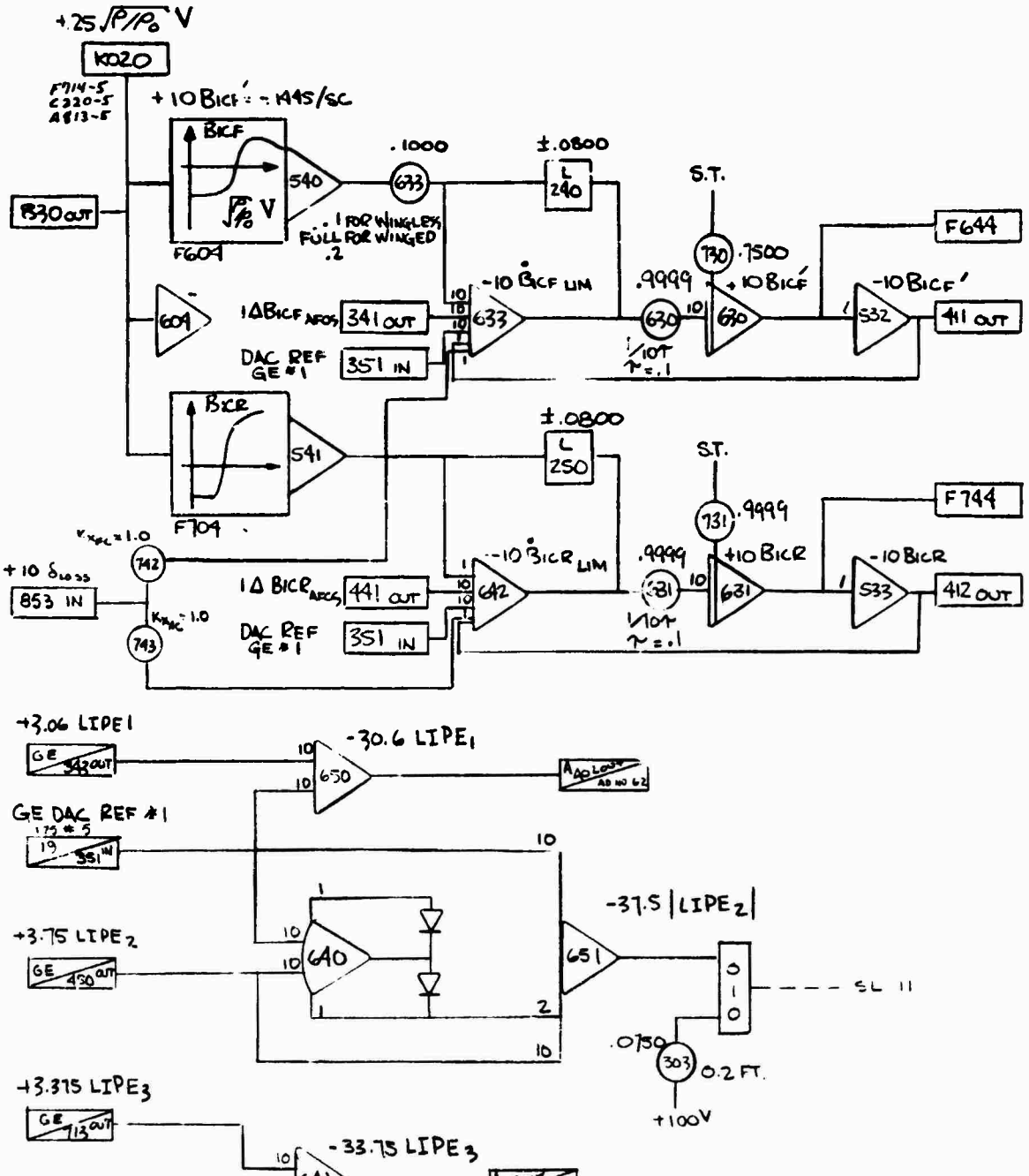

FRONT & REAR ROTOR TRANSFORMATION PARAMETERS

(LINEAR RATE COMPONENTS)

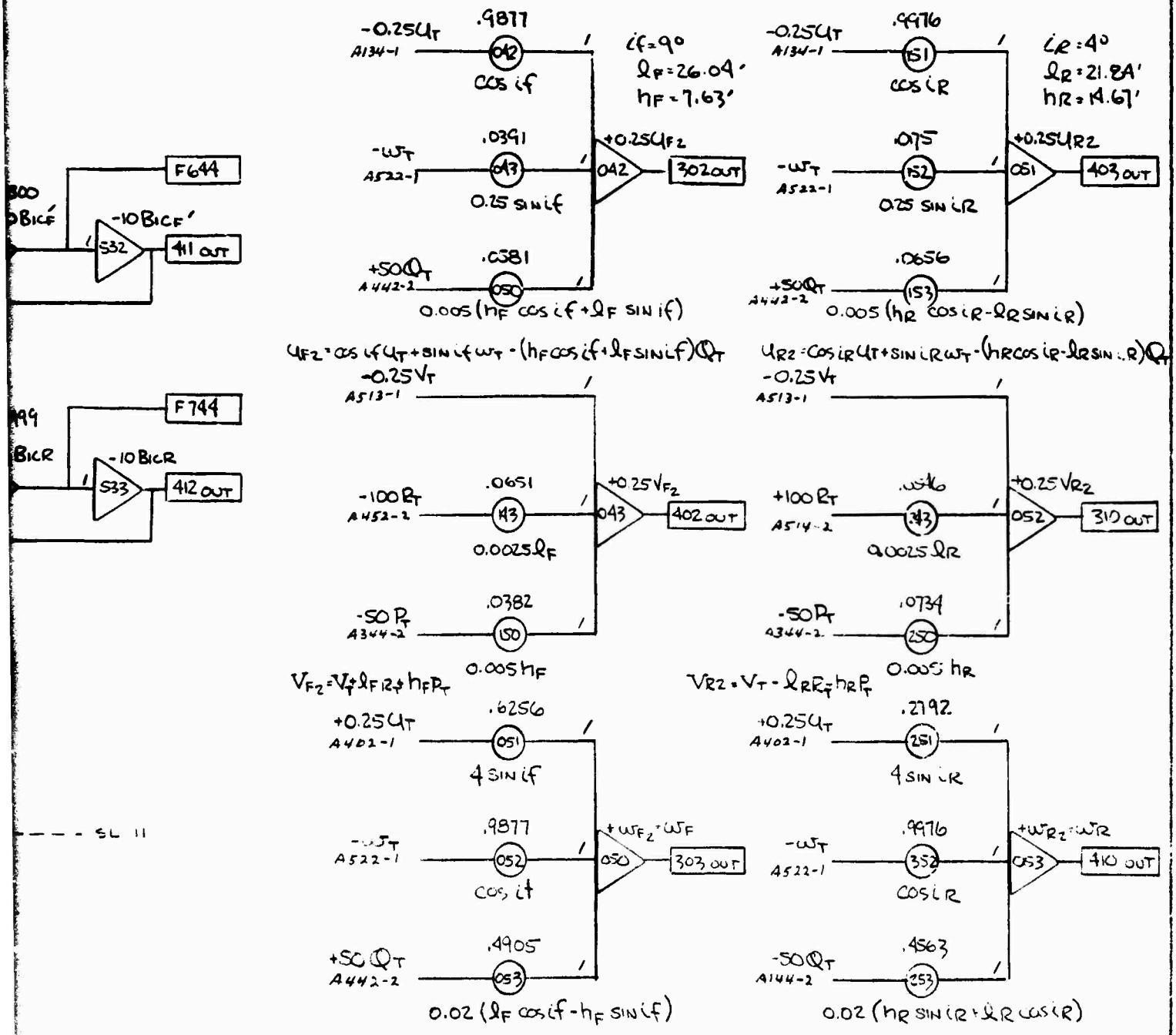

$\omega_{F2} = \omega_F = -\sin i_F U_T + \cos i_F \omega_T + (h_F \sin i_F - \ell_F \cos i_F) Q_T$

$\omega_{R2} = \omega_R = -\sin i_R U_T + \cos i_R \omega_T + (h_R \sin i_R + \ell_R \cos i_R) Q_T$

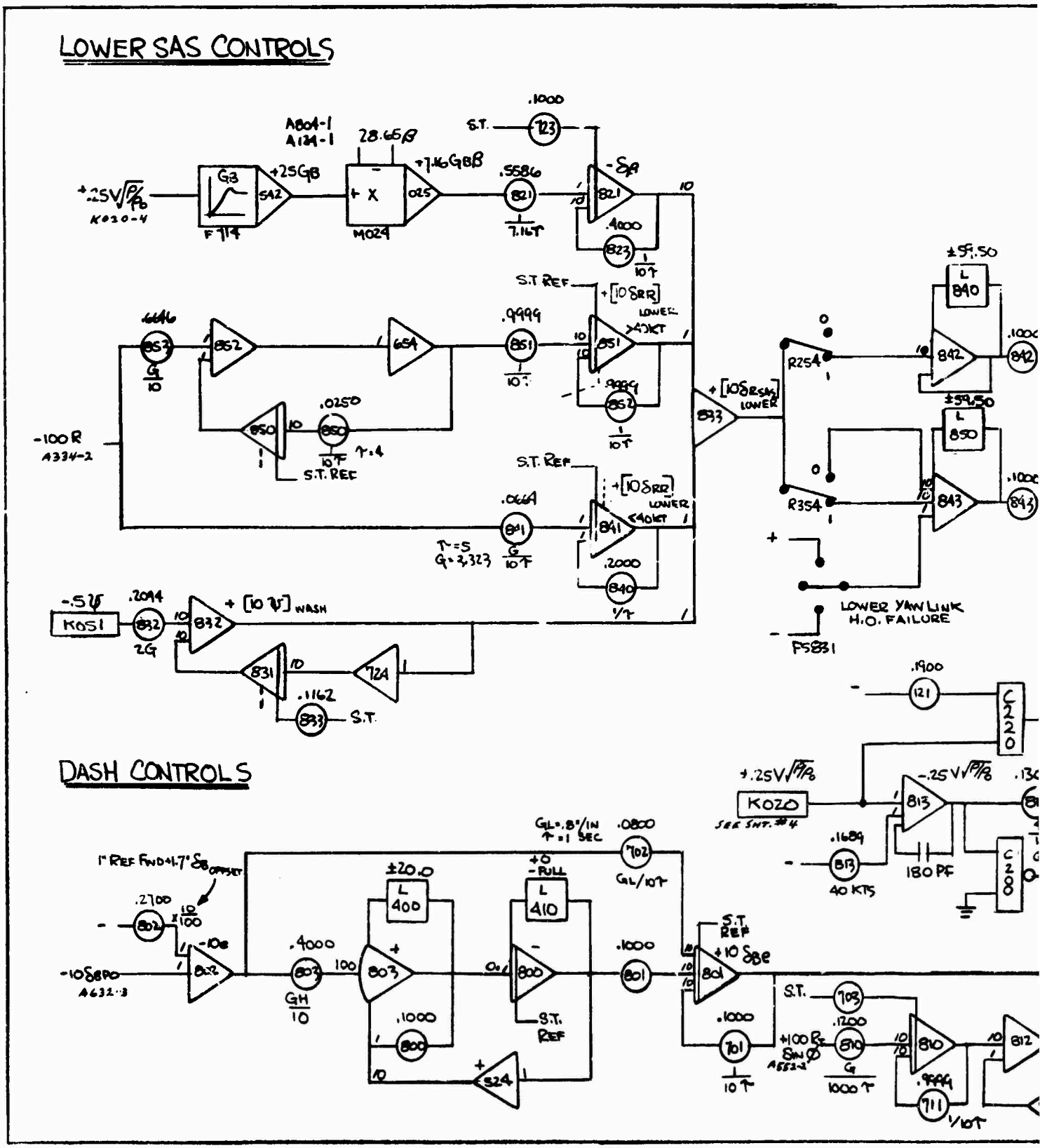

Preceding page blank

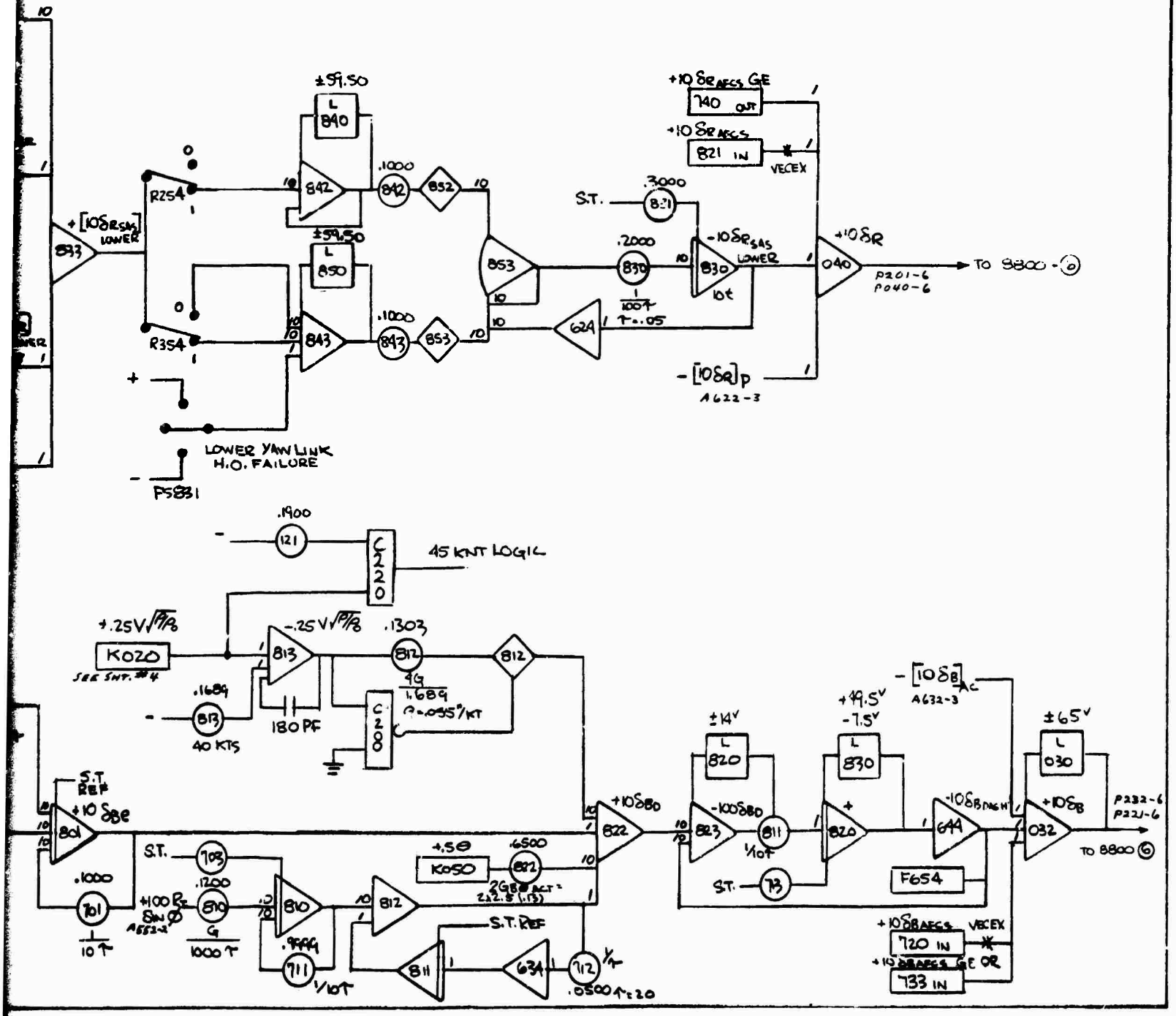
±59.50
L
840
R254
842
.1000
842
852
10
+[10δR SAS LOWER
853
.3000
S.T.
831
+10δR AEGS GE
740 OUT
+10δR AEGS
821 IN
VECEX
.2000
830
-10δR SAS LOWER
10t
040
+10δR
TO 9800 - (D)
P201-6
P040-6
±59.50
L
850
R354
843
.1000
843
853
624
1/100T
T=.05
-[10δR]p
A622-3
LOWER YAW LINK H.O. FAILURE
P5831
.1900
121
C220
45 KNT LOGIC
+.25V√PT/P0
K020
SEE SHT. #4
813
-.25V√PT/P0
.1303
812
812
.1689
813
40 KTS
180 PF
C208
.1689
Q=.095°/KT
-[10δB]AC
A632-3
±14V
L
820
+49.5V
-7.5V
L
830
±65V
L
030
S.T. REF
+10δBE
801
822
+10δBO
-100δBO
823
811
1/10T
820
-10δB PITCH
644
+10δB
032
P232-6
P22J-6
TO 8800 (G)
S.T.
703
.1000
701
1/10T
+100 BIAS δBE
A632-2
.1200
810
G
1000T
810
.9999
711
1/10T
812
+.5Θ
K050
.6500
822
2GB@ ACT=
2.2.5 (.13)
S.T.
73
F654
S.T. REF
811
634
712
1/T
.0500 T=20
+10δBAEGS
720 IN
+10δBAEGS GE
733 IN
VECEX
OR

MECHANICAL CONTROLS

FORWARD SWIVELING AND PIVOTING - UPPER BOOST ACTUATORS

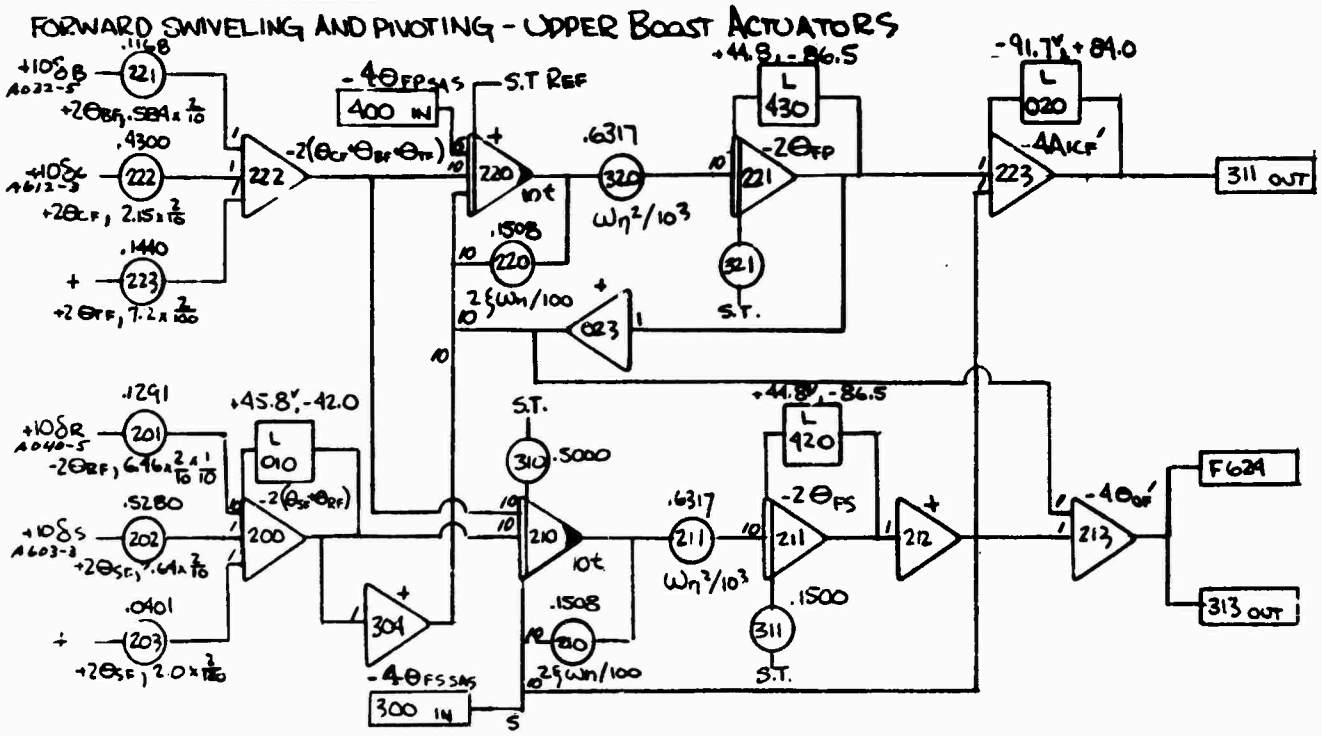

AFT SWIVELING AND PIVOTING - UPPER BOOST ACTUATORS

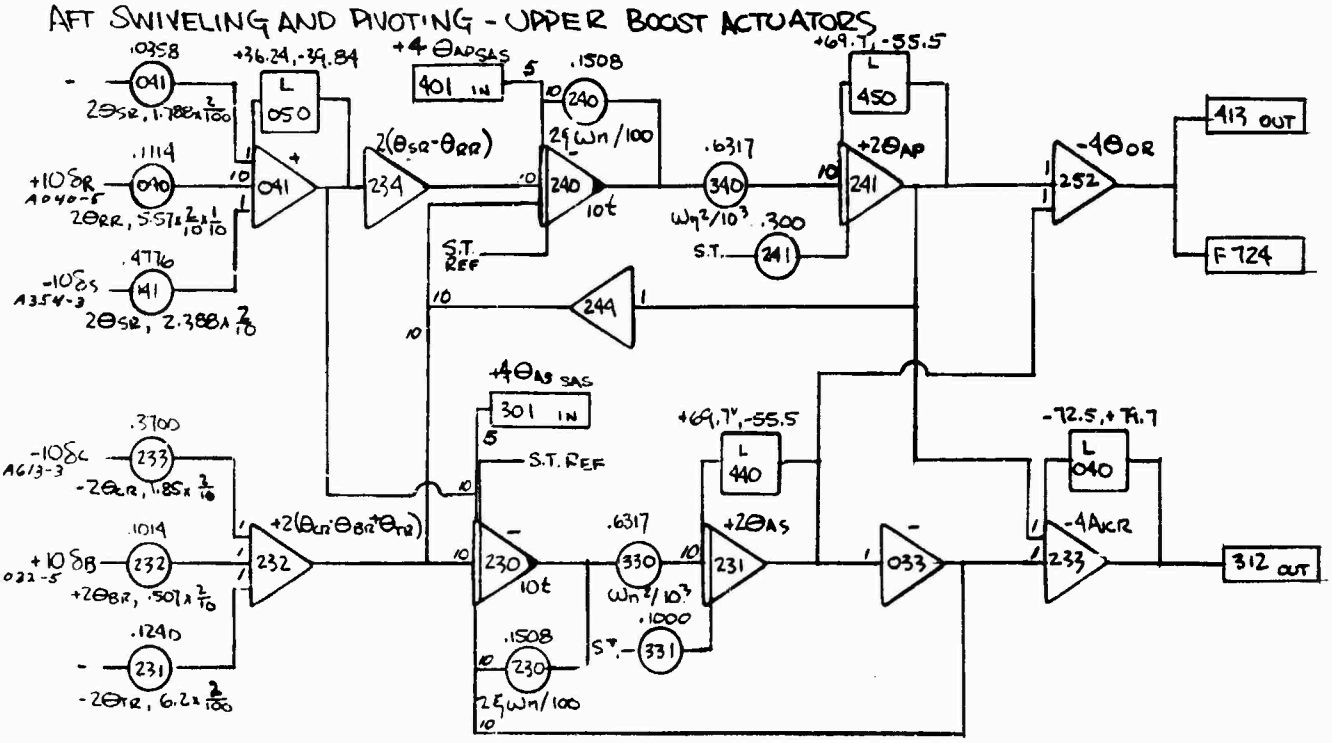

Preceding page blank

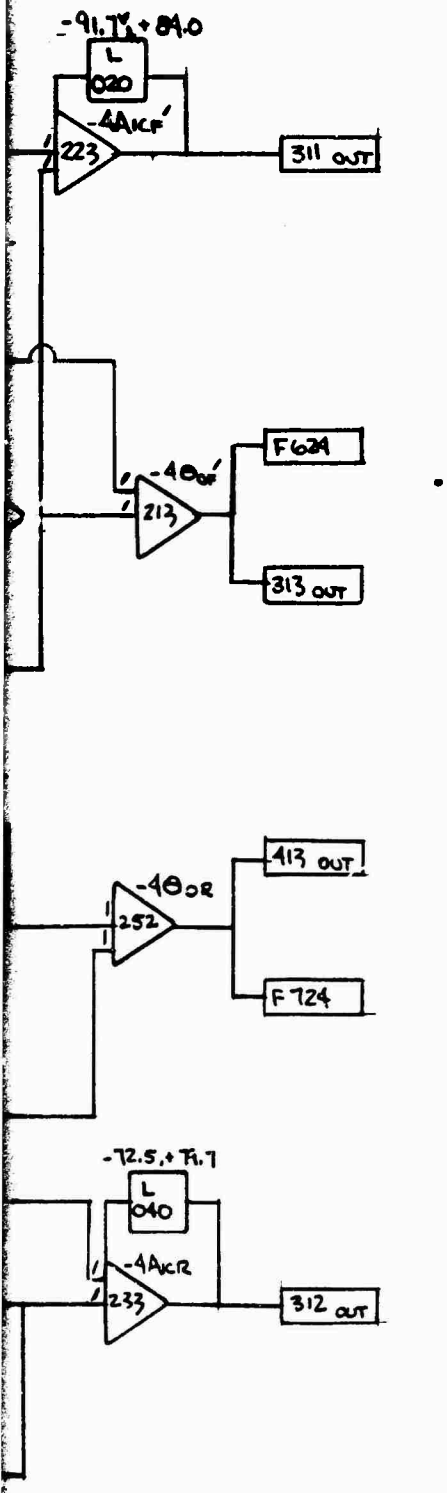

$\theta_{SF} = (2.2)(1.2)\delta_S + (1.67)(1.2) = 2.64\,\delta_S + 2.004$
$\theta_{CF} = 2.15\,\delta_C$
$\theta_{BF} = 5.84\,\delta_B$
$\theta_{RF} = (5.38)(1.2)\,\delta_R = 6.456\,\delta_R$
$\theta_{TF} = 7.2°$

$\theta_{SR} = (1.99)(1.2)\delta_S + (1.49)(1.2) = 2.388\,\delta_S + 1.788$
$\theta_{CR} = 1.85\,\delta_C$
$\theta_{BR} = .507\,\delta_B$
$\theta_{RR} = (4.64)(1.2)\,\delta_R = 5.568\,\delta_R$
$\theta_{TR} = 6.2°$

$\theta_{FSP} = \theta_{TF} + \theta_{BF} + \theta_{CF} + \theta_{SF} + \theta_{RF} + \theta_{FS\,SAS}$
$\theta_{FPP} = \theta_{TF} + \theta_{BF} + \theta_{CF} - \theta_{SF} - \theta_{RF} + \theta_{FP\,SAS}$
$\theta_{ASP} = \theta_{TR} - \theta_{BR} + \theta_{CR} + \theta_{SR} - \theta_{RR} + \theta_{AS\,SAS}$
$\theta_{APP} = \theta_{TR} - \theta_{BR} + \theta_{CR} - \theta_{SR} + \theta_{RR} + \theta_{AP\,SAS}$

$\theta_{OF}' = (\theta_{FS} + \theta_{FP})/2$
$\theta_{OR} = (\theta_{AS} + \theta_{AP})/2$
$A_{ICF}' = (\theta_{FS} - \theta_{FP})/2$
$-A_{ICR} = (\theta_{AS} - \theta_{AP})/2$

DUAL GOVERNOR

$$\left[\frac{\dot{\Omega}}{35}\right] = \frac{1}{10 I_T}(10)\left\{\frac{2\times10^5}{35}\left[\frac{Q'_G}{2\times10^5}\right] - \frac{2\times10^5}{35}\left[\frac{Q_{GF}}{2\times10^5}\right] - \frac{2\times10^5}{35}\left[\frac{Q_{GR}}{2\times10^5}\right] - \frac{3.5K_{DF}}{35}\left[\frac{\Delta\Omega_F}{3.5}\right] - \frac{3.5}{35}K_{DR}\left[\frac{\Delta\Omega_R}{3.5}\right]\right\}$$

$$\left[\frac{\dot{Q}_G}{2\times10^5}\right] = \frac{1}{100\tau_{\Omega 2}}(100)\left\{\left[\frac{\Sigma Q_{AERO} - Q_G}{2\times10^5}\right] + \frac{35G_1}{2\times10^5}\left[\frac{\Omega_0}{35}\right] - \frac{35G_1}{2\times10^5}\left[\frac{\Omega}{35}\right]\right\}$$

$$\left[\frac{Q'_G}{2\times10^5}\right] = \left[\frac{Q_G}{2\times10^5}\right] + \frac{35K}{2\times10^5}\left[\frac{\Omega_0}{35}\right] - \frac{35K}{2\times10^5}\left[\frac{\Omega}{35}\right]$$

CONSTANTS

$K_{DF} = K_{DR} = .49\times10^{-4}$
$G_1 = 62.850$
$I_T = 3190$ LB-SEC^2-FT
$\tau_{\Omega 2} = .05$ SEC
$K = .615$
$\tau_c = 1.0$ SEC

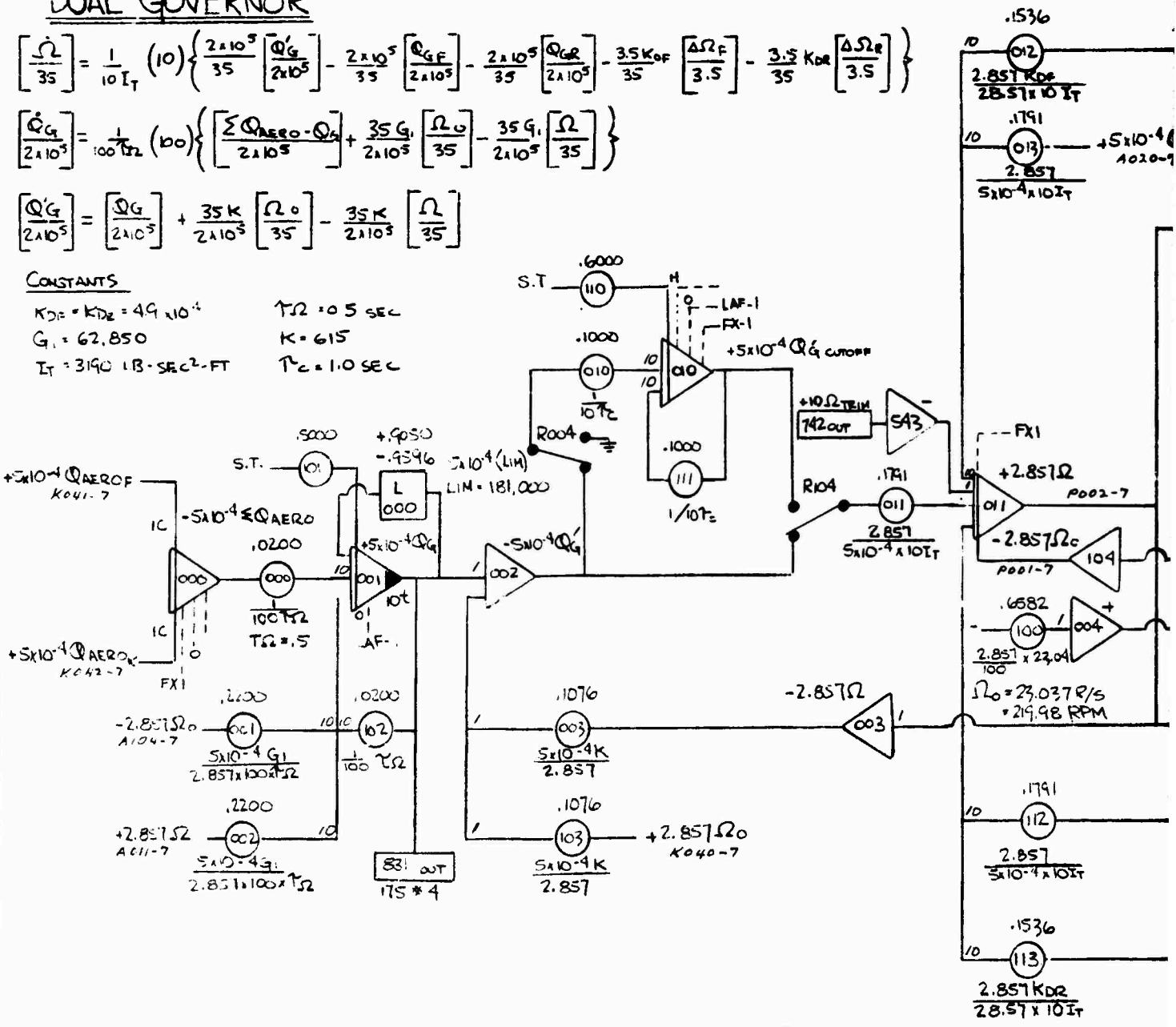

$$\left[\frac{\Delta\Omega_F}{35}\right] = \frac{1}{\tau s+1}\left\{\left[\frac{\Omega}{35}\right] - \left[\frac{\Omega_R}{35}\right]\right\} \qquad \left[\frac{Q_{GR}}{2\times10^5}\right] = \frac{3.5K_R}{2\times10^7}(100)\left[\frac{\Delta\Omega_R}{3.5}\right]$$

SAME EQUATIONS FOR SUBSCRIPT F REPU

$$\left[\frac{\dot{\Omega}_R}{35}\right] = \frac{1}{10 I_B}\left(10^1\left\{\frac{2\times10^5}{35}\left[\frac{Q_{GR}}{2\times10^5}\right] - \frac{2\times10^5}{35}\left[\frac{Q_{AERO}R}{2\times10^5}\right] + \frac{3.5K_{DR}}{35}\left[\frac{\Delta\Omega_R}{3.5}\right]\right.\right. \quad \text{AFT FAR}$$

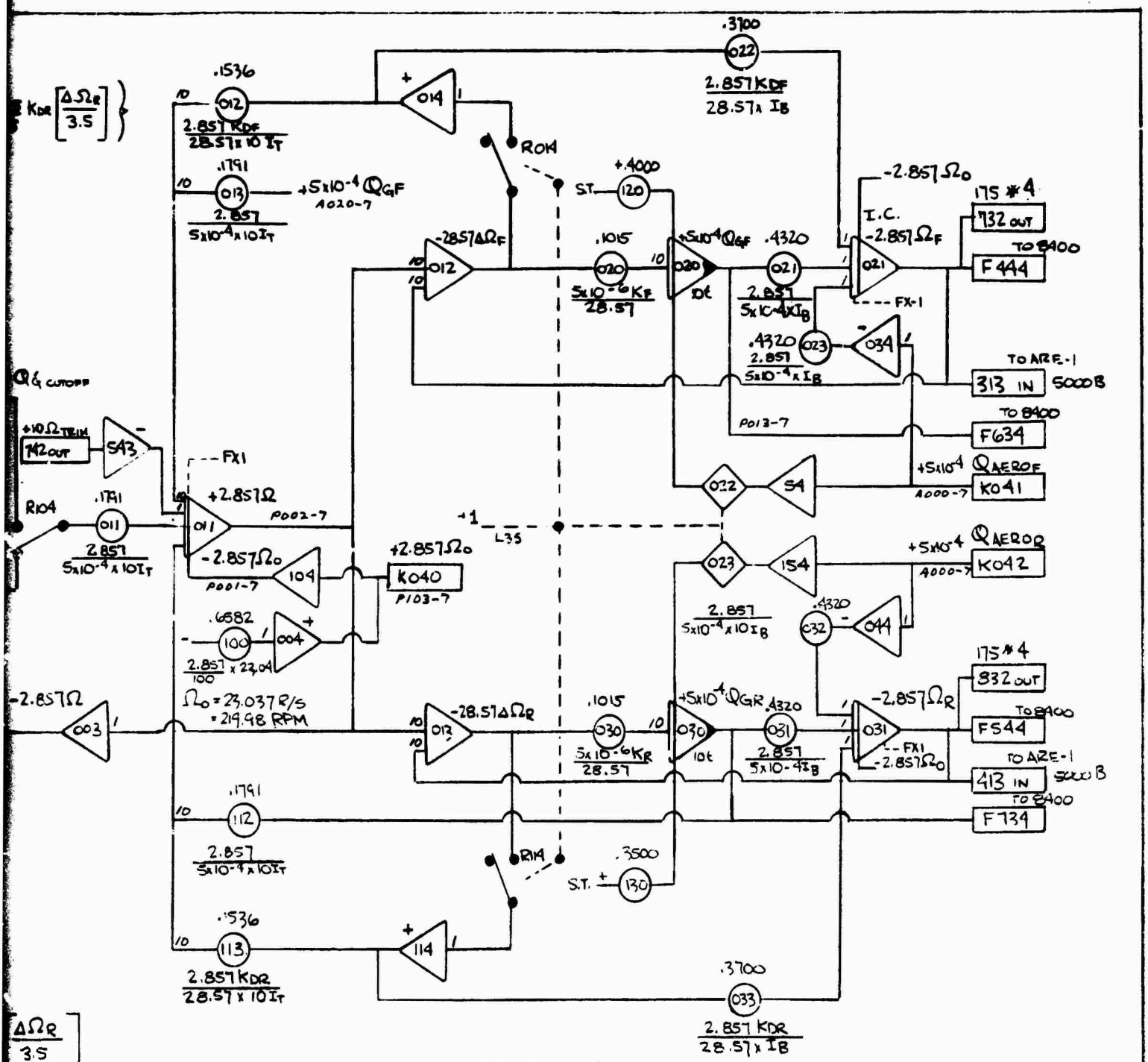

SAME EQUATIONS FOR FORWARD GOVERNOR
SUBSCRIPT F REPLACES R

CONSTANTS:

$K_{DF} = K_{DR} = 49 \times 10^4$

$I_B = .3230$ LB-SEC^2-FT

$K_R = K_F = 5.9 \times 10^5$

MAX RPM = 220

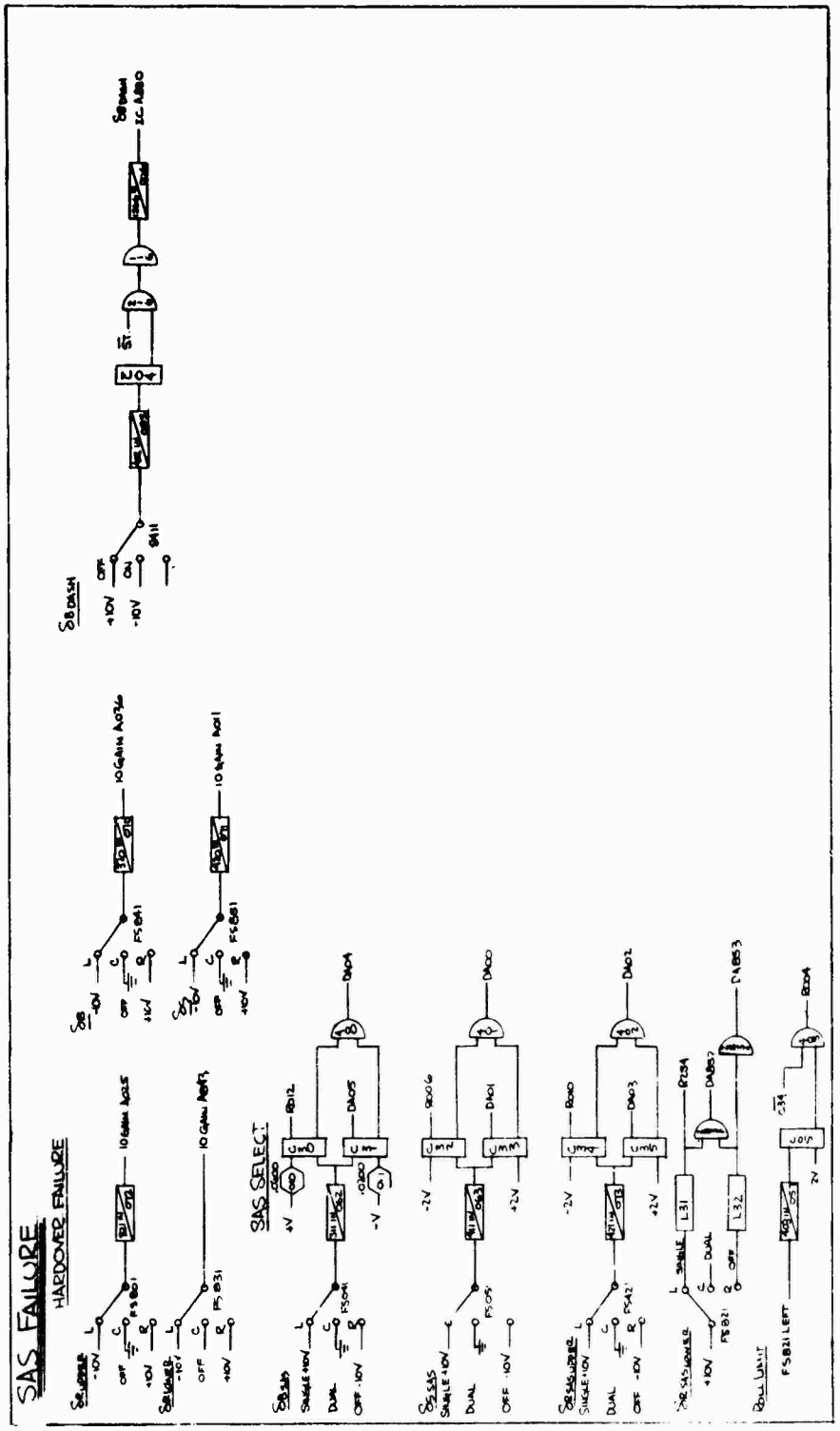

Preceding page blank

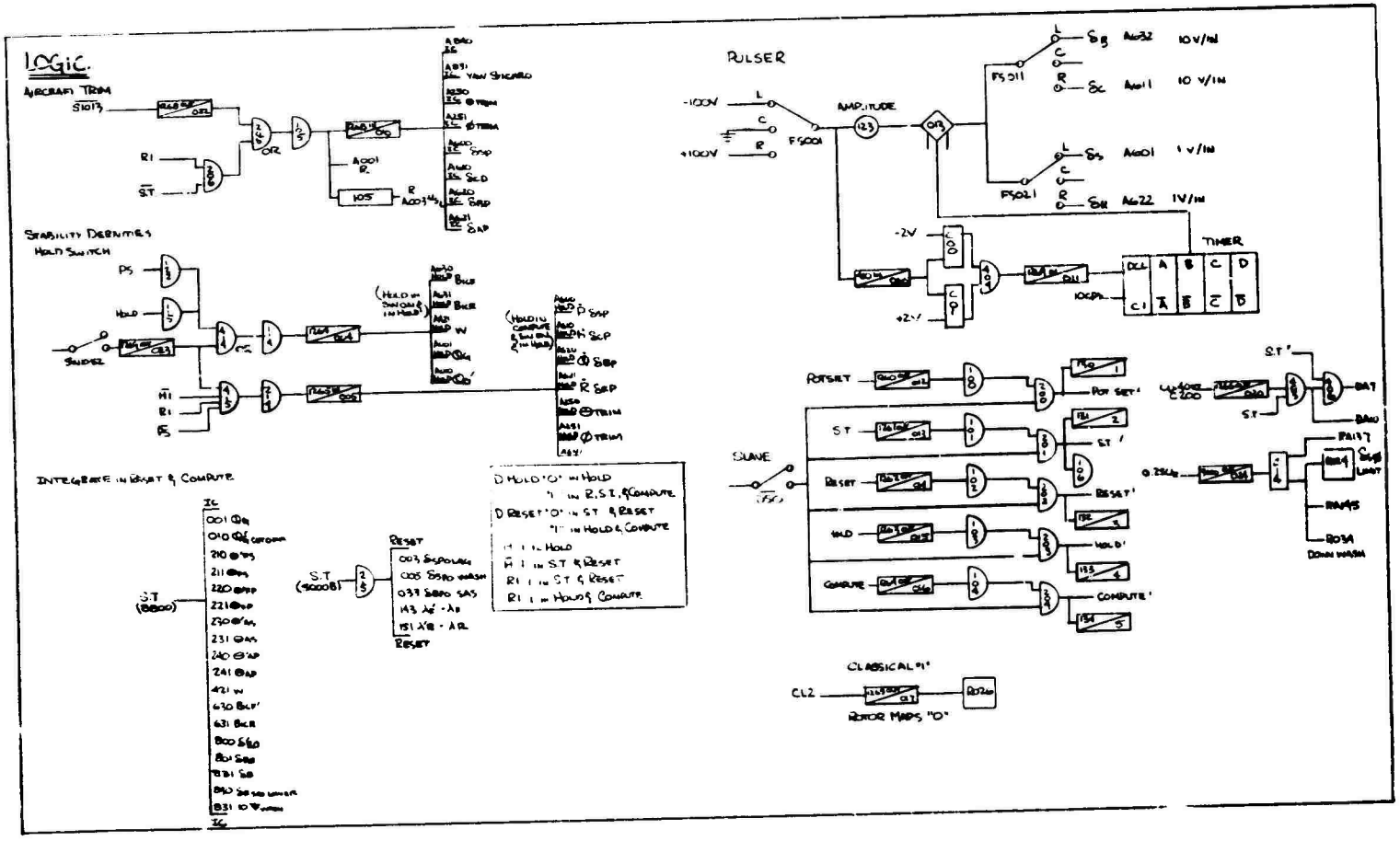
LOGIC.
AIRCRAFT TRIM
STAB
R1
ST
OR
YAW SHOULD
STABILITY DERIVATIVES
HOLD SWITCH
PS
HOLD
SWITCH
HI
R1
INTEGRATE IN RESET & COMPUTE
IC
S.T (8800)
RESET
S.T (40008)
D HOLD "0" IN HOLD
"1" IN R.S.I. & COMPUTE
D RESET "0" IN ST & RESET
"1" IN HOLD & COMPUTE
HI = 1 IN HOLD
HI = 1 IN ST & RESET
R1 = 1 IN ST & RESET
R1 = 1 IN HOLD & COMPUTE
PULSER
-100V
+100V
AMPLITUDE
FS001
FS011
FS021
TIMER
-2V
+2V
SLAVE
RESET
ST
HOLD
COMPUTE
POT SET'
ST'
RESET'
HOLD'
COMPUTE'
CLASSICAL "1"
CL2
ROTOR MAPS "0"
S.T'
PAIR 7
DOWN WASH

GE LOGIC INTERFACE AND RECORDER FORMAT CHANGE

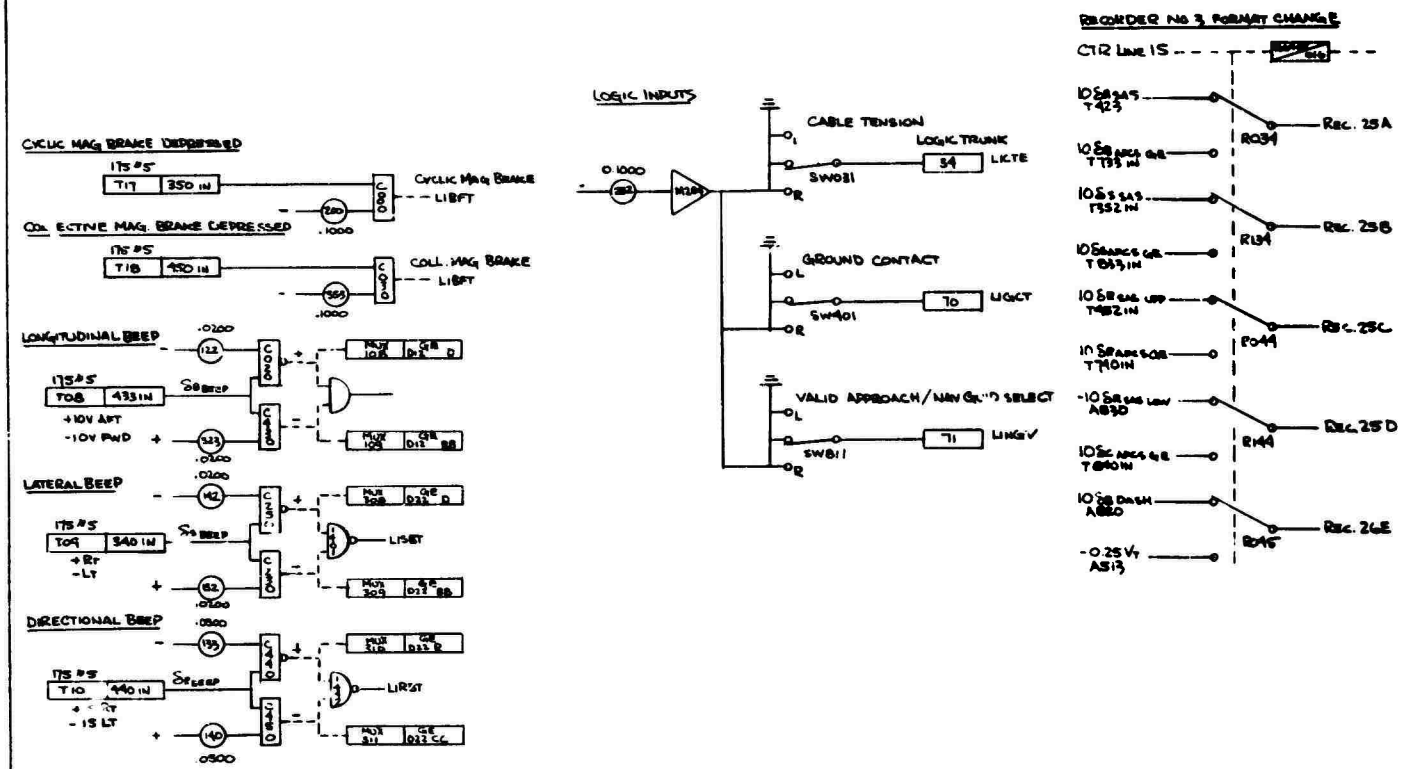

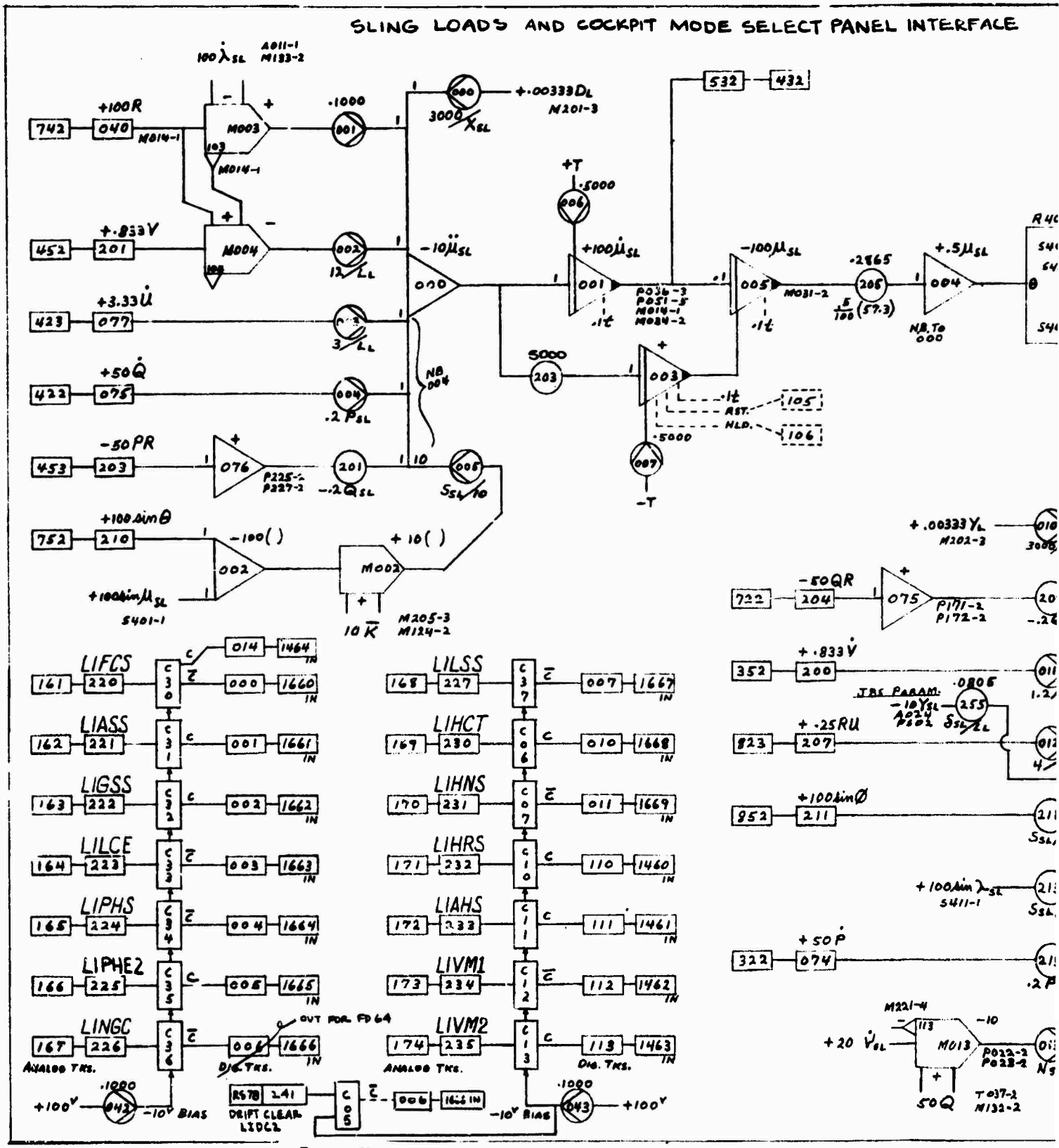

Preceding page blank

LECT PANEL INTERFACE

$$10\ddot{\mu}_{SL} = -\left(\frac{3000}{X_{SL}}\right).00333D_L - (.1)100R\dot{\lambda}_{SL} + \left(\frac{12}{L_L}\right).833RV - \left(\frac{3}{L_L}\right)3.33\dot{J}$$
$$-(.2P_{SL})50\dot{Q} + (-.2Q_{SL})50PR - \left(\frac{S_{SL}}{10}\right)10\left[10\bar{K}\left(\sin\Theta + \sin\mu_{SL}\right)\right]$$

$$100\lambda_{SL} = \left(\frac{3000}{X_{SL}}\right).00333Y_L(10) + (10)(-.2Q_{SL})50QR + (100)(1.2/L_L).833\dot{V} + (100)(4/L_L).25RU$$
$$-(10)(S_{SL}/10)100\sin\emptyset - (10)(S_{SL}/10)100\sin\lambda_{SL} - (10)(.2P_{SL})50\dot{P} + 100R\dot{\mu}_{SL}$$
$$-(N_{SL})100\dot{Q}Y_{SL}$$

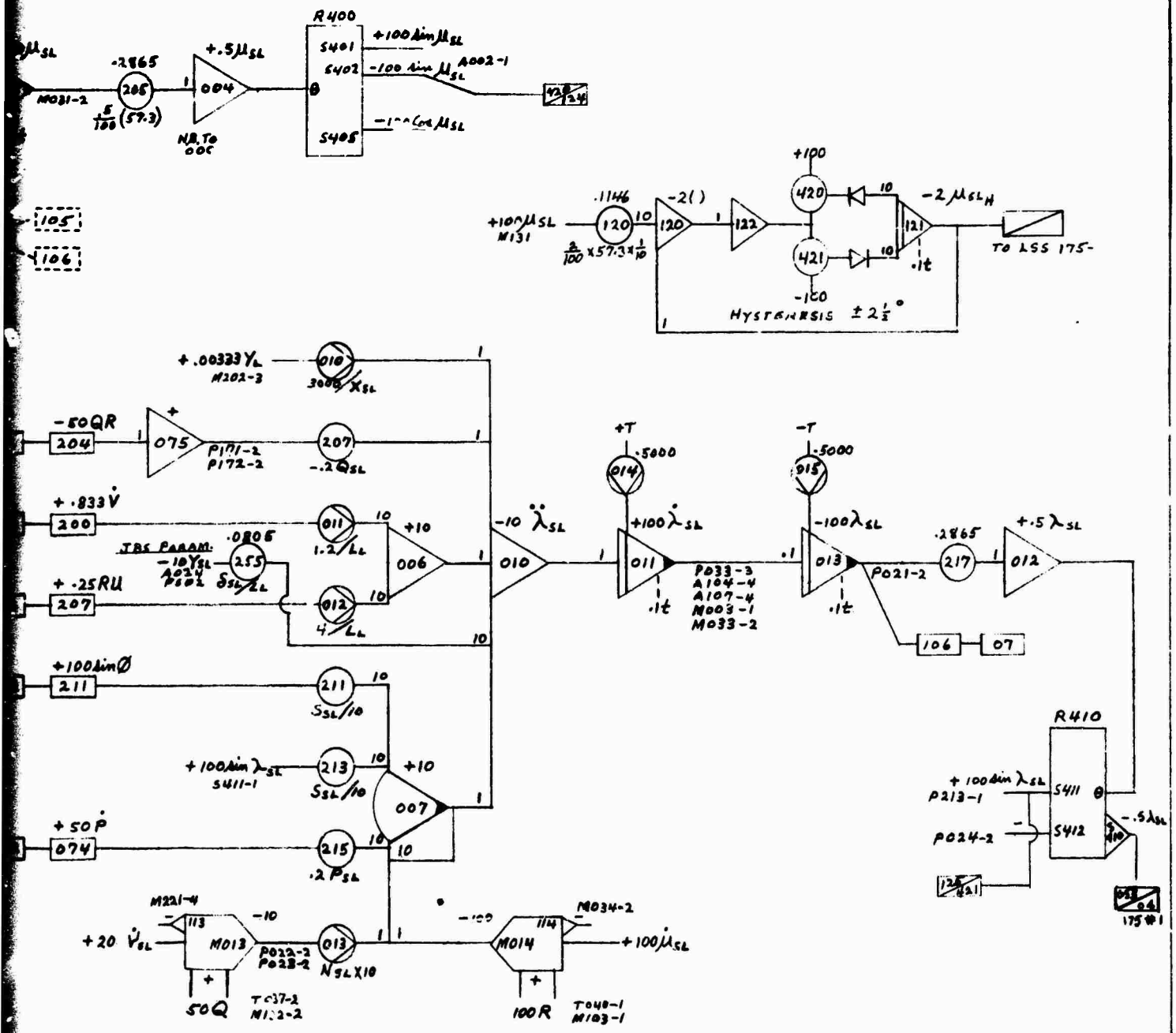

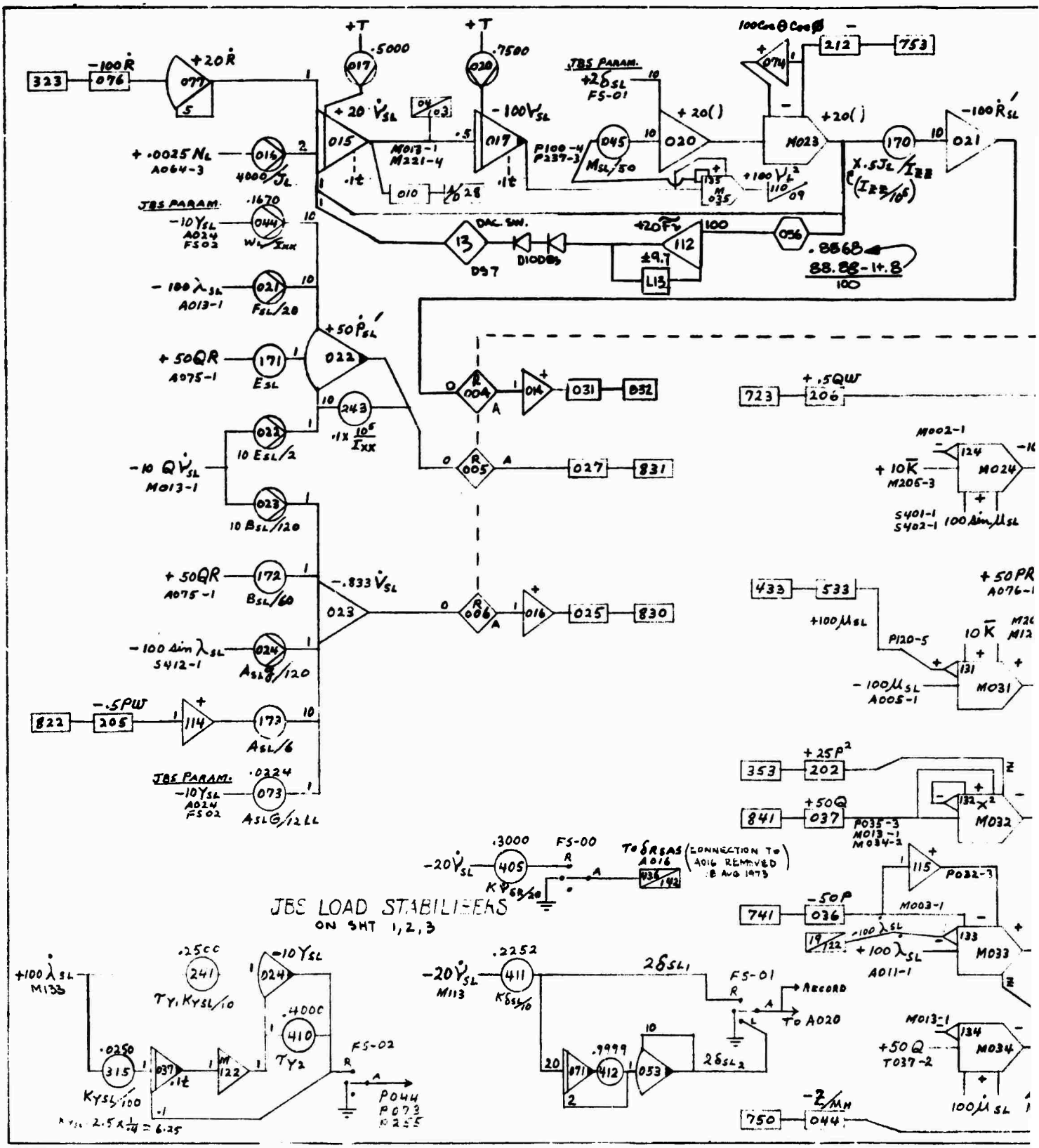

Preceding page blank

$$-200\ddot{V}_{SL} = .2(10)100\dot{R} - \left(\frac{8000}{J_{SL}}\right)10(.0025N_L) + \left(\frac{M_{SL}}{100}\right)100(200V_{SL}\cos\theta\cos\phi)$$

$$100\dot{R}_{SL} = \left(\frac{M_{SL}}{100}\right)100\left(\frac{\frac{F}{2}J_{SL}}{I_{E3}}\right)(200V_{SL}\cos\theta\cos\phi)$$

$$.833\dot{V}_{SL} = \left(\frac{B_{SL}}{1000}\right)10(100Q\dot{V}_{SL}) + \left(\frac{B_{SL}}{200}\right)10(50QR) + \left(\frac{A_{SL}2}{180}\right)100\sin\lambda_{SL} + \left(\frac{A_{SL}}{6}\right)10(.5PW)$$

$$-50\dot{P}_{SL} = \left(\frac{E_{SL}}{2}\right)100\lambda_{SL} + (E_{SL})50QR + \left(\frac{E_{SL}}{2}\right)100Q\dot{V}_{SL}$$

$$-3.33\dot{U}_{SL} = \left(\frac{A_{SL}2}{30}\right)10R\sin\mu_{SL}(10) - \left(\frac{2A_{SL}}{3}\right).5QW(10) - \left(\frac{B_{SL}}{1000}\right)50PR(100)$$

$$50\dot{Q}_{SL} = (G_{SL})50PR - \left(\frac{H_{SL}}{2}\right)10R\mu_{SL}(.5)$$

$$-\dot{\omega}_{SL} = -\left(1-\frac{1}{1+\frac{M_L}{M_N}}\right)\left(\frac{V_{SL}}{V_{MN}}\right)-\left[\left(\frac{C_{SL}}{100}\right)(25P^2+25Q^2)+\left(\frac{D_{SL}}{200}\right)(50Q\dot{\mu}_{SL}+50P\lambda_{SL})\right]4$$

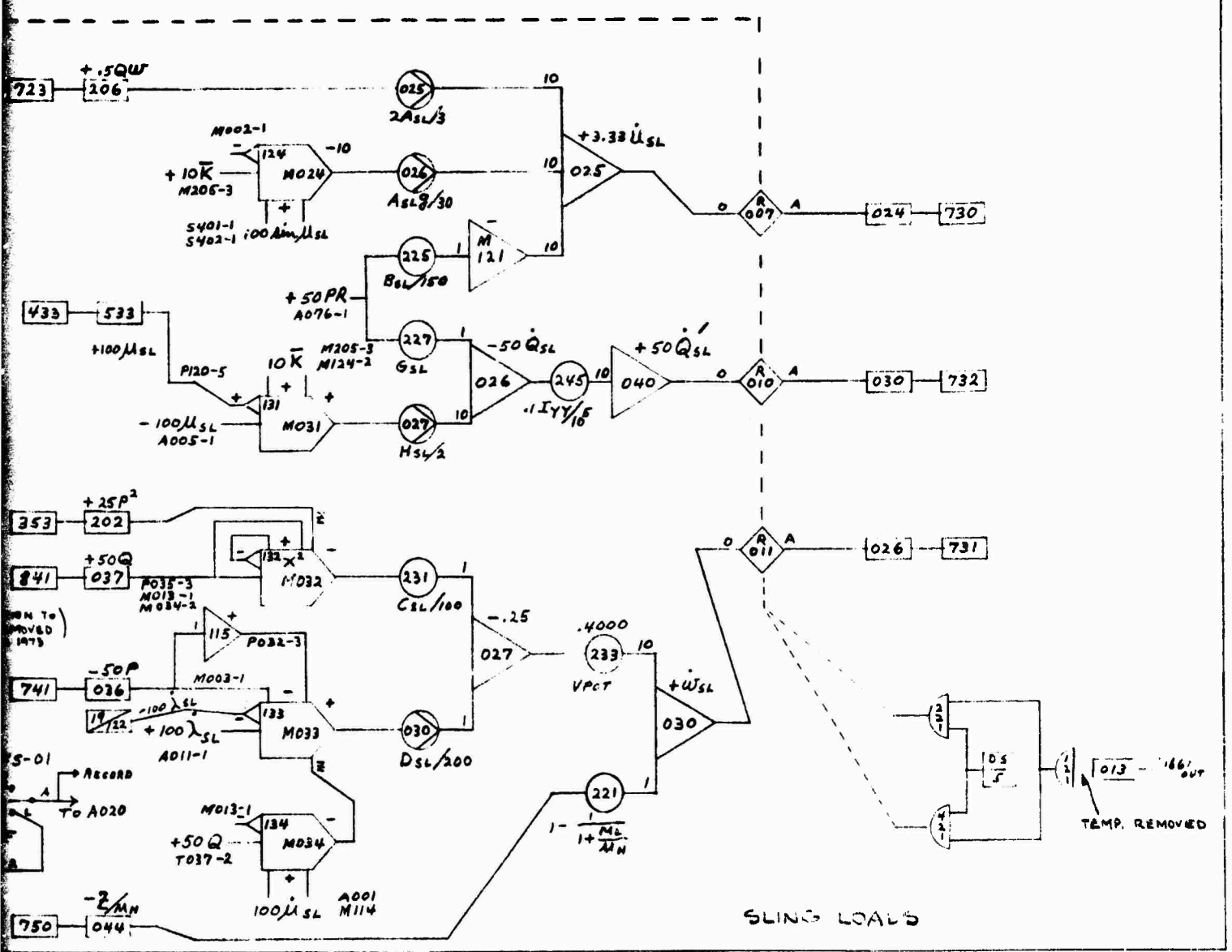

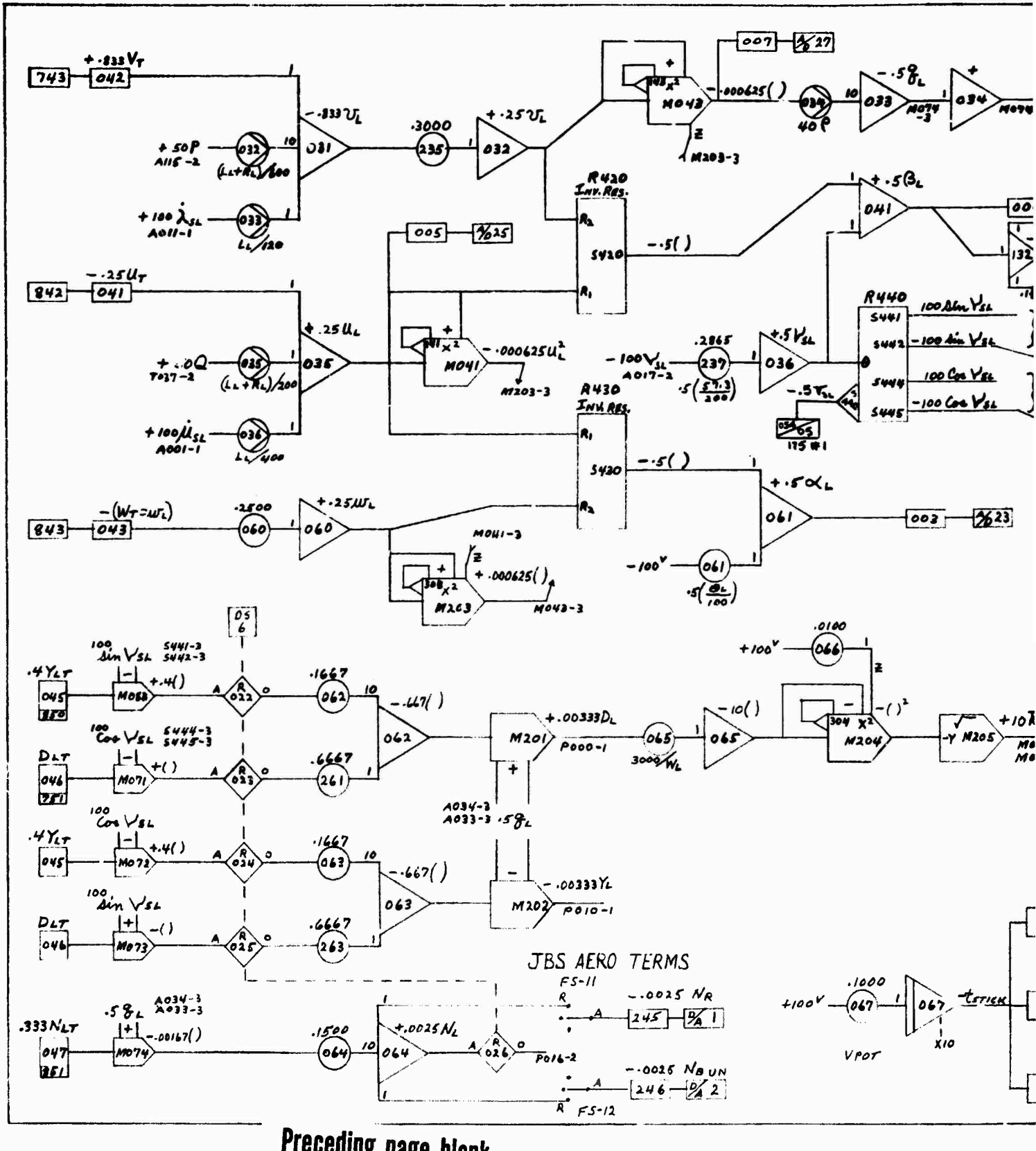

Preceding page blank

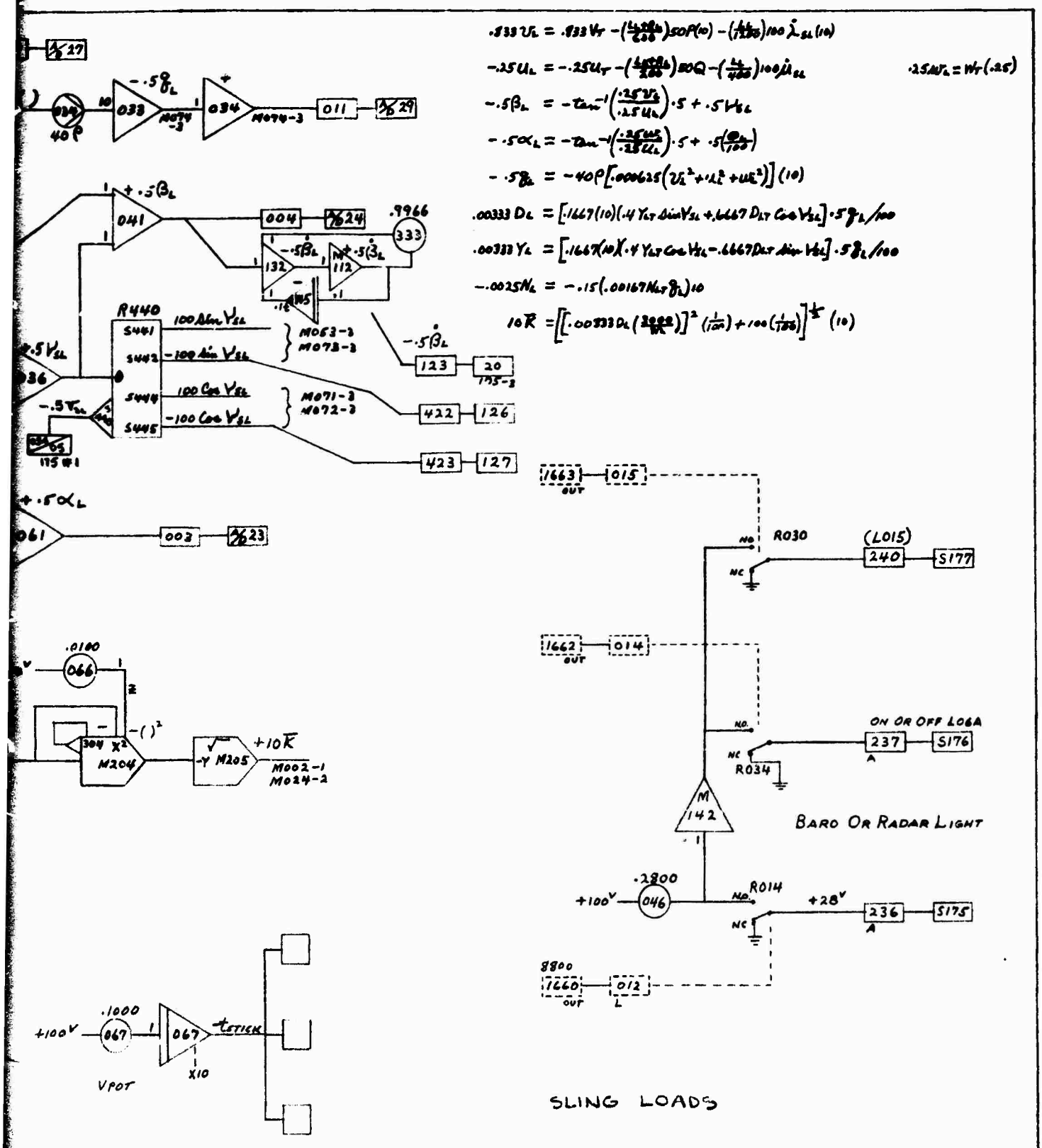
$.833\,U_L = .833\,V_T - \left(\frac{4}{200}\right).5OP(10) - \left(\frac{4}{1200}\right)100\,\dot{\lambda}_{SL}(10)$
$-.25\,U_L = -.25\,U_T - \left(\frac{4}{200}\right).5Q - \left(\frac{4}{400}\right)100\,\dot{\mu}_{SL}$
$.25\,W_L = W_T(.25)$
$-.5\,\beta_L = -\tan^{-1}\left(\frac{.25\,V_L}{.25\,U_L}\right).5 + .5\,V_{SL}$
$-.5\,\alpha_L = -\tan^{-1}\left(\frac{.25\,W_L}{.25\,U_L}\right).5 + .5\left(\frac{\theta}{100}\right)$
$-.5\,\theta_L = -40P\left[.000625\left(U_L^2 + V_L^2 + W_L^2\right)\right](10)$
$.00333\,D_L = \left[.1667(10)(.4\,Y_{LT}\sin V_{SL} + .6667\,D_{LT}\cos V_{SL}\right].5\,\theta_L/100$
$.00333\,Y_L = \left[.1667(10)(.4\,Y_{LT}\cos V_{SL} - .6667\,D_{LT}\sin V_{SL}\right].5\,\theta_L/100$
$-.0025\,N_L = -.15(.00167\,N_{LT}\,\theta_L)10$
$10\,\overline{R} = \left[\left[.00333\,D_L\left(\frac{2000}{ft}\right)\right]^2\left(\frac{1}{100}\right) + 100\left(\frac{1}{1200}\right)\right]^{\frac{1}{2}}(10)$
1/8 27
034 40 P
033
034
M074-3
011
1/6 29
041
004
1/6 24
.9966
333
132
112
115
.1
R440
S441
S442
S444
S445
100 Sin V_{SL}
-100 Sin V_{SL}
100 Cos V_{SL}
-100 Cos V_{SL}
M053-3
M073-3
M071-3
M072-3
123
20
195-3
422
126
423
127
036
1/6 65
195 #1
061
003
1/6 23
.0100
066
304
M204
M205
M002-1
M024-2
1663 OUT
015
1662 OUT
014
R030
(L015)
240
S177
NO
NC
NO.
237
S176
A
R034
ON OR OFF LOGA
M 142
BARO OR RADAR LIGHT
.2800
046
+100V
R014
+28V
236
S175
8800
1660 OUT
012
L
.1000
067
X10
VPOT
SLING LOADS

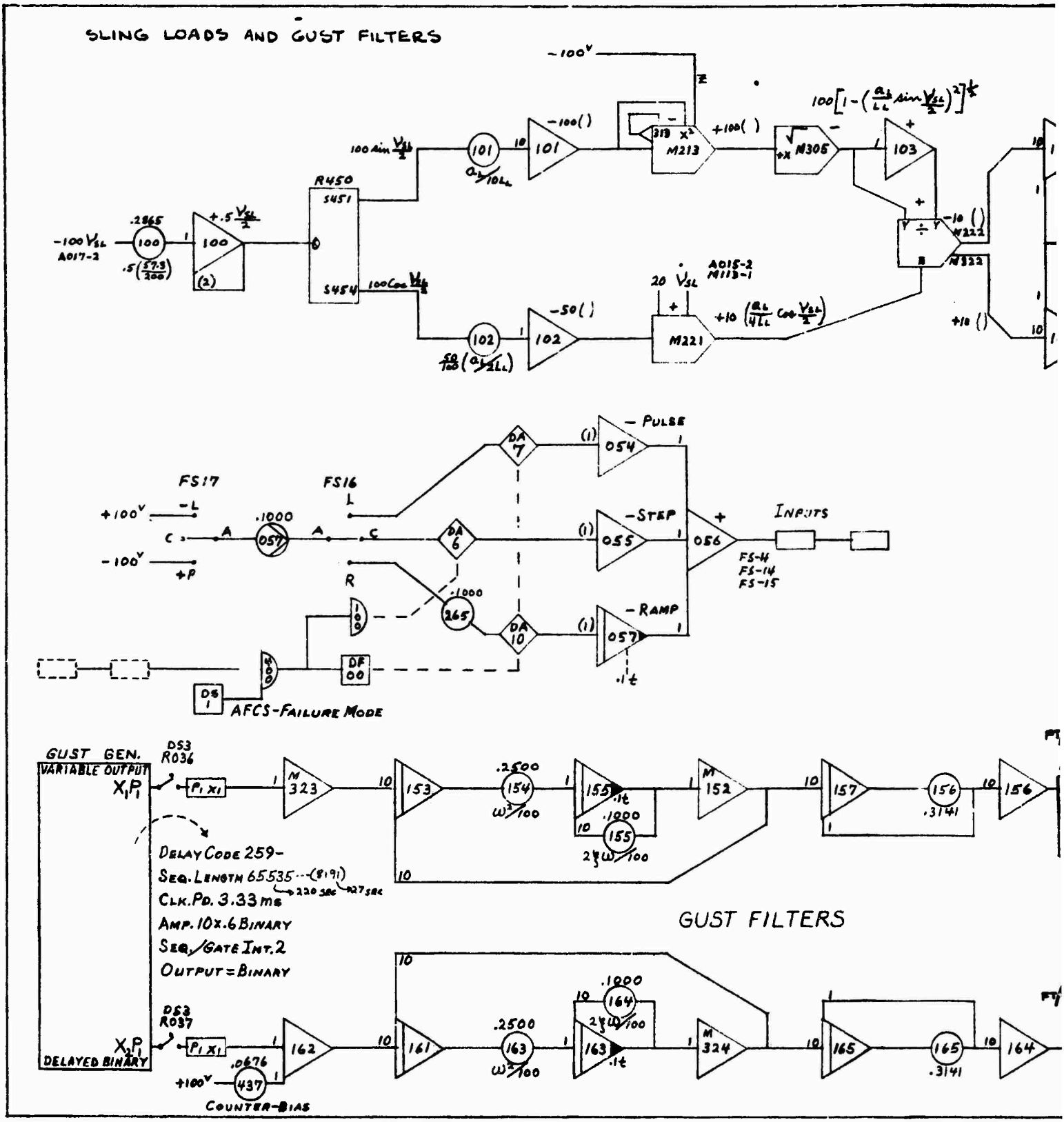

Preceding page blank

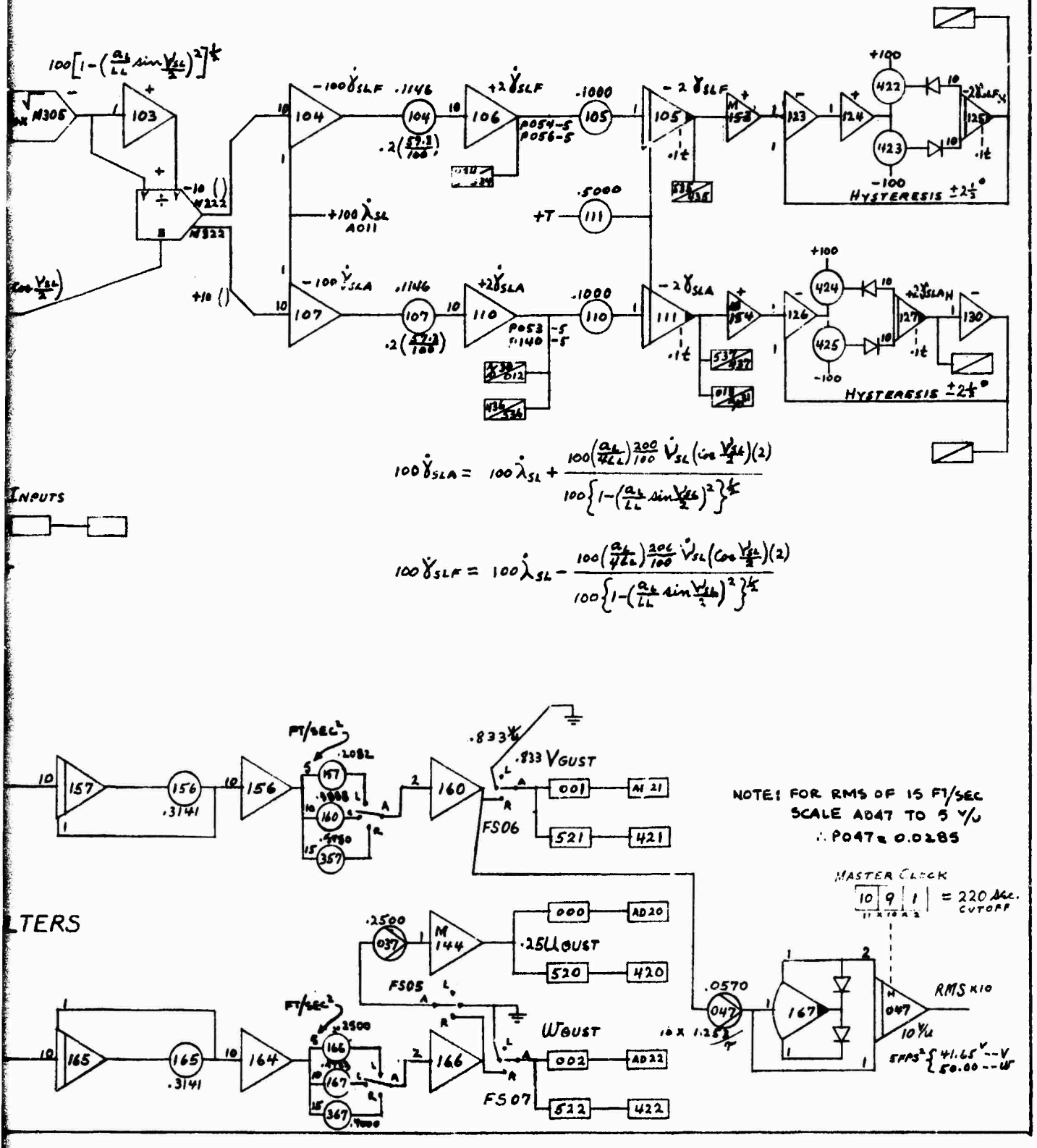

$$100\dot{\gamma}_{SLA} = 100\dot{\lambda}_{SL} + \frac{100\left(\frac{a_L}{4L_L}\right)\frac{200}{100}\dot{V}_{SL}\left(\cos\frac{V_{SL}}{2}\right)(2)}{100\left\{1-\left(\frac{a_L}{L_L}\sin\frac{V_{SL}}{2}\right)^2\right\}^{\frac{1}{2}}}$$

$$100\dot{\gamma}_{SLF} = 100\dot{\lambda}_{SL} - \frac{100\left(\frac{a_L}{4L_L}\right)\frac{200}{100}\dot{V}_{SL}\left(\cos\frac{V_{SL}}{2}\right)(2)}{100\left\{1-\left(\frac{a_L}{L_L}\sin\frac{V_{SL}}{2}\right)^2\right\}^{\frac{1}{2}}}$$

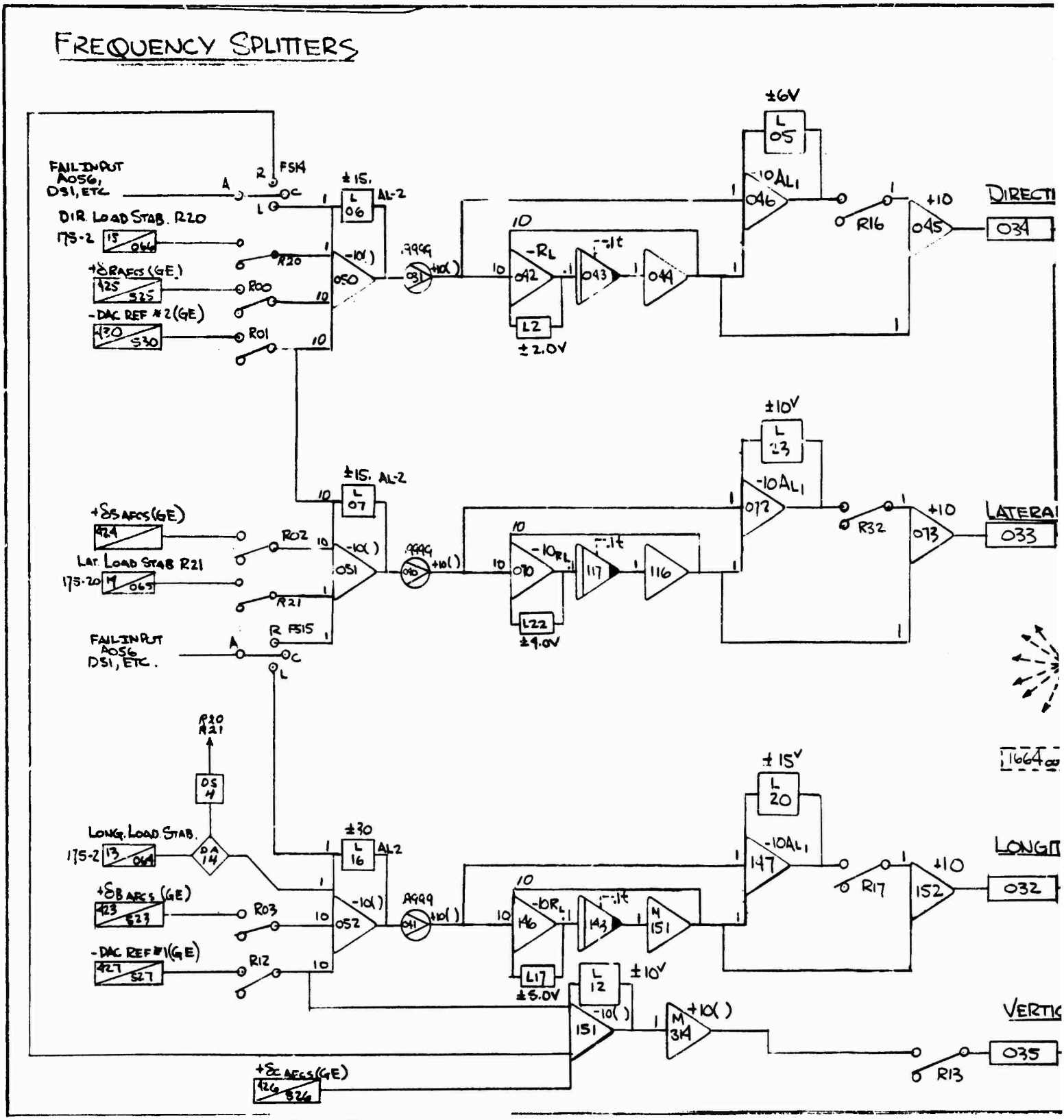
FREQUENCY SPLITTERS
FAIL INPUT A056, DS1, ETC
DIR. LOAD STAB. R20
175-2
+δR AFCS (GE)
-DAC REF #2 (GE)
±15.
AL-2
±6V
-10AL1
DIRECTI
034
R16
+10
LAT. LOAD STAB R21
175-20
+δS AFCS(GE)
±10V
LATERA
033
R32
FAIL INPUT A056 DS1, ETC.
R10 R21
LONG. LOAD STAB.
175-2
+δB AFCS (GE)
-DAC REF #1 (GE)
±30
±15V
LONGI
032
R17
±5.0V
±9.0V
±2.0V
VERTIC
035
R13
+δC AFCS(GE)
Preceding page blank

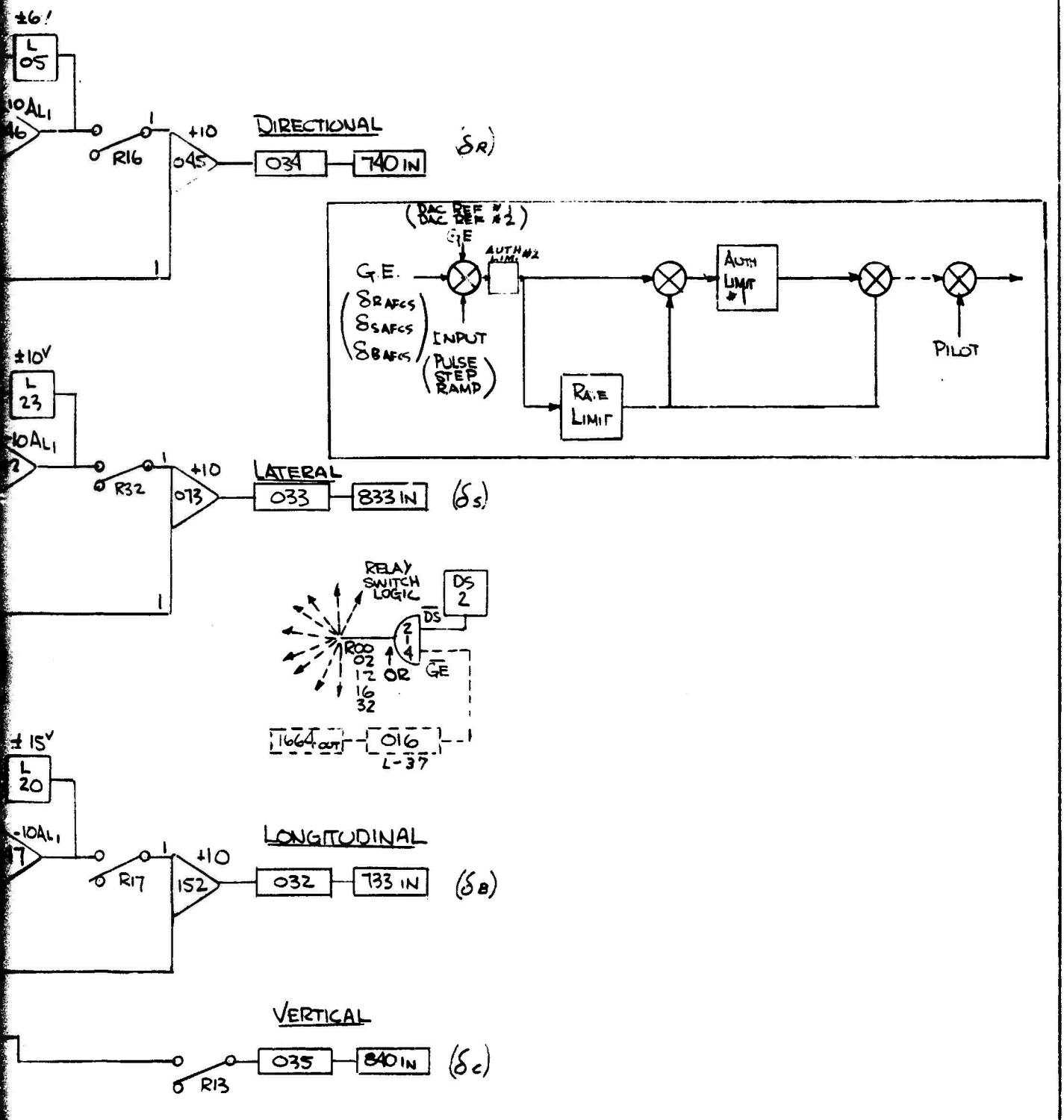
±6!
L 05
10AL1
46
R16
+10
045
DIRECTIONAL
034
740 IN
(δR)
(DAC DEF #1
DAC DEF #2)
G.E.
AUTH LIMIT #2
G.E.
(δRAFCS
δSAFCS
δBAFCS)
INPUT
(PULSE
STEP
RAMP)
RATE LIMIT
AUTH LIMIT
PILOT
±10V
L 23
10AL1
R32
+10
073
LATERAL
033
833 IN
(δS)
RELAY SWITCH LOGIC
DS 2
DS
R00
02
12
16
32
OR
GE
1664 OUT
016
L-37
±15V
L 20
-10AL1
17
R17
+10
152
LONGITUDINAL
032
733 IN
(δB)
VERTICAL
035
840 IN
(δC)
R13

FWD. AND AFT ROTOR INTERFERENCE & FWD ROTOR DOWNWASH COMPONENT

FORWARD AND AFT ROTOR INTERFERENCE CURVES PRE AND POST PROCESSING

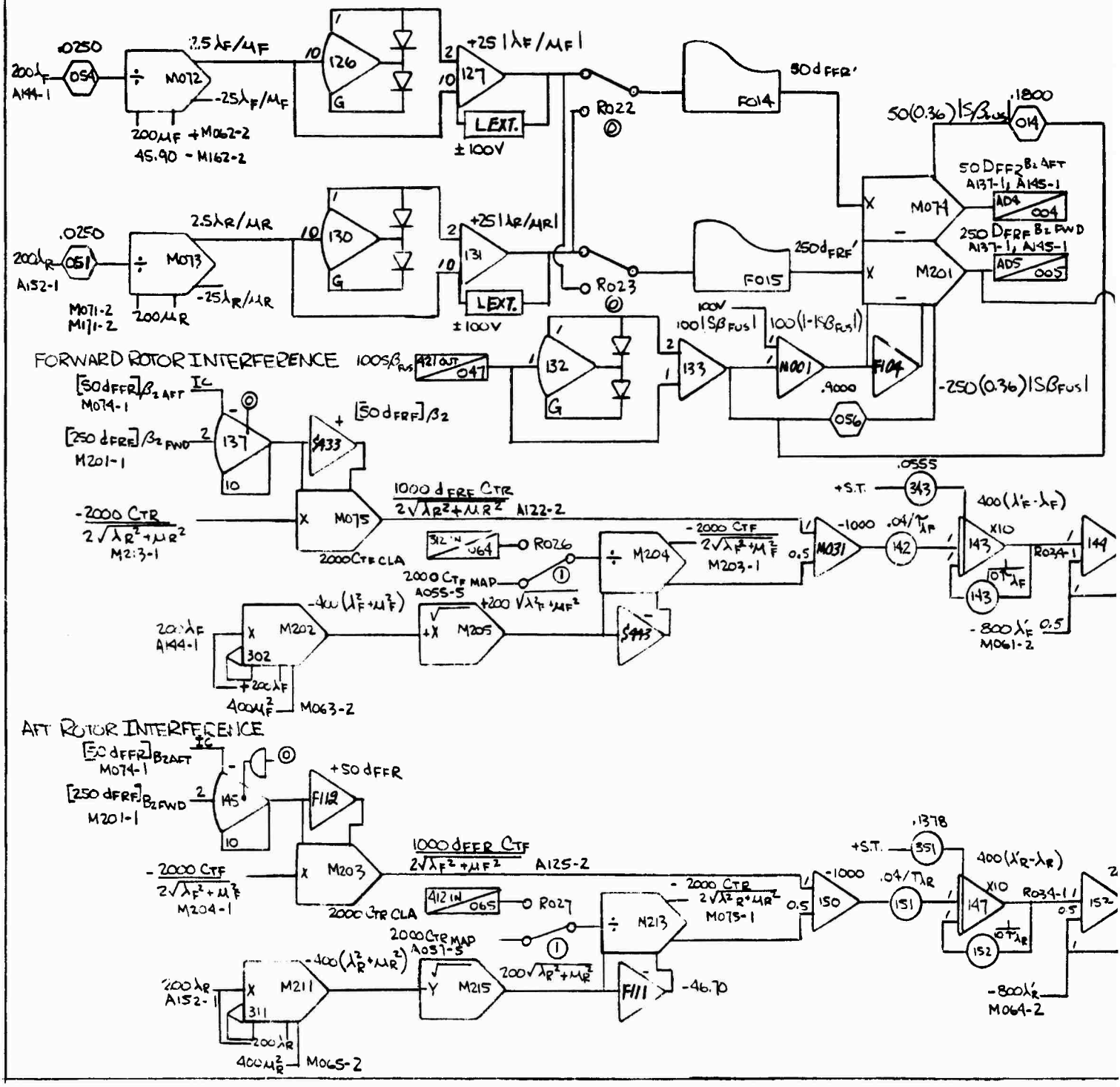

Preceding page blank

DOWNWASH COMPONENT ON FUSELAGE

CESSING

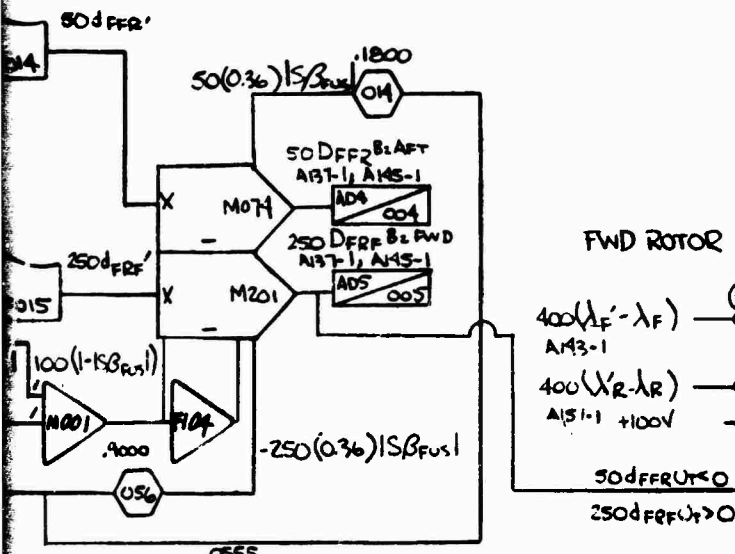

$d_{FFR}' = f|\lambda_F/\mu_F|$ FOR $u \geq 0$
$= f|\lambda_R/\mu_R|$ FOR $u < 0$
$d_{FFR} = d_{FFR}'(1-|\sin\beta_{Fus}|) + 0.36|\sin\beta_{Fus}|$
$d_{FRF}' = f|\lambda_R/\mu_R|$ FOR $u \geq 0$
$= f|\lambda_F/\mu_F|$ FOR $u < 0$
$d_{FRF} = d_{FRF}'(1-|\sin\beta_{Fus}|) + 0.36|\sin\beta_{Fus}|$

FWD ROTOR DOWNWASH COMPONENT ON FUSELAGE

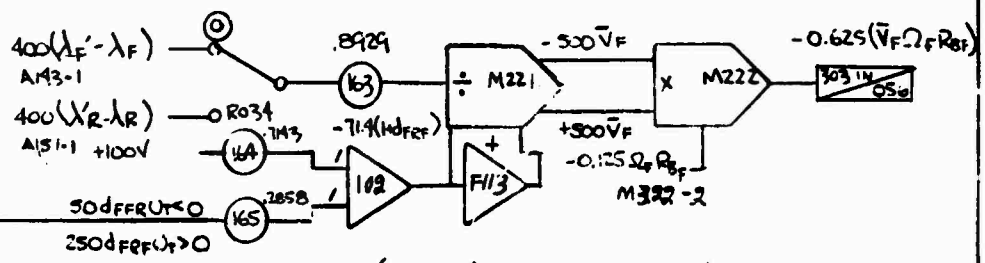

$\bar{V}_F = \frac{V}{\Omega R_B} = \frac{(\lambda_F' - \lambda_F)}{(Hd_{FRF})}$ $\quad \bar{V}_F\Omega_F R_{BF} = \bar{V}_F(\Omega_F R_{BF})$ FOR $u > 0$
R REPLACES F FOR $u < 0$

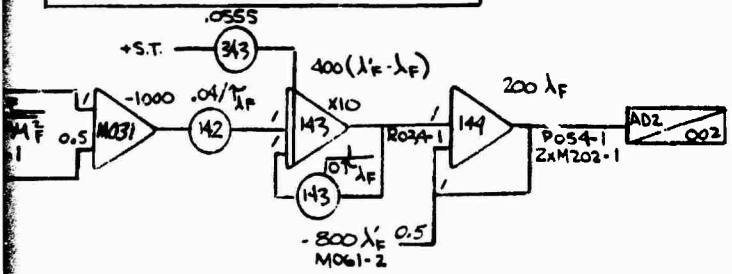

$\lambda_F = \lambda_F' - \left(\frac{C_{TF}}{2\sqrt{\lambda^2_F + \mu_F^2}} + \frac{d_{FRF}\,C_{YR}}{2\sqrt{\lambda_R^2 + \mu_R^2}}\right)\frac{1}{\tau\lambda_F S+1}$

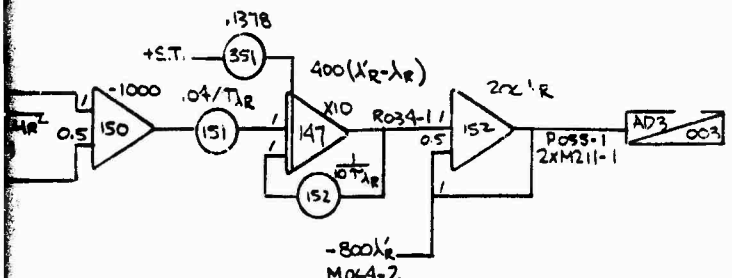

$\lambda_R = \lambda_R' - \left(\frac{C_{TR}}{2\sqrt{\lambda_R^2 + \mu_R^2}} + \frac{d_{FFR}\,C_{TF}}{2\sqrt{\lambda_F^2 + \mu_F^2}}\right)\frac{1}{\tau\lambda_R S+1}$

ROTOR ADVANCE & INFLOW RATIOS, SHAFT ANGLES, AND CYCLIC PITCH AXIS COO

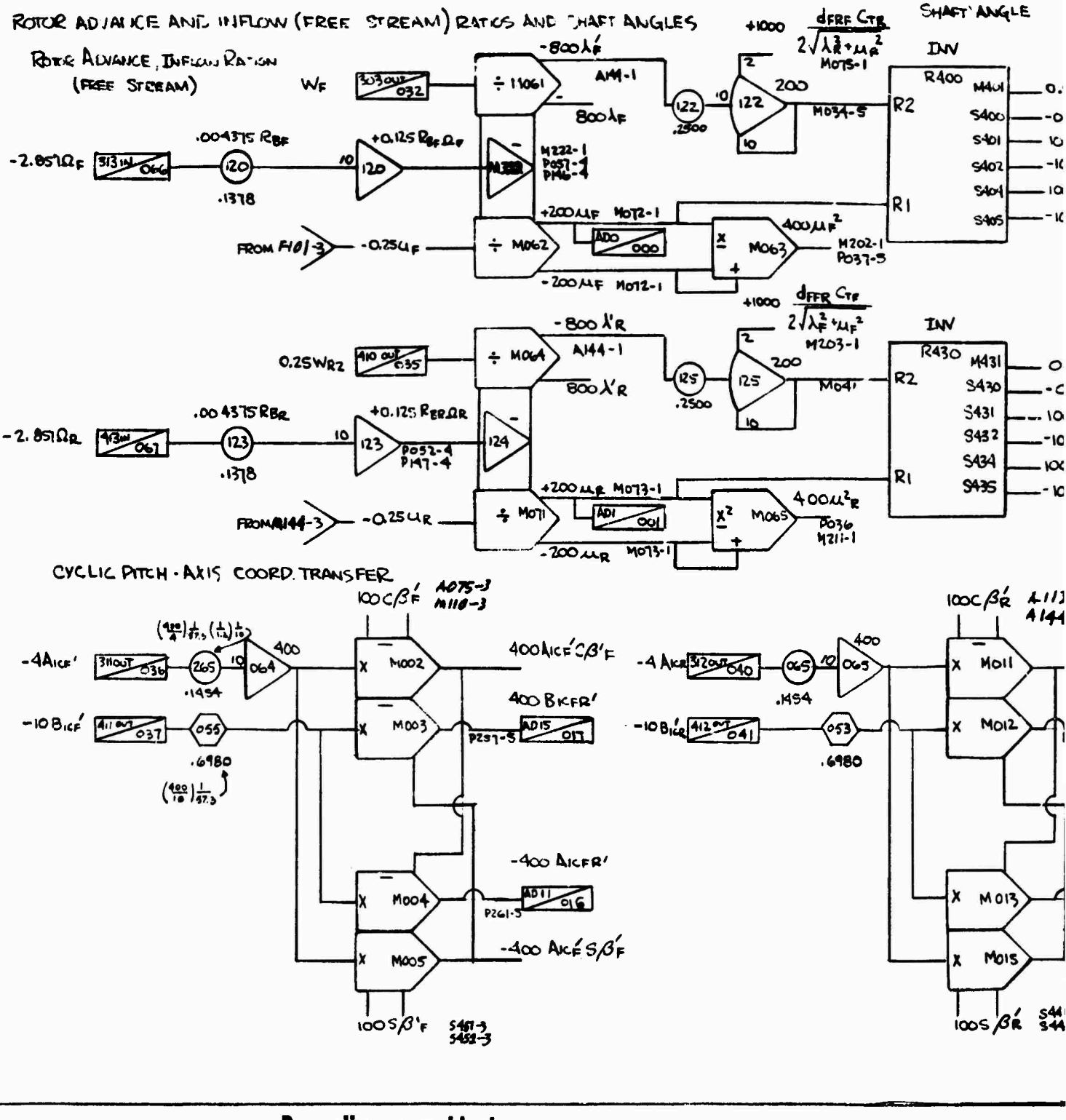

Preceding page blank

ND CYCLIC PITCH AXIS COORD. TRANSFER

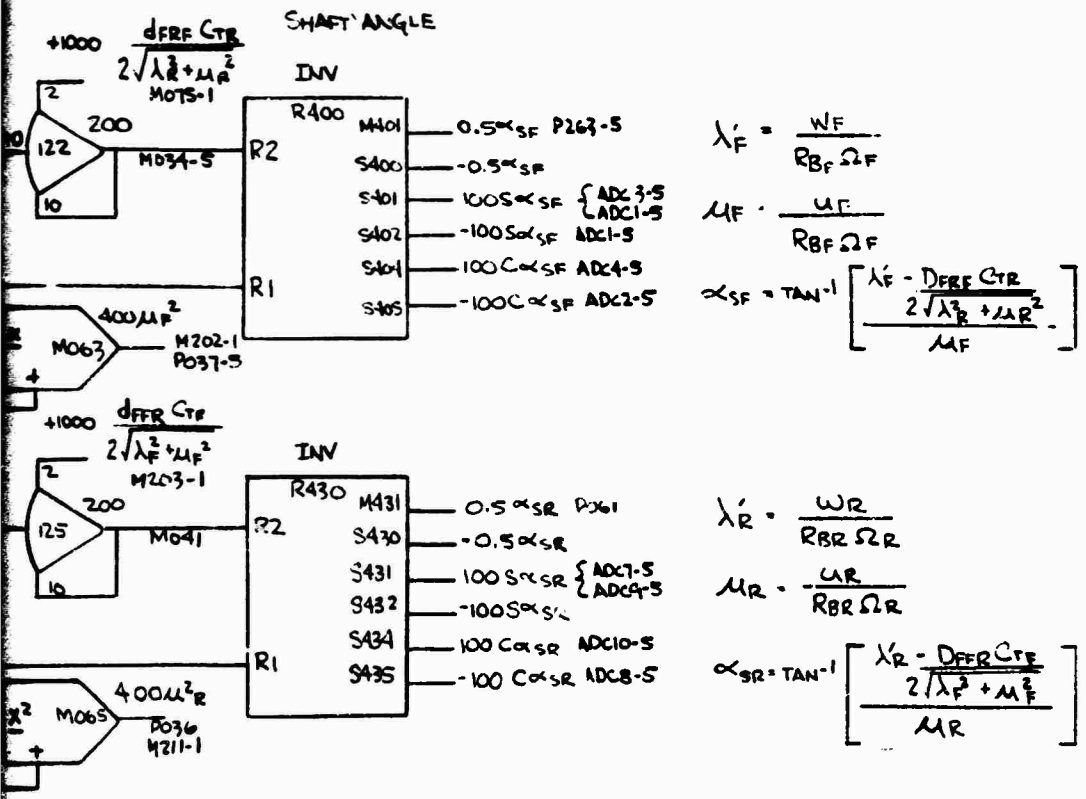

$$\lambda'_F = \frac{W_F}{R_{BF}\,\Omega_F}$$

$$\mu_F = \frac{u_F}{R_{BF}\,\Omega_F}$$

$$\alpha_{SF} = \tan^{-1}\left[\frac{\lambda'_F - \frac{D_{FRF}\,C_{TR}}{2\sqrt{\lambda_R^2+\mu_R^2}}}{\mu_F}\right]$$

$$\lambda'_R = \frac{W_R}{R_{BR}\,\Omega_R}$$

$$\mu_R = \frac{u_R}{R_{BR}\,\Omega_R}$$

$$\alpha_{SR} = \tan^{-1}\left[\frac{\lambda'_R - \frac{D_{FFR}\,C_{TF}}{2\sqrt{\lambda_F^2+\mu_F^2}}}{\mu_R}\right]$$

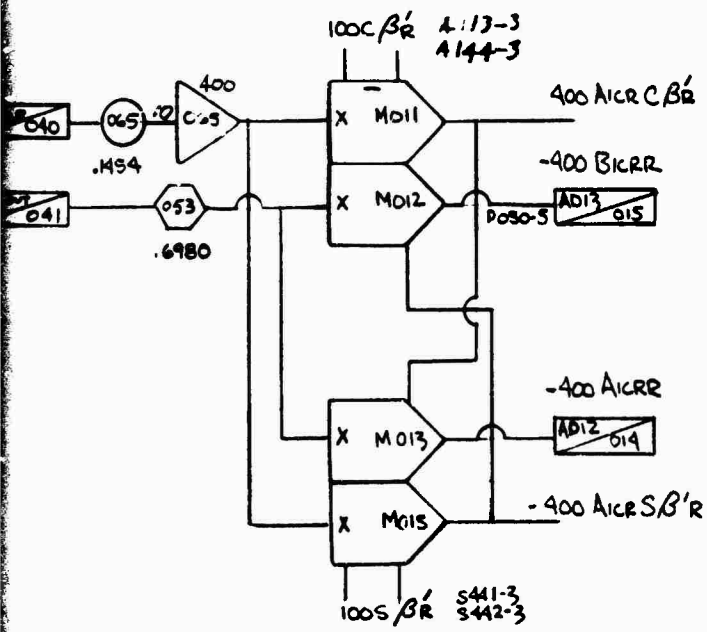

$$A_{ICF}R' = A_{ICF}\cos\beta_F' - B_{ICF}\sin\beta_F'$$

$$B_{ICF}R' = A_{ICF}\sin\beta_F' + B_{ICF}\cos\beta_F'$$

$$A_{ICR}R = A_{ICR}\cos\beta_R' + B_{ICR}\sin\beta_R'$$

$$B_{ICR}R = -A_{ICR}\sin\beta_R' + B_{ICR}\cos\beta_R'$$

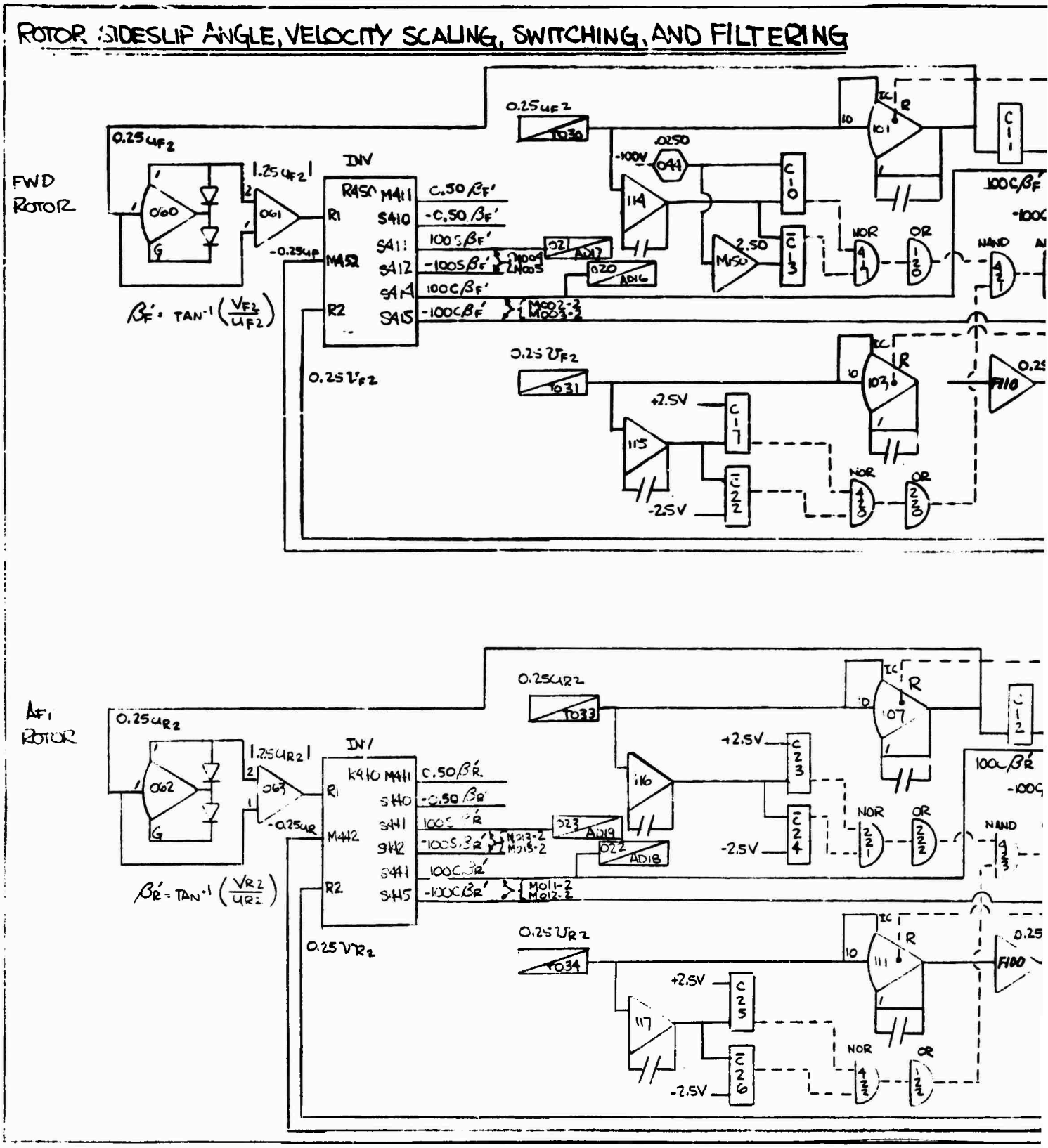

FILTERING

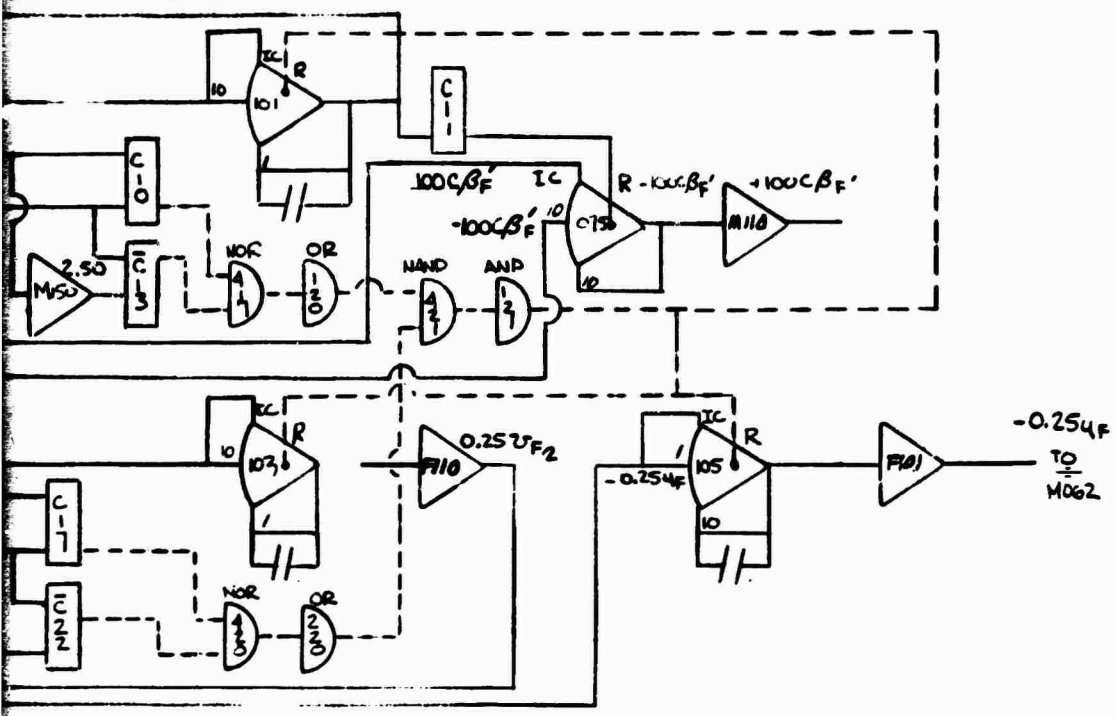
IC
R
101
10
1
C11
C10
C13
2.5V
MSU
NOR
OR
NAND
AND
100Cβ'F
-100Cβ'F
IC
R -100Cβ'F
+100Cβ'F
10
10
0136
M118
IC
R
103
10
1
0.25UF2
F110
C11
C22
NOR
OR
IC
R
105
1
10
-0.25UF
F101
-0.25UF
TO
M062

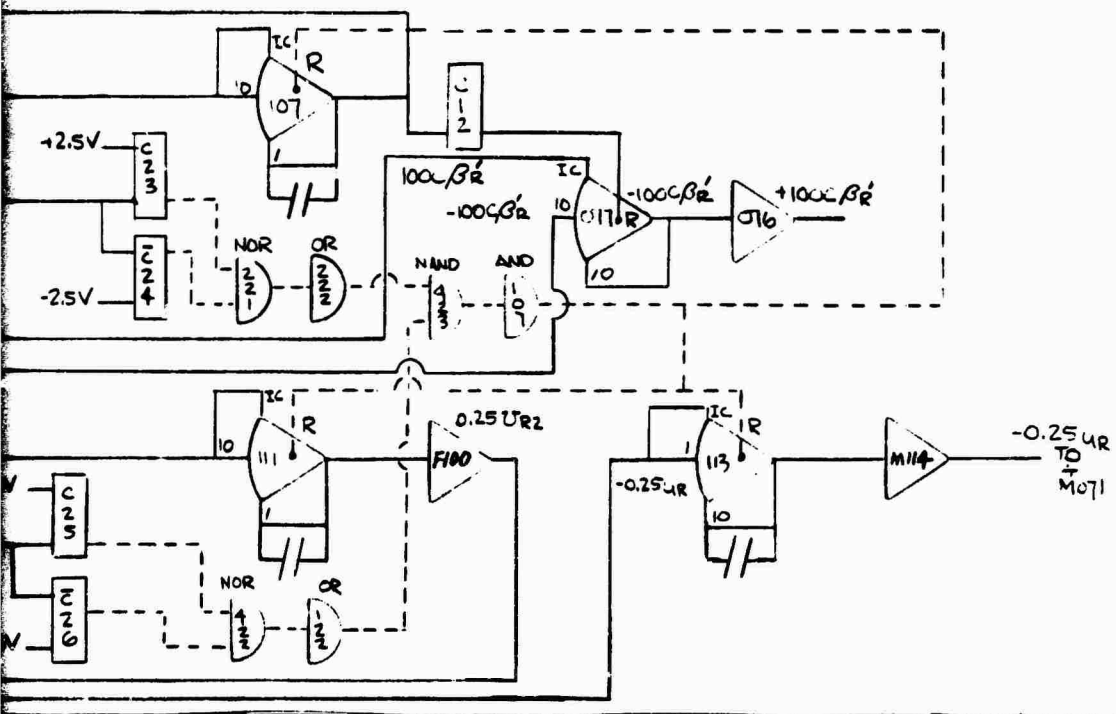
IC
R
107
10
1
C12
+2.5V
C23
C24
-2.5V
NOR
OR
NAND
AND
100Cβ'R
-100Cβ'R
IC
10
0117
R
-100Cβ'R
+100Cβ'R
0116
10
IC
R
111
10
1
0.25UR2
F100
C25
C26
NOR
OR
IC
R
113
1
10
-0.25UR
M114
-0.25UR
TO
M071

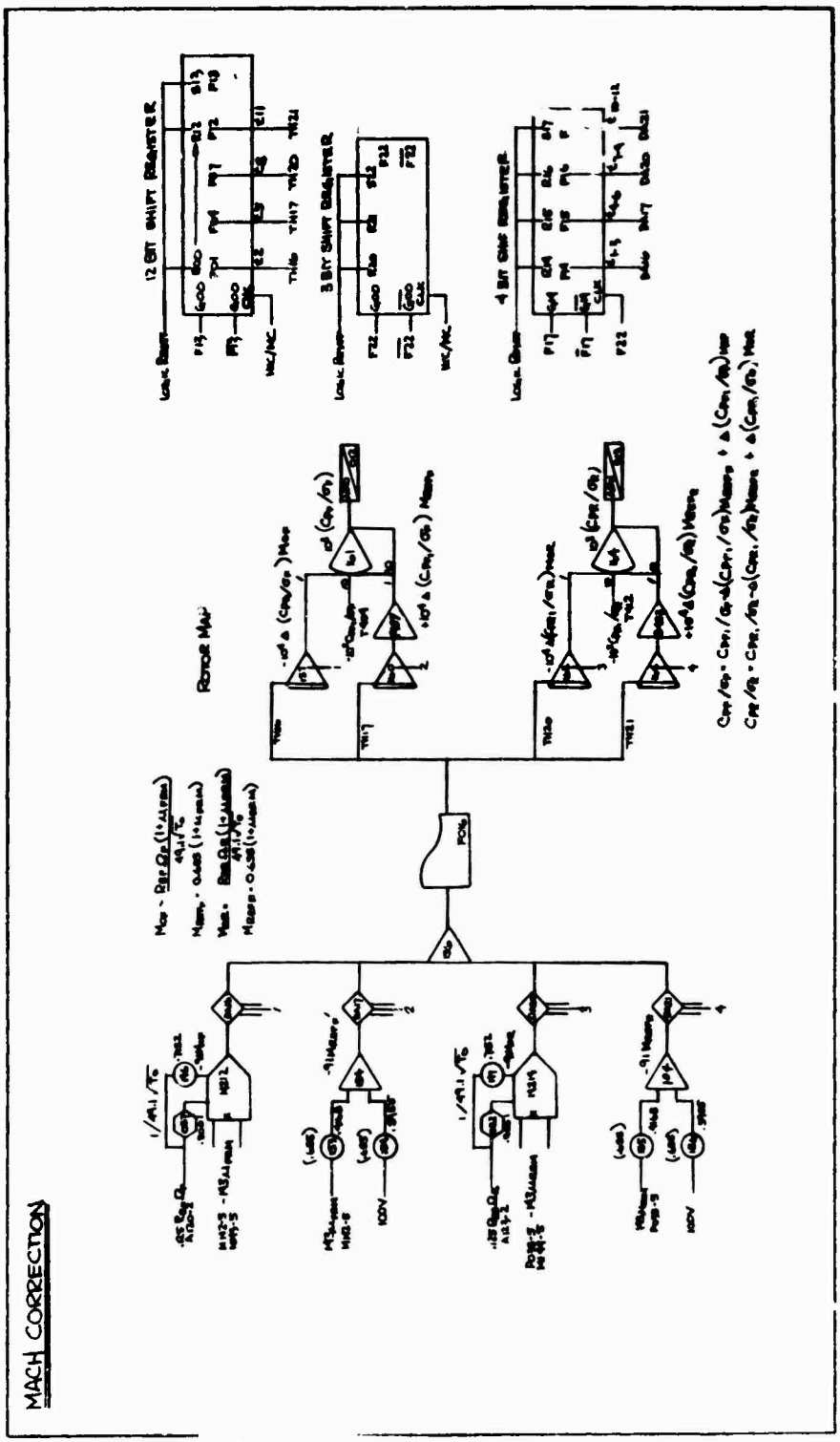

Preceding page blank

MAP ARGUMENT PROCESSING, ROTOR MAPS IN PDP-9, AND C_T MAP, C_H/σ CA

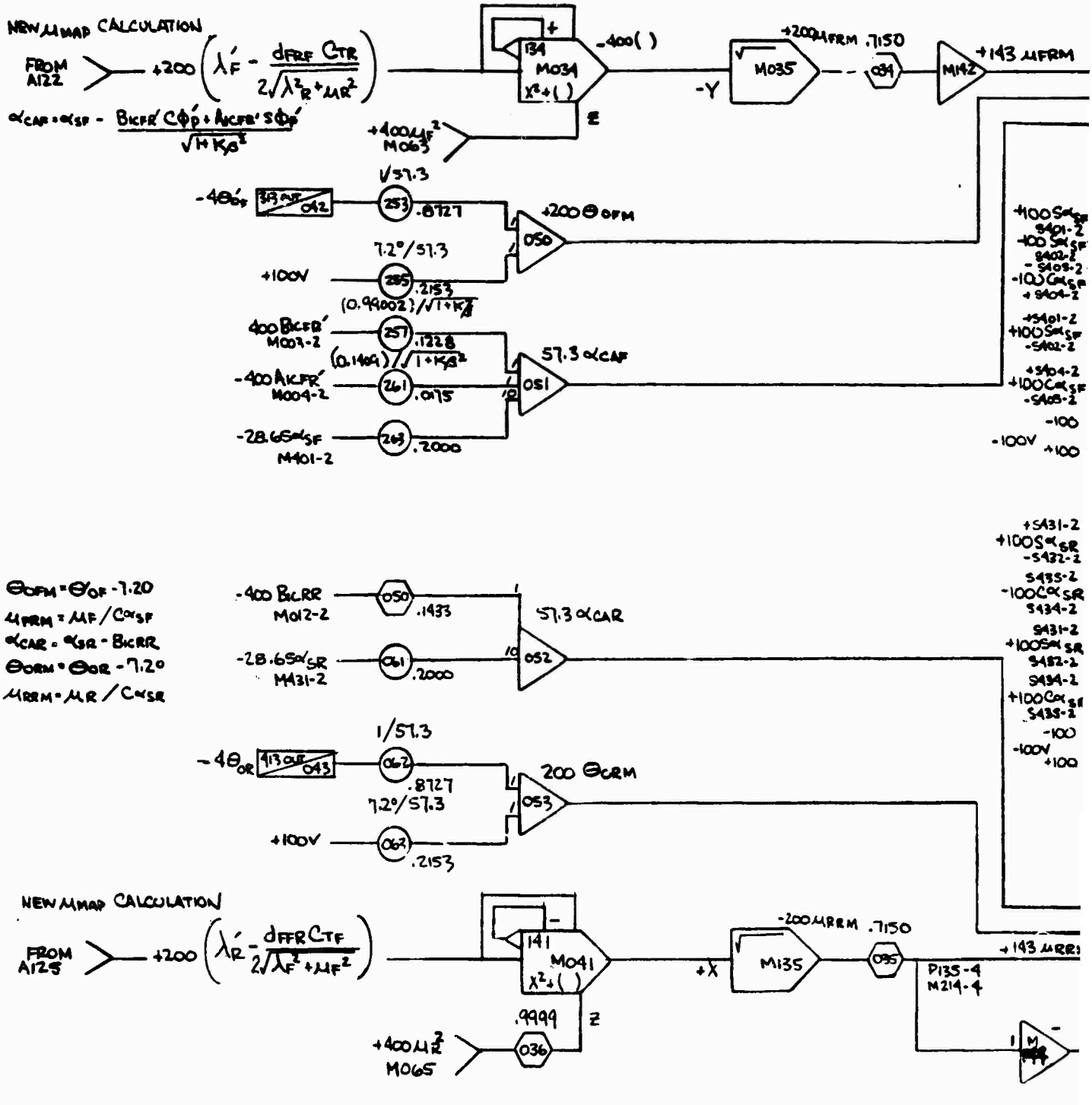

Preceding page blank

9, AND $C_{T\,MAP}$, C_H/σ CALCULATIONS

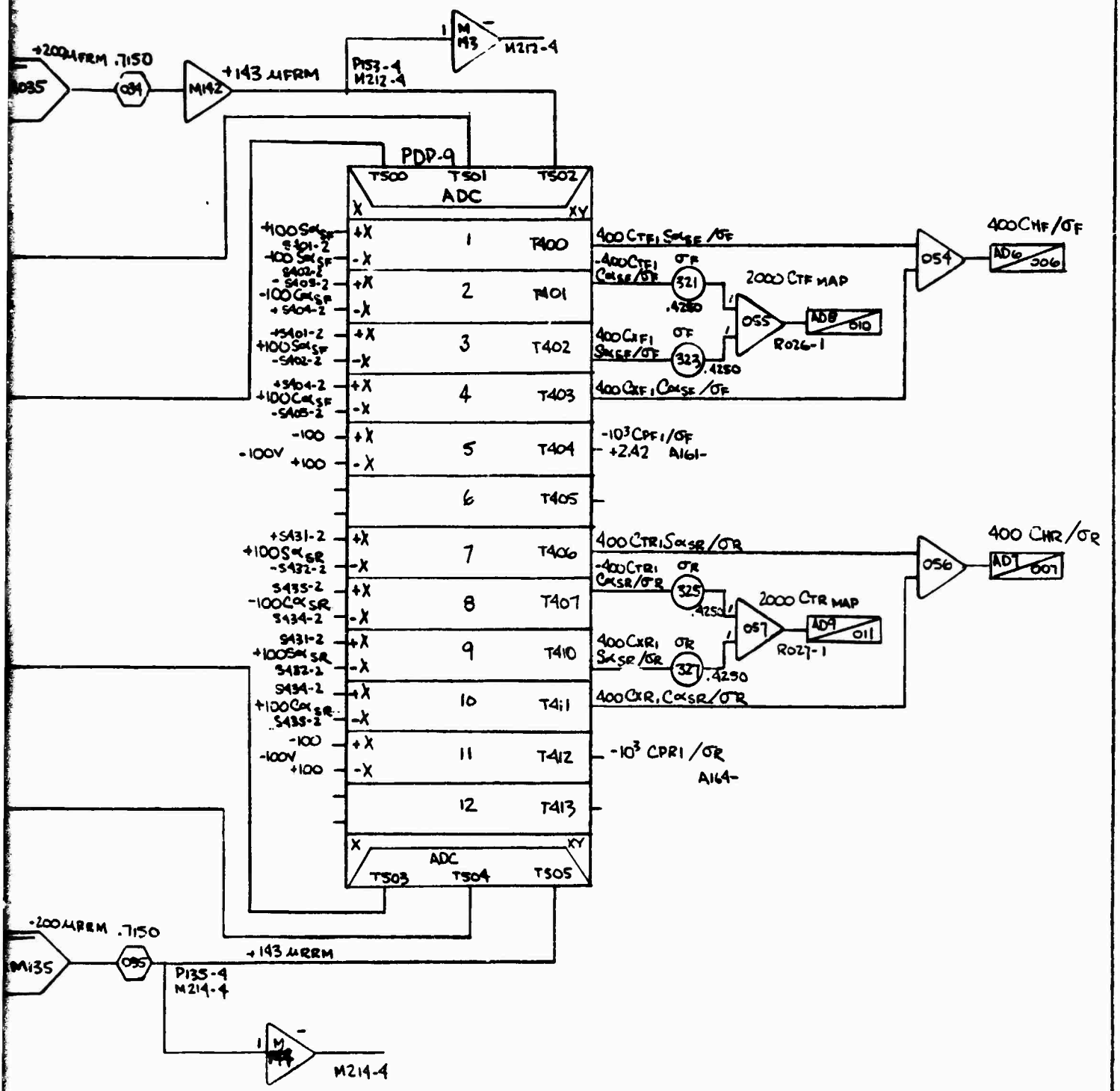

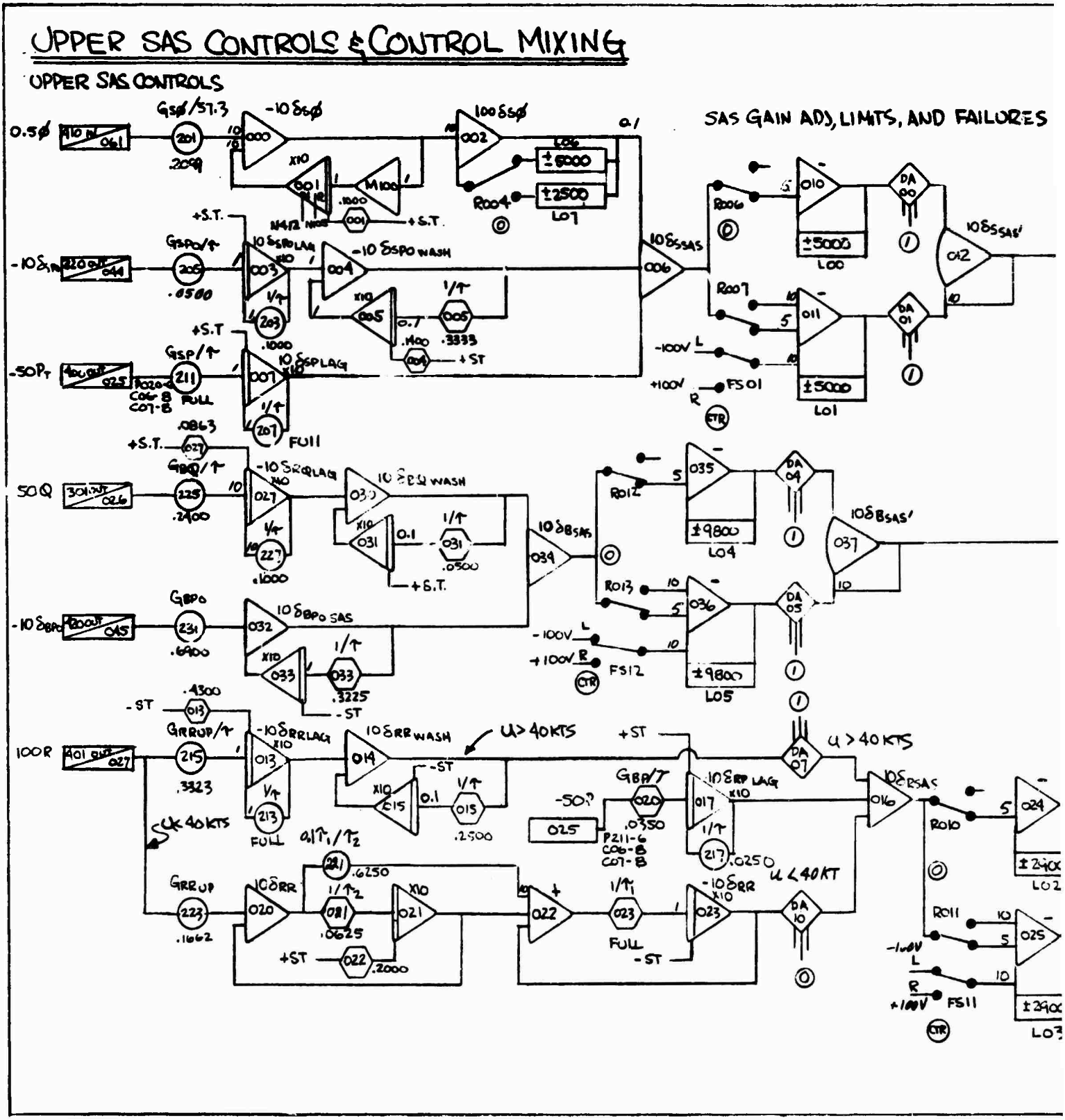

Preceding page blank

SAS GAIN ADJ, LIMITS, AND FAILURES

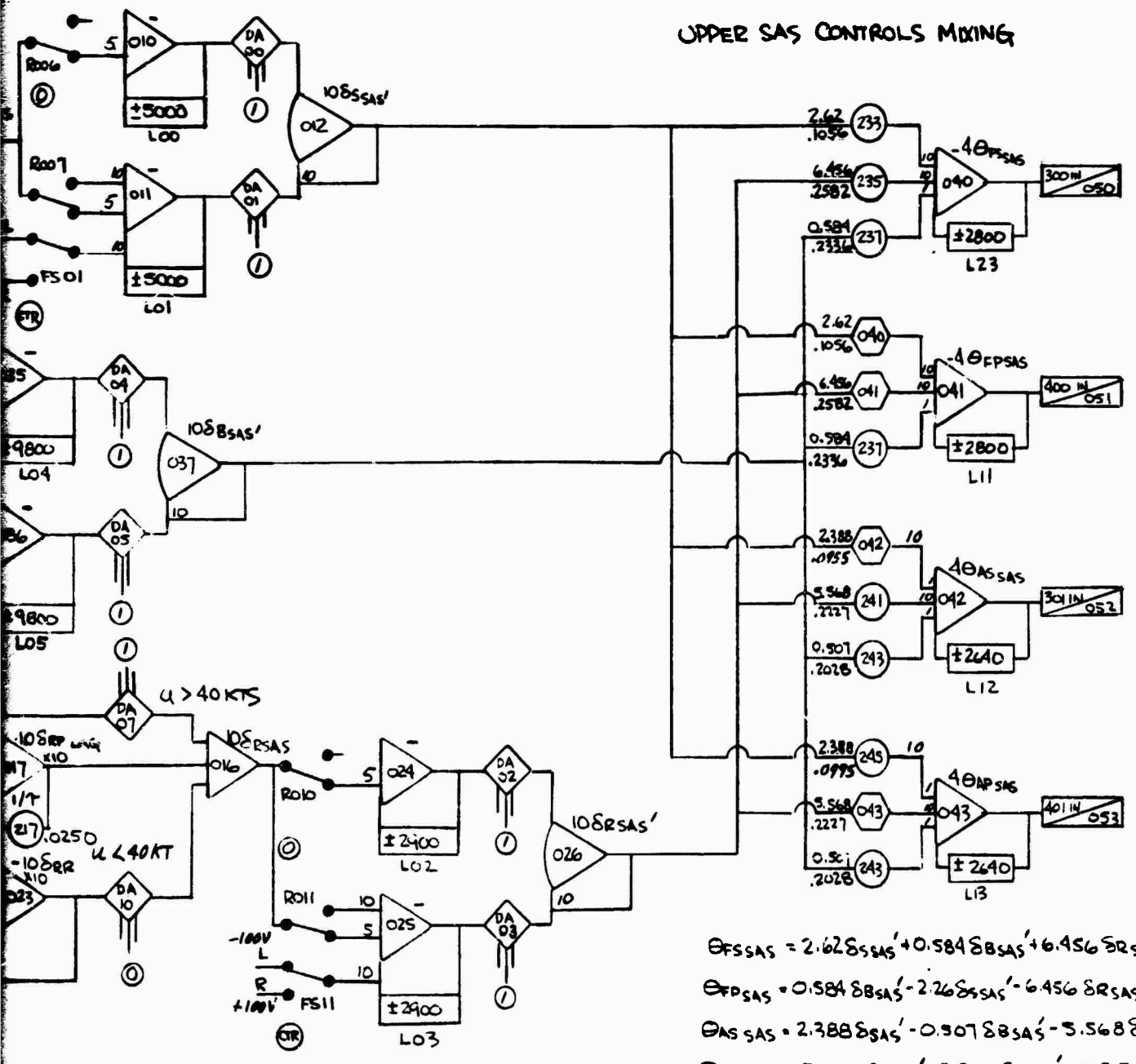

$\theta_{FSSAS} = 2.62\delta_{SSAS}' + 0.584\delta_{BSAS}' + 6.456\delta_{RSAS}'$

$\theta_{FPSAS} = 0.584\delta_{BSAS}' - 2.26\delta_{SSAS}' - 6.456\delta_{RSAS}'$

$\theta_{AS\,SAS} = 2.388\delta_{SAS}' - 0.907\delta_{BSAS}' - 5.568\delta_{RSAS}'$

$\theta_{AP\,SAS} = 5.568\delta_{RSAS}' - 2.388\delta_{SSAS}' - 0.507\delta_{BSAS}'$

GE ANALOG INTERFACE

LONGITUDINAL VERTICAL (GE #1)

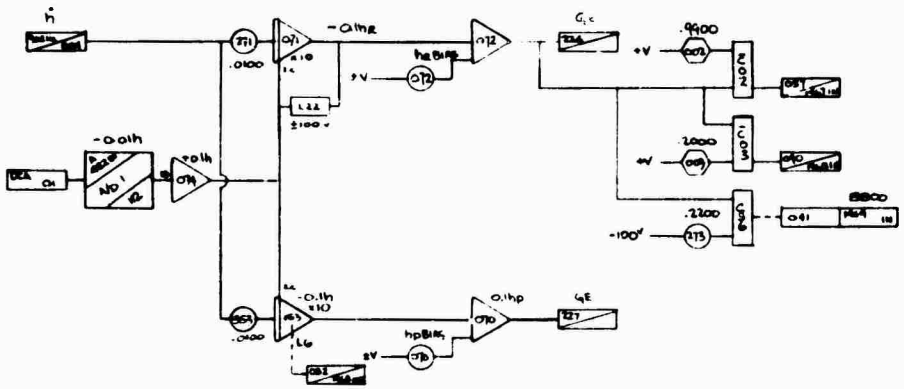

LATERAL DIRECTIONAL (GE #2)

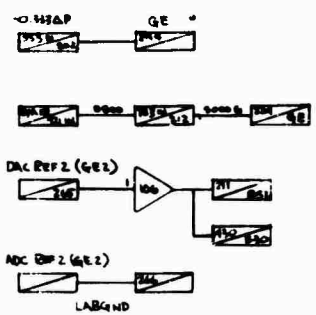

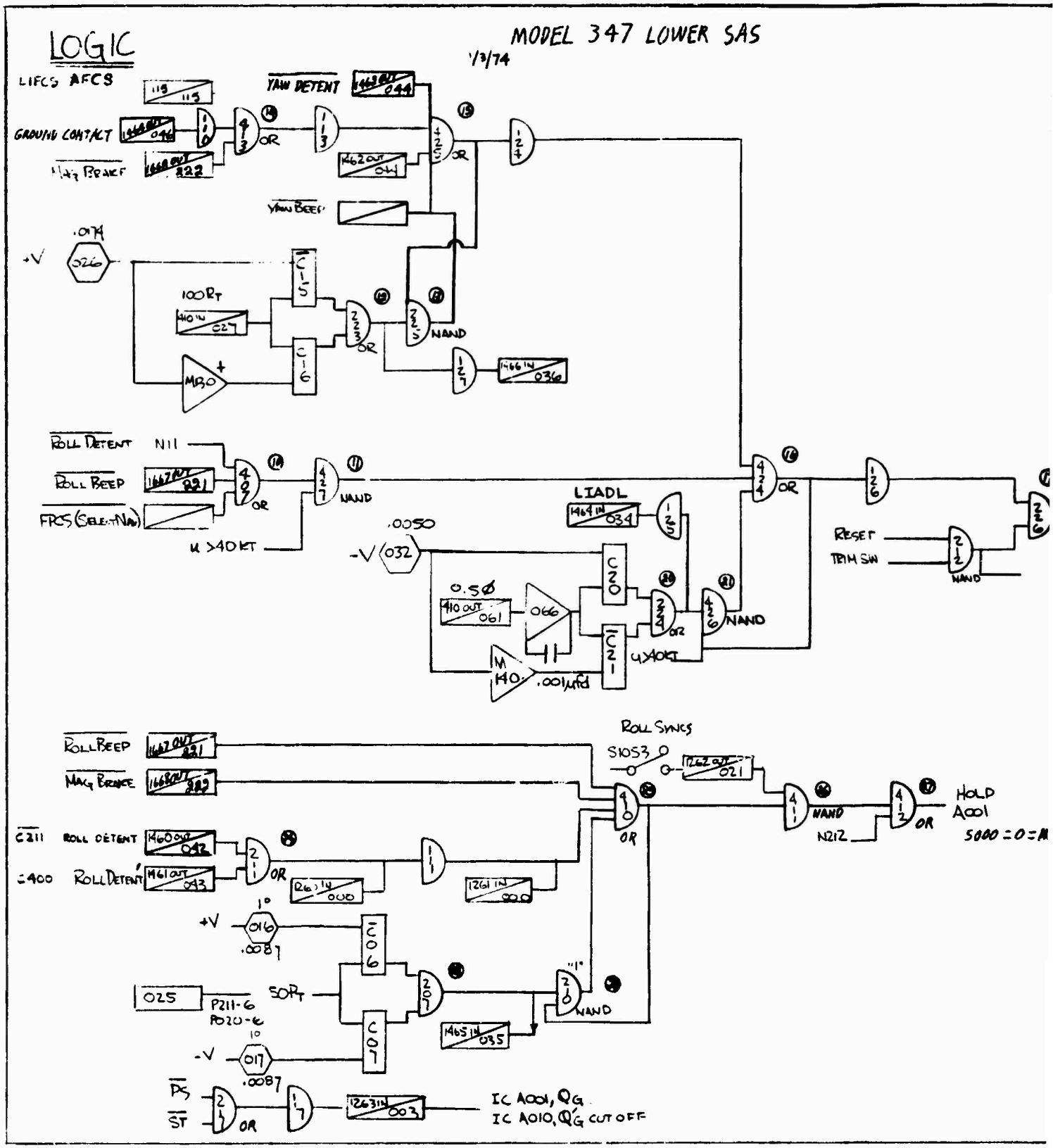
LOGIC
MODEL 347 LOWER SAS
1/3/74
LIFCS AFCS
YAW DETENT
GROUND CONTACT
MAG BRAKE
YAW BEEP
+V
.017
100 RT
ROLL DETENT
N11
ROLL BEEP
FRCS (SELECTED)
U >40 KT
LIADL
-V
.0050
0.5Ø
RESET
TRIM SW
NAND
OR
ROLL SYNCS
S1053
HOLD
A001
N212
C211
C400
ROLL DETENT
+V
.0087
025
P211-6
P020-6
SORT
-V
.0087
IC A001, Q̄G
IC A010, Q̄G CUT OFF

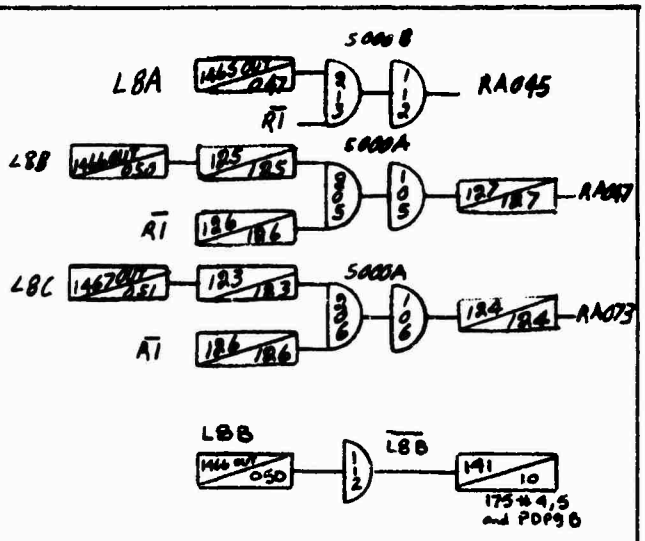
5000 B
LBA
RA045
RI
LBB
5000A
RA047
RA073
LBC
LBB
LBB
175 #4,5
and PD098

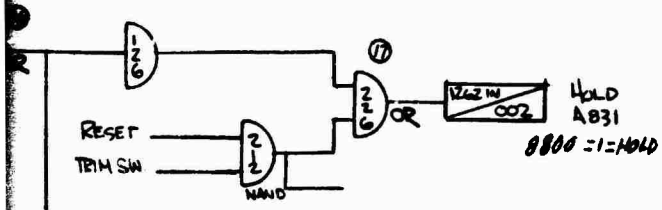
RESET
TRIM SW
NAND
OR
HOLD
A831
8800 = 1 = HOLD

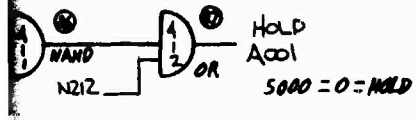
NAND
N212
OR
HOLD
A001
5000 = 0 = HOLD

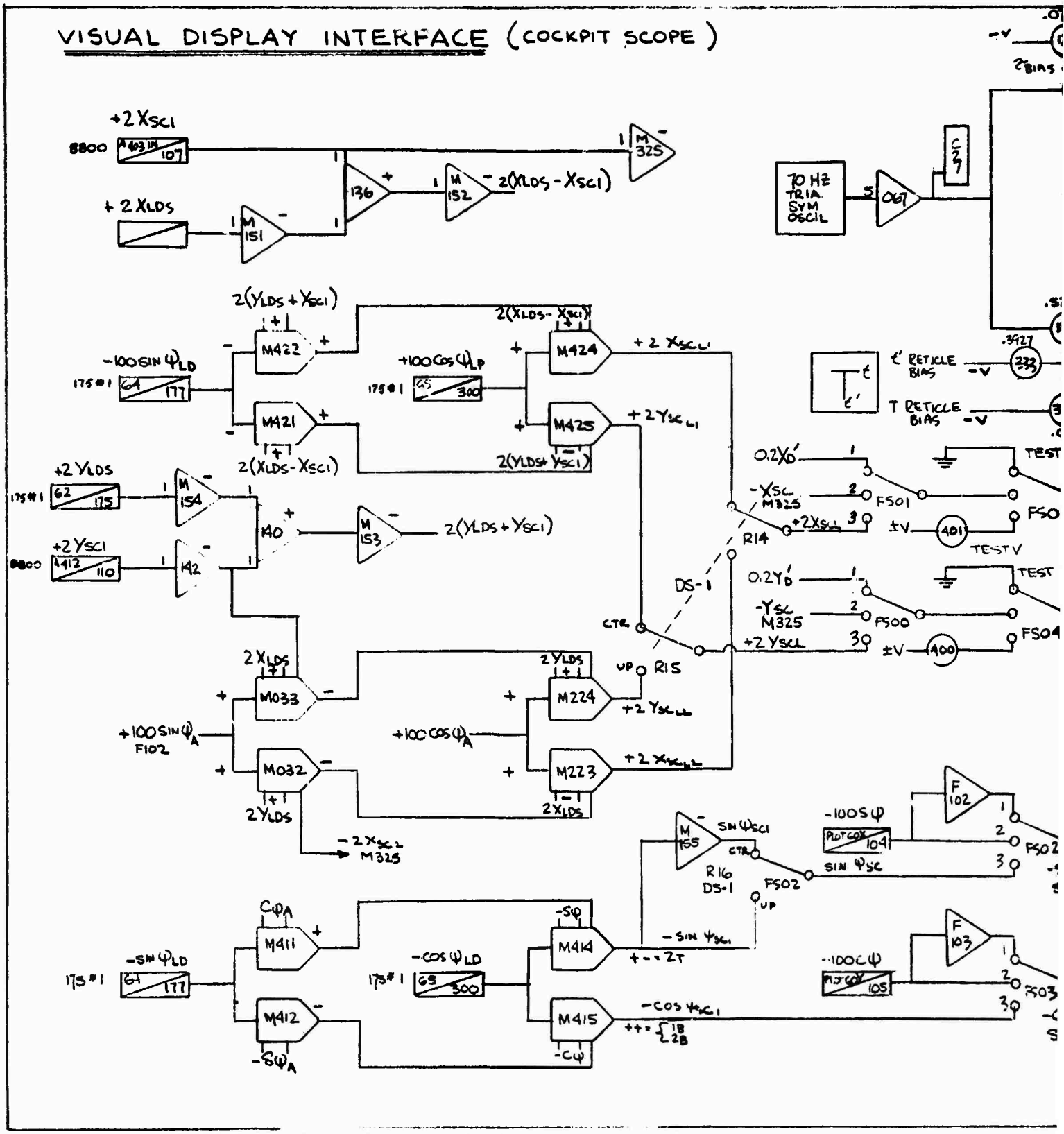

Preceding page blank

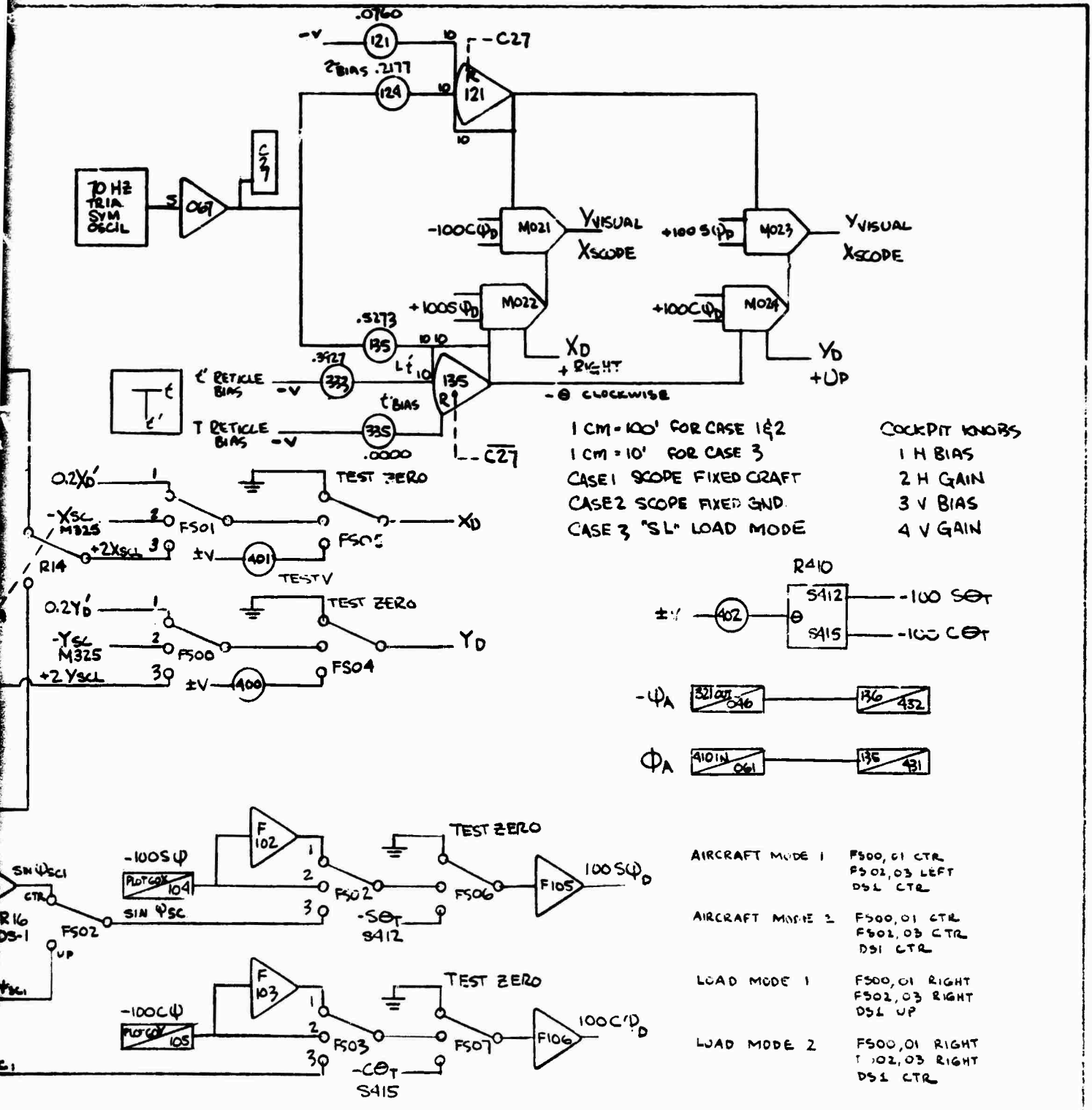
.0960
-V
121
10
-C27
ZBIAS .2177
124
10
R 121
10
70 HZ TRIA SYM OSCIL
S
C69
C27
-100CΨD
M021
YVISUAL
XSCOPE
+100SΨD
M023
YVISUAL
XSCOPE
+100SΨD
M022
+100CΨD
M024
.5273
135
10 10
XD
+ RIGHT
YD
+UP
.3927
t' RETICLE BIAS -V
372
Lt' 10
135 R
t'BIAS
- θ CLOCKWISE
T RETICLE BIAS -V
335
.0000
C27
1 CM = 100' FOR CASE 1&2
1 CM = 10' FOR CASE 3
CASE 1 SCOPE FIXED CRAFT
CASE 2 SCOPE FIXED GND
CASE 3 "SL" LOAD MODE
COCKPIT KNOBS
1 H BIAS
2 H GAIN
3 V BIAS
4 V GAIN
0.2XD'
TEST ZERO
-XSC M325
FS01
XD
+2XSCL
3
±V
401
FS05
TEST V
R14
0.2YD'
TEST ZERO
-YSC M325
FS00
YD
+2YSCL
30
±V
400
FS04
R410
±V
402
θ
S412
S415
-100 SθT
-100 CθT
-ΨA
321 an 046
136 432
ΦA
410 IN 061
136 431
-100SΨ
PLOTCOM 104
F 102
TEST ZERO
FS02
FS06
F105
100SΨD
SIN ΨSC1
CTR
R16 DS-1
FS02
SIN ΨSC
3
-SθT
S412
UP
ΨSC1
-100CΨ
PLOTCOM 105
F 103
TEST ZERO
FS03
FS07
F106
100C'D D
30
-CθT
S415
AIRCRAFT MODE 1
FS00, 01 CTR
FS02, 03 LEFT
DS1 CTR
AIRCRAFT MODE 2
FS00, 01 CTR
FS02, 03 CTR
DS1 CTR
LOAD MODE 1
FS00, 01 RIGHT
FS02, 03 RIGHT
DS1 UP
LOAD MODE 2
FS00, 01 RIGHT
FS02, 03 RIGHT
DS1 CTR

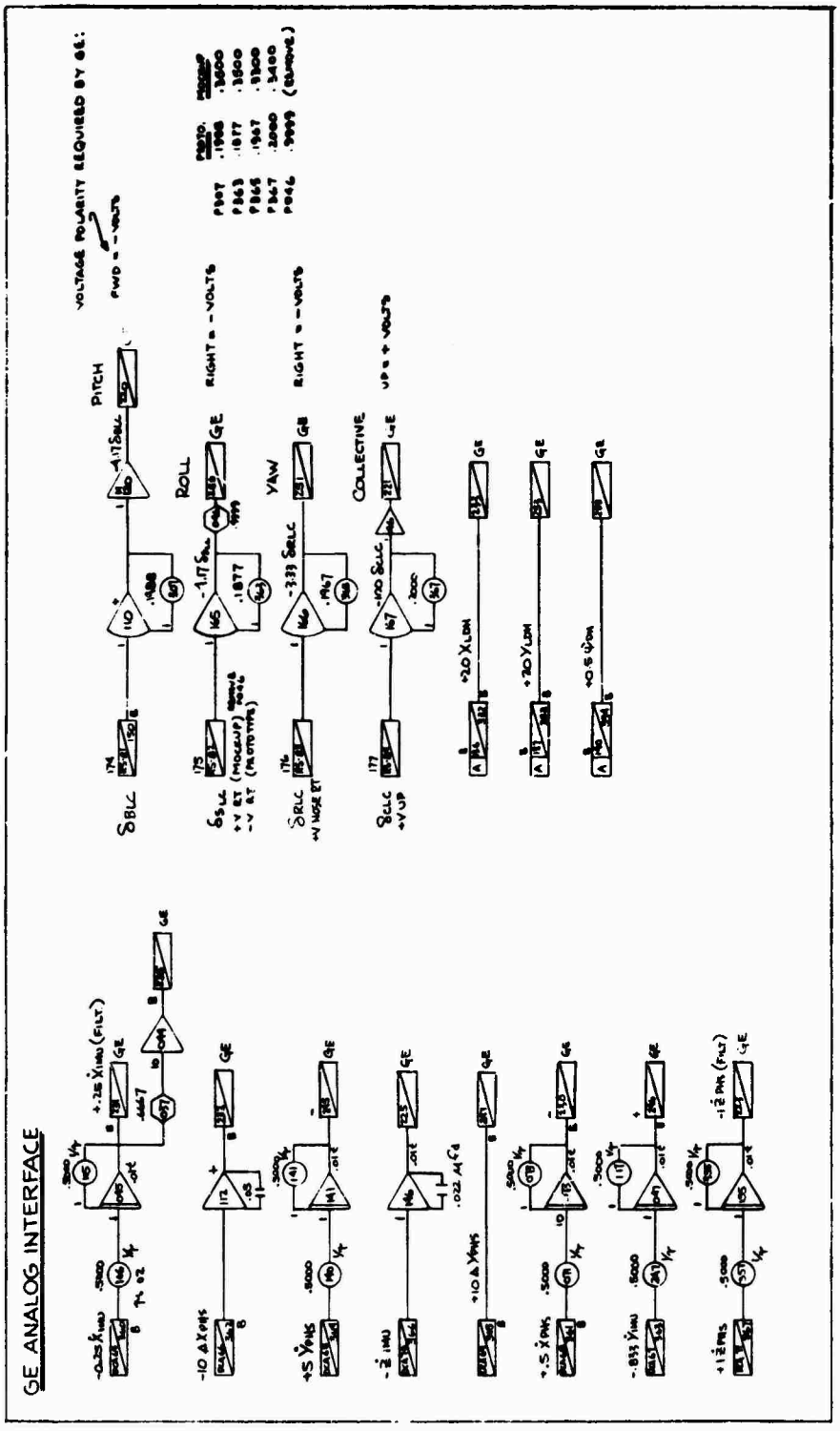

Preceding page blank

Motion Monitor ~ Rotational Simulator

175 # 4

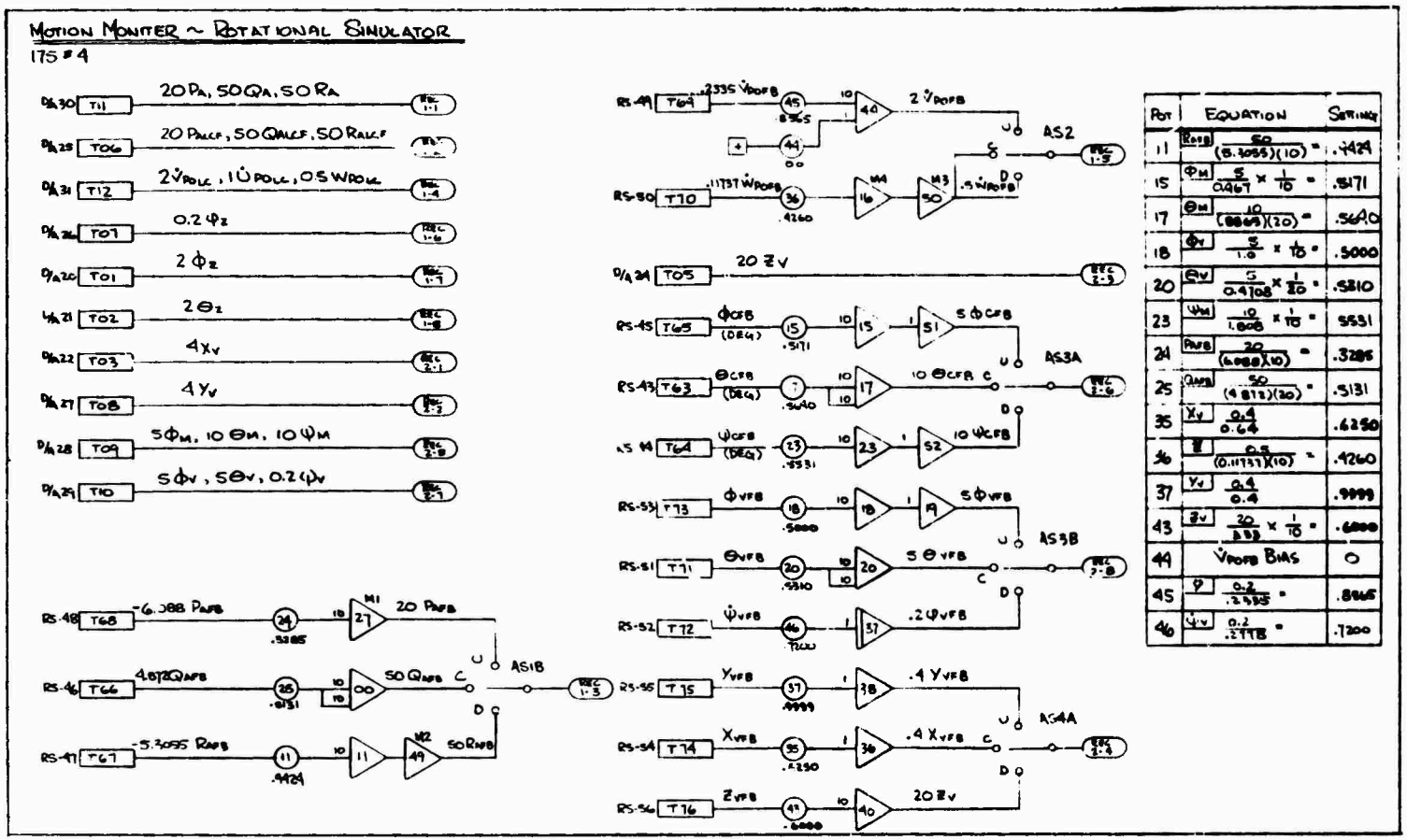

Pot	Equation	Setting
11	$\frac{50}{(5.3095)(10)}$ =	.9429
15	$\frac{5}{0467} \times \frac{1}{10}$ =	.5171
17	$\frac{10}{(8865)(20)}$ =	.5640
18	$\frac{5}{1.0} \times \frac{1}{10}$ =	.5000
20	$\frac{5}{0.9708} \times \frac{1}{10}$ =	.5810
23	$\frac{10}{1.808} \times \frac{1}{10}$ =	.5531
24	$\frac{20}{(6.088)(10)}$ =	.3286
25	$\frac{50}{(9.812)(20)}$ =	.5131
35	$\frac{0.4}{0.64}$	.6250
36	$\frac{0.5}{(0.11737)(10)}$ =	.4260
37	$\frac{0.4}{0.4}$	.9999
43	$\frac{20}{3.93} \times \frac{1}{10}$ =	.6000
44	V̇POFB BIAS	0
45	$\frac{0.2}{.2335}$ =	.8565
46	$\frac{0.2}{.2778}$ =	.7200

COCKPIT INSTRUMENT INTERFACE ~ ROTATIONAL SIMULATOR

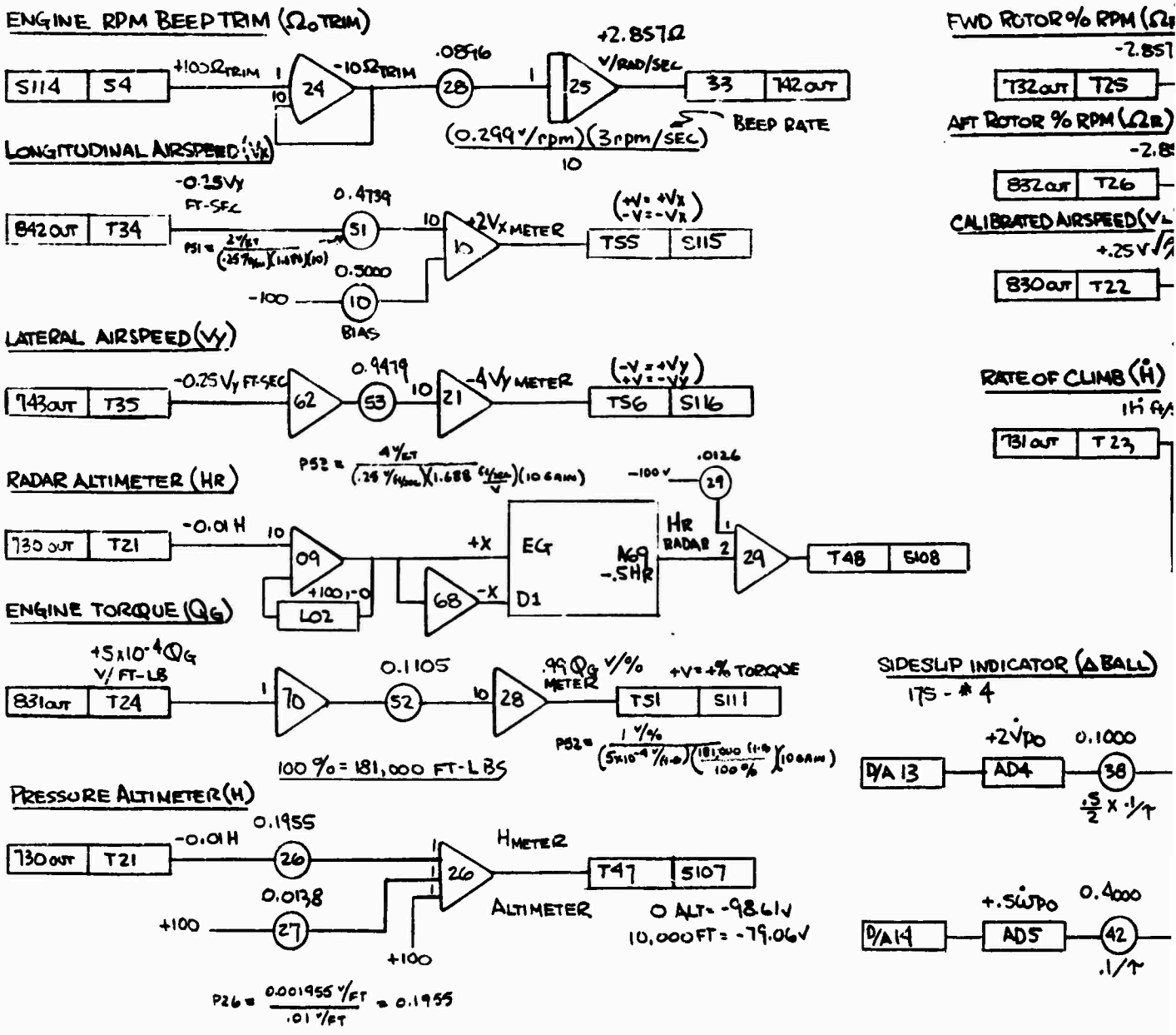

SIMULATOR

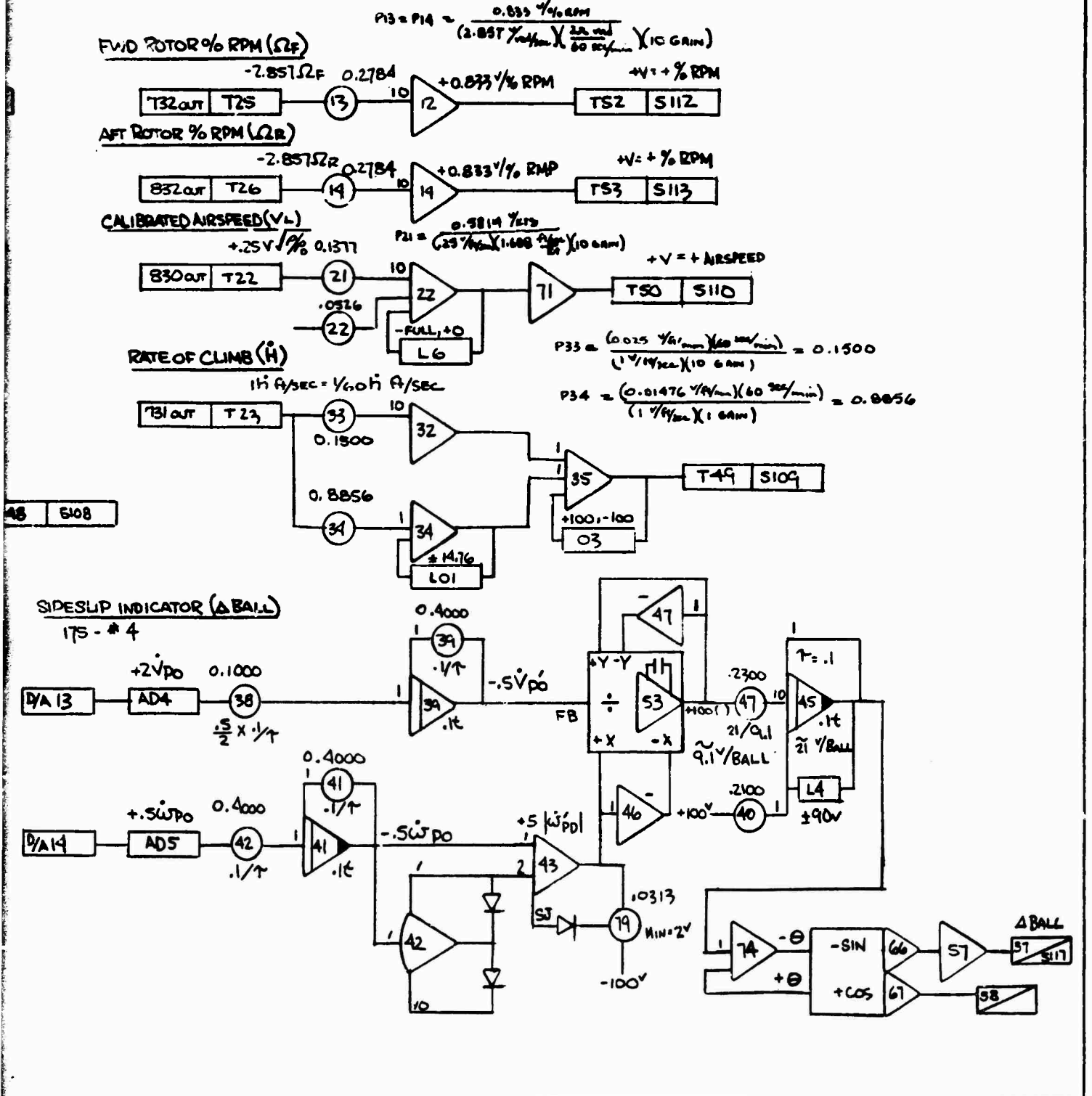
P13 = P14 = 0.833 %/% RPM / (2.857 %/rad/sec X 2π rad/60 sec/min X 10 GAIN)
FWD ROTOR % RPM (ΩF)
-2.857ΩF
0.2784
+0.833 V/% RPM
+V = + % RPM
T32 OUT
T25
13
10
12
TS2
S112
AFT ROTOR % RPM (ΩR)
-2.857ΩR
0.2784
+0.833 V/% RMP
+V = + % RPM
832 OUT
T26
14
10
19
TS3
S113
CALIBRATED AIRSPEED (VL)
+.25V √P/P0
0.1377
P21 = 0.5814 %/KTS / (25 %/in X 1.688 ft/sec/KT X 10 GAIN)
+V = + AIRSPEED
830 OUT
T22
21
10
22
.0326
22
-FULL, +0
L6
71
TS0
S110
RATE OF CLIMB (ḣ)
1 ḣ ft/SEC = 1/60 ḣ ft/SEC
P33 = (0.025 %/ft/min X 60 sec/min) / (1 %/ft/sec X 10 GAIN) = 0.1500
P34 = (0.01476 %/ft/min X 60 sec/min) / (1 %/ft/sec X 1 GAIN) = 0.8856
731 OUT
T23
33
0.1500
32
0.8856
34
± 14.76
L01
35
+100, -100
03
T49
S109
48
S108
SIDESLIP INDICATOR (ΔBALL)
175 - # 4
+2V̇po
0.1000
D/A 13
AD4
38
.5/2 X .1/τ
0.4000
39
.1/τ
39
.1τ
-.5V̇po
FB
47
+Y -Y
÷
53
+X -X
+100(-)
.2300
47
10
21/9.1
~9.1 V/BALL
τ = .1
45
.1τ
~21 V/BALL
L4
±90V
.2100
40
+100V
46
+.5ω̇po
0.4000
D/A 14
AD5
42
.1/τ
41
.1τ
-.5ω̇po
0.4000
41
.1/τ
+5 |ω̇PD|
43
SJ
.0313
79
MIN = 2V
-100V
42
10
74
-θ
+θ
-SIN
+COS
66
67
57
58
ΔBALL
57
S117

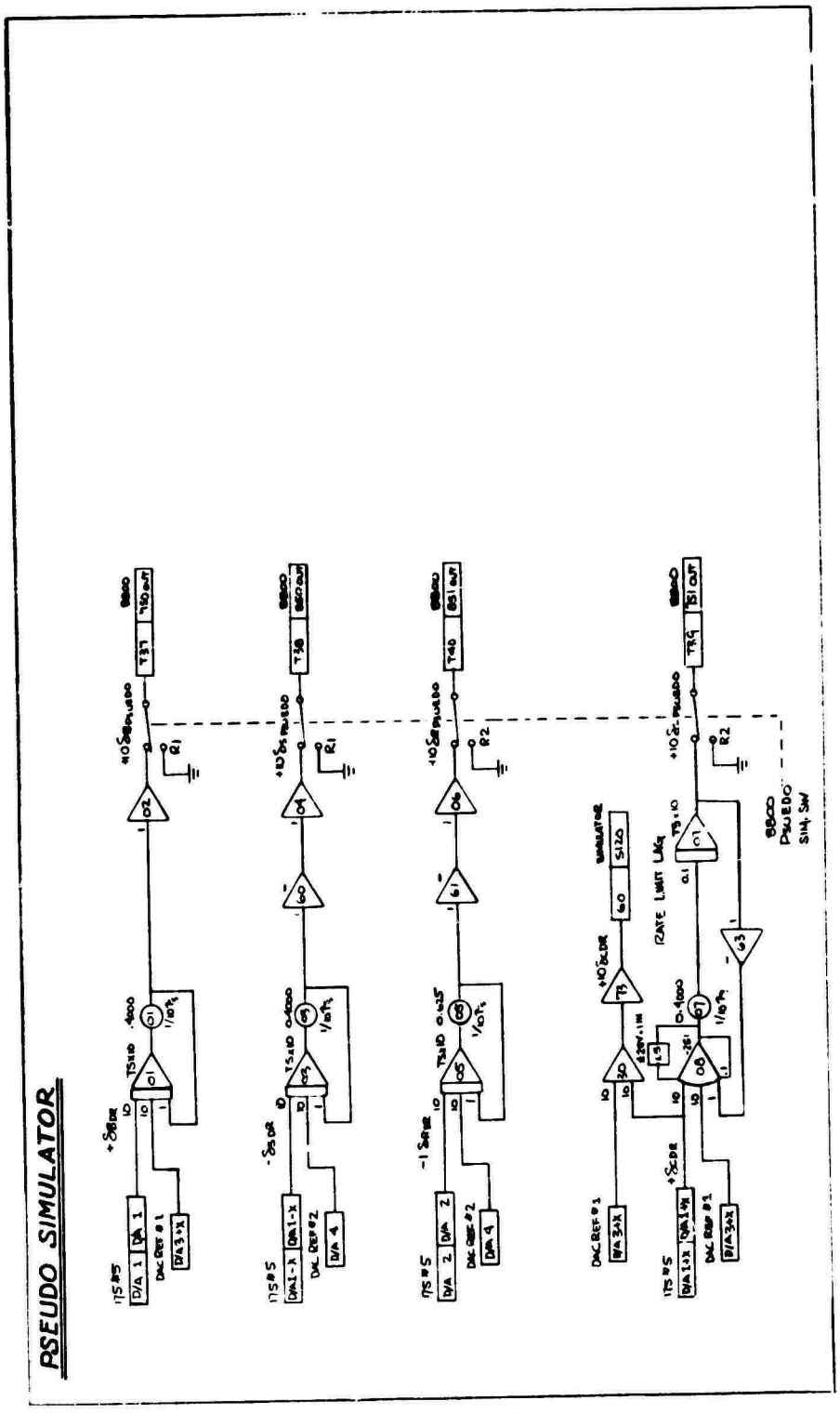

Preceding page blank

CITS's Slave Logic

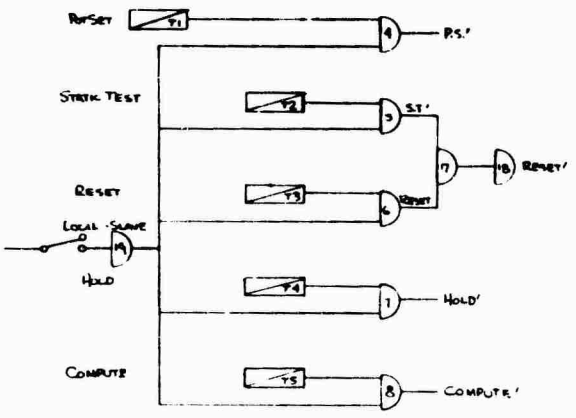

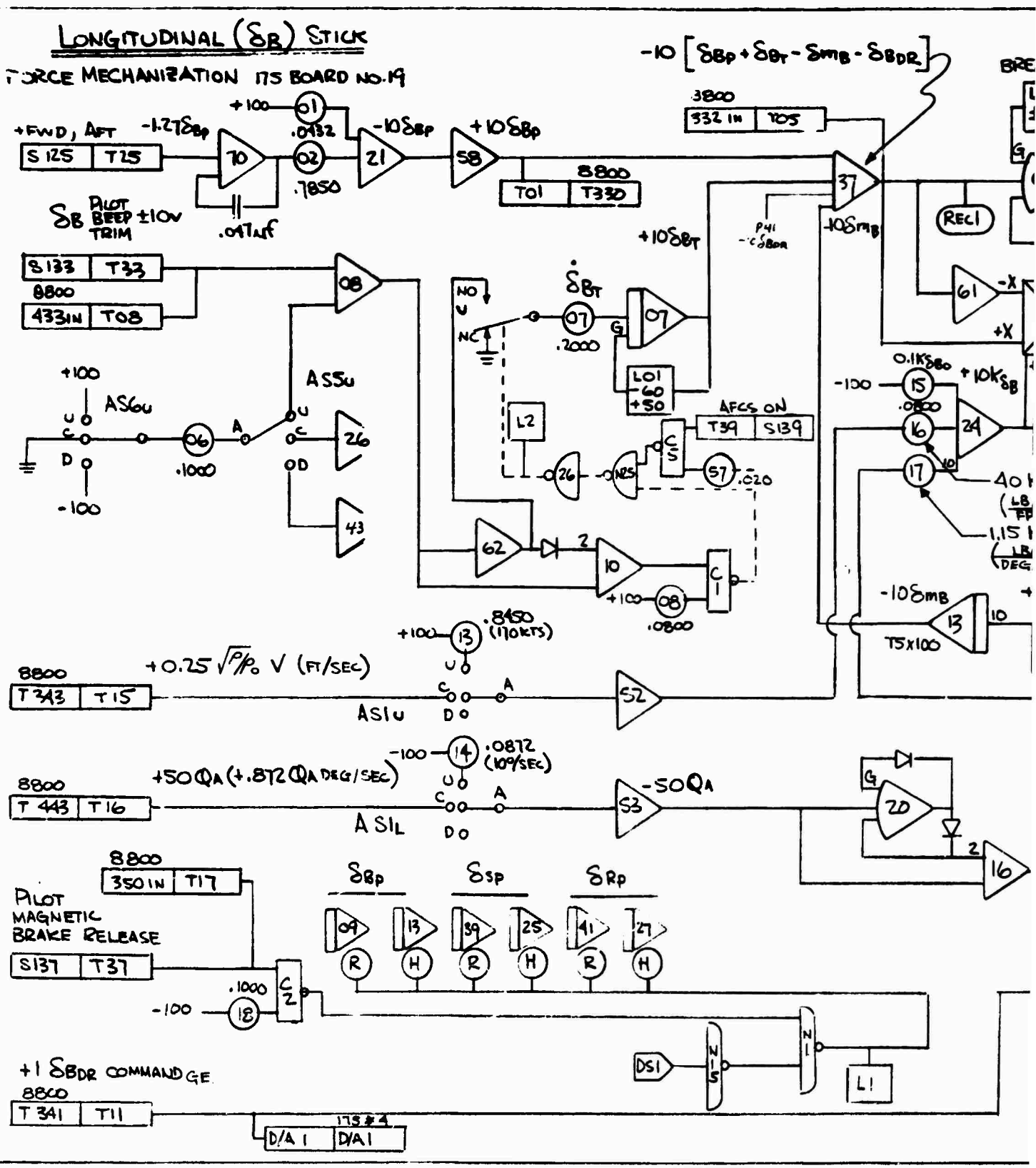
LONGITUDINAL (δ_B) STICK
FORCE MECHANIZATION 175 BOARD NO. 19
$-10\left[\delta_{Bp}+\delta_{BT}-\delta_{mB}-\delta_{BDR}\right]$
+FWD, AFT
$-1.27\delta_{Bp}$
S125 T25
+100
.0432
.7850
$-10\delta_{Bp}$
$+10\delta_{Bp}$
3800
332 IN T05
8800
T01 T330
δ_B PILOT BEEP TRIM ±10V
.047 MF
$+10\delta_{BT}$
P41 $-C\delta_{BDR}$
$-10\delta_{mB}$
REC1
S133 T33
8800
433IN T08
$\dot{\delta}_{BT}$
NO
NC
.2000
LO1 60 +50
AFCS ON
T39 S139
+100
AS6U
ASSU
.1000
-100
.0800
$0.1K\delta_{BO}$
$+10K\delta_B$
.020
$-10\delta_{mB}$
T5x100
8800
T343 T15
$+0.25\sqrt{P/P_0}$ V (FT/SEC)
.8450 (170KTS)
AS1U
$-50Q_A$
8800
T443 T16
$+50Q_A$ ($+.872Q_A$ DEG/SEC)
.0872 (10°/SEC)
AS1L
8800
350IN T17
PILOT MAGNETIC BRAKE RELEASE
S137 T37
.1000
δ_{Bp} δ_{Sp} δ_{Rp}
R H R H R H
$+1\ \delta_{BDR}$ COMMAND GE
8800
T341 T11
175 # 4
D/A 1 D/A 1

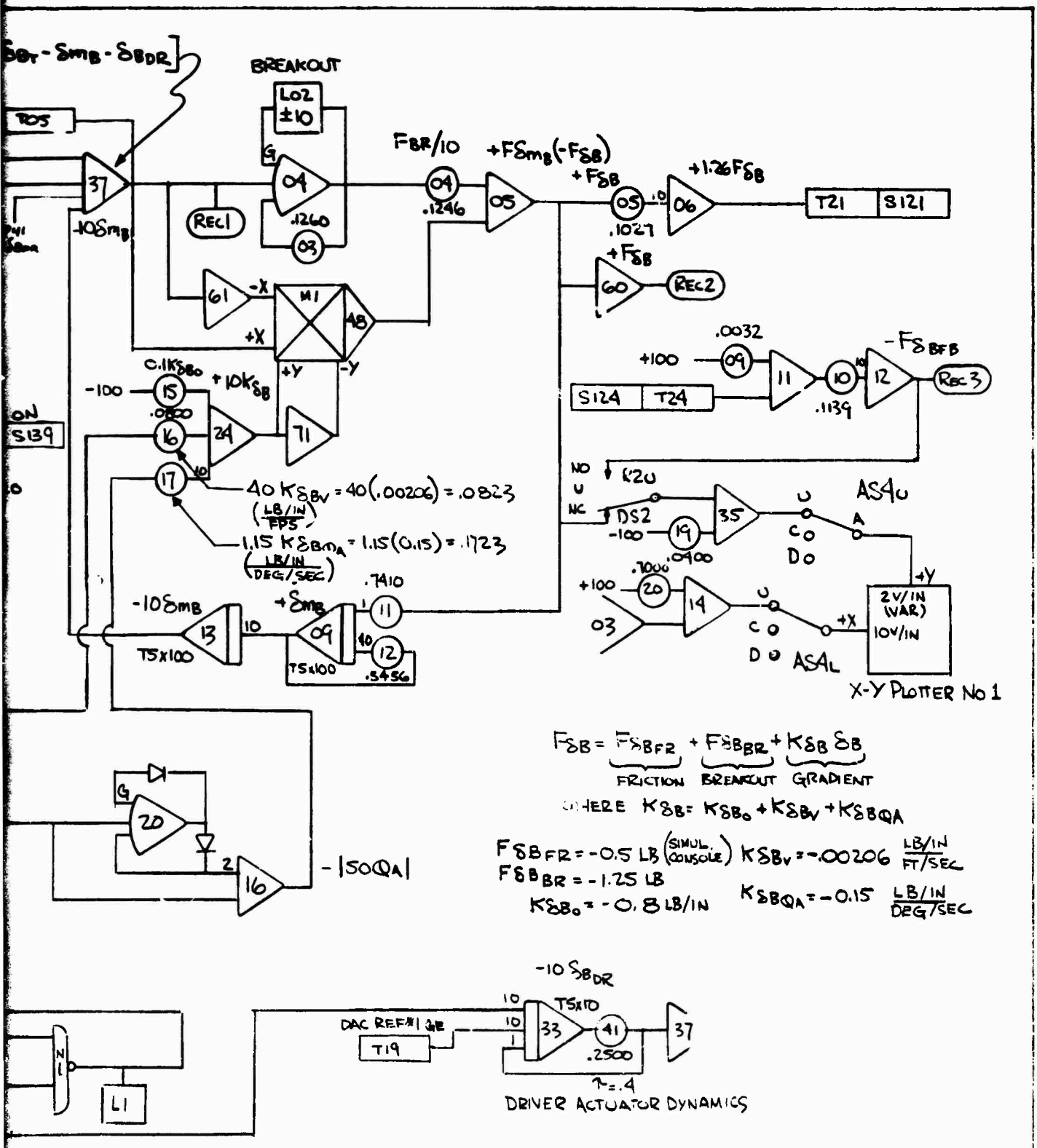

$F_{SB} = \underbrace{F_{SB_{FR}}}_{\text{FRICTION}} + \underbrace{F_{SB_{BR}}}_{\text{BREAKOUT}} + \underbrace{K_{SB}\,\delta_B}_{\text{GRADIENT}}$

WHERE $K_{SB} = K_{SB_0} + K_{SB_V} + K_{SB_{QA}}$

$F_{SB_{FR}} = -0.5$ LB (SIMUL. CONSOLE) $K_{SB_V} = -.00206$ $\frac{LB/IN}{FT/SEC}$

$F_{SB_{BR}} = -1.25$ LB

$K_{SB_0} = -0.8$ LB/IN $K_{SB_{QA}} = -0.15$ $\frac{LB/IN}{DEG/SEC}$

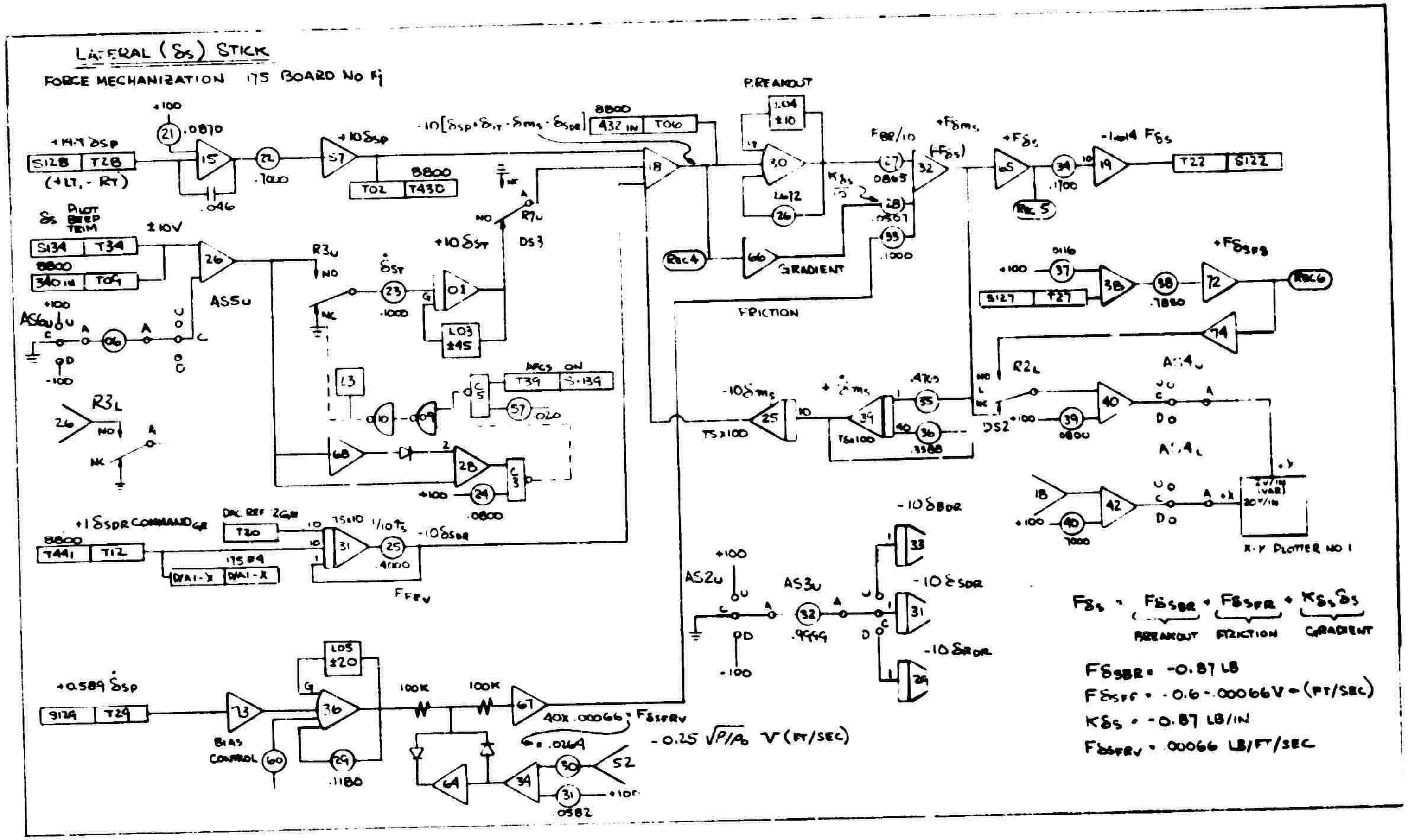

Preceding page blank

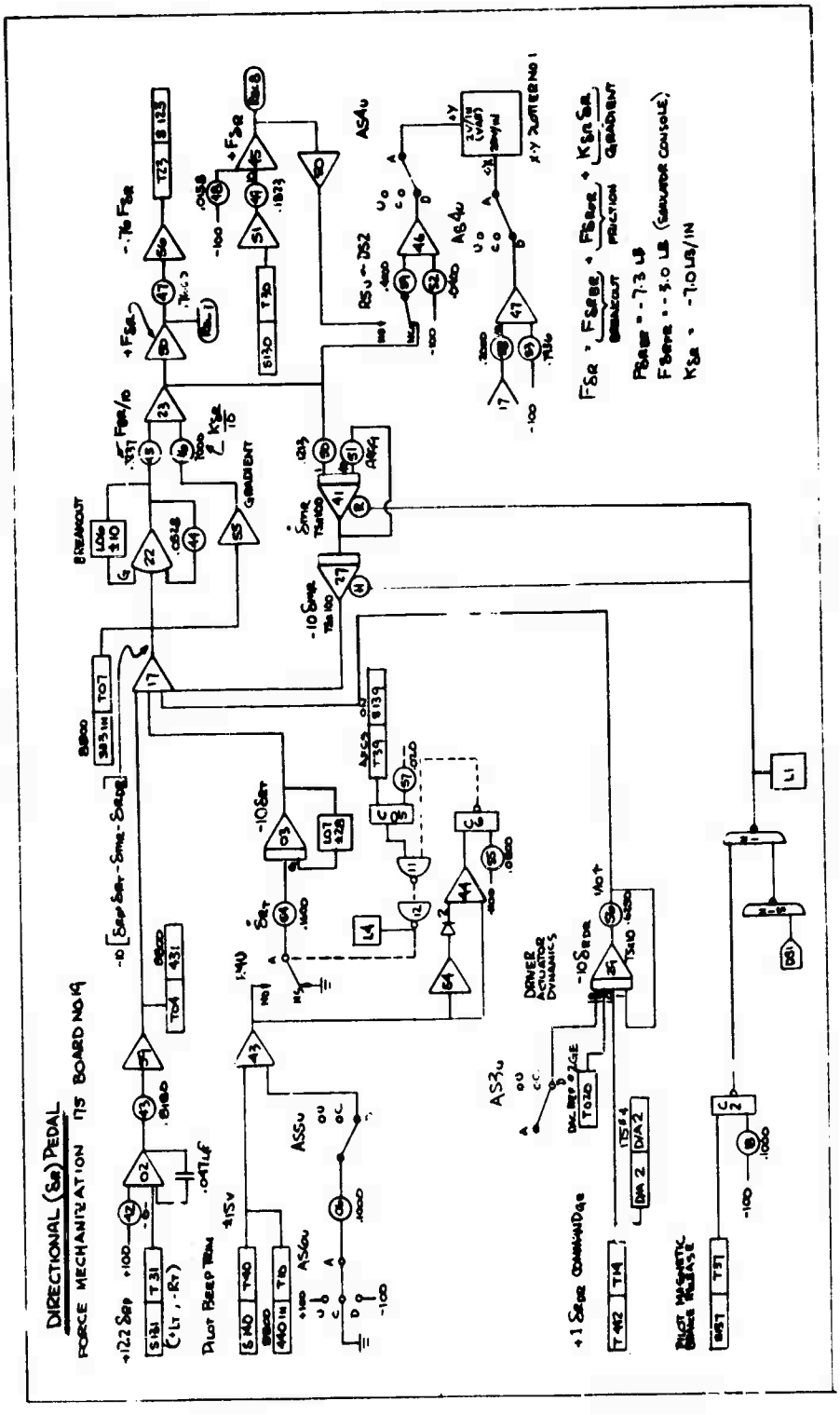
DIRECTIONAL (Sa) PEDAL
FORCE MECHANIZATION TIS BOARD NO.19
Fsa = Fsabe + Fbeep + Ksa Sa
FRICTION
GRADIENT
Fbeep = -7.3 LB
Fbeep = -5.0 LB (SIMULATOR CONSOLE)
Ksa = -7.0 LB/IN
BREAKOUT
GRADIENT
DRIVER ACTUATOR DYNAMICS
PILOT MAGNETIC BRAKE RELEASE

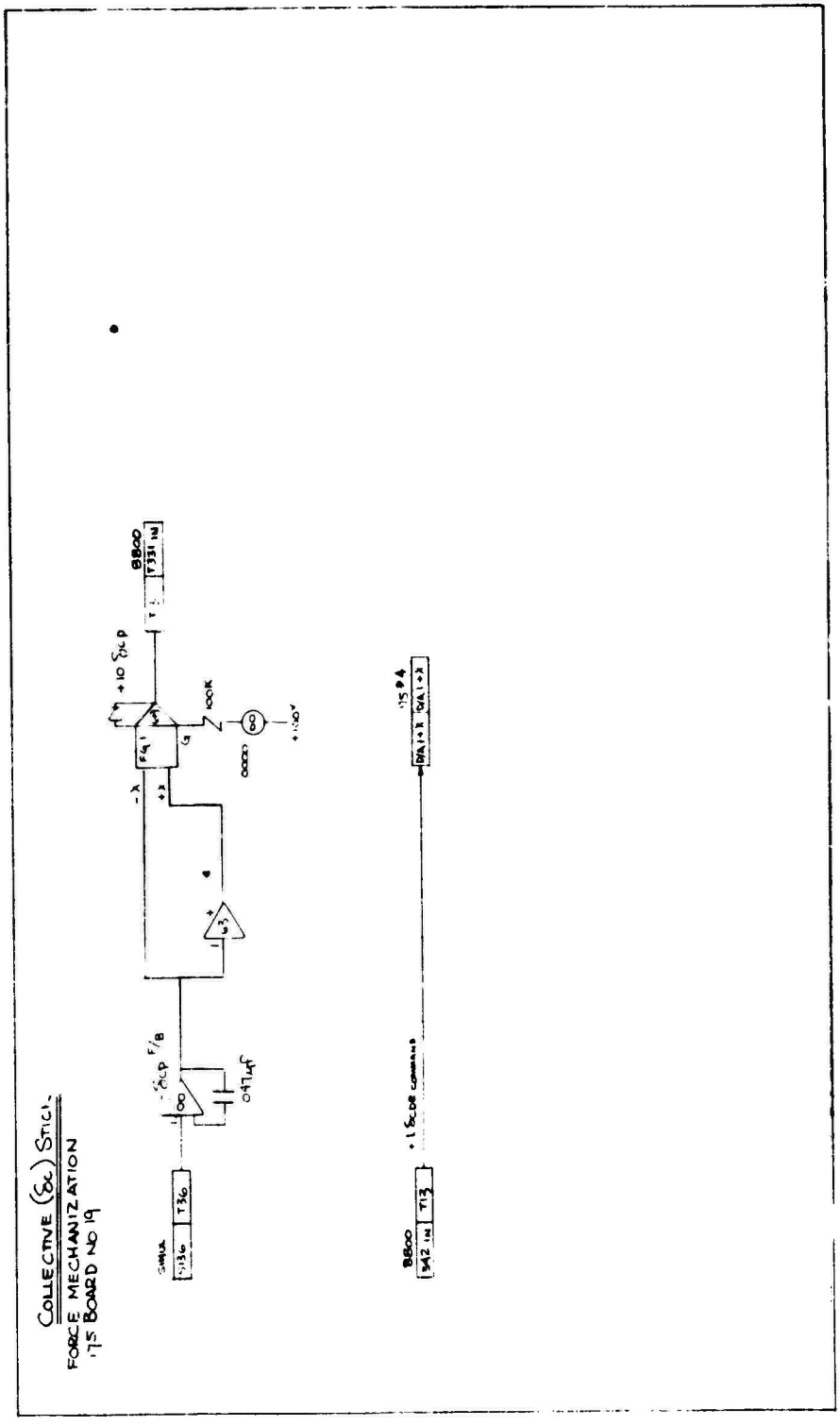
COLLECTIVE (6c) STICK
FORCE MECHANIZATION
175 BOARD NO 19
+10 Vdc
LOCK
+15V
-Vdc F/B
0.47μF
+15 Vdc COMMAND
8800
T331 IN
8800
T42 IN
T13
SIMUL
T136
T36
175 P4

LIST OF SYMBOLS - REPORT BODY

Symbol	Description	Unit
$[A]$	Axis transformation matrix from inertial to aircraft body axes	-
$[A]^T$	Transpose of the orthogonal matrix of direction cosine transformation from inertial to aircraft body axes	-
A_{IC}	Lateral cyclic pitch in body axis	Rad
$[B]$	Axis transformation from inertial to load body axes	-
$[B]^T$	Transpose of the orthogonal matrix of direction cosine transformation from inertial to load body axes	-
B_{IC}	Longitudinal cyclic pitch in body axis	Rad
C or $C_{N_{DYNAMIC}}$	Sling load unsteady yawing moment coefficient	-
C_N	Sling load yawing moment coefficient	-
$C_{N_{AERO}}$	Total aerodynamic sling load yawing moment coefficient due to static, dynamic and yaw rate components	-
C_{N_B}	Sling load yawing moment coefficient due to sideslip	1/Rad
$C_{N_{DAMPING}}$	Sling load yawing moment coefficient due to yaw rate, $C_{N_r} \frac{\dot{\psi} b_L}{2V_o}$	-
C_{N_r}	Sling load yawing moment coefficient due to non-dimensional yaw rate, $\frac{rb_L}{2V_o}$	1/Rad
$C_{N_{STATIC}}$	Sling load static load yawing moment coefficient	-

Symbol	Description	Unit
C_{Y_B}	Sling load side force coefficient due to sideslip	1/Rad
D/q	Nondimensional fuselage drag force in body axis	Ft^2
D_{LT}	Sling load drag in body axis of load ($D_{LT} = D/q$)	Ft^2
$G(j\omega)$	Amplitude ratio	Db
H_F, H_R	Rotor (H) drag force in S.N.P. wind axis	Lb
Hz	Frequency in cycles per second	-
I_{xx}	Airframe moment of inertia about X axis	$Slug-Ft^2$
I_{yy}	Airframe moment of inertia about Y axis	$Slug-Ft^2$
I_{zz}	Airframe moment of inertia about Z axis	$Slug-Ft^2$
I_{xz}	Airframe product of inertia about XZ plane	$Slug-Ft^2$
I_Z or J_L	Yaw moment of inertia of sling load	$Slug-Ft^2$
K_{ℓ_n}, $K^{\bullet}_{\ell_n}$	Linear n^{th} cable stretch (and angular rate) constant	Lb/Ft Lb/Ft/Sec
L	Total airframe rolling moment in aircraft body axis	Ft-Lb
L_{AT_n}	n^{th} cable tension rolling moment in helicopter axes	Ft-Lb
L_{BT_n}	n^{th} cable tension rolling moment in load body axes	Ft-Lb
M	Total airframe pitching moment in aircraft body axis	Ft-Lb
M_{AT_n}	n^{th} cable tension pitching moment in helicopter axes	Ft-Lb

Symbol	Description	Unit
M_{BT_n}	n^{th} cable tension pitching moment in load body axes	Ft-Lb
N	Total airframe yawing moment in aircraft body axis	Ft-Lb
N/q	Nondimensional fuselage yawing moment in body axis	Ft^3
N_{AERO}	Total sling load aerodynamic yawing moment in body axes of the load	Ft-Lb
N_{AT_n}	n^{th} cable tension yawing moment in helicopter axes	Ft-Lb
N_{BT_n}	n^{th} cable tension yawing moment in load body axes	Ft-Lb
N_{CABLES}	Sling load cable yawing moment	Ft-Lb
N_{LT}	Sling load yawing moment in body axis of load ($N_{LT} = N/q$)	Ft^3
N_{TOTAL}	Total sling load aerodynamic and cable yawing moment in body axes of the load	Ft-Lb
$N_{UNSTEADY}$	Sling load unsteady yawing moment	Ft-Lb
$P, \dot{P}$	Component of helicopter angular rate (or acceleration) about aircraft X axis	Rad/Sec_2 Rad/Sec^2
$Q, \dot{Q}$	Component of helicopter angular rate (or acceleration) about aircraft Y axis	Rad/Sec_2 Rad/Sec^2
Q_F, Q_R	Rotor torque required	Ft-Lb
$R, \dot{R}$	Component of helicopter angular rate (or acceleration) about aircraft Z axis	Rad/Sec_2 Rad/Sec^2
S_L	Load container planform area, $\ell_1 \times b_1$	Ft^2
S_T	Strouhal number, $\frac{\omega b}{V_o}$	Rad
T	Cable tension force	Lb

Symbol	Description	Unit
T_F, T_R	Rotor thrust in S.N.P. wind axis	
T_n	Tension force of the n^{th} cable	Lb
V_T or V_c	Total aerodynamic velocity	Ft/Sec
V_w	Total steady wind velocity	Ft/Sec
W_L or W	Weight of sling load	Lb
X	Total force along helicopter X axis	Lb
X_A	Helicopter body axis coordinate in X direction	-
X_{AT_n}	n^{th} cable tension force along helicopter X axis	Lb
X_B	Load body axis coordinate in X direction	-
X_{BT_n}	n^{th} cable tension force along load x axis	Lb
X_{B_L}	Load container half-length	Ft
$X_{c.}$	Horizontal distance between cable and load center of mass	Ft
Y	Total force along helicopter Y axis	Lb
Y/q	Nondimensional fuselage side force in body axis	Ft^2
Y_A	Helicopter body axis coordinate in y direction	-
Y_{AT_n}	n^{th} cable tension force along helicopter y axis	Lb
Y_B	Load body axis coordinate in y direction	-
Y_{BT_n}	n^{th} cable tension force along load y axis	Lb
Y_F, Y_R	Rotor side force in S.N.P. wind axis	Lb

Symbol	Description	Unit
Y_{LT}	Sling load side force in body axis of load ($Y_{LT} = Y/q$)	Ft^2
Z	Total force along helicopter Z axis	Lb
Z_A	Helicopter body axis coordinate in Z direction	-
Z_{AT_n}	n^{th} cable tension force along helicopter Z axis	Lb
Z_B	Load body axis coordinate in Z direction	-
Z_{BT_n}	n^{th} cable tension force along load Z axis	Lb
a_o, a_{o_F}, a_{o_R}	Rotor coning angle	Rad
a_1, a_{1_F}, a_{1_R}	Longitudinal first harmonic flapping coefficient	Rad
b_1, b_{1_F}, b_{1_R}	Lateral first harmonic flapping coefficient	Rad
b_L	Sling load container width	Ft
dt	Rate of change of time	Sec
f	Sling load unsteady yawing moment function	-
g	Acceleration due to gravity	Ft/Sec^2
j	$\sqrt{-1}$	-
ℓ, ℓ_n	Straight line distance between upper cable (or n^{th} cable) and lower cable (or n^{th} cable) sling attach points	Ft
ℓ_B	Bifilar length	Ft
ℓ_L	Sling load container length	Ft
$\dot{\ell}_n$	Rate of change of straight line distance between upper n^{th} cable and lower n^{th} cable sling attach points	Ft/Sec

Symbol	Description	Unit
ℓ_o, ℓ_{o_n}	Zero-tension straight line distance between upper cable (or n^{th} cable) and lower cable (or n^{th} cable) sling attach points	Ft
ℓ_P	Pendulum length	Ft
m	Mass of helicopter	Slugs
P_A	Component of helicopter angular rate about helicopter X axis	Rad/Sec
P_B	Component of load angular rate about load X axis	Rad/Sec
q_A	Component of helicopter angular rate about helicopter y axis	Rad/Sec
q_B	Component of load angular rate about load y axis	Rad/Sec
r_A	Component of helicopter angular rate about helicopter Z axis	Rad/Sec
r_B	Component of load angular rate about load Z axis	Rad/Sec
t	Time	Sec
$u, \dot{u}$ u or u_A	Linear inertial velocity (and acceleration) components along helicopter X axis	Ft/Sec_2 Ft/Sec^2
u_B	Linear inertial velocity along load X axis	Ft/Sec
$u_{BA_n}, \dot{x}_{BA_n}$	Difference between (n^{th} cable) lower attach point velocity and (n^{th} cable) upper attach point velocity, along helicopter X axis, relative to helicopter axes	Ft/Sec
$v, \dot{v}$ v or v_A	Linear inertial velocity (and acceleration) components along helicopter Y axis	Ft/Sec_2 Ft/Sec^2
v_B	Linear inertial velocity along load y axis	Ft/Sec
$v_{BA_n}, \dot{y}_{BA_n}$	Difference between (n^{th} cable) lower attach point velocity and (n^{th} cable) upper attach point velocity, along helicopter y axis, relative to helicopter axes	Ft/Sec

Symbol	Description	Unit
$\dot{w}$, w w or w_A	Linear inertial velocity (and acceleration) components along helicopter Z axis	Ft/Sec_2 Ft/Sec
w_B	Linear inertial velocity along load Z axis	Ft/Sec
w_{BA_n}, $\dot{z}_{BA_n}$	Difference between (n^{th} cable) lower attach point velocity and (n^{th} cable) upper attach point velocity, along helicopter Z axis, relative to helicopter axes	Ft/Sec
x	Body axis coordinate in X direction	-
x_A, x_{A_n}	Cable (or n^{th} cable) upper attach point along helicopter X axis relative to the helicopter-fixed axes	-
x_B, x_{B_n}	Cable (or n^{th} cable) lower attach point along load X axis relative to the load-fixed axes	-
x_{BA_n}	Difference between n^{th} cable lower attach point position and n^{th} cable upper attach point position, along helicopter x axis, relative to helicopter axes	Ft
y	Body axis coordinate in y direction	-
y_A, y_{A_n}	Cable (or n^{th} cable) upper attach point along helicopter y axis relative to the helicopter - fixed axes	-
y_B, y_{B_n}	Cable (or n^{th} cable) lower attach point along load y axis relative to the load-fixed axes	-
y_{BA_n}	Difference between n^{th} cable lower attach point position and n^{th} cable upper attach point position, along helicopter y axis, relative to helicopter axes	Ft
z	Body axis coordinate in z direction	-
z_A, z_{A_n}	Cable (or n^{th} cable) upper attach point along helicopter z axis relative to the helicopter - fixed axes	-
z_B, z_{B_n}	Lower cable (or n^{th} cable) lower attach point along load z axis relative to the load-fixed axes	-

Symbol	Description	Unit
z_{BA_n}	Difference between n^{th} cable lower attach point position and n^{th} cable upper attach point position, along helicopter z axis, relative to helicopter axes	Ft
$\angle G(j\omega)$	Phase angle	Deg
α_{FUS}	Angle of attack of fuselage (includes rotor downwash effects)	Rad
$\alpha_L, \dot{\alpha}_L$	Sling load angle of attack (and angular rate)	Rad Rad/Sec
β	Fuselage sideslip angle	Rad
β'	Local sideslip angle of rotors	Rad
$\beta_L, \dot{\beta}_L$	Sling load angle (and angular rate) of slip	Rad Rad/Sec
$\beta_{COMMAND}$ $\dot{\beta}_{COMMAND}$	Sling load sideslip (and angular rate) command	Rad Rad/Sec
$\beta_\epsilon, \dot{\beta}_\epsilon$	Sling load sideslip (and angular rate) error between command and actual sideslip angle (and angular rate)	Rad Rad/Sec
δ_3	Forward rotor delta three designation	Deg
δ_B	Longitudinal stick cockpit control	In
δ_C	Collective stick cockpit control	In
δ_R	Directional pedal cockpit control	In
δ_S	Lateral stick cockpit control	In
θ	Euler pitch angle	Rad
$\theta_{o_F}, \theta_{o_R}$	Root collective pitch (θ_{o_F} is corrected for δ_3)	Rad
$\theta_{oFM}, \theta_{oRM}$	"Rotor map" 75% blade radius collective pitch	Rad

Symbol	Description	Unit
$\lambda, \lambda_F, \lambda_R$	Complete inflow ratio	-
$\left[\lambda_n\right]^T$	Transpose of the orthogonal matrix of direction cosines of the taut cable after being rotated through the angles λ_{1n} and λ_{2n}	-
λ_1, λ_n	Longitudinal cable (or n^{th} cable) angle parallel to the XZ plane of the helicopter	Rad
$\dot{\lambda}_{1n}$	Longitudinal n^{th} cable velocity parallel to the XZ plane of the helicopter	Rad/Sec
λ_2, λ_n	Lateral cable (or n^{th} cable) angle parallel to the YZ plane of the helicopter	Rad
$\dot{\lambda}_{2n}$	Lateral n^{th} cable velocity parallel to the YZ plane of the helicopter	Rad/Sec
μ	Advance ratio $\frac{u_F}{\Omega R}$, $\frac{u_R}{\Omega R}$	-
ϕ	Euler roll angle and angular rate	Rad
$\Psi_L, \dot{\Psi}_L, \ddot{\Psi}_L$	Sling load yaw angle (and yaw rate) (and yaw acceleration)	Rad Rad/Sec Rad/Sec^2
Ψ_{LIMIT}	Allowable sling load limit cycle amplitude	Rad
Ψ_{max}	Maximum amplitude of the sling load yaw limit cycle	Rad
Ψ_w	Direction from which steady wind blows expressed from 0 to $\pm$ 180°	Rad
ω	Frequency	Rad/Sec
ω_Ψ	Bifilar frequency	Rad, Sec
σ	Real part of complex root	-

LIST OF SYMBOLS - APPENDIX

Symbol	Description	Unit
A_{IC}	Lateral cyclic pitch in body axis	Rad
$A_{ICF'}$	Lateral cyclic pitch control input in body axis - forward rotor	Rad
A_{ICR}	Lateral cyclic pitch control input in body axis - aft rotor	Rad
$A_{ICFR'}$	Lateral cyclic pitch in the shaft normal plane wind axis - forward rotor	Rad
A_{ICFR}	Lateral cyclic pitch in the shaft normal plane wind axis corrected for δ_3 hinging and control phasing - forward rotor	Rad
A_{ICRR}	Lateral cyclic pitch in the plane wind axis - aft rotor	Rad
A_{SL}	Sling load coefficient	-
B_{IC}	Longitudinal cyclic pitch in body axis	Rad
$B_{ICF'}$	Longitudinal cyclic pitch control input in body axis - forward rotor	Rad
B_{ICR}	Longitudinal cyclic pitch control input in body axis - aft rotor	Rad
$B_{ICFR'}$	Longitudinal cyclic pitch in the shaft normal plane wind axis - aft rotor	Rad
B_{ICFR}	Longitudinal cyclic pitch in the shaft normal plane wind axis corrected for δ_3 hinging and control phasing - aft rotor	Rad
B_{ICRR}	Longitudinal cyclic pitch in the shaft normal plane wind axis - aft rotor	Rad
B_{ICFRM}	"Rotor map" shaft normal plane wind axis longitudinal cyclic pitch corrected for δ_3 hinging and control phasing - forward rotor	Rad
B_{ICRRM}	"Rotor map" shaft normal plane wind axis longitudinal cyclic pitch - aft rotor ($B_{ICRRM} = B_{ICRR}$)	Rad

Symbol	Description	Unit
B_{ITF}	Longitudinal cyclic trim in the body axis - forward rotor	Deg
B_{ITR}	Longitudinal cyclic trim in the body axis - aft rotor	Deg
B_{SL}	Sling load coefficient	-
C_{HF}, C_{HR}	Rotor H (drag) force coefficient in shaft normal plane wind axis	-
$C_{H/\sigma}$	"Rotor map" derived rotor drag force coefficient in shaft normal plane wind axes	-
$C_{HF/\sigma}$ $C_{HR/\sigma}$	"Rotor map" derived rotor drag force coefficient in shaft normal plane wind axis	-
$2C_{HF/a\sigma}$ $2C_{HR/a\sigma}$	Rotor H force coefficient calculated with classical equation - shaft normal plane wind axis	-
$C_{HF_{TOT}}$ $C_{HR_{TOT}}$	"Rotor map" derived rotor drag force coefficient corrected for shaft pitching angular velocity	-
CP_F, CP_R	"Rotor map" power coefficient, adjusted for compressibility(Mach number correction applied)	-
$C_{PF/\sigma}$ $C_{PR/\sigma}$	Nondimensional "rotor map" power coefficient adjusted for Mach number correction	-
$C_{PF1/\sigma}$ $C_{PR1/\sigma}$	"Rotor map" nondimensional power coefficient (uncorrected)	-
C_{Q_F}, C_{Q_R}	Rotor torque coefficient ($C_Q = C_P$)	-
$\left[\frac{2C_Q}{a\sigma}\right]_{AERO_F}$	Rotor aero torque required coefficient computed with "classical" equation - forward rotor	-

Symbol	Description	Unit
$\left[\frac{2C_Q}{a\sigma}\right]_{AERO_R}$	Rotor aero torque required coefficient computed with "classical" equation - aft rotor	-
C_{SL}	Sling load coefficient	-
C_{T_F}, C_{T_R}	Rotor thrust coefficient in shaft normal plane wind axis	-
$C_{T_{MAP}}$	"Rotor map" thrust coefficient in shaft normal plane wind axis	-
$C_{T_{F/\sigma}}$ $C_{T_{R/\sigma}}$	"Rotor map" thrust coefficient resolved into shaft normal plane wind axis	-
$C_{TF1/\sigma}$ $C_{TR1/\sigma}$	"Rotor map" thrust coefficient as stored in map tables (rotor wind axis)	-
$\frac{2C_{T_F}}{a\sigma}$	Rotor thrust coefficient computed with classical equation (shaft normal plane wind axis)	-
$\frac{2C_{T_R}}{a\sigma}$		
C_{X_F}, C_{X_R}	Rotor propulsive force coefficient in rotor wind axis	-
$C_{X_{F_{1/\sigma}}}$ $C_{X_{R_{1/\sigma}}}$	"Rotor map" propulsive force coefficient as stored in map tables (rotor wind axis)	-
C_{Y_F}, C_{Y_R}	Rotor side force coefficient in shaft normal plane wind axis	-
$\frac{2C_{Y_F}}{a\sigma}$	Rotor side force coefficient computed with "classical" equation (shaft normal plane wind axis)	-
$\frac{2C_{Y_R}}{a\sigma}$		

Symbol	Description	Unit
D/q	Nondimensional fuselage drag force in body axis	Ft^2
D_{FFR}	Forward on aft rotor interference factor (percent of fwd rotor uniform induced velocity seen by aft rotor)	-
D_{FRF}	Aft on forward rotor interference factor (percent of aft rotor induced velocity seen by fwd rotor)	-
D_L	Sling load drag in body axis of fuselage	Lb
D_{LT}	Sling load drag in body axis of load ($D_{LT} = D/q$)	Ft^2
D_{SL}	Sling load coefficient	-
E_{SL}	Sling load coefficient	-
F	Rotor force coefficient parameter ($\rho\pi R_B^4$)	Lb/Sec^2
$F_{\delta_{B_{BR}}}$	Longitudinal stick breakout force	Lb
$F_{\delta_{B_{FR}}}$	Longitudinal stick frictional force	Lb
F_{SL}	Sling load coefficient	-
G_I, G_Ω	Engine governor torque/rpm gain	Ft-Lb/Rad/Sec
G_β	Sideslip SAS gain - 347 analog control system	$\frac{\text{In. Equiv. Pedal}}{\text{Rad Sideslip}}$
$G_{\Delta P}$	Sideslip SAS gain as mechanized in 347 Demonstrator Task III control	$\frac{\text{In. Equiv. Pedal}}{Lb/Ft^2 \text{ of } \Delta P}$
G_{SL}	Sling load coefficient	-
$G_{\delta_{R_R^\bullet}}, G_{\delta_{B_Q^\bullet}}$ $G_{\delta_{S_P^\bullet}}, G_{\theta_\theta^\bullet}$ $G_{\Phi_{\dot{\Phi}}^\bullet}, G_{\delta_{C_h^\bullet}}$	SAS gain	-

Symbol	Description	Unit
H	Pressure altitude	Ft
H_F, H_R	Rotor (H) drag force in shaft normal plane wind axis	Lb
H_{SL}	Sling load coefficient	-
I_B, I_∞	Individual rotor and drive system polar moment of inertia	Slug-Ft^2
I_{SL}	Sling load coefficient	-
I_T	Engine power turbine moment of inertia	Slug-Ft^2
I_{xx}	Airframe moment of inertia about X axis	Slug-Ft^2
I_{yy}	Airframe moment of inertia about Y axis	Slug-Ft^2
I_{zz}	Airframe moment of inertia about Z axis	Slug-Ft^2
I_{xz}	Airframe product of inertia about X plane	Slug-Ft^2
J_L	Yaw moment of inertia of sling load	Slug-Ft^2
K	Engine power turbine internal damping constant	Ft-Lb/Rad/Sec
K	Factor in sling load equations of motion	-
K_{DF}, K_{DR}	Special error rate damping feedback constant for rotor speed governor stabilization	Ft-Lb/Rad/Sec
K_F, K_R	Rotor shafting spring constant in rotor speed governor circuit	Ft-Lb
K_{SL}	Sling load coefficient	-
K_β	(-) Tangent of forward rotor delta three angle	-
ℓ, L	Total airframe rolling moment in aircraft body axis	Ft-Lb

Symbol	Description	Unit
$\mathcal{L}/q$	Nondimensional fuselage rolling moment, body axis	Ft^3
L/q	Nondimensional fuselage lift in body axis	Ft^2
L'	Rolling moment contribution of rotor T,H, and Y forces about aircraft c.g.	Ft-Lb
L_{FUS}	Fuselage rolling moment in body axis	Ft-Lb
L_{HF}, L_{HR}	Rotor lateral hub moment due to flapping expressed in shaft normal plane wind axis	Ft-Lb
L_L	Average sling load cable length below attachment point	Ft
M	Total airframe pitching moment in aircraft body axis	Ft-Lb
M/q	Nondimensional fuselage pitching moment in body axis	Ft^3
M'	Pitching moment contribution of rotor T, H, and Y forces about aircraft c.g.	Ft-Lb
M_{FUS}	Fuselage pitching moment in body axis	Ft-Lb
M_H	Helicopter mass in sling load equations of motion	Slugs
M_{HF}, M_{HR}	Rotor longitudinal hub moment due to flapping - expressed in shaft normal plane wind axis	Ft-Lb
M_{oF}, M_{oR}	Advancing tip Mach number of rotor for "rotor map" calculations	M
M_{REF_F}, M_{REF_R}	Reference advancing tip Mach number of rotor at which maps were calculated	M
M_{SL}	Sling load coefficient	-

Symbol	Description	Unit
M_T	Sling load coefficient	-
M_w	Mass moment of blade about flapping hinge used in hub moment calculations	Slug-Ft
N	Total airframe yawing moment in aircraft body axis	Ft-Lb
N/q	Nondimensional fuselage yawing moment in body axis	Ft^3
N'	Yawing moment contribution of rotor T, H, and Y forces about aircraft c.g.	Ft-Lb
N_{FUS}	Fuselage yawing moment in body axis	Ft-Lb
N_L	Sling load yawing moment resolved into fuselage body axis	Ft-Lb
N_{LT}	Sling load yawing moment in body axis of load (N_{LT} = N/q)	Ft^3
N_{SL}	Sling load coefficient	-
$P, P_A, \dot{P}$	Component of helicopter angular rate (or acceleration) about aircraft X axis	Rad/Sec Rad/Sec^2
P_{SL}	Sling load coefficient	-
$Q, Q_A, \dot{P}$	Component of helicopter angular rate (or acceleration) about aircraft Y axis	Rad/Sec Rad/Sec^2
Q_{AERO_F}, Q_{AERO_R}	Rotor aerodynamic torque required	Ft-Lb
Q_G	Total initial gas generator output torque	Ft-Lb
Q'_G	Engine output torque	Ft-Lb
Q_{G_F}, Q_{G_R}	Rotor shafting windup torque	Ft-Lb

Symbol	Description	Unit
Q_{SL}	Sling load coefficient	-
R, R_A $\dot{R}$	Component of helicopter angular rate (or acceleration) about aircraft Z axis	Rad/Sec, Rad/Sec^2
R_{B_F}, R_{B_R}	Rotor blade radius	Ft
R_L	Vertical distance between sling load hook attachment and aircraft c.g.	Ft
S	Laplace operator	-
S_{SL}	Sling load coefficient	-
T_F, T_R	Rotor thrust in shaft normal plane wind axis	Lb
T_o	Absolute temperature	°F
T_{SL}	Sling load coefficient	-
$\bar{V}_F(\Omega R_B)$	Average rotor induced velocity used in computing rotor downwash on fuselage	Ft/Sec
V_T	Total aerodynamic velocity	Ft/Sec
V_w	Total steady wind velocity	Ft/Sec
V_x	Longitudinal aircraft velocity in earth coordinates resolved along the helicopter x axis	Ft/Sec
V_y	Lateral aircraft velocity in earth coordinates resolved along the helicopter y axis	Ft/Sec
W_L	Weight of sling load	Lb
W_{SL}	Sling load coefficient	-
X, $\dot{X}$	Total force (and linear velocity) along helicopter X axis	Lb, Ft/Sec

Symbol	Description	Unit
X_{FUS}	Fuselage X force expressed in body axis	Lb
X_{M2}	Simulator fore and aft position	Ft
X_{SL}	Sling load coefficient	
$Y,\dot{Y}$	Total force (and linear velocity) along helicopter Y axis	Lb, Ft/Sec
Y_F,Y_R	Rotor side force in shaft normal plane wind axis	Lb
Y_{FUS}	Fuselage Y force expressed in body axis	Lb
Y/q	Nondimensional fuselage side force in body axis	Ft^2
Y_L	Sling load side force in body axis of fuselage	Lb
Y_{LT}	Sling load side force in body axis of load ($Y_{LT} = Y/q$)	Ft^2
Y_{M2}	Simulator side position	Ft
$Z,\dot{Z}$	Total force (and linear velocity) along helicopter Z axis	Lb, Ft/Sec
Z_{FUS}	Fuselage Z force expressed in body axis	Lb
Z_{M2}	Simulator vertical position	Ft
a	Rotor blade section lift curve slope	Rad^{-1}
a_L	Cable separation (distance from forward to aft cable attachment)	Ft
a_{o_F},a_{o_R}	Rotor coning angle	Rad
a_{1_F},a_{1_R}	Longitudinal first harmonic flapping coefficient	Rad
b	Number of blades per rotor	-
b_{1F},b_{1R}	Lateral first harmonic flapping coefficient	Rad

Symbol	Description	Unit
c	Blade chord	Ft
e	Rotor flapping hinge offset	Ft
f_e	Equivalent flat plate area (drag) of fuselage	Ft^2
g	Acceleration due to gravity	Ft/Sec^2
$\dot{h}$	Vertical rate of climb in inertial axis ($h = -Z$)	Ft/Sec
h_F, h_R	Vertical distance from helicopter c.g. to rotor hub measured parallel to helicopter Z axis	Ft
h_c	Vertical distance between the required helicopter c.g. and the wind tunnel model test c.g.	Ft
i_F, i_R	Rotor shaft incidence angles	Deg
ℓ_F, ℓ_R	Longitudinal distance from helicopter c.g. to projection of rotor hub on the X axis	Ft
ℓ_c	Longitudinal distance between the required helicopter c.g. and the wind tunnel test c.g.	Ft
m_L	Mass of sling load	Slugs
q	Local dynamic pressure on fuselage	Lb/Ft^2
q_L	Local dynamic pressure as seen by sling load	Lb/Ft^2
u, $\dot{u}$	Linear inertial velocity (and acceleration) components along helicopter X axis	Ft/Sec Ft/Sec^2
u_F, u_R	Longitudinal velocity component at the rotor parallel to local wind and in shaft normal plane	Ft/Sec

Symbol	Description	Unit
u_{F_1}, u_{R_1}	Longitudinal velocity component in body axis corrected for rotor angular pitching rate (includes wind)	Ft/Sec
u_{F_2}, u_{R_2}	Longitudinal velocity component at rotor corrected for rotor angular rate and resolved into shaft normal plane	Ft/Sec
u_{g_F}, u_{g_R}	Gust velocity component parallel to aircraft X axis as seen by forward rotor or aft rotor	Ft/Sec
u_L	Sling load longitudinal velocity expressed in fuselage body axis system	Ft/Sec
$\dot{u}_{Po}$	Longitudinal specific force	Ft/Sec^2
$\dot{u}_{PoF}$	Filtered specific force	Ft/Sec^2
$\dot{u}_{Po_{FB}}$	Simulator longitudinal specific force feedback	Ft/Sec^2
u_T	Total fuselage aerodynamic velocity component along body X axis (includes wind)	Ft/Sec
u_w	Component of steady wind velocity along aircraft X axis	Ft/Sec
$v, \dot{v}$	Linear inertial velocity (and acceleration) components along helicopter Y axis	Ft/Sec, Ft/Sec^2
v_{F_1}, v_{R_1}	Lateral velocity in body axis corrected for rotor angular rolling and yawing rates (includes wind)	Ft/Sec
v_{F_2}, v_{R_2}	Lateral velocity component at rotor corrected for rotor angular rate and resolved into shaft normal plane	Ft/Sec
v_{g_F}, v_{g_R}	Gust velocity component parallel to aircraft Y axis as seen by forward or aft rotor	Ft/Sec

Symbol	Description	Unit
$v_{INDUCED}$	Rotor uniform induced velocity $v = \sqrt{\frac{C_T \Omega R}{2 \sqrt{\mu^2 + \lambda^2}}}$	Ft/Sec
v_L	Sling load lateral velocity expressed in fuselage body axis system	Ft/Sec
$\dot{v}_{po}$	Lateral specific force	Ft/Sec^2
$\dot{v}_{poF}$	Filtered specific force	Ft/Sec
$\dot{v}_{po_{FB}}$	Simulator lateral specific force feedback	Ft/Sec^2
v_T	Total fuselage aerodynamic velocity component along body Y axis (includes wind)	Ft/Sec
v_w	Component of steady wind velocity along aircraft Y axis	Ft/Sec
$w, \dot{w}$	Linear inertial velocity (and acceleration) components along helicopter Z axis	Ft/Sec
w_F, w_R	$w_F = w_{F_2}$, $w_R = w_{R_2}$	Ft/Sec
w_{F_1}, w_{R_1}	Vertical velocity in body axis corrected for rotor angular pitching rate	Ft/Sec
w_{F_2}, w_{R_2}	Vertical velocity component at rotor corrected for rotor angular rate and resolved into shaft normal plane	Ft/Sec
w_{g_F}, w_{g_R}	Gust velocity component parallel to aircraft Z axis as seen by forward or aft rotor	Ft/Sec
w_L	Sling load vertical velocity expressed in fuselage body axis system	Ft/Sec
$\dot{w}_{Po}$	Normal specific force	Ft/Sec^2
$\dot{w}_{Po_F}$	Filtered normal specific force	Ft/Sec^2

Symbol	Description	Unit
$\dot{w}_{Po_{FB}}$	Simulator normal specific force feedback	Ft/Sec^2
w_T	Total fuselage aerodynamic velocity component along body Z axis (includes wind)	Ft/Sec
$w_{T'}$	Total vertical velocity acting on the fuselage modified for rotor downwash	Ft/Sec
w_w	Component of steady wind velocity along aircraft Z axis	Ft/Sec
x	Body axis coordinate in X direction	-
x_F, x_R	Rotor shaft normal plane wind axis coordinate in X direction	-
y	Body axis coordinate in Y direction	-
y_F, y_R	Rotor shaft normal plane wind axis coordinate in Y direction	-
z	Body axis coordinate in Z direction	-
z_F, z_R	Rotor shaft normal plane wind axis coordinate in Z direction	-
$\alpha_{CAF}, \alpha_{CAR}$	Control axis angle of attack in "rotor map" calculations	Rad
α_{FUS}	Angle of attack of fuselage (includes rotor downwash effects)	Rad
α_L	Sling load angle of attack	Rad
α_{SF}, α_{SR}	Angle of attack of the rotor shaft normal plane	Rad
β_{FUS}	Fuselage sideslip angle	Rad
β'_F, β'_R	Local sideslip angle of forward and aft rotors	Rad

Symbol	Description	Unit
β_L	Sling load angle of slip	Rad
γ	Rotor blade Lock number (blade inertia parameter)	-
γ_{SL_F}	Total left or right lateral swing angle of the forward sling load cable as viewed from rear of aircraft	Rad
γ_{SL_A}	Total left or right lateral swing angle of the aft sling load cable as viewed from rear of aircraft	Rad
δ	Average rotor blade section profile draft coefficient ($\delta = \delta_o + \delta_1 \alpha^2$)	-
δ_o	Constant term in section drag expression	-
δ_1	Coefficient of pressure drag due to lift term in section drag expression	-
δ_3	Forward rotor delta three designation	Deg
δ_B, δ_{B_p}	Longitudinal stick (and pilot) control input	In.
$\delta_{B_{DASH}}$	Longitudinal dash control input	In.
$\delta_{B_{DR}}$	Longitudinal stick driver command input	In.
$\delta_{B_{SAS}}$	Longitudinal SAS control input	In. of equivalent cockpit control
δ_{B_T}	Longitudinal stick trim control input	In.
δ_c, δ_{c_p}	Collective stick (and pilot) control input	In.
δ_{M_B}	Longitudinal stick magnetic brake control input	In.

Symbol	Description	Unit
δ_{M_R}	Rudder pedal magnetic brake control input	In.
δ_{M_S}	Lateral stick magnetic brake control input	In.
δ_R, δ_{R_p}	Directional pedal (and pilot) control input	In.
$\delta_{R_{DR}}$	Rudder pedal driver command input	In.
$\delta_{R_{SAS}}$	Directional SAS control input	In. of equivalent cockpit control
δ_{R_T}	Rudder pedal trim control input	In.
δ_S, δ_{S_p}	Lateral stick (and pilot) control input	In.
$\delta_{S_{DR}}$	Lateral stick driver command input	In.
$\delta_{S_{SAS}}$	Lateral SAS control input	In. of equivalent cockpit control
δ_{S_T}	Lateral stick trim control input	In.
$\Delta C_{HF}, \Delta C_{HR}$	Correction to "rotor map" derived rotor drag force coefficient arising from angular pitch rate at rotor	-
$\frac{\Delta C_{P_{F_1}}}{\sigma M_{oF}}$	"Rotor map" power coefficient component due to compressibility (reference value for Mach number at which maps were calculated)	-
$\frac{\Delta C_{P_{F_1}}}{\sigma M_{REF_F}}$	"Rotor map" power coefficient component due to compressibility (for Mach number at which aircraft is operating)	-

Symbol	Description	Unit
$\Delta(D/q)$	Nondimensional fuselage drag correction due to Δfe	Ft^2
Δfe	Difference between actual fuselage fe and fe used in fuselage aero tables	Ft^2
$\Delta (L/q)$	Nondimensional fuselage lift correction due to Δfe	Ft^2
ΔP	Differential SAS port pressure	Lb/Ft^2
$\Delta(Y/q)$	Nondimensional fuselage side force correction due to Δfe	Ft^2
$\Delta\Omega_F, \Delta\Omega_R$	$\Delta\Omega_F = \Omega - \Omega_F$, $\Delta\Omega_R = \Omega - \Omega_R$ = Engine speed (-) rotor speed	Rad/Sec
ζ	Second-order upper boost actuator critical damping ratio	
$\theta, \dot{\theta}$	Euler pitch angle and angular rate	Rad Rad/Sec
θ_B	Simulator beam pitch angle	Deg
θ_C	Simulator cockpit pitch angle	Deg
$\theta_{.75}$	.75 blade radius collective pitch angle	Rad
θ_{BF}, θ_{BR}	Longitudinal cockpit DCP control input expressed in terms of blade pitch angle	Deg
θ_{CF}, θ_{CR}	Cockpit collective control input expressed in terms of blade pitch angle	Deg
θ_L	Angle between load X axis and helicopter X axis	Rad
θ_{RF}, θ_{RR}	Cockpit directional control input expressed in terms of blade pitch angle	Deg
θ_{SF}, θ_{SR}	Cockpit lateral control input expressed in terms of blade pitch angle	Deg

Symbol	Description	Unit
θ_{TF}, θ_{TR}	Root collective pitch at full-down collective stick	Rad
θ_t	Linear rotor blade twist (root to tip)	Rad
$\theta_{AP}, \theta_{AS}, \theta_{FP}, \theta_{FS}$	Combined cockpit and SAS mixed controls at aft and forward swiveling and pivoting upper boost actuators	Deg
$\theta_{APP}, \theta_{ASP}, \theta_{FPP}, \theta_{FSP}$	Cockpit controls after mixing at aft (or forward) rotor pivoting and swiveling actuators	Deg
$\theta_{AP_{SAS}}, \theta_{AS_{SAS}}, \theta_{FP_{SAS}}, \theta_{FS_{SAS}}$	SAS controls after mixing at aft (or forward) rotor pivoting and swiveling SAS links	Deg
θ_{oF}, θ_{oR}	Root collective pitch (θ_{oF} is corrected for δ_3)	Rad
$\theta_{oFM}, \theta_{oRM}$	"Rotor map" .75 blade radius collective pitch	Rad
$\theta_{oF'}$	Actual control system root collective pitch input	Rad
$\theta_{oF'\delta_B}$	Rate of change of rotor collective pitch with longitudinal stick - forward rotor	Deg/In.
$\theta_{oF'\delta_C}$	Rate of change of rotor collective pitch with collective stick - forward rotor	Deg/In.
$\theta_{oR\delta_B}$	Rate of change of rotor collective pitch with longitudinal stick - aft rotor	Deg/In.
$\theta_{oR\delta_C}$	Rate of change of rotor collective pitch with collective stick - aft rotor	Deg/In.
λ_F, λ_R	Complete inflow ratio	-

Symbol	Description	Unit
λ'_F, λ'_R	Inflow ratio component normal to the rotor due to free-stream velocity	-
$\lambda_{SL}, \dot{\lambda}_{SL}, \ddot{\lambda}_{SL}$	Lateral cable angle, angular velocity, and angular acceleration (parallel to YZ plane of helicopter)	Rad Rad/Sec Rad/Sec^2
μ_F, μ_R	Advance ratio $\frac{u_F}{\Omega R}$, $\frac{u_R}{\Omega R}$	-
μ_{FRM}, μ_{RRM}	"Rotor map" advance ratio	-
$\mu_{SL}, \dot{\mu}_{SL}, \ddot{\mu}_{SL}$	Longitudinal cable angle, angular velocity, and angular acceleration (parallel to XZ plane of helicopter)	Rad Rad/Sec Rad/Sec^2
$\nu_{SL}, \dot{\nu}_{SL}, \ddot{\nu}_{SL}$	Lateral differential cable angle, angular velocity, and angular acceleration (parallel to XY plane of helicopter)	Rad Rad/Sec Rad/Sec^2
ρ_o	Air density	Slugs/Ft^3
ρ	Air density at sea level	Slugs/Ft^3
$\sigma, \sigma_F, \sigma_R$	Rotor solidity ratio $\frac{bc}{\pi R}$	-
ΣQ_{AERO}	Sum of forward and aft rotor aerodynamic torque required	Ft/Lb
τ	Rotor first harmonic flapping time constant	Sec
$\tau_{\lambda_F}, \tau_{\lambda_R}$	Rotor inflow lag time constant	Sec
τ_Ω	Engine gas generator lag time constant	Sec
$\phi, \dot{\phi}$	Euler roll angle and angular rate	Rad Rad/Sec
ϕ_c	Simulator cockpit roll angle	Deg

Symbol	Description	Unit
ϕ_P	Forward rotor δ_3 control phase angle	Deg
$\phi_{,P}$	Special control phase angle used to correct "rotor map" cyclic pitch values when rotor data is computed with phase angles equal to the δ_3 angle instead of control phase angle	Deg
$\Psi, \dot{\Psi}$	Euler yaw angle and angular rate	Rad Rad/Sec
ψ_B	Simulator beam yaw angle	Deg
ψ_C	Simulator cockpit yaw angle	Deg
ψ_w	Direction from which steady wind blows expressed from 0° to ±180°	Rad
ω_n	Undamped natural frequency of upper boost actuator	Rad/Sec
Ω	Engine output speed	Rad/Sec
Ω_o	Reference governor speed	Rad/Sec
Ω_F, Ω_R	Rotor speed	Rad/Sec
(ΩR_F) (ΩR_P)	Tip speed of the forward and aft rotors	Ft/Sec

14284-74